BioMed Research International

Classic Drugs with Novel Mechanisms for Orthopaedics

Lead Guest Editor: Shen Liu
Guest Editors: Yusheng Li, Xiao Wang, and wei Chen

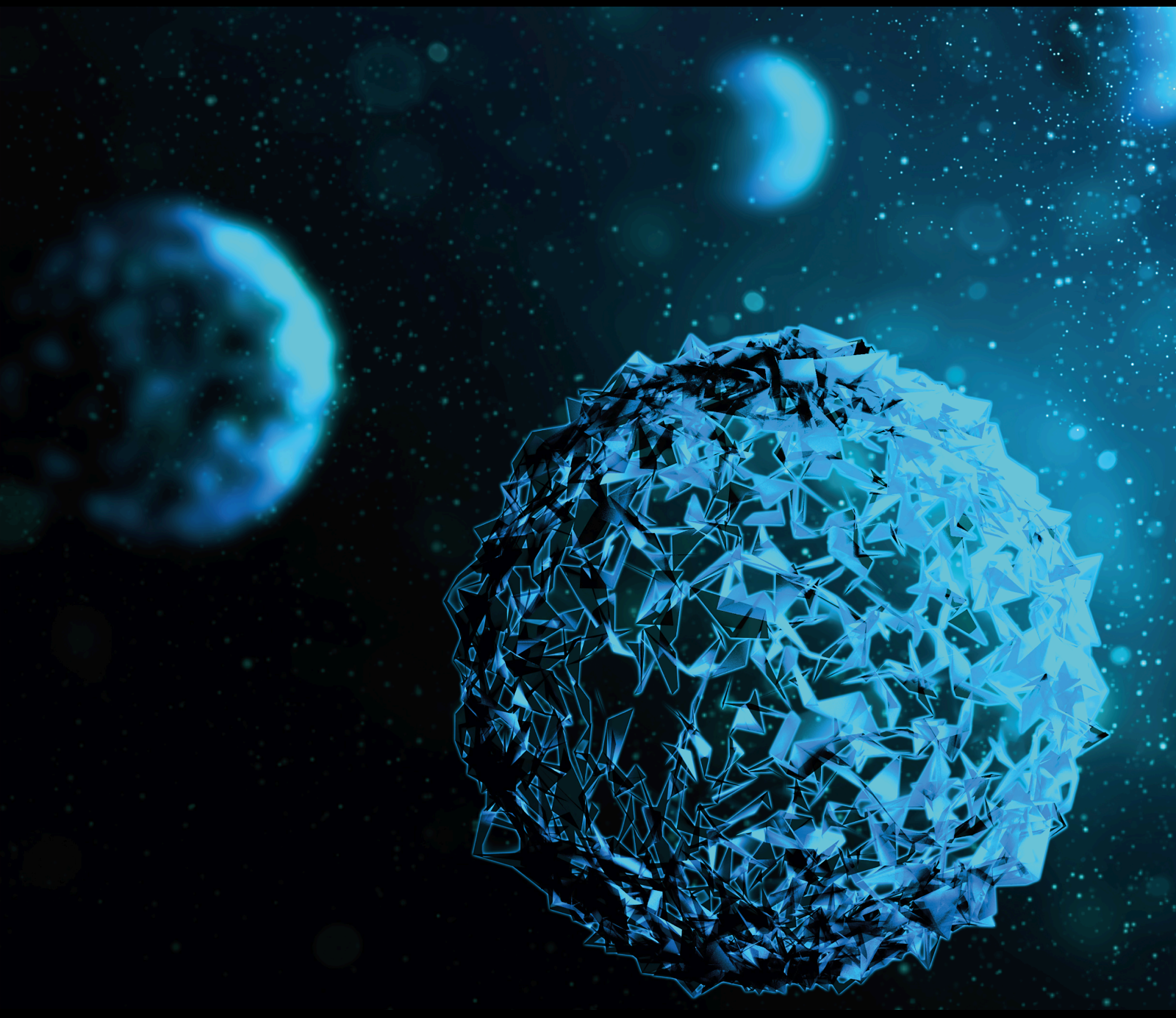

Classic Drugs with Novel Mechanisms for Orthopaedics

BioMed Research International

Classic Drugs with Novel Mechanisms for Orthopaedics

Lead Guest Editor: Shen Liu
Guest Editors: Yusheng Li, Xiao Wang, and wei Chen

Section Editors

Penny A. Asbell, USA
David Bernardo, Spain
Gerald Brandacher, USA
Kim Bridle, Australia
Laura Chronopoulou, Italy
Gerald A. Colvin, USA
Aaron S. Dumont, USA
Pierfrancesco Franco, Italy
Raj P. Kandpal, USA
Fabrizio Montecucco, Italy
Mangesh S. Pednekar, India
Letterio S. Politi, USA
Jinsong Ren, China
William B. Rodgers, USA
Harry W. Schroeder, USA
Andrea Scribante, Italy
Germán Vicente-Rodriguez, Spain
Momiao Xiong, USA
Hui Zhang, China

Academic Editors

Stem Cells and Tissue Engineering

Mohammad Amin Abdollahifar, Iran
Tarun Agarwal, India
François Berthiaume, USA
Jose' Luis Calvo-Guirado, Spain
Malay Chaklader, USA
Magali Cucchiarini, Germany
Willeke F. Daamen, The Netherlands
Costantino Del Gaudio, Italy
Li Duan, China
Francesco Fascetti Leon, Italy
Venkata N. S. Garikipati, USA
Kirsten Haastert-Talini, Germany
Esmaiel Jabbari, USA
Jangho Kim, Republic of Korea
Annunziata Mauro, Italy
Kibret Mequanint, Canada
Vitale Miceli, Italy
Bruna Sinjari, Italy
María Troya, Spain
Przemko Tylzanowski, Belgium
Imran Ullah, Pakistan
Junji Xu, China
Kai-Chiang Yang, Taiwan

Contents

Rapamycin-Induced Autophagy Promotes the Chondrogenic Differentiation of Synovium-Derived Mesenchymal Stem Cells in the Temporomandibular Joint in Response to IL-1β

Wenjing Liu, Haiyun Luo, Ruolan Wang, Yiyuan Kang, Wenting Liao, Yangpeng Sun, Guodong Chen, and Longquan Shao

Research Article (12 pages), Article ID 4035306, Volume 2020 (2020)

Hindawi
BioMed Research International
Volume 2021, Article ID 8882355, 7 pages
https://doi.org/10.1155/2021/8882355

Research Article

The Effect of Stromal-Derived Factor 1α on Osteoinduction Properties of Porous β-Tricalcium Phosphate Bioceramics

Fangchun Jin,[1] Qixun Cai,[1] Wei Wang,[2] Xiaohui Fan,[3] Xiao Lu,[4] Ning He,[5] and Jing Ding[1]

[1]*Department of Pediatric Orthopaedics, Xinhua Hospital, School of Medicine, Shanghai Jiao Tong University, No. 1665, Kongjiang Road, Shanghai 200092, China*
[2]*Department of Orthopaedics, Shanghai No. 6th Hospital, School of Medicine, Shanghai Jiao Tong University, No. 600, Yishan Road, Shanghai 200233, China*
[3]*Shanghai Key Laboratory of Advanced High Temperature Materials and Precision Forming, School of Materials Science and Engineering, Shanghai Jiao Tong University, Shanghai 200240, China*
[4]*School of Materials Science and Engineering, South China University of Technology, Guangdong 510641, China*
[5]*Department of Orthopaedics, Shanghai Eighth People's Hospital, No. 8 Caobao Rd., Shanghai 200235, China*

Correspondence should be addressed to Ning He; desmask@163.com and Jing Ding; dingjing@xinhuamed.com.cn

Received 30 August 2020; Revised 15 November 2020; Accepted 7 April 2021; Published 29 April 2021

Academic Editor: Valentina Russo

β-Tricalcium phosphate (TCP) is a type of bioceramic material which is commonly used for hard tissue repair and famous of its remarkable biocompatibility and osteoconductivity with similar composition to natural bone. However, TCP lacks osteoindcutive properties. Stromal-derived factor 1α (SDF-1α) can promote bone regeneration with excellent osteoinduction effect. In this study, SDF-1α was loaded into TCP to investigate the *in vitro* effects of SDF-1α on the osteoinductive properties of TCP. *In vitro* studies showed that SDF-1α/TCP scaffold significantly stimulated the expression of osteopontin and osteocalcin. As to the *in vivo* studies, the rabbit bone defect model showed that SDF-1α stimulated more new bone formation. In conclusion, SDF-1α/TCP bioceramic scaffolds could further promote bone regeneration compared to pure TCP bioceramics.

1. Introduction

Diseases such as infection, congenital deformity, trauma, and tumor excision can result in segmental bone defects, which always lead to dysfunction and osteogenesis obstacles [1]. Reconstruction of segmental bone defects generally requires multiple surgical interventions, each procedure being associated with risks of perioperative complications [2]. Bone tissue engineering techniques that seed cells, such as bone mesenchymal stem cells (BMSCs), into scaffolds provide an optimal method to repair large bone defects [3].

Bioceramics are crucial components for bone tissue engineering applications and have been widely studied [4]. Among them, β-tricalcium phosphate (β-$Ca_3(PO_4)_2$, TCP) is commonly used for hard tissue repair [5]. It is famous for its remarkable biocompatibility and osteoconductivity and its similarity in composition to natural bone [5]. It can also be used as scaffold for delivery of cells and growth factors. However, poor osteoinductive properties obviously limit its clinic application [6].

Cellular factors play an important role in bone regeneration, especially in bone tissue engineering [7]. Among them, stromal cell-derived factor-1α (SDF-1α) signaling pathway is well known for its osteoinductivity [8]. Moreover, SDF-1α can recruit migration of mesenchymal stem cells [9] and create a matrix environment conducive to cartilage and bone defect repair [10, 11]. However, loading techniques of SDF-1α into TCP remain a bottleneck in bone tissue engineering [12].

Taking all these aspects into consideration, combining SDF-1α and TCP bioceramics should be a promising path to create an osteoinductive scaffold. In this study, porous SDF-1α/TCP composite bioceramics were prepared to

investigate the *in vitro* and *in vivo* effects of SDF-1α on the osteogenesis and osteoinductive properties of TCP.

2. Materials and Methods

2.1. Preparation for SDF-1α-Loaded TCP Porous Ceramics. Cylindrical porous TCP bioceramics (5 mm diameter and 10 mm length) were prepared as described in a previous study [6], with a homogeneous porosity of 75%, pore diameter of $500 \pm 100\,\mu$m, and interconnection size of $120\,\mu$m. Briefly, TCP submicron powders were sieved and mechanically suspended in aqua pura. An organic skeleton made up of polymethylmethacrylate beads was impregnated with the TCP slurry. After drying, the ceramic/polymeric composite were debinded and sintered at 1100°C to obtain the porous bioceramic.

TCP were immersed in 5-time concentrated simulated body fluid at 37°C for 24 hours [13]. A dense layer of amorphous calcium phosphate that could be used as a seeding surface for the deposition of a crystalline layer was formed. The scaffolds were then immersed in a supersaturated solution of calcium phosphate containing SDF-1α at 37°C for 48 hours. TCP scaffolds that superficially absorbed SDF-1α by immersing in solution containing SDF-1α was used as positive control.

Before SEM characterization, the bioceramic specimens were thoroughly degreased and dried to eliminate any outgassing from organic contamination and water, then prepared by coating with a 10 nm thick Au film deposited by sputtering prior to microscopy. The microstructure of the porous samples was examined under SEM (XL-30, Phillips) with a lens detector at an accelerator voltage of 10.0 kV and different calibrated magnification levels.

2.2. In Vitro SDF-1α Release Kinetics. The release kinetics of the total amount of SDF-1α was assessed by measuring the extract ELISA using the SDF-1α ELISA Development kit under the manufacturer's instructions. Briefly, after fabrication, SDF-1α/TCP scaffolds were placed in PBS in 12-well plates and incubated at 37°C on a shaker table. At determined time points, the supernatant of each well was collected and replaced with fresh buffer solution. The amount of released SDF-1α was determined by the correlation of the measured amount to a standard curve.

2.3. Separation and Culture of Bone Marrow Mesenchymal Stem Cells (BMSCs). 5 ml bone marrow aspirate was collected from healthy volunteers [14], mixed with 10 ml of α-MEM medium (Gibco) (100 IU/ml heparinized), and then transferred to a 10 cm petri dish containing 10% fetal bovine serum (Hyclone), 1% 100 IU/ml penicillin, and 100 mg/ml streptomycin (Hyclone) and cultured in a humidified 37°C/5% CO_2 incubator. After 3 days, nonadherent cells were washed with phosphate-buffered saline (PBS). The medium was changed every 3 days until attaining 80–90% confluence; the BMSCs were digested with 0.25% trypsin (Gibco) and subcultured.

2.4. Combination and Cell Culture of BMSCs on Scaffolds. The scaffolds were placed into a 24-well plate; the second passage of BMSCs was suspended at a density of 4×10^4 cells/ml and loaded into TCP substrates. The cell–substrate complex was incubated at 37°C/5% CO_2 for 2 hours. After confirmation of BMSCs being attached to the substrate, the complex was removed in another 24-well plate and cultured for 4 hours, 7 days, 14 days, and 21 days, respectively. 2 ml medium was added in every well and replaced every other day.

2.5. Cell Viability and Assessment. After 4 hours and 7 days of cell–substrate complex culture, the plate was washed twice with sterile PBS, half of the substrate was then transferred to a new 24-well plate, and 1 ml MTT (Sigma company) working liquid (0.5 mg/ml) was added to each well. The substrates were immersed and incubated at 37°C/5% CO_2 for 4 hours. MTT working solution was then removed, and 1 ml isopropanol hydrochloride (0.04 N) was added to each well after the substrates were crushed. The purple crystal particles were repeatedly blown to ensure complete dissolution and then stood for 10 min. The purple solution was transferred to an EP tube and centrifuged at $12000 \times$ g for 5 min to remove the TCP powder. The supernatant was used to measure the light absorption value on the spectrophotometer, with the wavelength of 570 nm and the reference wavelength of 650 nm. The fragments of the carrier were weighed after drying at 50°C, and the cell activity was expressed as light absorption value per gram of the carrier.

2.6. Detection of Osteopontin. At 7, 14, and 21 days of culture, the culture medium was collected, stored at -70°C, dissolved at room temperature, and detected by anti-human ELISA kit. Standard solution or sample 50 μl was added to 96-well plates. 100 μl analytical solution was added to each well and incubated at room temperature for 2 hours. Each well was washed 4 times with buffer solution. 200 μl antibody containing horseradish peroxidase was added and incubated for 2 hours at room temperature. The content of each well was then removed and washed with buffer solution for 4 times; 200 μl substrate was then added and incubated at room temperature away from light for 30 minutes. The absorbance of 450 nm wavelength was determined by adding 50 μl termination solution to each well, and the corrected wavelength was 570 nm. The results were compared with the standard solution of human osteopontin.

2.7. Detection of Osteocalcin. At 7, 14, and 21 days of culture, the culture medium was collected, stored at -70°C, dissolved at room temperature, and detected by anti-human ELISA kit. 25 μl of standard solution or sample was added to 96-well plates. 100 μl antibody containing horseradish peroxidase was added to each well and incubated in a horizontal oscillator at room temperature for 2 hours. Each well was washed for 3 times, 100 μl chromogenic agent was then added, placed on a horizontal oscillator, and incubated at room temperature for 30 minutes. The absorbance of 450 nm wavelength was detected by adding 200 μl termination solution to each well, and the corrected wavelength was 650 nm. The results were compared with the standard solution of human osteocalcin.

2.8. Animal Experiments. The animal experiments were carried out according to the policies of Shanghai Jiao Tong University School of Medicine and the National Institutes

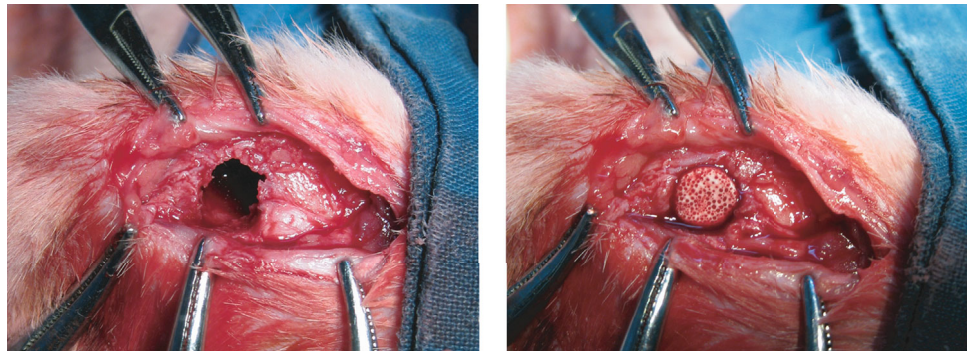

Figure 1: The bone defect model was established in the femoral condyle parallel of the New Zealand rabbits, and the bone cavity was filled with porous SDF-1α/TCP bioceramic.

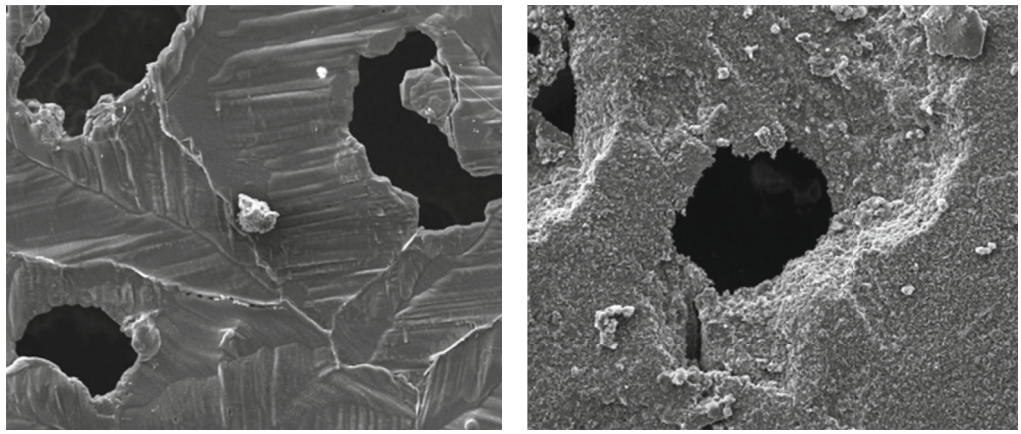

(a) (b)

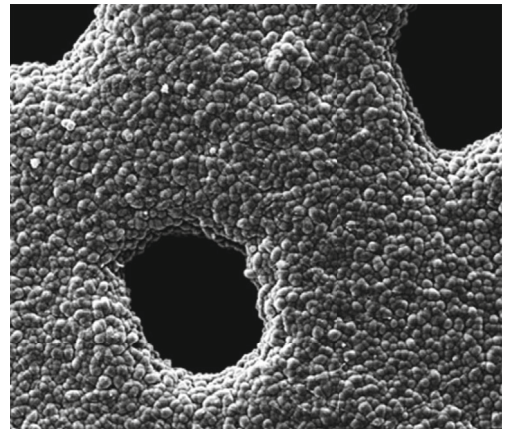

(c)

Figure 2: Electron microscopic view of the surface of the porous TCP bioceramics: (a) without pretreatment, the surface is smooth and not suitable for loading drugs; (b) after pretreatment, the surface becomes rough and can do well in drug loading; (c) TCP loaded with SDF-1α and Ca-P deposition.

of Health. In brief, 3-month-old New Zealand rabbits weighing 2.5 ± 0.3 kg were randomly divided into three groups. For the duration of the experiment, rabbits were housed individually in cages and provided free access to water and fed a commercial pellet diet. Six animals were used per material. The scaffolds were sterilized by gamma radiation before implantation. After administering anesthesia by 0.5 mg/kg of acepromazine (Calmivet–Vetoquinol) and 10 mg/kg of ketamine, rabbits were operated in rigorous aseptic conditions using the lateral knee approach. First, a femoral condylar cavity paralleling with the joint surface of 5 mm in diameter and 10 mm in depth was drilled at the point 1 cm above the femoral condyle, and the cortical bone window was removed with scissors. For both the SDF-1α/TCP

composite and TCP bioceramic groups, the scaffolds were then inserted in the cavity, as is shown in Figure 1. The cavity was left unfilled in the blank control group.

2.9. Histological Preparation and Analysis. The samples were harvested and observed 24 weeks after implantation. All rabbits were sacrificed, and the femoral condyles were extracted. The samples were fixed in 10% formaldehyde solution buffered with PBS (pH 7.3) for 2 weeks and then rinsed under tap water for 12 h. Gradient alcohol concentration (70–100%) was used in the dehydration process for 24 h. The samples were then embedded in methylmethacrylate without decalcification. The cross sections were cut to about 200 μm thickness with a Leitz Saw Microtome 1600 (Wetzlar, Germany), ground, and polished to about 50 μm thickness with an Exakt Grinder (Norderstedt, Germany). Finally, the samples were stained with Van Gieson's picrofuchsin stain (V-G stain).

2.10. Histomorphometric Analysis. New bone volume (NBV) was measured on two sections for five fields per V-G-stained section with the help of an eyepiece micrometer (KPL 16, Carl Zeiss, Germany) and an ocular integrator with 100 points (KPL 8, Zeiss, Germany). The results were studied in two sections per sample using light microscopy [15]. New bone volume (%) represents the percentage of implant occupied by new bone tissue.

2.11. Statistical Analysis. The data in this study were analyzed using SPSS11.0 statistical software (SPSS Inc., Chicago, IL). The results were expressed as mean ± standard deviation, the variable data were analyzed by one-way ANOVA, and $p < 0.05$ was considered significant.

3. Results

3.1. Characterization of the Composites. According to the previous studies, bioceramics have a homogeneous pore size of 500 ± 100 μm, an interconnection diameter of 120 μm, and a uniform porosity of 75%. As is shown in Figure 2, observed under an electron microscope, the surface of TCP without pretreatment is too smooth for drugs or cell factors to load. It becomes suitable for drug loading after surface roughening. The SDF-1α/TCP composite exhibited looser and rougher surfaces with more irregular micropores and larger crystals than TCP bioceramic scaffolds, which corresponds to the results of the specific surface of TCP.

3.2. In Vitro SDF-1α Release Kinetics. The total amount and released concentration of SDF-1α have a positive correlation with the loading method (supersaturated or coated), as is shown in Figure 3. The amount of SDF-1α released from TCP with supersaturated SDF-1α liquid is higher than that from SDF-1α-coated TCP. Almost no SDF-1α can be detected in supersaturated solution.

3.3. In Vitro Cell Viability and Osteogenic Assessment. TCP scaffold with supersaturated SDF showed the highest cell viability as well as more expression of osteopontin and osteocalcin. TCP scaffold with coating SDF-1α took the second place.

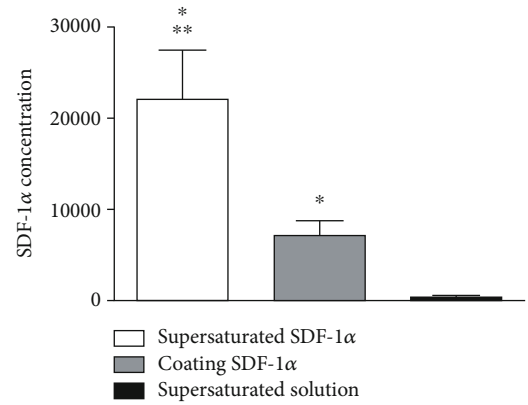

Figure 3: SDF-1α concentration in different preparation methods (*VS supersaturated solution, $p < 0.05$; **VS coating SDF-1α, $p < 0.05$).

Cell viability increased with time and was significantly higher in SDF-1α/TCP composites. The expression of OP and OC showed no significant difference between the TCP group and the other two groups on day 7 but was obviously lower than the others on day 14 and day 21, as is shown in Figure 4.

3.4. Histological Analysis. Newly formed bone, osteoid tissue, and residual material are, respectively, stained red, green, and black in V-G staining. After 24 weeks of implantation, newly formed bone, rich in osteocyte lacunae, was observed on the surface of all residual implants. The lining cells and osteoblastic cells are, respectively, indicated in Figures 5(e) and 5(f) to reflect the main actors of new bone formation. Furthermore, osteoblastic cells can be detected on the new bone in the SDF-1α/TCP group. Compared with the other two groups, the SDF-1α/TCP group has more volume of new bone, as is shown in Figure 5. No cellular dysplasia was observed on the surface of any of the materials or in their neighboring areas, and no acute inflammation appeared at the interface of the implants and surrounding tissue.

4. Discussion

Bone scaffolds are a major tool in bone tissue engineering. In this study, SDF-1α/TCP composite bioceramics were prepared to investigate the effects of SDF-1α on the osteoinductive properties of TCP. Our *in vitro* study showed that SDF-1α/TCP scaffolds significantly stimulated the expression of osteopontin and osteocalcin. Meanwhile, in the *in vivo* study, the rabbit bone defect model showed that SDF-1α stimulated more new bone formation. Thereafter, SDF-1α/TCP bioceramic scaffolds could promote bone regeneration and may be an effective way to treat bone defects.

SDF-1α is highly expressed in bone marrow stromal cells, but it is also widely expressed in diverse organs including the brain, heart, liver, and lungs. It has been suggested that SDF-1α is involved in the recruitment of stem cells that differentiate into the cells necessary to repair tissue damage [16, 17]; the function may relate with AKT and Wnt/β-catenin signaling pathway [18, 19]. Further study indicated that DLX2

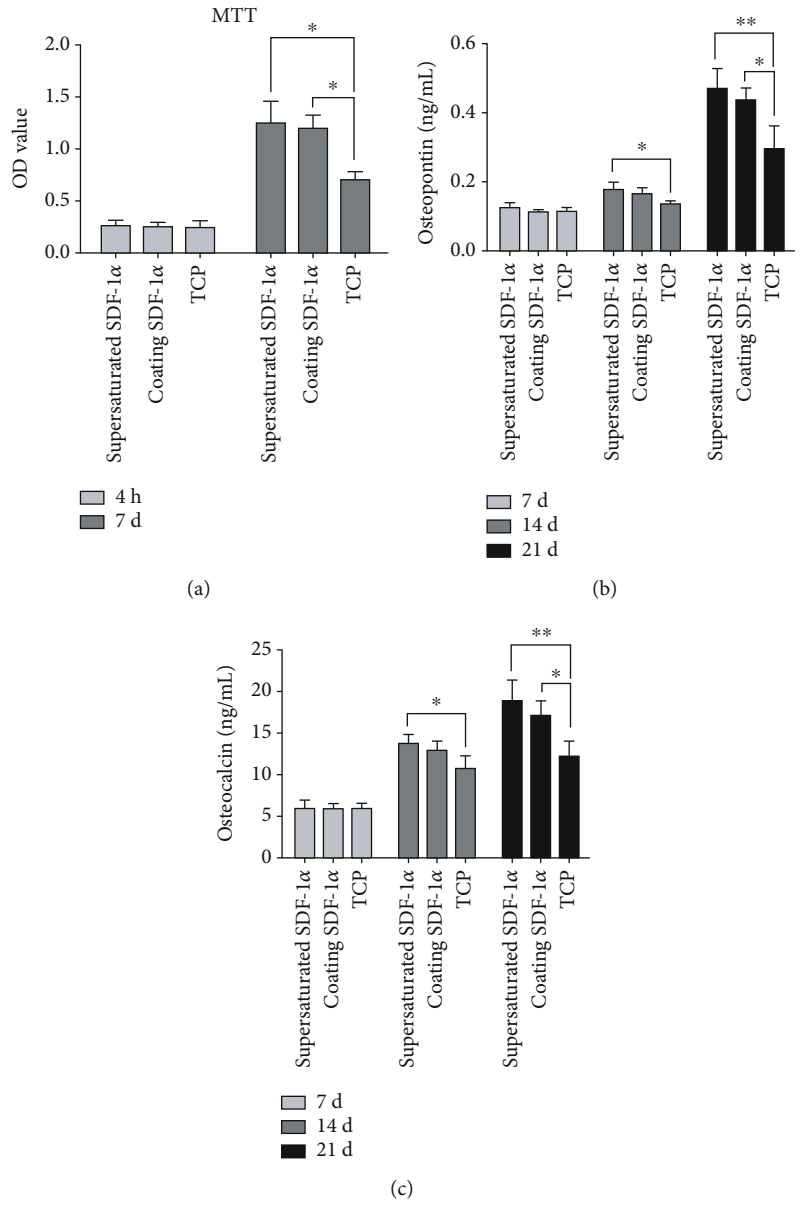

Figure 4: Comparison of different SDF-1α/TCP scaffolds on each time point. (a) OD volume showed after 7 days; cell viability in supersaturated SDF-1α/TCP was highest. (b) Osteopontin and (c) osteocalcin raised as time expansion, at each time point; the supersaturated SDF-1α/TCP group had more protein expression ($^{*}p < 0.05$, $^{**}p < 0.01$).

mediates Wnt/β-catenin signal to promote osteogenic differentiation of BMSCs [20]. A study also showed that TCP implanted in dog mandibles can increase the expression of SDF-1α [21], thus enhancing bone healing processes and stimulating the coordinated actions of osteoblasts and osteoclasts, leading to bone regeneration. In this study, SDF-1α was incorporated into TCP by a bioactive loading technique [13]. Based on the release test, SDF-1α was released from SDF-1α/TCP, which indicated that the osteoinductive properties of SDF-1α can be given to TCP bioceramics. The osteoinductive properties of SDF-1α/TCP is also proved by elevated levels of osteopontin and osteocalcin, but the signaling pathway should be investigated during further study.

The ideal biomaterial candidate for bone regeneration should be resorbable and gradually replaced by the newly formed bone. Based on previous studies of TCP, it has been shown to be gradually replaced by the newly formed bone as a process of osteoconduction [22]. However, despite the osteoconductive properties of biomaterials in bone tissues engineering, the implanted materials should also have osteoinductive properties. Various cellular factors have been used to promote the osteoconductive properties of TCP, but there is a great need of more cellular factors, especially with broad cellular effect. In our study, SDF-1α was loaded into TCP to give osteoinductive properties to TCP. As result, the rabbit bone defect model showed that SDF-1α stimulated more new bone formation although cell-free SDF-1α/TCP

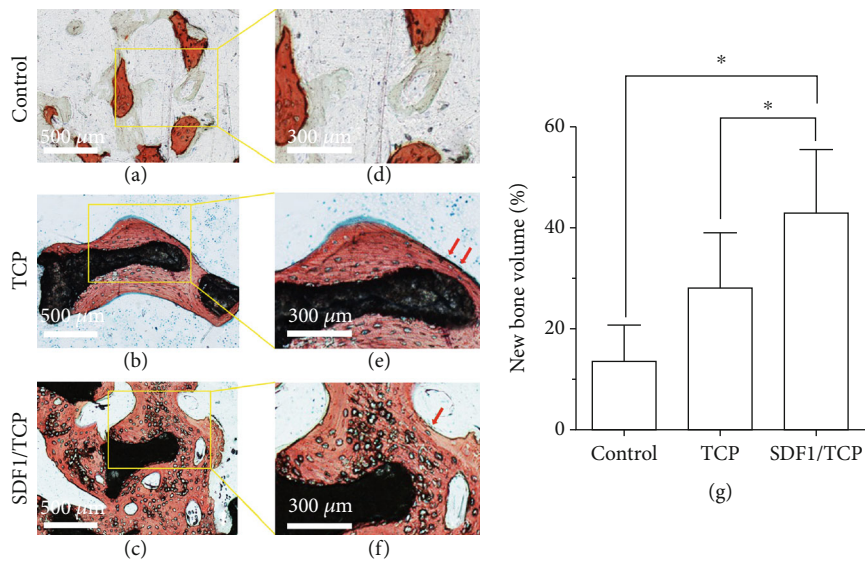

Figure 5: The newly formed bone (NB), osteoid tissue (OT), and residual material (M) are indicated as red, green, and black, respectively. Compared with the other two groups, the SDF-1α/TCP group got more volume of new bone. Red arrows indicate the lining cells and osteoblastic cells ($^*p < 0.05$).

scaffolds were implanted. This may be because SDF-1α can recruit migration of mesenchymal stem cells [23] and create a matrix environment inductive for bone defect repair [24, 25], but further studies should be performed.

Nevertheless, this study is limited in the number of animal model and the deep mechanism of SDF-1α/TCP in promoting bone regeneration needs further study. Additional micro-CT analysis of the newly formed bone would also provide more data. Therefore, clinic application of such SDF-1α/TCP bioceramics would require further studies about its biological safety.

5. Conclusion

In conclusion, the addition of SDF-1α into porous TCP bioceramics resulted in a higher cell viability and osteoinduction. *In vitro* and *in vivo* experiments proved that SDF-1α had a positive influence on osteogenesis compared to pure TCP. Thus, the porous SDF-1α/TCP bioceramics could be a promising new way to treat bone defects instead of traditional synthetic bone grafts.

Data Availability

All underlying data is available on request through email address of corresponding authors.

Conflicts of Interest

The authors declare that they have no conflicts of interest.

Authors' Contributions

Fangchun Jin, Qixun Cai, and Wei Wang contribute equally to this work. The authors alone are responsible for the content and writing of the paper.

Acknowledgments

This research was supported by the Foundation of Science and Technology Commission of Shanghai Municipality (17DZ1930507), the Shanghai Xuhui District Medical Peak and Plateau Discipline Construction Program (Grant No. SHXH201702), and 2021 Shanghai Jiao Tong University "Jiaotong University Star" Program Medical-Industrial Cross-Research Fund (Grant No. YG2021QN47).

References

[1] D. Logeart-Avramoglou, F. Anagnostou, R. Bizios, and H. Petite, "Engineering bone: challenges and obstacles," *Journal of Cellular and Molecular Medicine*, vol. 9, no. 1, pp. 72–84, 2005.

[2] P. K. McClure, H. M. Alrabai, and J. D. Conway, "Preoperative evaluation and optimization for reconstruction of segmental bone defects of the tibia," *Journal of Orthopaedic Trauma*, vol. 31, no. 5, pp. S16–S19, 2017.

[3] T. Masaoka, T. Yoshii, M. Yuasa et al., "Bone defect regeneration by a combination of a β-tricalcium phosphate scaffold and bone marrow stromal cells in a non-human primate model," *Open Biomedical Engineering Journal*, vol. 10, no. 1, pp. 2–11, 2016.

[4] D. Confalonieri, A. Schwab, H. Walles, and F. Ehlicke, "Advanced therapy medicinal products: a guide for bone marrow-derived MSC application in bone and cartilage tissue engineering," *Tissue Engineering. Part B, Reviews*, vol. 24, no. 2, pp. 155–169, 2018.

[5] R. Z. LeGeros, "Properties of Osteoconductive Biomaterials: Calcium Phosphates," *Clinical Orthopaedics and Related Research*, vol. 395, pp. 81–98, 2002.

[6] S. Liu, F. Jin, K. Lin et al., "The effect of calcium silicate on in vitro physiochemical properties and in vivo osteogenesis, degradability and bioactivity of porous β-tricalcium phosphate

bioceramics," *Biomedical Materials*, vol. 8, no. 2, article 025008, 2013.

[7] J. Y. Park, S. H. Park, M. G. Kim, S. H. Park, T. H. Yoo, and M. S. Kim, "Biomimetic scaffolds for bone tissue engineering," *Advances in Experimental Medicine and Biology*, vol. 1064, pp. 109–121, 2018.

[8] X. Yu, H. Sun, J. Yang et al., "Evaluation of bone-regeneration effects and ectopic osteogenesis of collagen membrane chemically conjugated with stromal cell-derived factor-1 *in vivo*," *Biomedical Materials*, vol. 15, no. 1, article 015009, 2020.

[9] Y. Jung, J. K. Kim, Y. Shiozawa et al., "Recruitment of mesenchymal stem cells into prostate tumours promotes metastasis," *Nature Communications*, vol. 4, no. 1, p. 1795, 2013.

[10] Y. Wang, X. Sun, J. Lv, L. Zeng, X. Wei, and L. Wei, "Stromal cell-derived factor-1 accelerates cartilage defect repairing by recruiting bone marrow mesenchymal stem cells and promoting chondrogenic differentiation," *Tissue Engineering. Part A*, vol. 23, no. 19-20, pp. 1160–1168, 2017.

[11] F. Wang, G. Yang, Y. Xiao et al., "Effect of SDF-1 with biphasic ceramic-like bone graft on the repair of rabbit radial defect," *Journal of Orthopaedic Surgery and Research*, vol. 14, no. 1, p. 231, 2019.

[12] T. T. Lau and D. A. Wang, "Stromal cell-derived factor-1 (SDF-1): homing factor for engineered regenerative medicine," *Expert Opinion on Biological Therapy*, vol. 11, no. 2, pp. 189–197, 2011.

[13] Y. Liu, K. de Groot, and E. B. Hunziker, "BMP-2 liberated from biomimetic implant coatings induces and sustains direct ossification in an ectopic rat model," *Bone*, vol. 36, no. 5, pp. 745–757, 2005.

[14] J. J. Yuan, B. X. Wang, C. Han et al., "Nanosized-Ag-doped porous β-tricalcium phosphate for biological applications," *Materials Science and Engineering: C*, vol. 114, article 111037, 2020.

[15] J. P. Royet, "Stereology: a method for analyzing images," *Progress in Neurobiology*, vol. 37, no. 5, pp. 433–474, 1991.

[16] W. Zhao, K. Jin, J. Li, X. Qiu, and S. Li, "Delivery of stromal cell-derived factor 1α for in situ tissue regeneration," *Journal of Biological Engineering*, vol. 11, no. 1, p. 22, 2017.

[17] N. Kawaguchi, T. T. Zhang, and T. Nakanishi, "Involvement of CXCR4 in normal and abnormal development," *Cell*, vol. 8, no. 2, p. 185, 2019.

[18] T. H. Hu, Y. Yao, S. Yu et al., "SDF-1/CXCR4 promotes epithelial-mesenchymal transition and progression of colorectal cancer by activation of the Wnt/β-catenin signaling pathway," *Cancer Letters*, vol. 354, no. 2, pp. 417–426, 2014.

[19] Y. Lu, B. Hu, G. F. Guan et al., "SDF-1/CXCR4 promotes F5M2 osteosarcoma cell migration by activating the Wnt/β-catenin signaling pathway," *Medical Oncology*, vol. 32, no. 7, p. 194, 2015.

[20] X. Zeng, Y. Wang, Q. Dong, M. X. Ma, and X. D. Liu, "DLX2 activates _Wnt1_ transcription and mediates Wnt/ β-catenin signal to promote osteogenic differentiation of hBMSCs," *Gene*, vol. 744, article 144564, 2020.

[21] J. Zhao, T. Watanabe, U. K. Bhawal, E. Kubota, and Y. Abiko, "Transcriptome analysis of β-TCP implanted in dog mandible," *Bone*, vol. 48, no. 4, pp. 864–877, 2011.

[22] F. Jin, Y. Xie, N. Wang et al., "Poor osteoinductive potential of subcutaneous bone cement-induced membranes for tissue engineered bone," *Connective Tissue Research*, vol. 54, no. 4-5, pp. 283–289, 2013.

[23] Y. Wan, C. Lu, J. Cao et al., "Osteoblastic Wnts differentially regulate bone remodeling and the maintenance of bone marrow mesenchymal stem cells," *Bone*, vol. 55, no. 1, pp. 258–267, 2013.

[24] C. H. Ryu, S. A. Park, S. M. Kim et al., "Migration of human umbilical cord blood mesenchymal stem cells mediated by stromal cell-derived factor-1/CXCR4 axis via Akt, ERK, and p38 signal transduction pathways," *Biochemical and Biophysical Research Communications*, vol. 398, no. 1, pp. 105–110, 2010.

[25] A. A. Peyvandi, N. A. Roozbahany, H. Peyvandi et al., "Critical role of SDF-1/CXCR4 signaling pathway in stem cell homing in the deafened rat cochlea after acoustic trauma," *Neural Regeneration Research*, vol. 13, no. 1, pp. 154–160, 2018.

Hindawi
BioMed Research International
Volume 2021, Article ID 5748069, 8 pages
https://doi.org/10.1155/2021/5748069

Research Article

The Topical Tranexamic Acid Have Potential Hazard of Promoting Biofilm Formation of *Staphylococcus aureus* in Microenvironment of the Prosthetic Joint

Feiyang Zhang,[1] **Wenjun Dong**,[1] **Fengyan Wang**,[1] **Jinlong Yu**,[1] **Feng Jiang**,[1] **Jin Tang**,[2] **Yan Qian**,[1] **and Hao Shen**[1]

[1]*Department of Orthopaedics, Shanghai Jiao Tong University Affiliated Sixth People's Hospital, #600, Yishan Rd, Shanghai, China*
[2]*Department of Clinical Laboratory, Shanghai Jiao Tong University Affiliated Sixth People's Hospital, #600, Yishan Rd, Shanghai, China*

Correspondence should be addressed to Jin Tang; tangjin6ph@163.com, Yan Qian; yanzilaoma@126.com, and Hao Shen; shenhao7212@sina.com

Received 11 August 2020; Revised 1 February 2021; Accepted 4 March 2021; Published 12 March 2021

Academic Editor: Yu Sheng Li

Background. Perioperative topical tranexamic acid as antifibrinolytic agent is often used for total joint replacement to reduce bleeding currently. *Staphylococcus aureus* was the most common isolates from perioperative infection of prosthetic joint. The influence of topical application with tranexamic acid on the incidence of acute prosthetic joint infection of *Staphylococcus aureus* has not been clarified. *Methods*. Mouse model of *Staphylococcus aureus* knee prosthesis infection was constructed. Tranexamic acid was intra-articular injected during the perioperative period. CFU counting from tissue and implant sample was evaluated 3 days and 7 days after inoculating of *Staphylococcus aureus*. Bacterial growth curve, biofilm formation, aggregation, and plasmin inhibition of *Staphylococcus aureus* were tested with tranexamic acid added to the synovial culture medium. *Results*. There were no significant differences of CFU counting from tissue and implant samples in knee prosthesis infection after a single local injection of tranexamic acid at the postoperative 3 or 7 days. The amount of bacterial colonization on the surface of implant increased after 3 days' continuous local injection of tranexamic acid. Tranexamic acid has no effect on bacterial growth at the concentration (10 mg/ml) of clinical application, but it can inhibit bacterial aggregation and mildly inhibit biofilm formation. Plasmin can significantly inhibit biofilm formation which can be revised by adding tranexamic acid. *Conclusion*. Although continuous local injection of tranexamic acid can promote the biofilm formation of *Staphylococcus aureus* on the surface of articular implant, it has clinical safety for using one single local injection of tranexamic acid during the perioperative period.

1. Introduction

Tranexamic acid can competitively inhibit the activation of plasminogen and the binding of plasmin to fibrin as synthetic analogues of the amino acid lysine, thus inhibiting fibrin degradation [1, 2]. A large number of studies have confirmed that tranexamic acid can significantly reduce the amount of blood loss during surgery without increasing the risk of thromboembolism [3–6]. Intravenous administration and local injection of tranexamic acid are usually used in the perioperative period of total joint replacement [7]. A large number of clinical studies showed that tranexamic acid can significantly reduce the incidence of postoperative adverse events [4, 8].

Prosthetic joint infection is considered to be the most severe complication related to total joint replacement [9, 10]. *Staphylococcus aureus* was predominant pathogen in postoperative and acute prosthetic joint infection [10–12]. Because of the numerous virulence factors and the ability to form biofilm on the surfaces of implant, *Staphylococcus aureus* leads to more severe clinical presentation and worse prognosis [12].

Some studies has found that application of tranexamic acid can exacerbate infections of *Staphylococcus aureus* in mice model [13, 14].

But in clinical practice, the topical application of tranexamic acid has been used more and more widely and has not shown increasing of infection rate [15–19]. The influence of topical tranexamic acid on *Staphylococcus aureus* infection is still controversial.

Therefore, it needs to be clarified whether local injection of tranexamic acid promotes the formation of biofilm and leads to the increased risk of *Staphylococcus aureus* infection.

2. Materials and Methods

2.1. Bacterial Strains, Reagents, and Ethics Statement. The strains used in this study were methicillin-susceptible *Staphylococcus aureus* (MSSA) ST1792 isolated from PJI prosthesis. The fluorescently label *Staphylococcus aureus* ST1792-sfGFP which was preserved in our laboratory were used for confocal microscopic assay. The tranexamic acid (Aladdin, Shanghai, China) was used in in vivo and in vitro study of bacterial growth, aggregation, and biofilm formation. The plasmin (PLM, Sigma Aldrich, St Louis, MO, USA) was used in in vitro study of biofilm formation was purchased from and used at final concentrations of 100 μg/ml. Synovial fluid (SF) was added to the medium and used in in vitro experiment. Collection of human synovial fluid from patients with osteoarthritis was approved by the Institutional Review Board of Shanghai Jiao Tong University Affiliated Sixth People's Hospital. Because synovial fluid was aspirated as part of the routine procedure before injection of hyaluronic acid and would have been discarded otherwise, and patient information not collected, a waiver for informed written consent was granted by the IRB.

2.2. Staphylococcus aureus Prosthetic Joint Infection Mouse Model. All procedures of animal experiment had been reviewed and approved by the Animal Care and Experiment Committee of Shanghai Jiao Tong University affiliated Sixth People's Hospital.

Six-week-old and weighing (20 ± 5) g male C57BL/6 mice were used to construct *Staphylococcus aureus* prosthetic joint infection model. The mice were anesthetized intraperitoneally with 3% pentobarbital sodium (0.1 ml per 10 g body weight) and then shaving the both knees. A medial parapatellar incision was made at the knee joint of mice after sterilized with 75% alcohol. Proximal tibia was exposed, and the medullary cavity was inserted with sterile stainless steel implant rods. After closing the wounds by sutures, tranexamic acid was injected into the joint cavity of one side at a dose of 10 mg/kg; the other side was injected with an equal volume of saline as control. Two hours later, both knee joints were inoculated with ST1792 solution of $\sim 5 * 10^6$. And then, the mice were randomly divided into three groups (Table 1). The first group was housed for 3 days, and the second group was housed for 7 days. The third group was continuous local injected with tranexamic acid at a dose of 10 mg/kg every 24 hours and housed for 3 days. Three days and 7 days after surgery, the mice with a single local injection of tranexamic acid (i.e., first and second groups) were euthanized, and the mice with continuous local injection of tranexamic acid were euthanized in 3 days after surgery. Peri-implant tissues and implant in tibia were harvested for CFU counting.

2.3. Bacteria CFU Counting. The peri-implant tissues were weighed and homogenized in tubes with 1 ml normal of saline (NS) by high-speed homogenizer (Jingxin Industrial Limited Company, Shanghai, China). The implant were washed gently 3 times with NS to remove the planktonic bacteria and placed in tube containing 1 ml of NS, sonicated, and homogenized to detach the adherent bacteria. The homogenates and suspensions were serially diluted in NS and spread on sheep blood agar (SBA). The plates were cultured overnight at 37°C. The colonies were counted and expressed by $\log_{10}$CFU/g of peri-implant tissues and $\log_{10}$CFU/per implanted rods.

2.4. The Effect Test of TXA In Vitro. The ST1792 were cultured overnight at 37°C on SBA plates before each experiment. Single colony of each strain was collected and cultured overnight in TSB at 37°C. The ST1792-sfGFP were cultured on Tryptic Soy Agar (TSA) plates with 10 μg/ml chloramphenicol and cultured overnight in TSB containing 10 μg/ml chloramphenicol at 37°C.

The preconditioning method of medium was divided into six groups: the first group containing 10% SF, the second group containing 10%SF and 10 mg/ml TXA, the third group containing 10%SF and 50 mg/ml TXA, the fourth group containing 10%SF and 100 μg/ml PLM, the fifth group containing 10%SF and 100 μg/ml PLM and 10 mg/ml TXA, and the sixth group containing 10%SF and 100 μg/ml PLM and 50 mg/ml TXA.

2.4.1. Staphylococcus aureus Growth Curve Assay. Overnight culture of ST1792 was serially diluted 1 : 1000 in groups 1, 2, and 3 with TSB and cultured at 37°C. 100 μl of solution were aspirated at 0-2-4-6-8-12 hours and transferred to the wells of a 96-well tissue culture plate (Corning Co., NY, USA). The absorbance was measured by a microplate reader (BIO-TEK, ELX 800) at a wavelength of 600 nm.

2.4.2. Staphylococcus aureus Aggregation Test. Overnight culture of ST1792 was serially diluted to 1 : 1000 in groups 1, 2, and 3 with TSB and three additional control groups without 10%SF and cultured at 37°C. Strain clumped together and sank to the bottom of the tube after 8 h; the turbidity of medium supernatant was significantly decreased. 100 μl of culture medium supernatant were aspirated and transferred to the wells of a 96-well tissue culture plate, measuring the absorbance at a wavelength of 490 nm by a microplate reader.

2.4.3. Biofilm Formation and Biomass. Overnight culture of ST1792 was serially diluted to 1 : 1000 in TSB supplemented with 0.5% glucose (TSBG). Diluted bacteria, with supplementation from group 1 to group 6, were used for assessment of biofilm formation on (1) the bottom of 96-well polystyrene microtiter plate (Corning Co., NY, USA) or (2) Ultra High Molecular Weight Polyethylene (UHMWPE) washers that

Table 1: The grouping of mouse.

Group	Treatment		Time (day)
	Left knee	Right knee	
1	A single local injection of TXA	A single local injection of NS	3
2	A single local injection of TXA	A single local injection of NS	7
3	Continuous local injection of TXA	Continuous local injection of NS	3

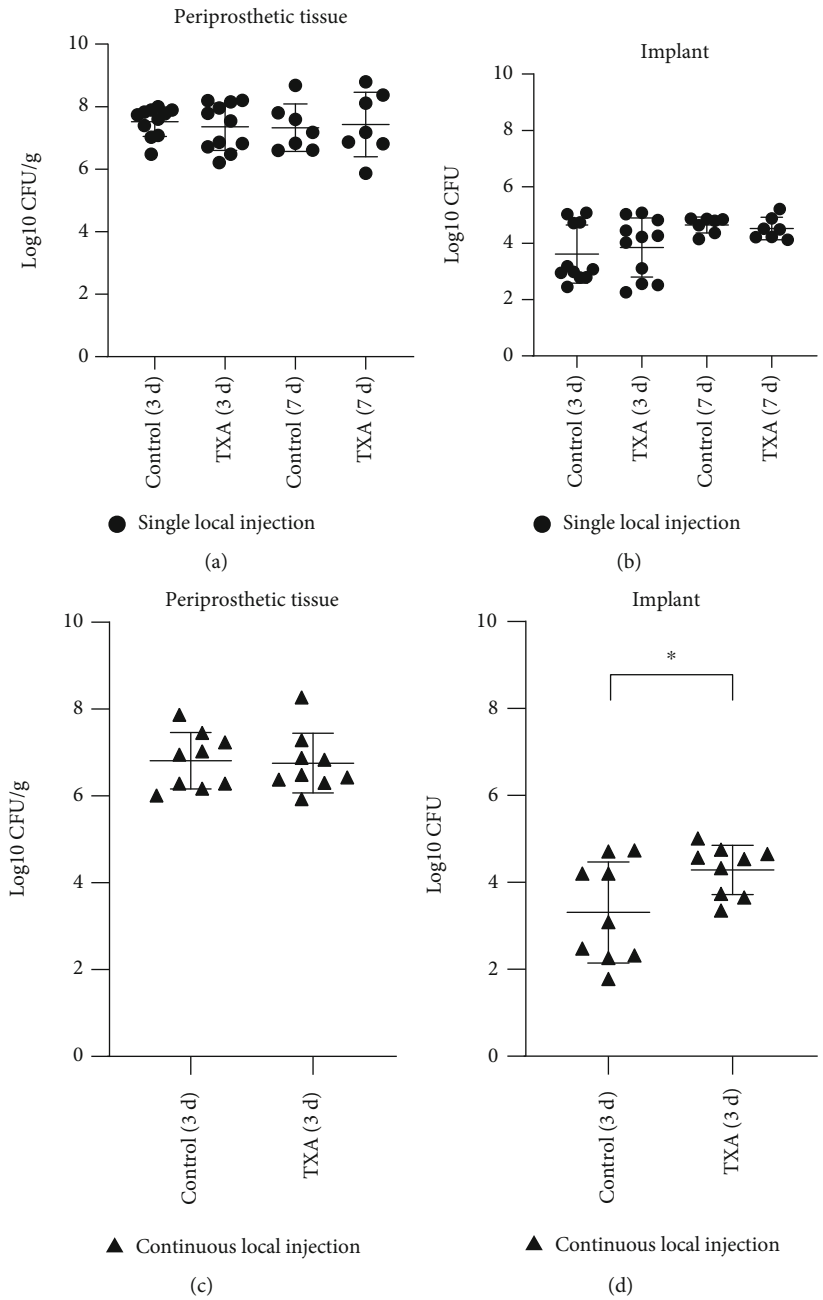

Figure 1: CFU counting after local injection of tranexamic acid on *Staphylococcus aureus* PJI mouse model. (a, b) The bacterial CFU of PJI mice with a single local injection of tranexamic acid in periprosthetic tissue (Figure 2(a)) and implants (Figure 2(b)) after 3 and 7 days. (c) The bacterial CFU of periprosthetic tissue after continuous local injection of tranexamic acid for 3 days. (d) The bacterial CFU of implants after continuous local injection of tranexamic acid for 3 days. $^{*}P < 0.05$; error bars represent standard deviations.

were affixed to bottom of 24-well polystyrene plates (Corning Co., NY, USA) with Lubriseal grease (Thomas Scientific) and sterilized by UV irradiation.

96-well plate were incubated overnight at 37°C. Completely aspiring the supernatant from each well and washing gently 3 times with 200 μl NS to remove the planktonic bacteria. Then, 100 μl methanol was used to fix the biofilm for 30 min and then dried. After that, biofilm was stained with 100 μl of 0.1% crystal violet for 15 min. The biofilm biomass on the bottom of the well was dissolved in 200 μl 33% acetic acid after the unbound crystal violet was rinsed by NS for 3 times. 100 μl solution of each well were transferred into a new 96-well tissue culture plate. The absorbance was measured by a microplate reader at a wavelength of 590 nm.

UHMWPE washer inoculated with ST1792 in groups 1, 2, 3, 4, 5, and 6 with TSBG was incubated overnight. The UHMWPE washers were washed 3 times with saline to remove nonadherent cells. The washed UHMWPE washers were transferred into a new 24-well polystyrene plate. Adherent biofilms were fixed with methanol and stained with crystal violet and washed 3 times with sterile water. Biomass on the surfaces of UHMWPE washers was determined by solubilizing crystal violet with 33% acetic acid as described above.

2.4.4. Confocal Laser Scanning Microscopy (CLSM). Overnight culture of ST1792-sfGFP was serially diluted 1 : 1000 in groups 1, 2, 3, 4, 5, and 6 with TSBG. 500 μl of bacteria suspension were incubated with cover glass overnight in 24-well tissue culture plate at 37°C. The cover glasses were washed gently 3 times with NS and imaged by CLSM. The ST1792-sfGFP showed green fluorescence.

3. Results

3.1. The Colonization on the Surface of Implant Were Increased by Continuous Use with TXA In Vivo. Mice with a single local injection of tranexamic acid during the perioperative period showed no significant difference in *Staphylococcus aureus* colonization of tissue and implant sample after 3 and 7 days (Figures 1(a) and 1(b)). Although mice with continuous local injection of tranexamic acid for 3 days showed no significant increase of bacterial colonization in tissue (Figure 1(c)), there was significant higher CFU counting from implant (Figure 1(d)). The experimental results suggested that the continuous local injection of tranexamic acid can promote biofilm formation.

3.2. Influence of Tranexamic Acid on the Growth of Staphylococcus aureus. For analysis of the influence of tranexamic acid on bacterial growth curve, tranexamic acid with clinically used concentration(10 mg/ml) and high concentration (50 mg/ml) was used. Compared to the medium without tranexamic acid, the medium containing tranexamic acid with clinically used concentration (10 mg/ml) has no influence on bacterial growth. Bacterial growth was inhibited by tranexamic acid with high concentration (50 mg/ml) (Figure 2). It showed that tranexamic acid has no antibacterial capacity in concentration of clinical use.

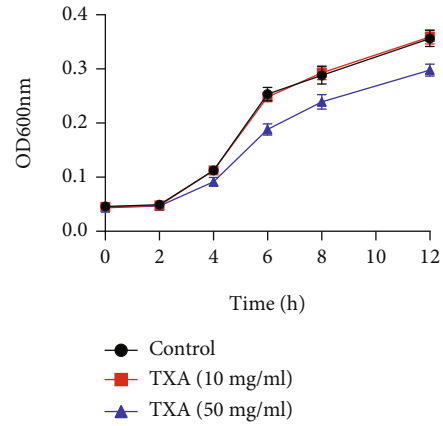

Figure 2: Bacterial growth curve of *Staphylococcus aureus* ST1792 cultured separately in TSB medium containing 10% SF (Blank,10 mg/ml TXA and 50 mg/ml TXA).

3.3. The Influence of Tranexamic Acid on the Bacterial Aggregation in Different Media. The aggregation of *Staphylococcus aureus* inhibited by tranexamic acid with clinically used concentration(10 mg/ml) in TSB medium. The inhibitory effect was attenuated in tranexamic acid with high concentration(50 mg/ml) (Figure 3(a)). However, the anti-aggregation capacity of tranexamic acid disappears when cultured in TSB medium containing 10% SF(Figure 3(b)). The results suggested that inhibitory effect of tranexamic acid on bacterial aggregation attenuated in the microenvironment of the prosthetic joint.

3.4. The Individual and Mutual Inhibition for Biofilm Formation of Staphylococcus aureus by Tranexamic Acid and Plasmin. Whether on 96-well plates or UHMWPE washer, the biofilm formation of *Staphylococcus aureus* was slight inhibited by tranexamic acid (Figures 4(a) and 4(b)). Biofilm formation were inhibited more significantly by tranexamic acid in high concentration (50 mg/ml) with the inhibitory ability of bacterial growth. When plasmin was added into the culture medium, the biofilm formation was significantly inhibited. However, the antibiofilm formation ability of plasmin inhibited by tranexamic acid; thus, the culture medium exhibited a weak antibiofilm formation effect.

3.5. Tranexamic Acid Offset the Inhibition of Biofilm Formation with Plasmin via CLSM. Biofilm formed obviously in TSBG with 10%SF by ST1792 and slight inhibited with TXA(10 mg/ml). The inhibitory effect of TXA at high concentration (50 mg/ml) was more obvious. However, the biofilm disappeared after PLM was added, and it can be found that antibiofilm formation function of plasmin much more strong than TXA in TSBG with 10%SF (Figure 5). The weak antibiofilm formation function exhibited in medium when acting simultaneously with tranexamic acid and plasmin. The results of CLSM provide further confirmation that tranexamic acid offset the inhibition of biofilm formation with plasmin.

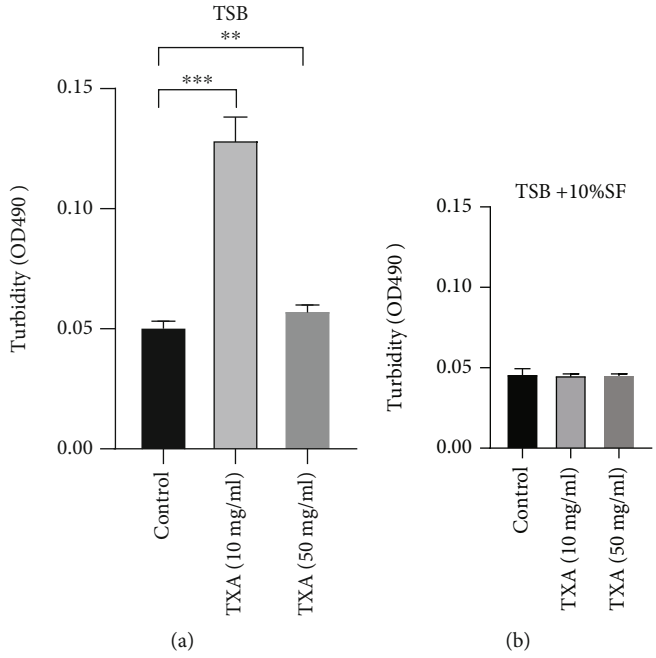

Figure 3: Tranexamic acid shows difference of inhibiting bacterial aggregation in TSB with or without SF. (a) The turbidity of medium supernatant increased in TSB medium containing TXA ($n = 6$). (b) No significant difference of the turbidity was observed in TSB medium containing SF and TXA. $^{**}P < 0.01$, $^{***}P < 0.001$. Error bars represent standard deviations.

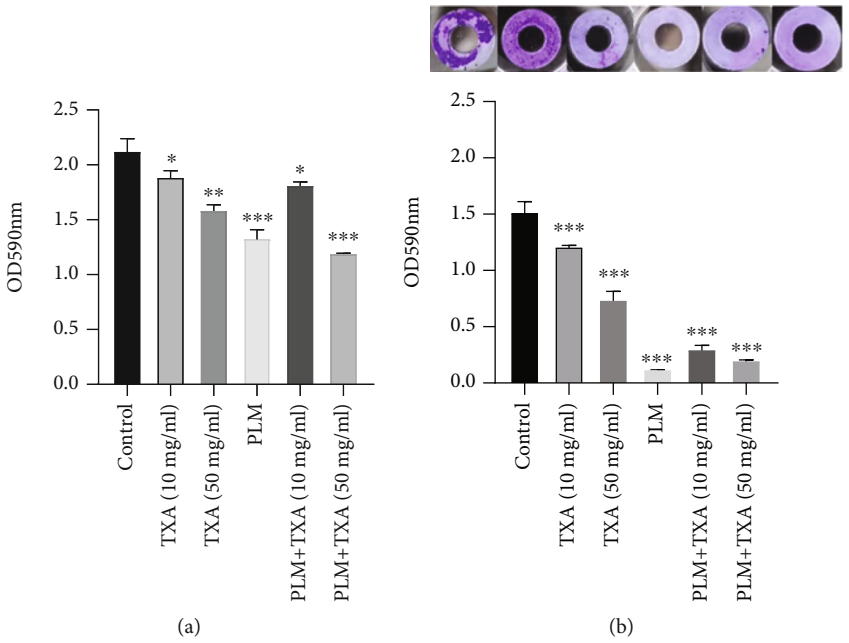

Figure 4: Inhibitory effect of biofilm formation with tranexamic acid were observed in 96-well tissue culture plate (Figure 4(a)) and on the surface of UHMWPE washer (Figure 5(b)). Biofilm formation inhibited more obviously by plasmin and the inhibition of plasmin were reversed by tranexamic acid. $^{*}P < 0.05$, $^{**}P < 0.01$, $^{***}P < 0.001$. Error bars represent standard deviations.

4. Discussion

Mice studies with staphylococcal sepsis or septic arthritis showed increasing severity and mortality of infection by treatment with tranexamic acid; however, the mice were infused with tranexamic acid at a dose of 700-800 mg/kg every 8 hours [14] which was much higher dosage than that for clinical use [14], and previous study had proposed that high-dose tranexamic acid caused significant cytotoxicity [20]. In present study, we constructed *Staphylococcus aureus*

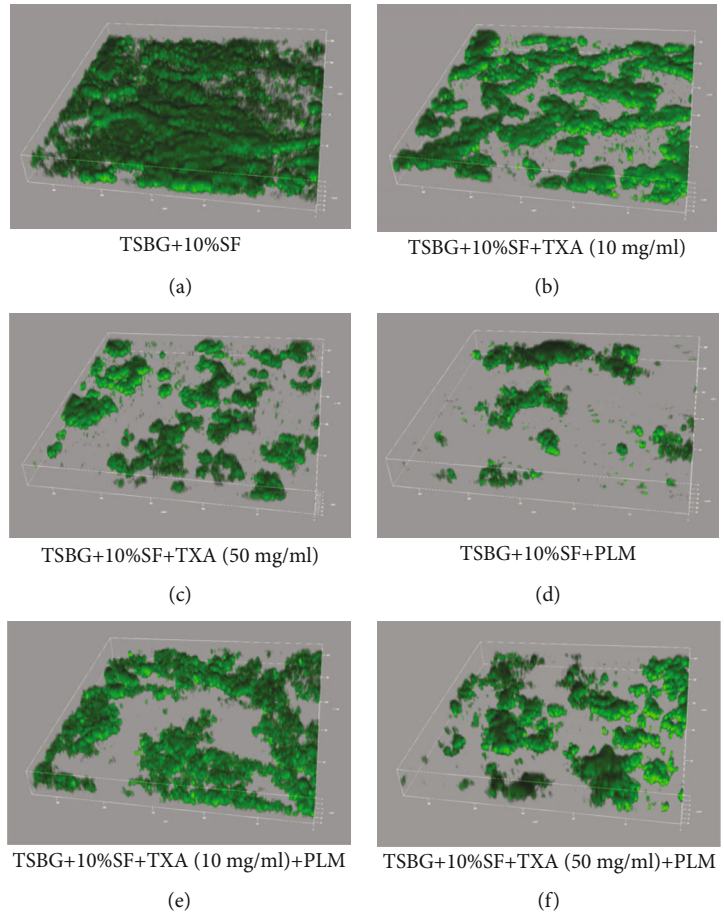

Figure 5: CLSM results of biofilm forming with ST1792-sfGFP. (a) Biofilm formation of *Staphylococcus aureus* in TSBG medium containing 10% SF. (b) Biofilm formation was inhibited by tranexamic acid (10 mg/ml). (c) Biofilm formation was significantly inhibited by tranexamic acid (50 mg/ml). (d) Biofilm formation was significantly inhibited by plasmin. (e, f) Tranexamic acid offset the inhibition of biofilm formation with plasmin.

prosthetic joint infection model with topical tranexamic acid at 10 mg/kg which dose was similar with that using clinically and found that continuous local injection of tranexamic acid promoted biofilm formation in vivo.

Clinically, a single local injection of tranexamic acid is commonly used in joint replacement surgery, and the safety of this method is well documented [15, 16, 18]. In our in vivo experiments, it was observed that a single local injection of tranexamic acid did not aggravate *Staphylococcus aureus* infection. However, for patients bleeding after joint implanted surgery, we hope to explore the feasibility of continuous local injection of tranexamic acid. With the help of mice model, continuous local injection of tranexamic acid was observed to promote the formation of *S. aureus* biofilm, which is the potential risk of using tranexamic acid. Continuous local injection of tranexamic acid is not recommended for clinical treatment.

In order to clarify action of tranexamic acid against *Staphylococcus aureus*, bacterial growth, aggregation, and biofilm formation has been studied in vitro experiment. Results indicated no influence of tranexamic acid with clinical concentration (10 mg/ml) on *Staphylococcus aureus* growth. However, tranexamic acid showed inhibitory function on aggregation and biofilm formation of *Staphylococcus aureus*. The function of antibacterial aggregation disappeared in microenvironment containing synovial fluid. High concentration of TXA (50 mg/ml) showed inhibition of bacterial growth and relatively stronger function of antibiofilm formation, but the significant cytotoxicity exhibited in the high concentration of TXA which was not used in clinically cases [20].

We can observe some special phenomenon in bacteria aggregation experiments. In the infected setting, polysaccharide-based aggregates and biofilms can be regarded as different phases of the same process. Aggregate seeding biofilms, while biofilms dispersing into free floating aggregates [21]. The aggregates can enhance the protection from phagocytosis and be more tolerant to antibiotic treatment [22]. Therefore, the supernatant of bacteria in TSB with TXA had higher turbidity, which proves that the clinical concentration of TXA can inhibit bacteria aggregation, and the high concentration of TXA can inhibit the growth of *Staphylococcus aureus*, resulting in lower turbidity. However, tranexamic acid's inhibitory ability on bacterial aggregation

disappeared in synovial fluid environment, which may be related to the complex joint microenvironment, and further research is needed.

The primary target of action for tranexamic acid was plasmin [2]. The double-sided effect of plasmin in the process of *Staphylococcus aureus* infection has been shown in previous studies. On one hand, plasmin can act in a proinflammatory manner via triggering chemotaxis and cytokine release [23], and the histones in neutrophil extracellular traps (NETs) cleaved by plasmin, which lead to protection of *Staphylococcus aureus* in vivo [24]. Therefore, plasmin showed the function of promoting infection. On the other hand, fibrin-containing bacterial biofilms were decomposed by the specifically targeting fibrin function of plasmin, and the antibiotic efficiency were greatly improved [22, 25]. Thus, plasmin showed the function of inhibiting infection.

In this study, the significant antibiofilm function of plasmin was found in experiments compared with tranexamic acid. The obvious inhibitory effect of plasmin on *Staphylococcus aureus* biofilm formation was mentioned in previous studies [22], but this significant antibiofilm function of plasmin inhibited by tranexamic acid. Therefore, the increased colonization of *Staphylococcus aureus* made it easier to form biofilms by tranexamic acid on the surface of implant. While tranexamic acid promoted biofilm by inhibiting plasmin, it also inhibited the degradation of histones in NETs. Therefore, one single local injection has not shown to promote infection in vivo, but continuous use of tranexamic acid in vivo has shown increased *Staphylococcus aureus* colonization, which suggested the potential risk of topical tranexamic acid.

There are still some limitations in this study. Although the clinical used concentration of tranexamic acid has been applied to avoid the cytotoxicity caused by high concentration, the viewing time of mouse model was relatively short and the effect of continuous topical tranexamic acid for a longer time has not been tested. The influence of tranexamic acid on antibiotic sensitivity of *Staphylococcus aureus* has not been explored in the present study. Although *Staphylococcus aureus* ST1792 was used in terms of strains, the response of various *Staphylococcus aureus* subtypes to tranexamic acid has not been verified.

5. Conclusions

In summary, here, we clarified the function of topical tranexamic acid use with *Staphylococcus aureus*. Continuous topical injection of tranexamic acid promoted biofilm formation of *Staphylococcus aureus* which has potential risks to patients undergoing total joint replacement. Although it has clinical safety for using one single local injection of tranexamic acid, it is recommended to use antibiotics in combination with topical using of tranexamic acid in clinic to minimizing the rate of infection.

Data Availability

The data used to support the findings of this study are available from the corresponding author upon request.

Conflicts of Interest

The authors have no conflicts of interest.

Authors' Contributions

Zhang, Feiyang, Dong, Wenjun, and Wang, Fengyan contributed equally to this work.

Acknowledgments

This study was supported by National Natural Science Foundation of China (Grant no: 81772364) and Medical Guidance Scientific Research Support Project of Shanghai Science and Technology Commission (Grant no: 19411962600).

References

[1] C. Longstaff, "Studies on the mechanism of action of aprotinin and tranexamic acid as plasmin inhibitors and antifibrinolytic agents," *Blood Coagulation & Fibrinolysis: an International Journal in Haemostasis and Thrombosis*, vol. 5, pp. 537–542, 1994.

[2] P. L. McCormack, "Tranexamic acid: a review of its use in the treatment of hyperfibrinolysis," *Drugs*, vol. 72, no. 5, pp. 585–617, 2012.

[3] R. Gandhi, H. M. Evans, S. R. Mahomed, and N. N. Mahomed, "Tranexamic acid and the reduction of blood loss in total knee and hip arthroplasty: a meta-analysis," *BMC Research Notes*, vol. 6, no. 1, p. 184, 2013.

[4] J. Poeran, R. Rasul, S. Suzuki et al., "Tranexamic acid use and postoperative outcomes in patients undergoing total hip or knee arthroplasty in the United States: retrospective analysis of effectiveness and safety," *BMJ*, vol. 349, no. aug12 8, article g4829, 2014.

[5] J. T. Moskal and S. G. Capps, "Intra-articular tranexamic acid in primary total knee arthroplasty: meta-analysis," *The Journal of Knee Surgery*, vol. 31, no. 1, pp. 056–067, 2017.

[6] Z. Wang and X. Shen, "The efficacy of combined intra-articular and intravenous tranexamic acid for blood loss in primary total knee arthroplasty: a meta-analysis," *Medicine*, vol. 96, no. 42, article e8123, 2017.

[7] D. Gulabi, Y. Yuce, K. H. Erkal, N. Saglam, and S. Camur, "The combined administration of systemic and topical tranexamic acid for total hip arthroplasty: is it better than systemic?," *Acta Orthopaedica et Traumatologica Turcica*, vol. 53, no. 4, pp. 297–300, 2019.

[8] H. Yazdi, M. R. Klement, M. Hammad et al., "Tranexamic acid is associated with reduced periprosthetic joint infection after primary total joint arthroplasty," *The Journal of Arthroplasty*, vol. 35, no. 3, pp. 840–844, 2020.

[9] S. M. Kurtz, E. Lau, H. Watson, J. K. Schmier, and J. Parvizi, "Economic burden of periprosthetic joint infection in the United States," *The Journal of Arthroplasty*, vol. 27, no. 8, pp. 61–65.e1, 2012.

[10] J. L. Del Pozo and R. Patel, "Clinical practice. Infection associated with prosthetic joints," *The New England Journal of Medicine*, vol. 361, no. 8, pp. 787–794, 2009.

[11] V. K. Aggarwal, H. Bakhshi, N. U. Ecker, J. Parvizi, T. Gehrke, and D. Kendoff, "Organism profile in periprosthetic joint infection: pathogens differ at two arthroplasty infection

referral centers in Europe and in the United States," *The Journal of Knee Surgery*, vol. 27, no. 5, pp. 399–406, 2014.

[12] M. Titécat, E. Senneville, F. Wallet et al., "Bacterial epidemiology of osteoarticular infections in a referent center: 10-year study," *Orthopaedics & Traumatology, Surgery & Research*, vol. 99, no. 6, pp. 653–658, 2013.

[13] D. F. Draxler, M. M. Awad, G. Hanafi et al., "Tranexamic acid influences the immune response, but not bacterial clearance in a model of post-traumatic brain injury pneumonia," *Journal of Neurotrauma*, vol. 36, no. 23, pp. 3297–3308, 2019.

[14] M. Kłak, N. Anäkkälä, W. Wang et al., "Tranexamic acid, an inhibitor of plasminogen activation, aggravates staphylococcal septic arthritis and sepsis," *Scandinavian Journal of Infectious Diseases*, vol. 42, no. 5, pp. 351–358, 2010.

[15] J. Y. Chen, N. N. Lo, D. K. Tay, P. L. Chin, S. L. Chia, and S. J. Yeo, "Intra-articular administration of tranexamic acid in total hip arthroplasty," *Journal of Orthopaedic Surgery (Hong Kong)*, vol. 23, no. 2, pp. 213–217, 2015.

[16] J. S. Kang, K. H. Moon, B. S. Kim, and S. J. Yang, "Topical administration of tranexamic acid in hip arthroplasty," *International Orthopaedics*, vol. 41, no. 2, pp. 259–263, 2017.

[17] C. Wang, G. J. Xu, Z. Han et al., "Topical application of tranexamic acid in primary total hip arthroplasty: a systemic review and meta-analysis," *International Journal of Surgery*, vol. 15, pp. 134–139, 2015.

[18] B. S. Waddell, T. Zahoor, M. Meyer, L. Ochsner, and G. Chimento, "Topical tranexamic acid use in knee periprosthetic joint infection is safe and effective," *The Journal of Knee Surgery*, vol. 29, no. 5, pp. 423–429, 2016.

[19] F. Reichel, C. Peter, V. Ewerbeck, and M. Egermann, "Reducing blood loss in revision total hip and knee arthroplasty: tranexamic acid is effective in aseptic revisions and in second-stage reimplantations for periprosthetic infection," *BioMed Research International*, vol. 2018, Article ID 3891870, 9 pages, 2018.

[20] M. McLean, K. McCall, I. D. M. Smith et al., "Tranexamic acid toxicity in human periarticular tissues," *Bone & Joint Research*, vol. 8, no. 1, pp. 11–18, 2019.

[21] H. A. Crosby, J. Kwiecinski, and A. R. Horswill, "_Staphylococcus aureus_ aggregation and coagulation mechanisms, and their function in host-pathogen interactions," *Advances in Applied Microbiology*, vol. 96, pp. 1–41, 2016.

[22] S. Dastgheyb, J. Parvizi, I. M. Shapiro, N. J. Hickok, and M. Otto, "Effect of biofilms on recalcitrance of staphylococcal joint infection to antibiotic treatment," *The Journal of Infectious Diseases*, vol. 211, no. 4, pp. 641–650, 2015.

[23] D. F. Draxler and R. L. Medcalf, "The fibrinolytic system–more than fibrinolysis?," *Transfusion Medicine Reviews*, vol. 29, no. 2, pp. 102–109, 2015.

[24] G. Pietrocola, G. Nobile, M. J. Alfeo et al., "Fibronectin-binding protein B (FnBPB) from _Staphylococcus aureus_ protects against the antimicrobial activity of histones," *The Journal of Biological Chemistry*, vol. 294, no. 10, pp. 3588–3602, 2019.

[25] Y. Guo, J. Li, E. Hagström, and T. Ny, "Protective effects of plasmin (ogen) in a mouse model of Staphylococcus aureus-induced arthritis," *Arthritis and Rheumatism*, vol. 58, no. 3, pp. 764–772, 2008.

Hindawi
BioMed Research International
Volume 2021, Article ID 6674570, 8 pages
https://doi.org/10.1155/2021/6674570

Research Article

Purinergic Signaling Mediates PTH and Fluid Flow-Induced Osteoblast Proliferation

Yanghui Xing,[1] **Liang Song**,[2] **Yingying Zhang**,[2] **Tengyu Zhang**,[2] **Jian Li**,[2] **and Chunjing Tao**[3]

[1]*Department of Biomedical Engineering, Shantou University, Shantou 515063, China*
[2]*National Research Center for Rehabilitation Technical Aids, Beijing 100176, China*
[3]*Beijing Advanced Innovation Centre for Biomedical Engineering, Beihang University, Beijing 100083, China*

Correspondence should be addressed to Yanghui Xing; xingyanghui@hotmail.com and Chunjing Tao; chunjingtao@buaa.edu.cn

Received 30 October 2020; Revised 9 December 2020; Accepted 13 January 2021; Published 29 January 2021

Academic Editor: Xiao Wang

Both parathyroid hormone (PTH) and mechanical signals are able to regulate bone growth and regeneration. They also can work synergistically to regulate osteoblast proliferation, but little is known about the mechanisms how PTH and mechanical signals interact with each other during this process. In this study, we investigated responses of MC3T3-E1 osteoblasts to PTH and oscillatory fluid flow. We found that osteoblasts are more sensitive to mechanical signals in the presence of PTH according to ERK1/2 phosphorylation, ATP release, CREB phosphorylation, and cell proliferation. PTH may also reduce the osteoblast refractory period after desensitization due to mechanical signals. We further found that the synergistic responses of osteoblasts to fluid flow or ATP with PTH had similar patterns, suggesting that synergy between fluid flow and PTH may be through the ATP pathway. After we inhibited ATP effects using apyrase in osteoblasts, their synergistic responses to mechanical stimulation and PTH were also inhibited. Additionally, knocking down P2Y2 purinergic receptors can significantly attenuate osteoblast synergistic responses to mechanical stimulation and PTH in terms of ERK1/2 phosphorylation, CREB phosphorylation, and cell proliferation. Thus, our results suggest that PTH enhances mechanosensitivity of osteoblasts via a mechanism involving ATP and P2Y2 purinergic receptors.

1. Introduction

Mechanical signals play very important roles in regulating bone growth and remodeling [1, 2]. Oscillatory fluid flow, a potent and widely used mechanical stimulus for bone cells, can induce osteoblast intracellular calcium mobilization, MAPK activation, ATP release, c-fos expression, and other intracellular events and subsequently regulates bone metabolism [3–5]. On the other hand, parathyroid hormone (PTH) is able to regulate bone cell extracellular calcium and phosphate metabolism and controls bone growth and remodeling [6, 7]. It is well established that the intermittent administration of PTH stimulates bone formation by increasing osteoblast number and subsequently increases bone mass and reduces the incidence of fracture in the elderly [8, 9]. PTH enhances osteoblast proliferation, inhibits osteoblast apoptosis, and reactivates lining cells to resume their matrix synthesizing function through a series of pathways, including cAMP, PKA, Runx2, and Wnt signals [9–11]. Both mechanical stimulation and PTH are able to regulate osteoblast metabolism and bone remodeling; thus, their synergistical effects on bone are of great interests of researchers. Previous literatures demonstrated that PTH may potentiate response of bone cells to mechanical stimulation in terms of intracellular calcium release [12, 13]. It is possibly because that PTH induced actin polymerization in cells, which resulted in an increase in cell mechanosensitivity [13]. In addition, PTH has been shown to increase the activity and conductance of a stretch-activated ion channels in osteoblastic cells [14], suggesting its direct action on the cell membranes. Meanwhile,

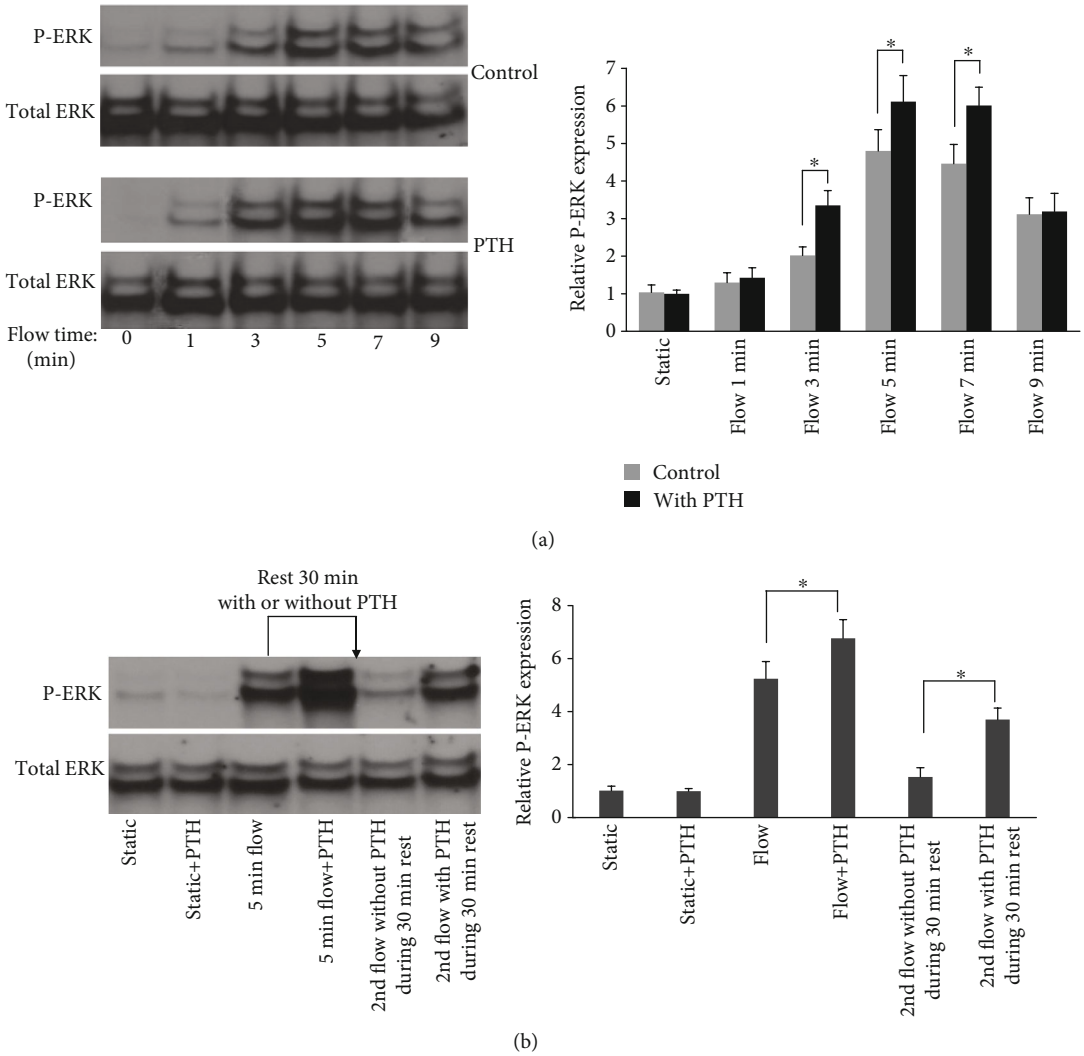

Figure 1: Osteoblast ERK1/2 phosphorylation in response to PTH and oscillatory fluid flow. (a) ERK1/2 phosphorylation in response to fluid flow was significantly increased after PTH treatment. (b) PTH reduces osteoblast desensitization time after mechanical stimulation. ($n = 4$, $^{*}p < 0.05$, each bar represents the mean ± SEM).

an animal study demonstrated that PTH enhanced mechanically induced bone formation [15]. These studies demonstrated that PTH and mechanical stimulation can work together to improve bone growth and regeneration, but the underlying mechanism remains elusive.

Under mechanical stimulation, osteoblasts release ATP from cytosol to extracellular space. Subsequently, ATP binds to purinergic receptors such as P2Y2 and initiates intracellular calcium mobilization and ERK1/2 activation [4, 16]. ATP is also responsible for fluid flow-induced prostaglandin E2 release in osteoblasts [17]. Furthermore, ATP is able to mediate osteoblast growth and mineralization [18, 19]. ATP is also able to stimulate primary human adipose tissue-derived stem cells and bone marrow stromal cell proliferation through the ERK1/2 pathway and intracellular calcium mobilization, respectively [20, 21]. On the other hand, ATP can modulate bone cell metabolism synergistically with PTH. Osteoblasts may release ATP and become more sensitive after PTH treatment [22]. It has been shown that when ATP and PTH are added together on UMR-106 rat osteoblasts and primary human osteoblasts, there is a synergistic increase in intracellular calcium release and c-fos expression [23, 24]. Thus, ATP is closely associated with the osteoblast mechanotransduction pathway and PTH pathway.

Previously, we have demonstrated that P2Y2 receptor is involved in bone growth and remodeling as well as osteoblast mechanotransduction [4]. Thus, P2Y2 may also have important functions in the synergistic effects resulted from combining mechanical stimulation and PTH. In this study, ERK1/2 phosphorylation was used as a major indictor to measure osteoblast activities because ERK1/2 can initiate many downstream pathways such as COX-2, Runx2, OPG, OPN, and MMP13 and subsequently plays a key role in regulating bone cell activities, including migration, survival, proliferation, and differentiation [25, 26]. We also examined phosphorylated CREB and cell proliferation in order to study mechanisms of the synergy between mechanical stimulation and PTH, which are closely related to bone regeneration.

2. Materials and Methods

2.1. Cell Culture and Experiment Protocols. The mouse osteoblastic cell line MC3T3-E1 was cultured in minimal essential α medium (MEM-α) containing 10% fetal bovine serum, 1% penicillin, and streptomycin and maintained in a humidified incubator at 37°C with 5% CO_2. For oscillatory fluid flow experiments, all cells were cultured on glass slides for 2 days prior to experiments, and 1.5×10^5 cells were seeded on glass slides ($75 \times 38 \times 1.0$ mm) for oscillatory fluid flow experiments. Cells were exposed to oscillatory fluid flow in MEM-α without FBS for all experiments. The fluid flow chamber employed in this study is a parallel plate design, and the flow delivery device generated 1 Hz sinusoidal oscillating flow with 10 dyne/cm^2 fluid shear stress on cells as described in previous studies [16, 27]. For ATP effects, 10 mM final concentration ATP was added to cell culture plates directly. For PTH effects, 50 nM final concentration PTH (1-34) was added to cell culture plates or fluid flow medium directly.

2.2. Overexpression and siRNA Knockdown of P2Y2. To overexpress P2Y2 in cells, full length cDNA plasmid pcDNA3-P2Y2 was transfected into MC3T3-E1 osteoblasts using the FuGENE 6 transfection reagent kit from Roche according to manufacturer's protocols. For siRNAs against P2Y2, si-P2Y2 sense/antisense was designed and manufactured by Qiagen, Inc. The efficiency of knocking down was confirmed by mRNA and protein expression using RT-PCR and western blotting, respectively.

2.3. Western Blot. Immediately after experiments, cells were lysed with RIPA buffer, and total protein concentrations were measured by the bicinchoninic acid assay. Twenty-five micrograms of the total protein from each sample was separated by SDS–PAGE and transferred to PVDF membranes. Membranes were incubated with the desired primary antibody overnight at 4°C and subsequently with the secondary antibody for 1 hour. Visualization of proteins was achieved by using an ECL detection system and membrane exposure to film.

2.4. ATP Detection. Samples of conditioned media were collected, and ATP concentration in the samples was measured using a Roche ATP bioluminescence kit. Briefly, ATP was used to convert D-luciferin into oxyluciferin and light. The light density from each sample was measured by a luminometer and compared with a standard curve created by ATP standards. Three measurements were taken from each sample. Results were normalized to protein concentration using the bicinchoninic acid assay.

2.5. Cell Proliferation Assay. Cell proliferation was measured with the FITC 5-bromo-2-deoxyuridine (BrdU) flow kit according to the manufacturer's protocols. After exposed to oscillatory fluid flow for 1 hour, MC3T3-E1 osteoblasts were placed back into incubator for 24 hours. After that, cells were labeled with BrdU and then quantified using fluorescence-activated cell sorting with a FITC-conjugated antibody specific for BrdU.

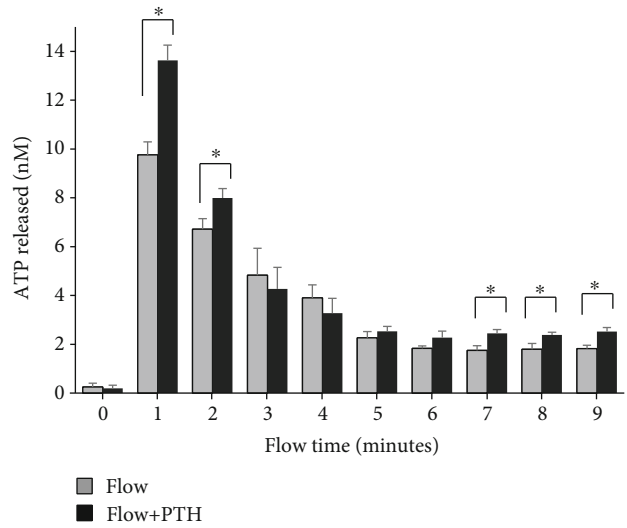

Figure 2: Osteoblast ATP release in response to oscillatory fluid flow with or without PTH. ($n = 3$, $^*p < 0.05$, each bar represents the mean ± SEM).

2.6. Data Analysis. Data are expressed as mean ± standard error (SE). To compare two groups, two-sample Student's t -test was used in which sample variance was not assumed to be equal. To compare observations from more than two groups, a one-way analysis of variance was employed followed by a Bonferroni selected-pairs multiple comparisons test. $p < 0.05$ was considered statistically significant.

3. Results

3.1. PTH Enhances Osteoblast Responses to Mechanical Stimulation. We first examined the effect of PTH on MC3T3-E1 osteoblastic cells in terms of ERK1/2 phosphorylation in response to oscillatory fluid flow. We treated cells with 50 nM PTH for 30 minutes and found that PTH alone did not alter ERK1/2 phosphorylation. However, PTH-treated MC3T3-E1 cells have a significantly greater phosphorylated ERK1/2 expression in response to fluid flow, compared with cells without PTH treatments (Figure 1(a)). Additionally, ERK1/2 phosphorylation quickly reaches its maximum value at round minute 5, then decreases. Thus, we used only 5-minute oscillatory fluid flow in our rest experiments to study ERK1/2 phosphorylation.

3.2. PTH Reduces Osteoblast Desensitization Time after Mechanical Stimulation. After subjected to oscillatory fluid flow for 5 minutes, MC3T3-E1 osteoblast may take up to 120 minutes to completely recover its sensitivity to respond to another oscillatory fluid flow according to our previous experiments [28]. In this study, MC3T3-E1 cells were treated with or without PTH for 30 minutes after first fluid flow stimulation, then exposed to second fluid flow stimulation. We found that PTH-treated cells have significantly higher phosphorylated ERK1/2 expression level compared to non PTH-treated cells (Figure 1(b)). The result suggests that PTH may be able to reduce the osteoblast refractory period after mechanical stimulation.

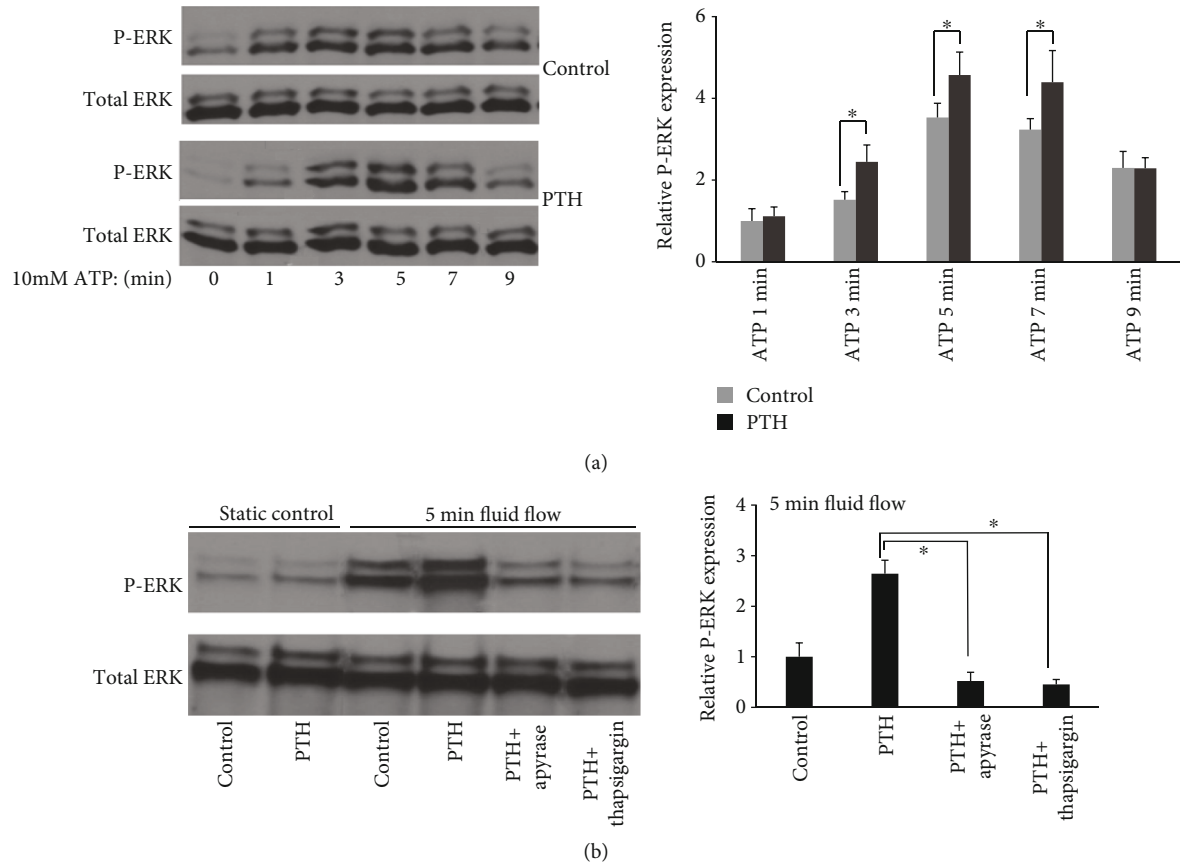

Figure 3: ATP is involved in the synergistic responses of osteoblasts to PTH and oscillatory fluid flow. (a) ERK1/2 phosphorylation in response to ATP with or without PTH treatment for different times. (b) Apyrase and thapsigargin inhibit the synergy between PTH and fluid flow. ($n = 4$, $^*p < 0.05$, each bar represents the mean ± SEM).

3.3. PTH Alters ATP Release Pattern Induced by Mechanical Stimulation. We also checked ATP release of PTH-treated MC3T3-E1 cells in response to oscillatory fluid flow. We found that the amount of ATP released of PTH-treated cells is significantly increased after 1 minute which is the maximum point of the ATP release curve, compared with non-treated cells. After that, ATP concentration is quickly diminishing. After minute 5, ATP release from cells reached a relatively stable stage, and the changes from minute 5 to minute 9 are very small and insignificant (Figure 2). Similar to the P-ERK expression, the ATP release result suggests that MC3T3-E1 cells are more sensitive to oscillatory fluid flow after PTH treatment.

3.4. PTH Enhances Osteoblast Responses to ATP. Since MC3T3-E1 cells release ATP when subjected to fluid flow stimulation, we also examined the responses of osteoblast after treated with both ATP and PTH. We found that ATP induced ERK1/2 activation, and PTH enhanced this response in a similar pattern to mechanical stimulation. (Figure 3(a)). The results suggest that PTH may potentiate osteoblast responses to mechanical stimulation through the ATP pathway.

3.5. The ATP Pathway Is Involved in the Synergistic Responses of Osteoblasts to PTH and Mechanical Stimulation. When we used apyrase (1 U/ml), an enzyme able to rapidly hydrolyzes ATP, together with PTH for MC3T3-E1 during fluid flow experiments, we found that the cell response in terms of ERK1/2 phosphorylation was significantly decreased. If we pretreated cells with thapsigargin (5 μM), an endoplasmic reticulum (ER) ATPase inhibitor, we also found that cell responses to PTH and fluid flow were significantly decreased in terms of ERK1/2 phosphorylation (Figure 3(b)).

3.6. PTH May Potentiate Fluid Flow-Induced Effects through P2Y2 Purinergic Receptors. We have showed previously that the P2Y2 receptor is responsible for fluid flow-induced intracellular calcium release and ERK1/2 phosphorylation. In this study, we found that when the P2Y2 expression was knocked down by siRNA in MC3T3-E1 cells, the ERK1/2 phosphorylation level was also significantly decreased even in the presence of PTH. When P2Y2 is overexpressed in MC3T3-E1 cells, the phosphorylated ERK1/2 level was significantly increased with PTH (Figure 4(a)). We also examined CREB phosphorylation when MC3T3-E1 cells were exposed to both PTH and oscillatory fluid flow (Figure 4(b)). We found similar results to ERK1/2 phosphorylation. The results suggest that P2Y2 purinergic receptors may be involved in the crosstalk between the PTH pathway and mechanotransduction pathway of osteoblasts.

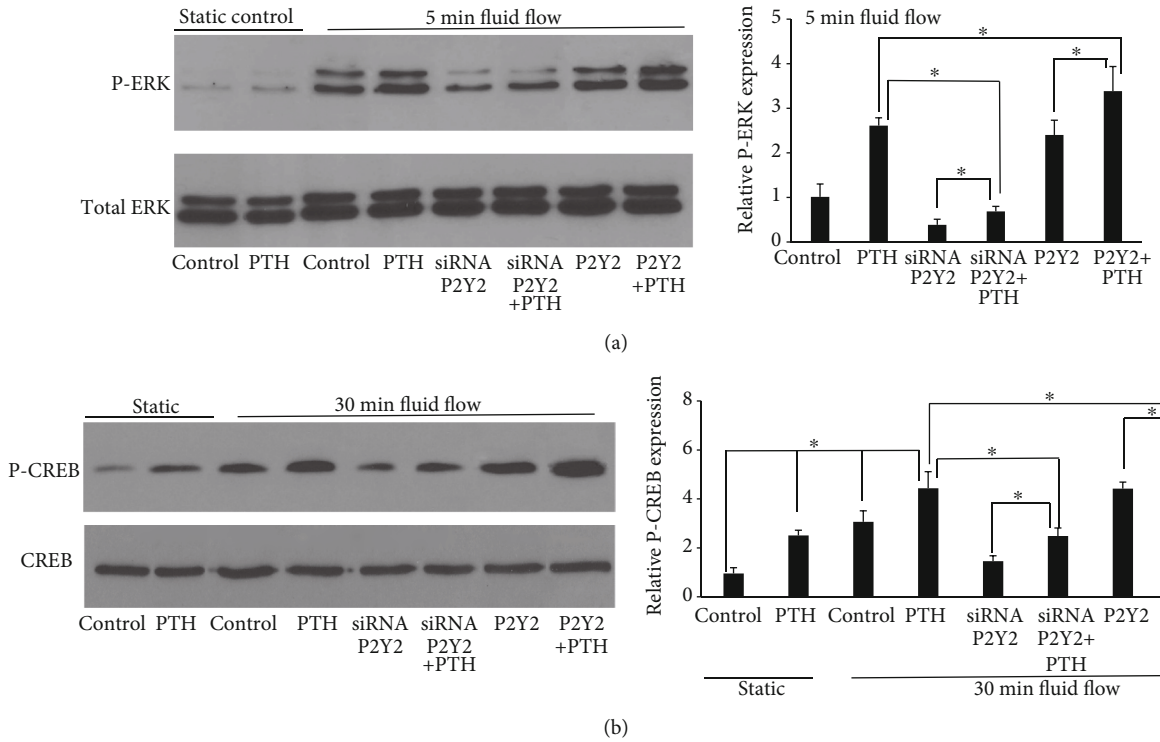

Figure 4: P2Y2 purinergic receptors are involved in PTH and oscillatory fluid flow-induced osteoblast responses. (a) Knockdown of P2Y2 inhibits ERK1/2 phosphorylation while the overexpression of P2Y2 enhances ERK1/2 phosphorylation. (b) Knockdown of P2Y2 inhibits CREB phosphorylation while the overexpression of P2Y2 enhances CREB phosphorylation. ($n = 4$, $^*p < 0.05$, each bar represents the mean ± SEM).

3.7. ATP and Its Receptor P2Y2 Are Important for Osteoblast Proliferation. Osteoblast proliferation is a crucial factor for bone growth and remodeling. So, we examined MC3T3-E1 cell proliferation when exposed to fluid flow and PTH. We found that fluid flow and PTH are able to increase cell proliferation significantly as shown in Figure 5. When combining them together, PTH and fluid flow can increase cell proliferation even greater. When we use apyrase to quickly remove ATP, or use siRNA to knock down the cell P2Y2 expression level, we found that cell proliferation was significantly inhibited.

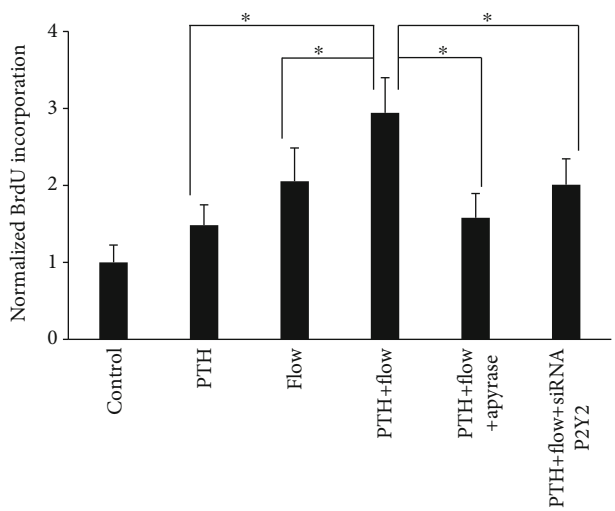

Figure 5: ATP and P2Y2 purinergic receptors are involved in PTH and fluid flow-induced osteoblast proliferation. Removal of ATP by apyrase or knockdown of P2Y2 receptors inhibited PTH and fluid flow-induced cell proliferation. ($n = 3$, $^*p < 0.05$, each bar represents the mean ± SEM).

4. Discussion

Mechanical signals mediate bone growth and regeneration, and the intermittent administration of PTH can enhance the effects [15, 29], but the mechanism how they work together is still elusive. We previously examined the role of P2Y2 purinergic receptors in the bone mechanotransduction pathway [4, 30] and found it is closely related to ATP and calcium signaling pathways. Other researchers demonstrated that osteoblast calcium signaling induced by mechanical loads may be enhanced by PTH, and ATP may sensitize PTH receptor [13, 22]. Thus, we believe that P2Y2 purinergic receptors may play an important role in synergistical responses of the combined action of PTH and mechanical signals.

In the present study, we firstly showed that PTH is able to work synergically with oscillatory fluid flow to potentiate osteoblast ERK1/2 phosphorylation, which play important roles in bone formation. The result is similar to previous

findings that PTH can enhance the COX-2 expression, calcium release, and c-fos expression from osteoblasts in response to mechanical signals [12, 22, 24]. We also found that PTH is able to reduce the osteoblast refractory period after mechanical stimulation in terms of ERK1/2 phosphorylation. This effect may cause osteoblast response to mechanical signals more often. As a result, osteoblast's total effective response time is increased during mechanical stimulation, which may subsequently lead to further cell proliferation and bone regeneration.

We further found that the osteoblast ATP release induced by oscillatory fluid flow is also enhanced. Since ATP stimulation is able to cause ERK1/2 activation, thus we subsequently examined the synergistic effects of PTH and ATP using osteoblast ERK1/2 activation. We found that PTH is also able to potentiate ATP-induced ERK1/2 activation in the exact same pattern as induced by oscillatory fluid flow. Previous literatures have demonstrated that ATP can synergize with PTH to increase intracellular calcium release and c-fos expression [31, 32]. ATP is also able to synergize with PDGF to increase DNA synthesis in MC3T3-E1 cells [33]. Thus, we suspect that the combined effects of PTH and mechanical signals on osteoblast are through the ATP pathway. For these reasons, we used apyrase to remove fluid flow induced-ATP from extracellular space and checked osteoblast responses. We found that the synergistic effects from fluid flow and PTH were significantly attenuated. Additionally, when we used thapsigargin to inhibit ER calcium mobilization, the synergistic effects were also significantly attenuated. The results suggest that synergy of mechanical signals with PTH may be through the ATP-calcium-ERK1/2 pathway.

Due to the importance of ATP, we examined the role of the P2Y2 purinergic receptor in this process. We knocked down or overexpressed the P2Y2 expression level in MC3T3-E1 cells and compared their synergistic responses to oscillatory fluid flow and PTH to normal MC3T3-E1 cells. We found that P2Y2 knockdown inhibited such synergistic responses in terms of ERK1/2 and CREB phosphorylation. Furthermore, the P2Y2 overexpression in cells enhanced their responses to PTH and mechanical stimulation. These results confirmed that purinergic signaling is involved in the synergy of mechanical signals with PTH. Since both PTH receptor and P2Y2 receptor are GPCRs, they can be desensitized by GPCR kinases (GRKs). We have previous demonstrated that GRKs may be involved in fluid flow-induced osteoblast desensitization [28]. If PTH receptors are desensitized by the same GRK as P2Y2 receptors, then the administration of PTH may lead to recruitment of GRK to PTH receptors. In this situation, desensitization of P2Y2 receptors will be more difficult because the amount of free GRKs is reduced. As a result, PTH can work synergistically with oscillatory fluid flow to enhance osteoblast responses.

Osteoblast proliferation is important for bone growth and regeneration. ERK1/2 has been shown to regulate osteoblast proliferation through a number of pathways, including c-fos and Runx2 [34–37]. For these reasons, we examined the involvement of P2Y2 receptors and ATP in osteoblast proliferation induced by PTH and fluid flow. We found that removal of ATP by apyrase or knockdown of P2Y2 receptors by siRNA inhibited osteoblast proliferation. The results are reasonable since reduction of ATP and P2Y2 inhibited ERK1/2 and CREB phosphorylation based on our previous findings. Additionally, other researchers have demonstrated that purinergic receptors were closely related to cell proliferation [38].

5. Conclusions

In this study, we demonstrated that PTH enhanced oscillatory fluid flow-induced osteoblast ERK1/2 phosphorylation, ATP release, CREB phosphorylation, and cell proliferation and decreased the osteoblast refractory period due to mechanical stimulation. We also showed that depletion of extracellular ATP during fluid flow or knockdown of purinergic receptor P2Y2 expression can inhibit above synergistic responses. Our results suggest that osteoblast is more responsive to mechanical signals in the presence of PTH, and P2Y2 purinergic receptors play important roles in the process. Both P2Y2 receptors and PTH receptors are GPCRs, so they may use the same desensitization pathway. As a result, it may become harder to deactivate both of them at the same time.

Data Availability

The figures and data used to support the findings of this study are included within the article.

Conflicts of Interest

The authors declare that they have no conflict of interests.

Acknowledgments

This work was funded by Grant #11672078 from the National Natural Science Foundation of China (NSFC).

References

[1] N. Rosa, R. Simoes, F. D. Magalhães, and A. T. Marques, "From mechanical stimulus to bone formation: a review," *Medical Engineering & Physics*, vol. 37, no. 8, pp. 719–728, 2015.

[2] M. Wall, D. Butler, A. el Haj, J. C. Bodle, E. G. Loboa, and A. J. Banes, "Key developments that impacted the field of mechanobiology and mechanotransduction," *Journal of Orthopaedic Research*, vol. 36, no. 2, pp. 605–619, 2018.

[3] R. Alfieri, M. Vassalli, and F. Viti, "Flow-induced mechanotransduction in skeletal cells," *Biophysical Reviews*, vol. 11, no. 5, pp. 729–743, 2019.

[4] Y. Xing, Y. Gu, J. J. Bresnahan, E. M. Paul, H. J. Donahue, and J. You, "The roles of P2Y2 purinergic receptors in osteoblasts and mechanotransduction," *PLoS One*, vol. 9, no. 9, article e108417, 2014.

[5] G. Iolascon, G. Resmini, and U. Tarantino, "Mechanobiology of bone," *Aging Clinical and Experimental Research*, vol. 25, Supplement 1, pp. S3–S7, 2013.

[6] L. J. Suva and P. A. Friedman, "PTH and PTHrP actions on bone," in *Handbook of Experimental Pharmacology*, Springer, Cham, 2020.

[7] D. B. Burr, "Does early PTH treatment compromise bone strength? The balance between remodeling, porosity, bone

mineral, and bone size," *Current Osteoporosis Reports*, vol. 3, no. 1, pp. 19–24, 2005.

[8] A. B. Hodsman, D. C. Bauer, D. W. Dempster et al., "Parathyroid hormone and teriparatide for the treatment of osteoporosis: a review of the evidence and suggested guidelines for its use," *Endocrine Reviews*, vol. 26, no. 5, pp. 688–703, 2005.

[9] R. L. Jilka, "Molecular and cellular mechanisms of the anabolic effect of intermittent PTH," *Bone*, vol. 40, no. 6, pp. 1434–1446, 2007.

[10] Z. Saidak, C. le Henaff, S. Azzi, C. Marty, and P. J. Marie, "Low-dose PTH increases osteoblast activity via decreased Mef2c/Sost in senescent osteopenic mice," *The Journal of Endocrinology*, vol. 223, no. 1, pp. 25–33, 2014.

[11] A. Chandra, T. Lin, J. Zhu et al., "PTH1-34 blocks radiation-induced osteoblast apoptosis by enhancing DNA repair through canonical Wnt pathway," *The Journal of Biological Chemistry*, vol. 290, no. 1, pp. 157–167, 2015.

[12] K. D. Ryder and R. L. Duncan, "Parathyroid hormone modulates the response of osteoblast-like cells to mechanical stimulation," *Calcified Tissue International*, vol. 67, no. 3, pp. 241–246, 2000.

[13] J. Zhang, K. D. Ryder, J. A. Bethel, R. Ramirez, and R. L. Duncan, "PTH-induced actin depolymerization increases mechanosensitive channel activity to enhance mechanically stimulated 2+ signaling in osteoblasts∗," *Journal of Bone and Mineral Research*, vol. 21, no. 11, pp. 1729–1737, 2006.

[14] R. L. Duncan, K. A. Hruska, and S. Misler, "Parathyroid hormone activation of stretch-activated cation channels in osteosarcoma cells (UMR-106.01)," *FEBS Letters*, vol. 307, no. 2, pp. 219–223, 1992.

[15] C. H. Kim, E. Takai, H. Zhou et al., "Trabecular bone response to mechanical and parathyroid hormone stimulation: the role of mechanical microenvironment," *Journal of Bone and Mineral Research*, vol. 18, no. 12, pp. 2116–2125, 2003.

[16] J. You, C. R. Jacobs, T. H. Steinberg, and H. J. Donahue, "P2Y purinoceptors are responsible for oscillatory fluid flow-induced intracellular calcium mobilization in osteoblastic cells," *The Journal of Biological Chemistry*, vol. 277, no. 50, pp. 48724–48729, 2002.

[17] D. C. Genetos, D. J. Geist, D. Liu, H. J. Donahue, and R. L. Duncan, "Fluid shear-induced ATP secretion mediates prostaglandin release in MC3T3-E1 osteoblasts," *Journal of Bone and Mineral Research*, vol. 20, no. 1, pp. 41–49, 2005.

[18] Y. Nakano, W. N. Addison, and M. T. Kaartinen, "ATP-mediated mineralization of MC3T3-E1 osteoblast cultures," *Bone*, vol. 41, no. 4, pp. 549–561, 2007.

[19] A. Pines, M. Romanello, L. Cesaratto et al., "Extracellular ATP stimulates the early growth response protein 1 (Egr-1) via a protein kinase C-dependent pathway in the human osteoblastic HOBIT cell line," *The Biochemical Journal*, vol. 373, no. 3, pp. 815–824, 2003.

[20] A. M. Weihs, C. Fuchs, A. H. Teuschl et al., "Shock wave treatment enhances cell proliferation and improves wound healing by ATP release-coupled extracellular signal-regulated kinase (ERK) activation," *The Journal of Biological Chemistry*, vol. 289, no. 39, pp. 27090–27104, 2014.

[21] R. C. Riddle, A. F. Taylor, J. R. Rogers, and H. J. Donahue, "ATP release mediates fluid flow-induced proliferation of human bone marrow stromal cells," *Journal of Bone and Mineral Research*, vol. 22, no. 4, pp. 589–600, 2007.

[22] A. Bond, J. P. Dillon, E. L. Pacheco-Pantoja, W. D. Fraser, J. C. Jarvis, and J. A. Gallagher, "ATP is released from osteoclasts and osteoblasts and sensitises bone to the action of PTH and other systemic hormones," *Purinergic Signal*, vol. 6, pp. 143-144, 2010.

[23] W. B. Bowler, C. J. Dixon, C. Halleux et al., "Signaling in human osteoblasts by extracellular nucleotides. Their weak induction of the c-fos proto-oncogene via Ca2+ mobilization is strongly potentiated by a parathyroid hormone/cAMP-dependent protein kinase pathway independently of mitogen-activated protein kinase," *The Journal of Biological Chemistry*, vol. 274, no. 20, pp. 14315–14324, 1999.

[24] K. A. Buckley, S. C. Wagstaff, G. McKay et al., "Parathyroid hormone potentiates nucleotide-induced [Ca2+]iRelease in rat osteoblasts independently of Gqactivation or cyclic monophosphate accumulation," *The Journal of Biological Chemistry*, vol. 276, no. 12, pp. 9565–9571, 2001.

[25] R. T. Franceschi, C. Ge, G. Xiao, H. Roca, and D. Jiang, "Transcriptional regulation of osteoblasts," *Annals of the New York Academy of Sciences*, vol. 1116, no. 1, pp. 196–207, 2007.

[26] R. T. Franceschi and C. Ge, "Control of the osteoblast lineage by mitogen-activated protein kinase signaling," *Current Molecular Biology Reports*, vol. 3, no. 2, pp. 122–132, 2017.

[27] C. R. Jacobs, C. E. Yellowley, B. R. Davis, Z. Zhou, J. M. Cimbala, and H. J. Donahue, "Differential effect of steady versus oscillating flow on bone cells," *Journal of Biomechanics*, vol. 31, no. 11, pp. 969–976, 1998.

[28] Y. Xing, Y. Gu, X. Shan, L. Wang, and J. You, "GRK2 desensitizes flow-induced responses in osteoblasts," *Genetics and Molecular Research*, vol. 16, no. 1, 2017.

[29] M. Ellegaard, T. Kringelbach, S. Syberg et al., "The effect of PTH(1-34) on fracture healing during different loading conditions," *Journal of Bone and Mineral Research*, vol. 28, no. 10, pp. 2145–2155, 2013.

[30] Y. Xing, Y. Gu, R. R. Gomes Jr., and J. You, "P2Y(2) receptors and GRK2 are involved in oscillatory fluid flow induced ERK1/2 responses in chondrocytes," *Journal of Orthopaedic Research*, vol. 29, no. 6, pp. 828–833, 2011.

[31] A. D. Kaplan, W. J. Reimer, R. D. Feldman, and S. J. Dixon, "Extracellular nucleotides potentiate the cytosolic Ca2+, but not cyclic adenosine 3', 5'-monophosphate response to parathyroid hormone in rat osteoblastic cells," *Endocrinology*, vol. 136, no. 4, pp. 1674–1685, 1995.

[32] E. L. Pacheco-Pantoja, J. P. Dillon, P. J. M. Wilson, W. D. Fraser, and J. A. Gallagher, "C-Fos induction by gut hormones and extracellular ATP in osteoblastic-like cell lines," *Purinergic Signal*, vol. 12, no. 4, pp. 647–651, 2016.

[33] S. Shimegi, "ATP and adenosine act as a mitogen for osteoblast-like cells (MC3T3-E1)," *Calcified Tissue International*, vol. 58, no. 2, pp. 109–113, 1996.

[34] M. Liu, F. Fan, P. Shi et al., "Lactoferrin promotes MC3T3-E1 osteoblast cells proliferation via MAPK signaling pathways," *International Journal of Biological Macromolecules*, vol. 107, Part A, pp. 137–143, 2018.

[35] M. Awazu, M. Nagata, and M. Hida, "BMP7 dose-dependently stimulates proliferation and cadherin-11 expression via ERK and p38 in a murine metanephric mesenchymal cell line," *Physiological Reports*, vol. 5, no. 16, article e13378, 2017.

[36] Y. X. Yan, Y. W. Gong, Y. Guo et al., "Mechanical strain regulates osteoblast proliferation through integrin-mediated ERK activation," *PLoS One*, vol. 7, no. 4, article e35709, 2012.

[37] A. Raucci, P. Bellosta, R. Grassi, C. Basilico, and A. Mansukhani, "Osteoblast proliferation or differentiation is regulated by relative strengths of opposing signaling pathways," *Journal of Cellular Physiology*, vol. 215, no. 2, pp. 442–451, 2008.

[38] N. Mikolajewicz and S. V. Komarova, "Role of UDP-sugar receptor P2Y(14) in murine osteoblasts," *International Journal of Molecular Sciences*, vol. 21, no. 8, 2020.

Hindawi
BioMed Research International
Volume 2020, Article ID 8412468, 8 pages
https://doi.org/10.1155/2020/8412468

Research Article

Panax Notoginseng Saponins Prevent Bone Loss by Promoting Angiogenesis in an Osteoporotic Mouse Model

Hao Hu,[1] **Yan Chen**,[1] **Zhiyuan Zou**,[1] **Liangping Li**,[1] **Fuxin Wei**,[2] **Chun Liu**,[3] **Zemin Ling**,[1] **and Xuenong Zou**[1]

[1]*Guangdong Provincial Key Laboratory of Orthopedics and Traumatology, Department of Spinal Surgery, The First Affiliated Hospital of Sun Yat-sen University, Guangzhou 510080, China*
[2]*Department of Orthopaedic Surgery, The Seventh Affiliated Hospital and Orthopedic Research Institute of Sun Yat-sen University, Shenzhen 518107, China*
[3]*Precision Medicine Institute, The First Affiliated Hospital of Sun Yat-sen University, Guangzhou 510080, China*

Correspondence should be addressed to Zemin Ling; lingzm@mail2.sysu.edu.cn and Xuenong Zou; zouxuen@mail.sysu.edu.cn

Hao Hu and Yan Chen contributed equally to this work.

Received 22 August 2020; Revised 6 November 2020; Accepted 27 November 2020; Published 14 December 2020

Academic Editor: Shen Liu

With the aging of the population and the extension of life expectancy, osteoporosis is becoming a global epidemic. Although there are several drugs used to treat osteoporosis in clinical practice, such as parathyroid hormone or bisphosphonates, they all have some serious side effects. Therefore, a safer drug is called for osteoporosis, especially for the prevention in the early stage of the disease, not only the treatment in the later stage. Panax notoginseng saponin (PNS), a traditional Chinese herb, has been used as anti-ischemic drug due to its function on improving vascular circulation. In order to verify whether Panax notoginseng saponins (PNS) could be used to prevent osteoporosis, ovariectomy (OVX) was induced in female C57BL/C6J mice, followed by orally administration with 40 mg/kg/d, 80 mg/kg/d, and 160 mg/kg/d of three different dosages of PNS for 9 weeks. Serum biochemical analysis, micro-CT, histological evaluation, and immunostaining of markers of osteogenesis and angiogenesis were performed in the sham, osteoporotic (OVX), and treatment (OVX+PNS) groups. Micro-CT and histological evaluation showed that compared to sham group, the bone mass of OVX group reduced significantly, while it was significantly restored in the moderate-dose PNS (40 mg/kg and 80 mg/kg) treatment groups. The expression of CD31 and osteocalcin (OCN) in the bone tissue of treatment group also increased, suggesting that PNS activated osteogenesis and angiogenesis, which subsequently increased the bone mass. These results confirmed the potential function of PNS on the prevention of osteoporosis. However, in the high dose of PNS (160 mg/kg) group, the antiosteoportic effect had been eliminated, which also suggested the importance of proper dose of PNS for the prevention and treatment of osteoporosis in postmenopausal women.

1. Introduction

Osteoporosis is a metabolic disease characterized by decreased bone mass, increased bone fragility, and micro-architectural deterioration of bone tissue. In addition to increasing the risk of fragility fracture, osteoporosis may also increase the risk of hospitalization associated with certain complications. With the increasing aging of China's population, the prevalence of osteoporosis has increased remarkably in the past decade (from 14.94% before 2012 to 27.96% in 2015), and the prevalence in women was significantly higher than that in men (25.41% vs. 15.33%) [1].

With aging, decreased angiogenesis in bone and bone marrow is a principal cause of osteoporosis [2]. Because estrogen is also an important regulator for angiogenesis, its deficiency can lead to osteoporosis for postmenopausal women or those who have undergone tumor-related ovariectomy. Traditional Chinese medicine has been used for thousands

of years and still plays an important role in the prevention and the treatment of diseases in modern China. The dried root of Panax notoginseng, namely, Sanchi (San Qi), is a famous traditional Chinese herb. The active ingredients of Panax notoginseng include saponins, dencichine, flavonoids, and polysaccharides, among which the pharmaceutical effects of the saponins had been studied extensively [3]. The total saponins of Panax notoginseng mainly include ginsenosides Ra3, Rg1, Rb1, and Rd and notoginsenoside R1. Blood concentration of ginsenosides Ra3, Rb1, and Rd was significantly higher than other compounds after an oral administration of Panax notoginseng extract in a rat model [4]. Panax notoginseng saponin (PNS) is a vasoactive drug [5], which has been used as an anti-ischemic agent to promote blood circulation in traditional Chinese medicine; however, it also displayed anti-inflammatory [6, 7], antioxidant [8–11], and estrogen-like [12, 13] activities in vitro, making it a potential cure for postmenopausal osteoporosis.

Some previous studies confirmed that Panax notoginseng saponins facilitate the osteogenic process of the skeletal progenitor cells in vitro [14, 15], including the proliferation, differentiation, and mineralization. The possible mechanism is that PNS promotes the expression of downstream osteogenesis-related genes by activating ERK and p38 [16] as well as TGF-β1 [17] signaling pathways. Angiogenesis plays an indispensable role in osteogenesis [18], and the most important pharmacological function of PNS is its vasoactive effect, indicating that PNS could preserve bone mass by promoting the coupling of angiogenesis and osteogenesis during osteoporosis. Although other two studies had also proved the pharmacological effect of PNS on alleviating osteoporosis in rat ovariectomy model [19, 20], the underlying mechanisms were not investigated, especially there were no studies to evaluate the function of PNS on preventing bone loss at the early stage of menopause. In this study, we established an ovariectomy-induced osteoporosis mouse model to fully investigate whether early PNS treatment can prevent bone loss by targeting the vascular microarchitecture.

2. Materials and Methods

2.1. Materials. PNSs, the total saponins of Panax notoginseng, were purchased from KPC Xuesaitong Pharmaceutical Co., Ltd (Yunnan, China). C57BL/6J mice were purchased from SPF (Beijing) Biotechnology Co., Ltd (Beijing, China). Mouse NTXI(cross linked N-telopeptide of type I collagen) ELISA kit (E-EL-M3022) was purchased from Elabscience (Wuhan, China). Anti-osteocalcin antibody (ab93876), recombinant anti-CD31 antibody (ab182981), goat anti-rabbit IgG H&L (Alexa Fluor® 488) (ab150077), and goat anti-rabbit IgG H&L (HRP) (ab205718) were purchased from Abcam (USA).

2.2. Animal Model and PNS Treatment. All the animal experiments were carried out carefully in accordance with the principles and guidelines of the Animal Ethics Committee of the First Affiliated Hospital of Sun Yet-sen University. 30 twelve-week-old female C57BL/6J mice were housed in individual ventilated cages under controlled conditions (temperature, 20-26°C; humidity, 40-70%) for a 12-hour light-dark cycle and were allowed free access to water and food.

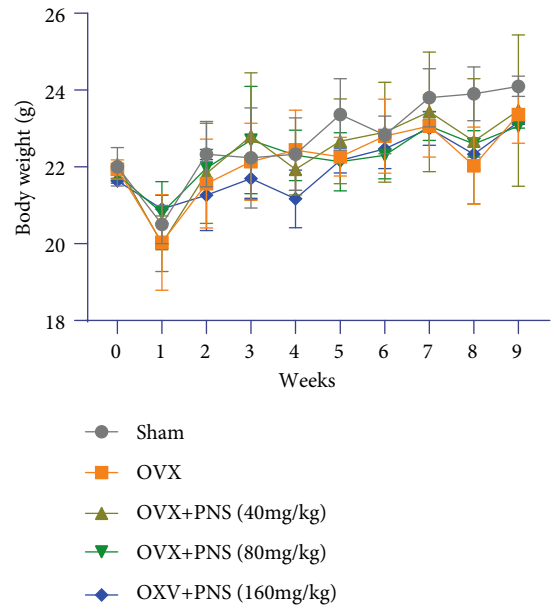

Figure 1: Plot of body weight of mice with respect to time, recorded over a period of pre- and 9 weeks postoperation. Values are presented as means ± S.D. ($N = 6$).

After one-week adaptation period, the animals were randomly divided into 5 equal groups (six in one cage): (1) sham operation (sham group), (2) ovariectomy (OVX group), (3) ovariectomy+40 mg/kg/d PNS (low-dose group), (4) ovariectomy+80 mg/kg/d PNS (medium-dose group), and (5) ovariectomy+160 mg/kg/d PNS (high-dose group). Ovariectomy or a sham operation was performed under pentobarbital sodium (90 mg/kg, i.p.) anesthesia. Two longitudinal incisions were made inferior to the rib cage on the dorsolateral body wall, and then the bilateral ovaries were exteriorized, ligated, and excised. Mice in the sham surgical group had only a piece of fat excised. After the surgery, mice in PNS-treated groups were orally administered (oral gavage) with different dosages for 9 weeks, while mice in the sham group and the OVX group were also orally administered with water in the same volume. After 9-week treatment, all mice were euthanized. Eyeball blood collection was conducted, and serum was separated by centrifugation at 1,800 rpm for 10 minutes, then were aliquoted and stored at -20°C for further analysis. PBS and then paraformaldehyde were perfused into the whole body through the left ventricle. Femora were dissected and stored at 4% paraformaldehyde at 4°C for further analysis.

2.3. Serum Biochemical Analysis. Serum samples were sent to Kingmed Diagnostic (Group Co., Ltd) for conventional biochemical analysis, including serum alanine aminotransferase (ALT), creatinine (CREA), serum calcium (S-Ca), and serum phosphorus (S-P). Serum bone turnover markers like N-telopeptide of type I collagen (NTX) were tested by using a commercial ELISA kit (E-EL-M3022). Serum ALT and CREA were tested to verify whether PNS reveals a dose-

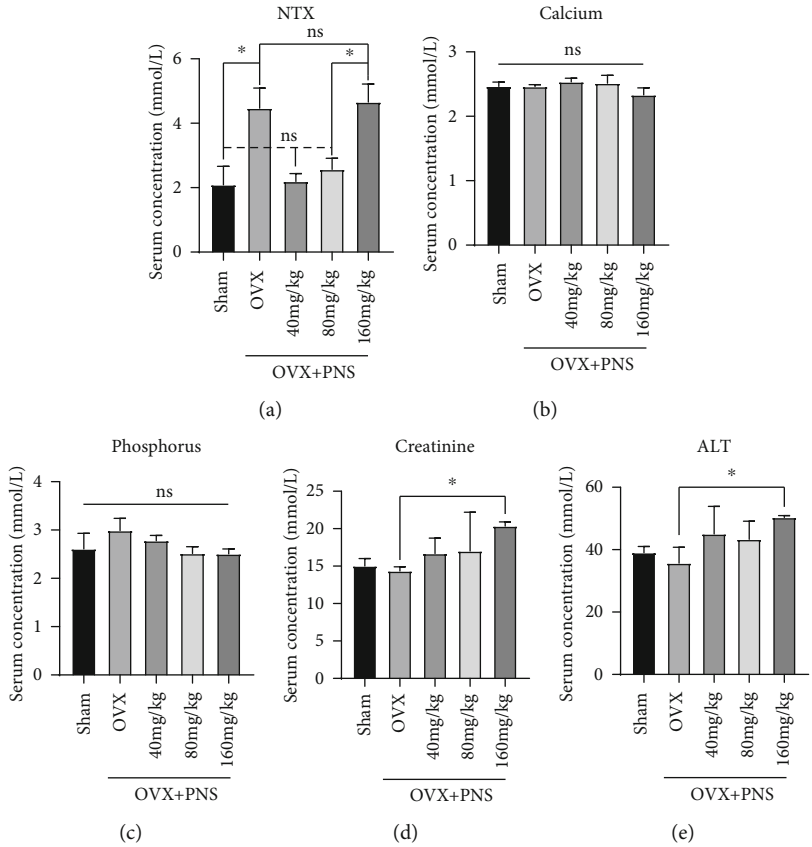

Figure 2: Serum biochemical quantitative analysis of N-telopeptide of (a) type I collagen (NTX), (b) serum calcium, (c) phosphorus, (d) creatinine, and (e) alanine aminotransferase (ALT) in the sham, OVX, and PNS-treated groups ("ns" represents no significant difference; $^{*}P < 0.05$; $N = 6$).

dependent hepatorenal toxicity. S-Ca, S-P, and NTX were tested for bone metabolism.

2.4. Micro-CT Analysis. The microarchitectures of the distal femurs were analyzed by a desktop Micro-CT SkyScan1276 (Bruker Micro CT, Belgium). In our work, micro-CT scanner was operated at 85 kV and 200 μA. 1 mm thickness aluminium filter was used for optimal image contrast. Images were reconstructed and processed with a spatial scanning resolution of 10.0 μm. Software CTAn (Bruker micro-CT, Belgium) was used to perform image analysis. Trabecular bone was separated from cortical bone by free-drawing region of interest (ROI). Volume of interest (VOI, 1 mm proximal to the metaphyseal line) was chosen within 100 continuous slices. We performed bone morphologic measurements in CTAn and obtained corresponding parameters, including trabecular bone volume fraction (BV/TV; %), trabecular thickness (Tb.Th; μm), trabecular number (Tb.N; μm^{-1}), and trabecular separation (Tb.Sp; μm). Then, the 3D models of VOI were reconstructed with CTAn for visualization in the software CTVol (Bruker micro-CT, Belgium). The operator conducting the micro-CT analysis was blinded to the treatments associated with samples.

2.5. Histological Assessment and Immunostaining. After micro-CT analysis, all femur specimens were prefixed at 4% paraformaldehyde for 48 h, decalcified in 10% EDTA (pH 7.4) for 21 d at 4°C, and then embedded in paraffin. We processed 4 μm thick sagittal-oriented (longitudinally) sections of bone including the metaphysis and diaphysis. All slides were stored at 4°C in case of any further analysis. HE staining and Safranin O-Fast Green staining were performed for the analysis of bone microstructure.

Immunohistochemistry and immunofluorescence staining were applied to analyze osteogenesis and angiogenesis according to standard protocols. The sections were incubated at 4°C overnight with primary antibodies anti-osteocalcin (ab182981, Abcam, 1 : 500) and anti-CD31 (ab93876, Abcam, 1 : 500), respectively; the corresponding secondary antibodies were added onto the sections for 1 h. For osteocalcin immunohistochemistry, slides were stained with DAB (ab64238, Abcam) and then counterstained with hematoxylin (Sigma-Aldrich). For CD31 immunofluorescence, slides were counterstained with DAPI. The slide images were observed and captured by Eclipse Ti-SR microscope (Nikon, Japan). ImageJ was used for the following quantitative analysis.

2.6. Statistical Analysis. Statistical analysis was performed by using the SPSS 22.0 software (IBM Corp., Armonk, NY, USA). All data were presented as mean ± S.D. All error bars in figures represent S.D. Group comparison was made by using unpaired, two-tailed Student's t-test. For all statistical analysis, $^{*}P < 0.05$ was considered to be significant.

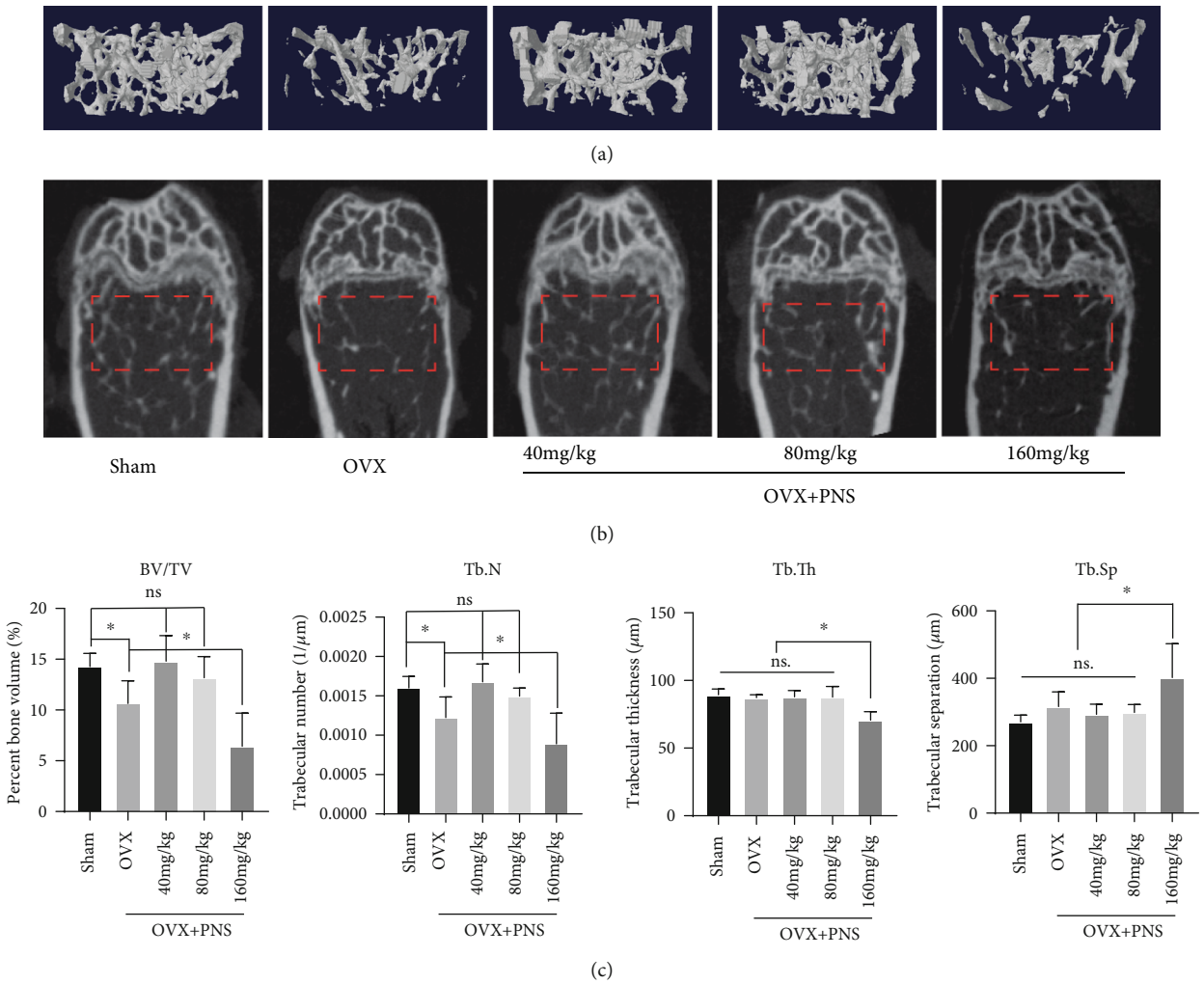

FIGURE 3: (a) Representative micro-CT 3D reconstructed images and (b) coronal images of trabecular bone in distal femur of sham, OVX, and PNS-treated groups. The red dotted line area represents the VOI for 3D reconstruction, and the quantitative analysis of the histomorphometry (c), including percent bone volume (BV/TV), trabecular thickness (Tb.Th), trabecular number (Tb.N), and trabecular separation (Tb.Sp), was measured ("ns" represents no significant difference; $^{*}P < 0.05$; $N = 6$).

3. Results

3.1. Body Weight. All the animals had normal activities and feeding during the whole experimental period. We monitored the body weight of mice in each group before operation and 1-9 weeks postoperation (Figure 1). Generally, the body weight of mice in all groups increased until they were sacrificed. Because of the surgical trauma, the body weight of each group decreased significantly ($P < 0.05$) one week right after operation. With the rehabilitation and growth of the mice, the body weight in each group gradually increased. There was no significant difference in body weight among the OVX and PNS-treated groups at each time point, indicating that the intake of PNS did not have a significant impact on body weight. Specially, the body weight of the sham operation group was significantly higher ($P < 0.05$) than that of the OVX group at the eighth week, which may due to less surgical trauma.

3.2. Serum Biochemical Analysis. In order to evaluate the pharmaceutic effects of PNS on bone, liver, and kidney metabolism, the serum collected from each group were tested for several indicators (Figure 2). NTX is a specific biochemical indicator of bone resorption that is generated as a result of osteoclast activity on bone. Compared with the sham operation group, the serum NTX (Figure 2(a)) of OVX group and OVX+PNS (160 mg/kg) group were significantly higher, while OVX+PNS (40 and 80 mg/kg) group showed no significant difference. These results indicated that PNS (40 and 80 mg/kg) inhibited the activities of osteoclasts in osteoporotic mice, but higher dose (160 mg/kg) of PNS intake would reverse the effect. As for the serum calcium and phosphorus (Figures 2(b) and 2(c)), there was no significant difference among the groups. The serum CREA and ALT (Figures 2(d) and 2(e)) were tested to access the function of kidney and liver, and high levels of them could reflect drug-induced liver and kidney injury. Notably, the creatinine and ALT in OVX+PNS (160 mg/kg) were significantly higher than the OVX group, and there are no significant differences among other groups. High dose (160 mg/kg) of PNS intake could cause damage to kidney and liver, which may be the

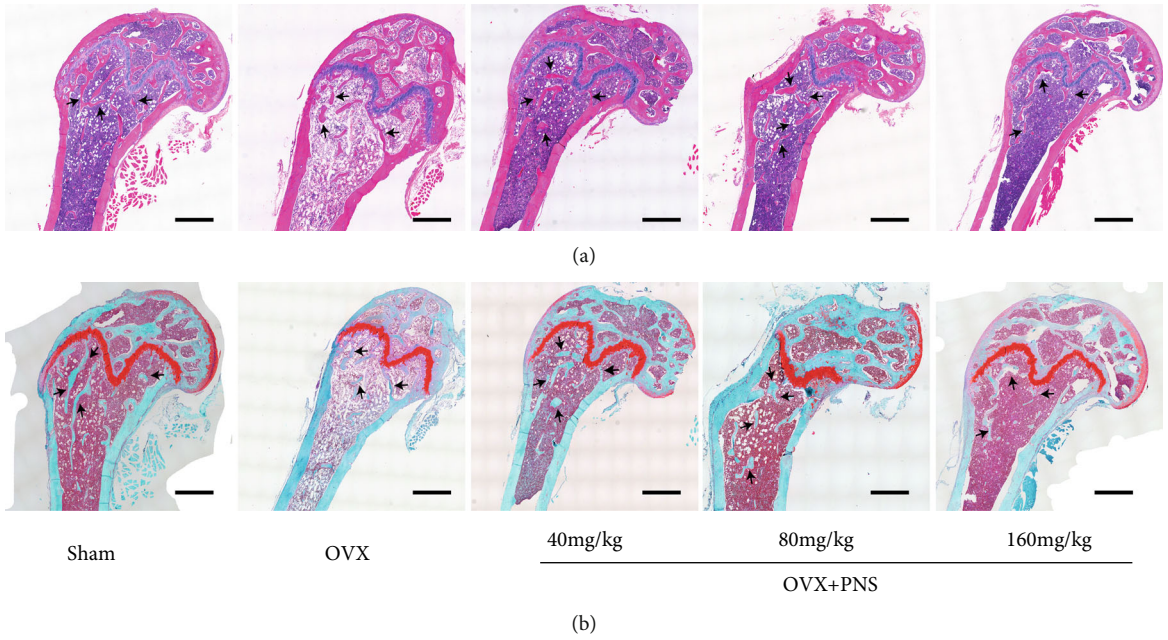

FIGURE 4: Representative sagittal images of (a) HE staining (scale bars = 500 μm) and (b) Safranin O-Fast Green staining (scale bars = 500 μm) of trabecular bone in distal femur of sham, OVX, and PNS-treated groups. Black arrowheads point out the typical trabecular bone in different groups.

reason why it had the opposite pharmacological effect compared with the lower-dose (40 and 80 mg/kg) PNS groups.

3.3. Micro-CT Analysis. Micro-CT 3D reconstructed images and coronal images (Figure 3) of trabecular bone in distal femur showed distinct differences among sham operation, OVX, and PNS-treated groups. In general, compared with sham operation group, bone mass reduced significantly in OVX group, which means the osteoporotic mouse model was successful. When treated with 40 mg/kg or 80 mg/kg PNS, the bone mass restored significantly. However, if the concentration of PNS increased to 160 mg/kg, the antiosteoporosis effect disappeared. Specifically, in the quantitative analysis of BV/TV and Tb.N, the sham group, 40 mg/kg, and 80 mg/kg PNS group showed no significant difference ($P > 0.05$), but OVX group showed significantly decrease ($P < 0.05$), and 160 mg/kg PNS group showed even more decrease. Then, in the quantitative analysis of Tb.Th and Tb.Sp, the sham, OVX, 40 mg/kg, and 80 mg/kg PNS groups showed no significant difference ($P > 0.05$), while the 160 mg/kg PNS group significantly decreased ($P < 0.05$) in Tb.Th and increased ($P < 0.05$) in Tb.Sp.

The above results indicated that intake of appropriate dose of PNS can increase the number of trabecular bone and bone volume and in general reveal an antiosteoporotic effect; however, high dose of PNS intake would even worsen the bone loss in the osteoporotic mouse model.

3.4. HE Staining and Safranin O-Fast Green Staining. In order to analyze the subtle changes of bone microstructure at histological and cytological levels, we performed HE staining and Safranin O-Fast Green staining among each groups (Figure 4). Bones were dyed pink in HE staining and were dyed green in Safranin O-Fast Green staining. It showed that the trabecular bone mass in the sham group and OVX+PNS (40 and 80 mg/kg) group were evidently higher than the OVX group and OVX+PNS(160 mg/kg) group, which was in consonance with the results of micro-CT morphometry.

3.5. Immunostaining of Osteoblasts and Vascular Endothelial Cells. Osteocalcin is one of the major noncollagenous proteins of the bone matrix, which is synthesized and secreted by osteoblasts and is specific for bone. In the immunostaining of osteocalcin, OVX group showed a significantly decrease in the number of osteoblasts when compared with the sham operation group (Figures 5(a), 5(c), and 5(d)). Interestingly, intake of proper dosage of PNS (40 mg/kg and 80 mg/kg) could reverse the phenotype of osteoblast decrease in the ovariectomy-induced osteoporosis model. However, excessive intake of PNS (160 mg/kg) had no protection on the decrease of osteoblast.

CD31 is the most widely used markers of endothelial differentiation, although it is not entirely specific. In this study, we used immunofluorescent staining of CD31 to represent the vascular endothelial cells. Very similar to the immunohistochemistry results of osteocalcin, intake of proper dosage of PNS (40 mg/kg and 80 mg/kg) could reverse the decrease of the number of endothelial cells (Figures 5(b), 5(c), and 5(e)) caused by deficiency of estrogen, while excessive intake of PNS (160 mg/kg) had no such effect.

4. Discussion

In this study, we applied ovariectomy-induced osteoporosis model [21, 22] to verify our hypothesis that PNS could prevent osteoporosis by coactivating osteogenesis and

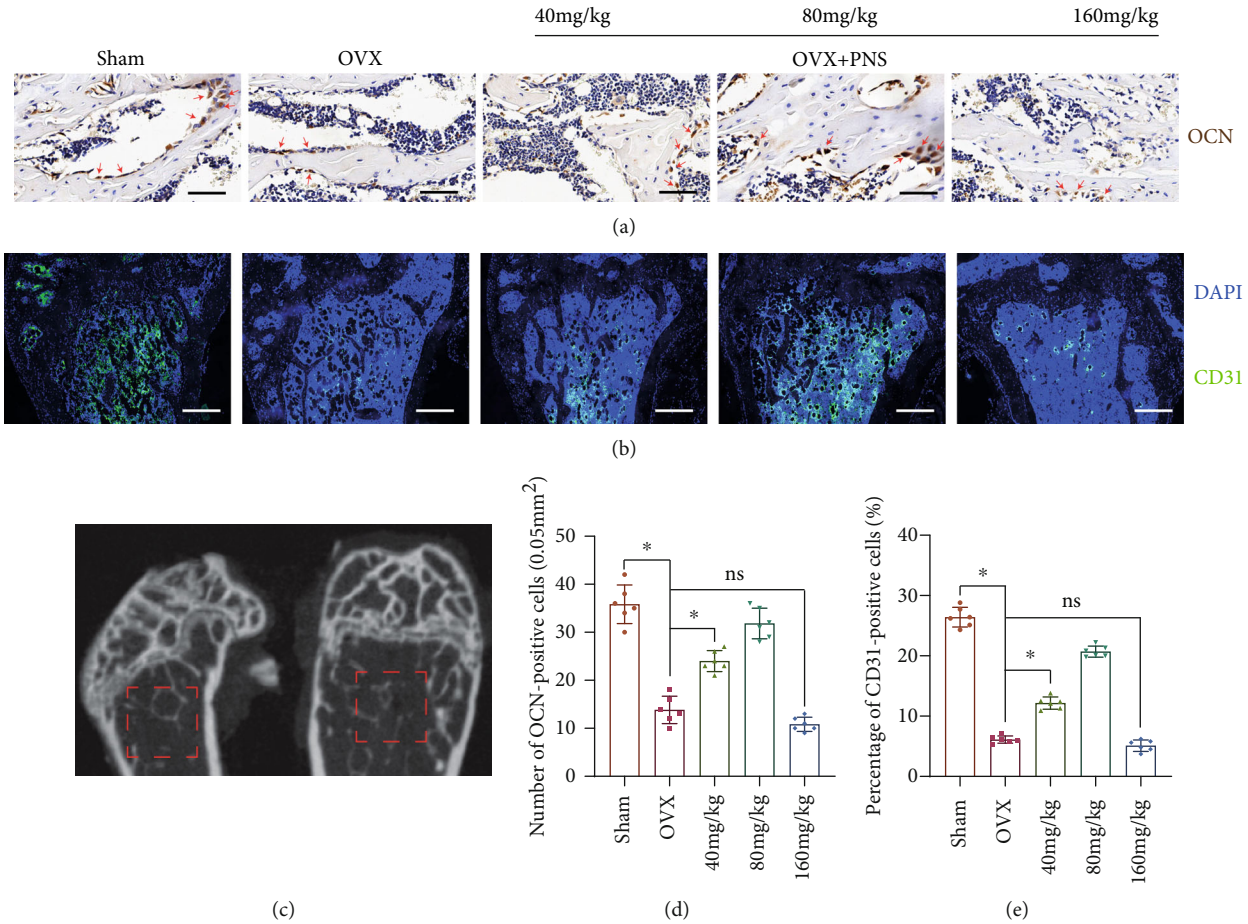

FIGURE 5: Representative images of (a) immunohistochemistry staining (scale bars = 50 μm) of osteocalcin (brown) in the sham, OVX, and PNS-treated groups. Representative images of (b) immunofluorescent staining (scale bars = 200 μm.) of CD31 (green) and DAPI (blue) in the sham, OVX, and PNS-treated groups. The (c) CT schematic diagram shows the approximate location of ROI (the red dotted line area) for calculating the number and percentage of OCN positive and CD31-positive cells, respectively, in each groups. Quantitative analysis of the (d) number of OCN-positive cells per 0.05 mm^2 and the (e) percentage of CD31-positive cells was made according to the ROI ("ns" represents no significant difference; $^*P < 0.05$; $N = 6$).

angiogenesis in vivo. After a series of experiments, including serum biochemical analysis, micro-CT morphometry, and histological assessment, we proved that a moderate dose of PNS (40 mg/kg and 80 mg/kg) could prevent bone loss by promoting angiogenesis and osteogenesis. The decrease in ovarian estrogen secretion after menopause is the initial cause of rapid bone loss in middle aged and elderly women, with an annual bone loss rate of 3-5% within 10 years, which mainly affects the trabecular bone [23]. In our experiments, micro-CT images clearly show the trabecular bone loss in the distal femur (Figure 3) 9 weeks after the OVX operation, indicating that the OVX mouse model could perfectly simulate the rapid occurrence of postmenopausal osteoporosis in human.

In traditional Chinese medicine, PNS has vasoactive effect [24], and many studies had also proved its function in promoting angiogenesis. For instance, a study found that PNS can promote several features of angiogenesis in HUVECs in vitro and in zebrafish in vivo through the activation of the VEGF-KDR and PI3K-Akt-eNOS pathways [25], and another study confirmed the efficacy of PNS in upregulating VEGF-A, VEGFR-1, and VEGFR-2 signal systems in BMSCs [26]. It is well known that the coupling of angiogenesis and osteogenesis plays a central role in the anabolism maintaining bone homeostasis [18, 27], but no research had explored whether the antiosteoporotic effect of PNS was due to promoting angiogenesis. In this study, we had observed that appropriate dose (40 mg/kg to 80 mg/kg) of PNS intake could prevent the loss of osteoblast and vascular endothelial cell caused by estrogen deficiency at the same time, and the difference of bone mass between groups was not related to body weight, which confirmed our notion to some extent. However, high dose (160 mg/kg) of PNS intake had not only no effect in preventing bone loss but even caused more serious osteoporosis, which may be due to the damage of liver and kidney function caused by excessive dose of the PNS extract, leading to a further deterioration in bone homeostasis. During the experimental design phase, we estimated the appropriate dose in mice (40~80 mg/kg/day) according to the recommendation in the human body (150-300 mg/day), and the safety of these doses was confirmed by our study. The reason why we set up a high dose of

160 mg/kg is because we want to observe the pharmacological effects and toxicity of PNS in a high dosage, which are rarely discussed in other similar researches. Our study also indicates that when the intake of PNS was doubled from its recommended amount, it showed reverse pharmacological effects and hepatorenal toxicity.

Besides the angiogenesis promoting effect, PNS had been reported to reveal estrogen-like activities in vivo [12, 13]. Estrogen is an important regulator of osteoblast differentiation and activity, which can promote osteogenic differentiation of mesenchymal stem cell and prolong the life span of osteoblasts by inhibiting apoptosis [28]. Estrogen receptors (ER) include ER α and ER β subtypes. ER α mediates most of the effects of natural estrogen ligands, mainly expressed in cortical bone, while ER β mediates the effect of phytoestrogens on bone, mainly expressed in trabecular bone [29, 30]. PNS is one of the phytoestrogens, so we got an interesting hypothesis that PNS promotes osteogenesis and angiogenesis simultaneously or their coupling through activating ER β and its downstream signaling pathway in trabecular bone, which will be the next stage of our work. What is more, in the serum biochemical analysis part, the serum NTX result may indicate that PNS could have effect on osteoclasts; however, it needs more experimental evidence in the future.

Although it has been confirmed that appropriate concentration of PNS can prevent bone loss, the mechanism of the opposite pharmacological effect of high-dose PNS is not clear, and the specific mechanism of PNS promoting angiogenesis is not well explained. However, compared with the injection administration route of classic antiosteoporosis drugs, like PTH and bisphosphonate, the oral administration characteristics of PNS would make it easier for patients to take and therefore improve compliance [23, 31]. And because PNS has been used clinically for many years, it is easier to apply for clinical trials with expanded indications, making it a potential antiosteoporotic drug in the future.

5. Conclusions

In this study, we strongly confirmed the pharmacological effects of appropriate dose of PNS on promoting angiogenesis and preventing bone loss in a mouse osteoporotic model, which may provide a new potential treatment for the prevention of osteoporosis in postmenopausal women.

Data Availability

All the data in this manuscript are available on request through contacting the author Hao Hu directly, and the contact email address is huhao7@mail2.sysu.edu.cn.

Conflicts of Interest

The authors declare that they have no conflict of interest.

Authors' Contributions

HH, YC, ZML, and XNZ conceived and designed the experiments. HH and YC performed the animal model experiments and drafted the manuscript. ZML performed the μCT scan and image analysis for animals. ZYZ and LPL performed the histomorphometry staining and image analysis. FXW and CL helped to check and analyzed the data and revise the manuscript. All of the authors had read and approved the final version of this manuscript. Hao Hu and Yan Chen contributed equally to this work and should be considered co-first authors.

Acknowledgments

This work was supported by research grants from Science and Technology Program of Guangzhou (201704030082 and 201804020011), the National Natural Science Foundation of Guangdong Province-Major Fundamental Research Fostering Program, China (2017A030308004), and Key Project of NSFC-Guangdong Joint Program (U1601220).

References

[1] P. Chen, Z. Li, and Y. Hu, "Prevalence of osteoporosis in China: a meta-analysis and systematic review," *BMC Public Health*, vol. 16, no. 1, p. 1039, 2016.

[2] D. A. Towler, "Angiogenesis and marrow stromal cell fates: roles in bone strength," *Osteoporosis International*, vol. 14, pp. 46–53, 2003.

[3] H. Liu, J. Yang, F. du et al., "Absorption and disposition of ginsenosides after oral administration of *Panax notoginseng* extract to rats," *Drug Metabolism and Disposition*, vol. 37, no. 12, pp. 2290–2298, 2009.

[4] T. T. X. Dong, X. M. Cui, Z. H. Song et al., "Chemical assessment of roots of Panax notoginseng in China: regional and seasonal variations in its active constituents," *Journal of Agricultural and Food Chemistry*, vol. 51, no. 16, pp. 4617–4623, 2003.

[5] T. B. Ng, "Pharmacological activity of sanchi ginseng (*Panax notoginseng*)," *The Journal of Pharmacy and Pharmacology*, vol. 58, no. 8, pp. 1007–1019, 2006.

[6] Y. G. Zhang, H. G. Zhang, G. Y. Zhang et al., "*Panax notoginseng* saponins attenuate atherosclerosis in rats by regulating the blood lipid profile and an anti-inflammatory action," *Clinical and Experimental Pharmacology & Physiology*, vol. 35, no. 10, pp. 1238–1244, 2008.

[7] Y. J. Jang, M. E. Kim, and S. Y. Ko, "n-Butanol extracts of *Panax notoginseng* suppress LPS-induced MMP-2 expression in periodontal ligament fibroblasts and inhibit osteoclastogenesis by suppressing MAPK in LPS-activated RAW264.7 cells," *Archives of Oral Biology*, vol. 56, no. 11, pp. 1319–1327, 2011.

[8] G. Zhao, Z. Xiang, T. Ye, Y. Yuan, and Z. Guo, "Antioxidant activities of *Salvia miltiorrhiza* and *Panax notoginseng*," *Food Chemistry*, vol. 99, no. 4, pp. 767–774, 2006.

[9] T. B. Ng, F. Liu, and H. X. Wang, "The antioxidant effects of aqueous and organic extracts of *Panax quinquefolium*, *Panax notoginseng*, *Codonopsis pilosula*, *Pseudostellaria heterophylla* and *Glehnia littoralis*," *Journal of Ethnopharmacology*, vol. 93, no. 2-3, pp. 285–288, 2004.

[10] N. W. He, Y. Zhao, L. Guo, J. Shang, and X. B. Yang, "Antioxidant, antiproliferative, and pro-apoptotic activities of a saponin extract derived from the roots of *Panax notoginseng* (Burk.) F.H. Chen," *Journal of Medicinal Food*, vol. 15, no. 4, pp. 350–359, 2012.

[11] H. Qiang, C. Zhang, Z. B. Shi, H. Q. Yang, and K. Z. Wang, "Protective effects and mechanism of *Panax Notoginseng* saponins on oxidative stress-induced damage and apoptosis of rabbit bone marrow stromal cells," *Chinese Journal of Integrative Medicine*, vol. 16, no. 6, pp. 525–530, 2010.

[12] R. Y. K. Chan, W. F. Chen, A. Dong, D. Guo, and M. S. Wong, "Estrogen-like activity of ginsenoside Rg1 derived from *Panax notoginseng*," *Journal of Clinical Endocrinology & Metabolism*, vol. 87, no. 8, pp. 3691–3695, 2002.

[13] X. Meng, G. Sun, J. Ye, H. Xu, H. Wang, and X. Sun, "Notoginsenoside R1-mediated neuroprotection involves estrogen receptor-dependent crosstalk between Akt and ERK1/2 pathways: a novel mechanism of Nrf2/ARE signaling activation," *Free Radical Research*, vol. 48, no. 4, pp. 445–460, 2014.

[14] Z. Ji, Y. Cheng, P. Yuan, X. Dang, X. Guo, and W. Wang, "*Panax notoginseng* stimulates alkaline phosphatase activity, collagen synthesis, and mineralization in osteoblastic MC3T3-E1 cells," *In Vitro Cellular & Developmental Biology. Animal*, vol. 51, no. 9, pp. 950–957, 2015.

[15] X.-D. Li, B. Chang, B. Chen et al., "*Panax notoginseng* saponins potentiate osteogenesis of bone marrow stromal cells by modulating gap junction intercellular communication activities," *Cellular Physiology and Biochemistry*, vol. 26, no. 6, pp. 1081–1092, 2010.

[16] X.-d. Li, Z.-y. Liu, B. Chang et al., "*Panax notoginseng* saponins promote osteogenic differentiation of bone marrow stromal cells through the ERK and P38 MAPK signaling pathways," *Cellular Physiology and Biochemistry*, vol. 28, no. 2, pp. 367–376, 2011.

[17] Y. Wang, X. Huang, Y. Tang, H. Lin, and N. Zhou, "Effects of panax notoginseng saponins on the osteogenic differentiation of rabbit bone mesenchymal stem cells through TGF-β1 signaling pathway," *BMC Complementary and Alternative Medicine*, vol. 16, no. 1, p. 319, 2016.

[18] A. P. Kusumbe, S. K. Ramasamy, and R. H. Adams, "Coupling of angiogenesis and osteogenesis by a specific vessel subtype in bone," *Nature*, vol. 507, no. 7492, pp. 323–328, 2014.

[19] J. Z. Fan, Y. Wang, Y. Meng et al., "*Panax notoginseng* saponins mitigate ovariectomy-induced bone loss and inhibit marrow adiposity in rats," *Menopause*, vol. 22, no. 12, pp. 1343–1350, 2015.

[20] Y. Shen, Y. Q. Li, S. P. Li, L. Ma, L. J. Ding, and H. Ji, "Alleviation of ovariectomy-induced osteoporosis in rats by *Panax notoginseng* saponins," *Journal of Natural Medicines*, vol. 64, no. 3, pp. 336–345, 2010.

[21] S. Negri, Y. Wang, T. Sono et al., "Human perivascular stem cells prevent bone graft resorption in osteoporotic contexts by inhibiting osteoclast formation," *STEM CELLS Translational Medicine*, vol. 16, no. 9, pp. 1617–1630, 2001.

[22] D. N. Kalu, "The ovariectomized rat model of postmenopausal bone loss," *Bone and Mineral*, vol. 15, no. 3, pp. 175–191, 1991.

[23] F. Cosman, S. J. de Beur, M. S. LeBoff et al., "Erratum to: Clinician's guide to prevention and treatment of osteoporosis," *Osteoporosis International*, vol. 26, no. 7, pp. 2045–2047, 2015.

[24] S. Chen, J. Liu, X. Liu et al., "Panax notoginseng saponins inhibit ischemia-induced apoptosis by activating PI3K/Akt pathway in cardiomyocytes," *Journal of Ethnopharmacology*, vol. 137, no. 1, pp. 263–270, 2011.

[25] S. J. Hong, J. B. Wan, Y. Zhang et al., "Angiogenic effect of saponin extract from *Panax notoginseng* on HUVECs *in vitro* and zebrafish *in vivo*," *Phytotherapy Research*, vol. 23, no. 5, pp. 677–686, 2009.

[26] H. Zheng, C. Liu, Y. Ou, Y. Zhang, and X. Fu, "Total saponins of *Panax notoginseng* enhance VEGF and relative receptors signals and promote angiogenesis derived from rat bone marrow mesenchymal stem cells," *Journal of Ethnopharmacology*, vol. 147, no. 3, pp. 595–602, 2013.

[27] M. Yang, C. J. Li, X. Sun et al., "MiR-497~195 cluster regulates angiogenesis during coupling with osteogenesis by maintaining endothelial Notch and HIF-1α activity," *Nature Communications*, vol. 8, no. 1, p. 16003, 2017.

[28] S. Khosla, "New insights into androgen and estrogen receptor regulation of the male skeleton," *Journal of Bone and Mineral Research*, vol. 30, no. 7, pp. 1134–1137, 2015.

[29] V. Cagnetta and V. Patella, "The role of the immune system in the physiopathology of osteoporosis," *Clinical Cases in Mineral and Bone Metabolism*, vol. 9, no. 2, pp. 85–88, 2012.

[30] M. N. Weitzmann and R. Pacifici, "Estrogen deficiency and bone loss: an inflammatory tale," *The Journal of Clinical Investigation*, vol. 116, no. 5, pp. 1186–1194, 2006.

[31] S. Jha, Z. Wang, N. Laucis, and T. Bhattacharyya, "Trends in media reports, oral bisphosphonate prescriptions, and hip fractures 1996-2012: an ecological analysis," *Journal of Bone and Mineral Research*, vol. 30, no. 12, pp. 2179–2187, 2015.

Hindawi
BioMed Research International
Volume 2020, Article ID 6976317, 12 pages
https://doi.org/10.1155/2020/6976317

Research Article

Synergistic Utilization of Necrostatin-1 and Z-VAD-FMK Efficiently Promotes the Survival of Compression-Induced Nucleus Pulposus Cells via Alleviating Mitochondrial Dysfunction

Songfeng Chen,[1] Qing Tian,[1] Chunfeng Shang,[1] Lin Yang,[2] Na Wei,[3] Guowei Shang,[1] Yanhui Ji,[1] Hongwei Kou,[1] Shitao Lu,[1] and Hongjian Liu[1]

[1]*Department of Orthopaedics, The First Affiliated Hospital of Zhengzhou University, Zhengzhou 450052, China*
[2]*Department of Paediatrics, The Zhengzhou Central Hospital Affiliated to Zhengzhou University, Zhengzhou 450007, China*
[3]*Department of Pathology, The First Affiliated Hospital of Zhengzhou University, Zhengzhou 450052, China*

Correspondence should be addressed to Shitao Lu; lst19287@hotmail.com and Hongjian Liu; fccliuhj@zzu.edu.cn

Received 19 August 2020; Revised 23 October 2020; Accepted 19 November 2020; Published 8 December 2020

Academic Editor: Yu Sheng Li

We recently reported that necroptosis contributed to compression-induced nucleus pulposus (NP) cells death. In the current study, we investigated the regulative effect of necroptosis inhibitor Necrostatin-1 on NP cells apoptosis and autophagy. Necrostatin-1, autophagy inhibitor 3-Methyladenine and apoptosis inhibitor Z-VAD-FMK were employed, and NP cells were exposed to 1.0 MPa compression for 0, 24 and 36 h. Necroptosis-associated molecules were measured by Western blot and RT-PCR. Autophagy and apoptosis levels were evaluated by Western blot and quantified by flow cytometry after monodansylcadaverine and Annexin V-FITC/propidium iodide staining, respectively. The cell viability and cell death were also examined. Furthermore, we measured mitochondrial membrane potential (MMP), mitochondrial permeability transition pore (MPTP) and indices of oxidative stress to assess mitochondrial dysfunction. The results established that Necrostatin-1 blocked NP cells autophagy, and 3-Methyladenine had little influence on NP cells necroptosis. The Necrostatin-1+3-Methyladenine treatment exerted almost the same role as Necrostatin-1 in reducing NP cells death. Necrostatin-1 restrained NP cells apoptosis, while Z-VAD-FMK enhanced NP cells necroptosis. The Necrostatin-1+Z-VAD-FMK treatment provided more prominent role in blocking NP cells death compared with Necrostatin-1, consistent with increased MMP, reduced opening of MPTP and oxidative stress. In summary, the synergistic utilization of Necrostatin-1 and Z-VAD-FMK is a very worthwhile solution in preventing compression-mediated NP cells death, which might be largely attributed to restored mitochondrial function.

1. Introduction

Low back pain is an important cause of disability worldwide [1, 2], which is strongly linked with intervertebral disc (IVD) degeneration [3, 4]. Many factors could lead to IVD degeneration, including aging, nutritional deficiency, and mechanical stimulation, in which mechanical compression is generally considered as a critical pathogenic factor [5, 6]. More and more researches focus on exploring compression-mediated nucleus pulposus (NP) cells death because these cells play a key role in the production of collagen II and aggrecan, which contribute in maintaining IVD homeostasis [7, 8].

The decrease in NP cells number is largely attributed to the degree of programmed cell death (PCD) [9]. For decades, apoptosis and autophagy, which were known as type I and II PCD, respectively, were viewed as the only two forms of regulated cell death [10]. Apoptosis is generally characterized by apoptotic body formation, intact plasma membrane, chromosome condensation, and caspase activation [11]. Autophagy is a "self-eating" process for maintaining cellular homeostasis, in which the injured proteins or organelles are encased in autophagic vesicles with bilayer membrane structure and then degraded for recycling [12]. Remarkably, necroptosis, also termed type III PCD, has received great

attention in recent years [13, 14]. Unlike apoptosis, it is a caspase-independent mode of death. The initiation and execution of necroptosis are largely dependent on the activation of the receptor-interacting protein kinase 1 (RIPK1)/receptor-interacting protein kinase 3 (RIPK3)/mixed lineage kinase domain-like (MLKL) signaling pathway in most cases [13, 14].

Our latest studies reported that necroptosis inhibitor Necrostatin-1 exerted important protective role on compression-treated NP cells [15, 16]. Treatment with Necrostatin-1 in a singular manner efficiently protected against compression-induced NP cells death. Literatures demonstrated that there exists an interaction between necroptosis and autophagy; meanwhile, necroptosis and apoptosis pathways appear to be interrelated with each other under certain circumstances [12, 17]. However, the interactive effect between necroptosis and autophagy as well as necroptosis and apoptosis are intricate and mysterious [12, 17]. So systematically investigating the regulative effect of Necrostatin-1 on apoptosis and autophagy is expected to provide a more excellent strategy in reducing NP cells death during compression condition.

It has been well documented that mitochondrial dysfunction, which includes mitochondrial membrane potential (MMP) loss, ultrastructure disruption of mitochondria, enhanced opening of mitochondrial permeability transition pore (MPTP), overconsumption of adenosine-triphosphate (ATP), and overproduction of reactive oxygen species (ROS), is positively correlated to necroptosis, autophagy, and apoptosis [18, 19]. However, other literatures suggest that mitochondrial dysfunction is not closely related to necroptosis, autophagy, or apoptosis [20, 21]. Likewise, the exact mechanism of oxidative stress in compression-induced NP cells necroptosis, autophagy, and apoptosis has not been elucidated too.

In the current study, we investigated the mutual regulation between necroptosis and autophagy as well as necroptosis and apoptosis during compression-induced NP cells death. To gain a deeper understanding from the organelle level, we also interrogated the regulatory role of combined inhibition of the different PCDs on mitochondrial dysfunction of NP cells.

2. Materials and Methods

2.1. Isolation and Culture of Primary Rat NP Cells. All the animal experiments were performed in accordance with the protocol approved by the animal experimentation committee of the First Affiliated Hospital of Zhengzhou University. The 3-month-old Sprague-Dawley rats were purchased from the Experimental Animal Center of the First Affiliated Hospital of Zhengzhou University. We performed the rat NP cell isolation and culture as previously described [15, 16]. The second generation of NP cells was used in this study.

2.2. Compression and Pharmacological Treatment of Rat NP Cells. The model system was used as previously described, in which 1.0 MPa compression was loaded on NP cells to imitate *in vivo* condition [15, 16]. The cells were treated with DMSO (Control, Sigma, USA), necroptosis inhibitor Necronstatin-1 (Nec-1, Sigma, USA), autophagy inhibitor 3-Methyladenine (3-MA, Sigma, USA), and apoptosis inhibitor Z-VAD-FMK (Z-VAD, Merck, Germany) and then using a combination of the inhibitors: Nec-1+3-MA and Nec-1+Z-VAD. The bottom of the pressure vessel was filled with distilled water to preserve sufficient humidity and keep the device in an incubator at 37°C. 0 h mentioned in the experiment means the beginning of compression. The 0, 24, and 36 h compression-treated time points were selected in the current experiment according to our previous studies [15, 16].

2.3. Monodansylcadaverine (MDC) Staining. The autophagic vacuoles of NP cells were detected by MDC (Sigma, USA). At each time point, the cells were washed three times with PBS and incubated with 0.05 mM MDC solution for 15 min at 37°C in the dark. Finally, the intracellular MDC fluorescence was quantified under flow cytometry (BD LSRII, Becton Dickinson).

2.4. Determination of Cell Viability. NP cells were seeded into 96-well culture plates at a density of 5×10^3 cells per well. 24 h later, the cells underwent 0, 24, or 36 h compression, and cell viability was evaluated using the CCK-8 detection kit (Dojindo, Japan) according to the manufacturer's instructions. The cell viability was quantified by absorbance detection at 450 nm with a spectrophotometer (BioTek, USA).

2.5. Lactate Dehydrogenase (LDH) Release. Following 0, 24, and 36 h compression, the release of LDH into the culture medium was measured to evaluate the cytotoxicity of NP cells using an automated chemistry analyzer as previously described (Beyotime, China). The LDH activity (reflecting cell death) was expressed as the percentage of LDH in the cell culture medium to total cellular LDH.

2.6. Annexin V-FITC and Propidium Iodide (PI) Positive Ratio. The Annexin V-FITC Apoptosis Detection Kit (Beyotime, China) was introduced to quantify apoptotic and necrotic ratio of NP cells. Following 0, 24, and 36 h compression, the cells were harvested, stained as previously described [15, 16], and analyzed using flow cytometry. The Annexin V-FITC and PI double staining was utilized to detect the apoptotic incidence (Annexin V ratio) of NP cells.

2.7. Evaluation of MMP. After 0, 24, and 36 h compression, the NP cells were labeled by fluorescence probe 5,5′,6,6′-tetrachloro-1,1′,3,3′-tetraethyl-benzimidazolylcarbocyanine iodide (JC-1, Keygen Biotech, China) as we previously described [15]. Finally, the samples were quantified by flow cytometry. The evaluation of MMP is expressed as the ratio of red to green fluorescence intensity.

2.8. Measurement of MPTP Opening. The MPTP opening of NP cells was assessed by the MPTP Assay Kit (Genmed, China) as previously described [15]. After 0, 24, and 36 h compression, the cells were collected; afterward, 500 μl preheated cleaning solution (Reagent A) and isopyknic working solution containing neutralization and staining solution

(Reagent B) were added into the cell suspension. Then, the above cell suspension was mixed gently and fully and incubated for 20 min at 37°C in the dark. Lastly, the samples were resuspended in Reagent A and analyzed by flow cytometry.

2.9. Measurement of ROS. Intracellular ROS of NP cells was examined by ROS-specific fluorescent probe 2′-7′-dihydrodichlorofluorescein diacetate (DCFH-DA, Sigma, USA). Briefly, following 0, 24, and 36 h compression, cells were stained with 10 μM DCFH-DA for 30 min at 37°C in the dark. Then, the mean fluorescence intensity (MFI) was assayed by flow cytometry.

2.10. Mitochondrial ROS (mtROS) Analysis. The MitoSOX red (Merck, Germany), a live-cell permeant fluorescence dye for selective detection of superoxide in mitochondria, could emit red fluorescence after being oxidized by superoxide. Following 0, 24, and 36 h compression, the cells were incubated with 5 μM MitoSOX red for 30 min at 37°C in the dark. Finally, the samples were washed three times, suspended in 200 μl of PBS, and assayed via flow cytometry.

2.11. Measurement of MDA Content and SOD Activity. The MDA content of NP cells was detected using the Lipid Peroxidation MDA Assay Kit (Beyotime, China), and the SOD activity of NP cells was evaluated by the SOD Assay Kit (Beyotime, China). At each time point, the cells were lysed in lysis buffer and centrifuged at 12000 rpm for 15 min and the cell deposits were discarded. The supernatant was reacted with thiobarbituric acid (TBA), and then, the MDA content was analyzed via a spectrophotometer (BioTek, USA) at 532 nm. For SOD activity detection, the cells were collected, lysed, and centrifuged at 12000 rpm for 15 min. Then, the supernatant was obtained to evaluate SOD activity by a spectrophotometer. Finally, the MDA content was represented as nmol/mg protein and the SOD activity was represented as U/mg protein.

2.12. Western Blot Analysis. The NP cells were lysed in lysis buffer containing of 1% protease inhibitor. The protein concentration of lysate was determined using the enhanced BCA protein assay kit (Keygen Biotech, China). The whole lysate was separated by SDS polyacrylamide gel electrophoresis (SDS-PAGE) and then transferred onto polyvinylidene fluoride membranes. Membranes were blocked with 5% bovine serum albumin in TBST for 1 h at room temperature and then incubated overnight at 4°C with primary antibodies against RIPK1 (1 : 500, CST, USA), phospho-PKA substrate (1 : 1000, CST, USA), RIPK3 (1 : 500, Abcam, UK), pRIPK3 (phosphoS232, 1 : 1000, Abcam, UK), MLKL (1 : 500, Abcam, UK), LC3B (1 : 1000, Sigma, USA), Beclin1 (1 : 500, CST, USA), Cleaved Caspase-3 (1 : 500, Abcam, UK), Cleaved Caspase-8 (1 : 500, Proteintech, China), Cleaved Caspase-9 (1 : 200, Proteintech, China), and GAPDH (1 : 5000, Abcam, UK). After incubation, membranes were gently washed three times and incubated with respective peroxidase-conjugated secondary antibodies for 2 h at 4°C and washed again. Finally, the protein bands were developed and quantified by enhanced chemiluminescence procedure and normalized to GAPDH.

2.13. Quantitative Real-Time Polymerase Chain Reaction (qRT-PCR). Total RNA was isolated from harvested NP cells using TRIzol reagent (Invitrogen, USA) according to the manufacturer's instructions. Then, the obtained RNA was transcribed into complementary DNA (cDNA). The primer sequences used for RT-PCR analysis were designed as follows: RIPK1: 5′-TCCTCGTTGACCGTGAC-3′, 5′-GCCTCCCTCTGCTTGTT-3′; RIPK3: 5′-CCAGCTCGTGCTCCTTGACT-3′, 5′-TTGCGGTCCTTG TAGGTTTG-3′; MLKL: 5′-TCTCCCAACATCCTGCGTAT-3′, 5′-TCCCGAGTGGTGTAACCTGTA-3′; and GAPDH: 5′-CGCTAACATCAAATGGGGTG-3′, 5′-TTGCTGACAATCTTGAGGGAG-3′. The RT-PCR analysis was performed via SYBR Green mix (ToYobo, Japan) in a Step One Plus Real-Time PCR System (Applied Biosystems, CA, USA). The gene expression was subjected to analysis of amplification curve, and the data was analyzed using the $2^{-\Delta\Delta CT}$ method and normalized to GAPDH.

2.14. Statistical Analysis. Numerical data were shown as mean ± standard deviation (SD) from at least three independent repetitive experiments. Statistical analyses were carried out using IBM SPSS software package 22.0. Multiple groups were analyzed by one-way analysis of variance (ANOVA), followed by Bonferroni's post hoc test. Student's t test was used to analyze the differences between the two groups. The difference was considered statistically significant when $P < 0.05$.

3. Results

3.1. Nec-1 Attenuates Compression-Induced NP Cells Autophagy. To evaluate whether Nec-1 blocked NP cells autophagy, we measured the autophagy-associated molecules LC3B-II and Beclin1 expression. The 24 and 36 h compression provoked a distinguished upregulation expression of LC3B-II and Beclin1 compared with the 0 h group (Figures 1(a) and 1(b)). Treatment with 20 μM Nec-1 or 5 mM 3-MA blocked the increased expression of LC3B-II and Beclin1 (Figures 1(a) and 1(b)). MDC labeling, which can be incorporated into lipids in autophagic vacuoles, was increased after 24 and 36 h compression (Figures 1(c) and 1(d)). Also, the Nec-1 or 3-MA treatment attenuated MDC positive ratio at 24 and 36 h (Figures 1(c) and 1(d)). These results implied that Nec-1 downregulated compression-induced NP cells autophagy.

3.2. 3-MA Has Little Influence on Compression-Induced NP Cells Necroptosis. To explore the regulatory effect of 3-MA on NP cells necroptosis, the expression level of necroptosis-associated molecules RIPK1, pRIPK1, RIPK3, pRIPK3, and MLKL were measured by Western blot and RT-PCR. The results demonstrated that compared with 0 h, the protein expression of RIPK1, pRIPK1, RIPK3, pRIPK3, and MLKL as well as the gene expression of RIPK1, RIPK3, and MLKL significantly increased following 24 and 36 h compression (Figures 2(a)–2(c)). Treatment with Nec-1 reduced RIPK1, pRIPK1, RIPK3, pRIPK3 and MLKL expression at both 24 and 36 h (Figures 2(a)–2(c)). 3-MA had little influence on

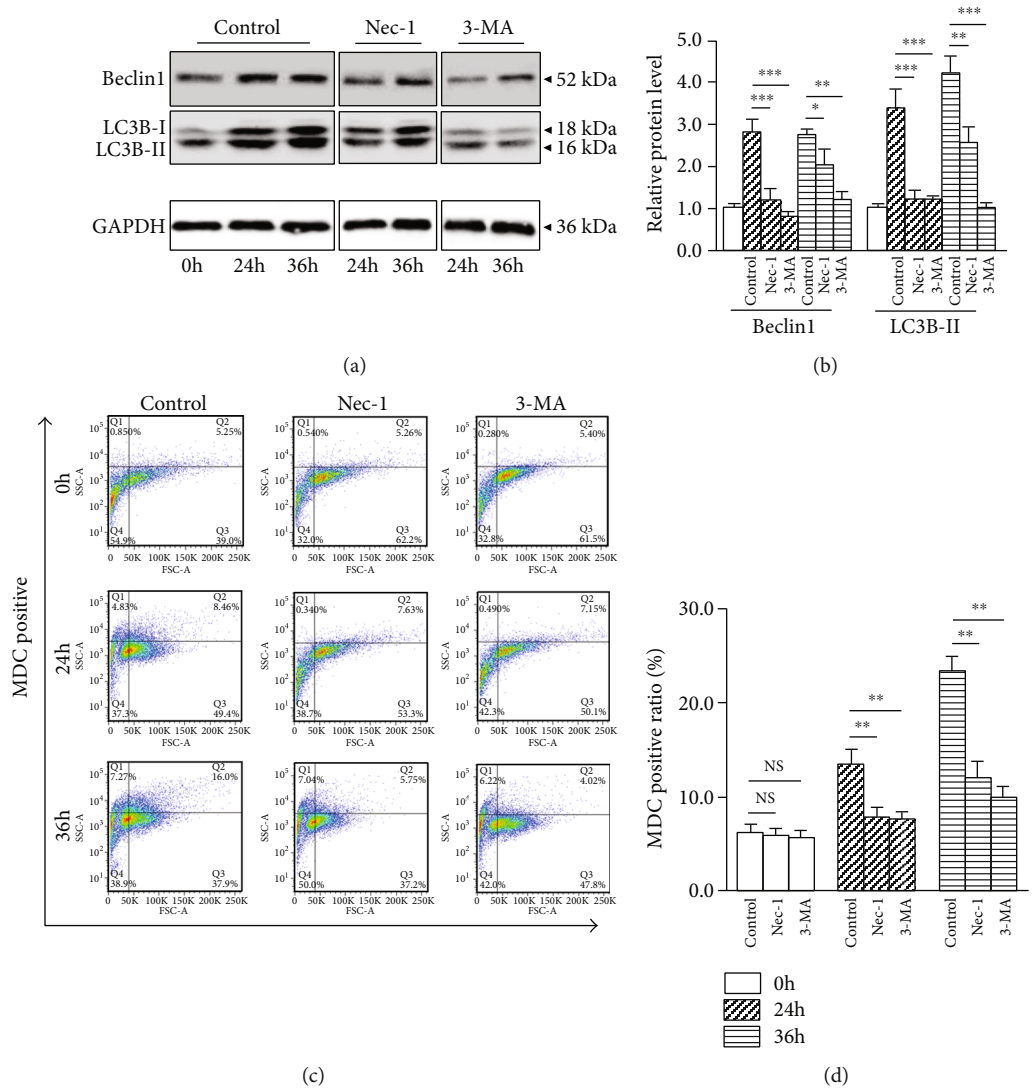

Figure 1: Nec-1 (20 μM) or 3-MA (5 mM) attenuated 24 and 36 h compression-induced NP cells autophagy. (a, b) Western blot and quantitative analysis of autophagy-related molecules LC3B-II, Beclin1, and GAPDH in NP cells. (c, d) Representative dot plot images by flow cytometry after MDC staining and quantitative analysis of MDC positive ratio in NP cells. Data from treated groups have been normalized to GAPDH. NS means no significant statistical significance ($^{*}P < 0.05$, $^{**}P < 0.01$, and $^{***}P < 0.001$ vs. control).

RIPK1, RIPK3 and MLKL in both protein and gene levels at 24 and 36 h; meanwhile, 3-MA had little effect on pRIPK1 and pRIPK3 too (Figures 2(a)–2(c)). Considering that Nec-1 blocked NP cells autophagy, we speculated that necroptosis might be an upstream mediator of autophagy.

3.3. Nec-1+3-MA Achieves Almost the Same Effect as Nec-1 in Protecting against Compression-Induced NP Cells Death. The cell viability and LDH release were examined to determine NP cells survival capability. After 24 and 36 h compression, Nec-1+3-MA or Nec-1 treatment increased NP cells viability compared with the control group. This beneficial effect was almost the same between the Nec-1+3-MA and Nec-1 group (Figure 2(d)). Likewise, Nec-1+3-MA or Nec-1 treatment exerted a more effective role than control in reducing LDH release at 24 and 36 h (Figure 2(e)). No apparent differences were observed between the Nec-1+3-MA and Nec-1 group. These results indicated that Nec-1+3-MA exerted almost the same effect as Nec-1 in preventing compression-induced NP cells death.

Hence, the following study mainly focuses on researching the mutual regulation between necroptosis and apoptosis and the synergistic inhibition of necroptosis and apoptosis on compression-induced NP cells death.

3.4. Nec-1 Blocks Compression-Induced NP Cells Apoptosis. To assess whether Nec-1 restrained compression-induced NP cells apoptosis, the proapoptotic molecules Cleaved Caspases were measured. Compared with the 0 h group, 24 and 36 h compression increased Cleaved Caspase-3, Cleaved Caspase-8 and Cleaved Caspase-9 expression (Figures 3(a) and 3(b)). Nec-1 or Z-VAD prevented the upregulation of Cleaved Caspase-3, Cleaved Caspase-8 and Cleaved Caspase-9 at 24 and 36 h (Figures 3(a) and

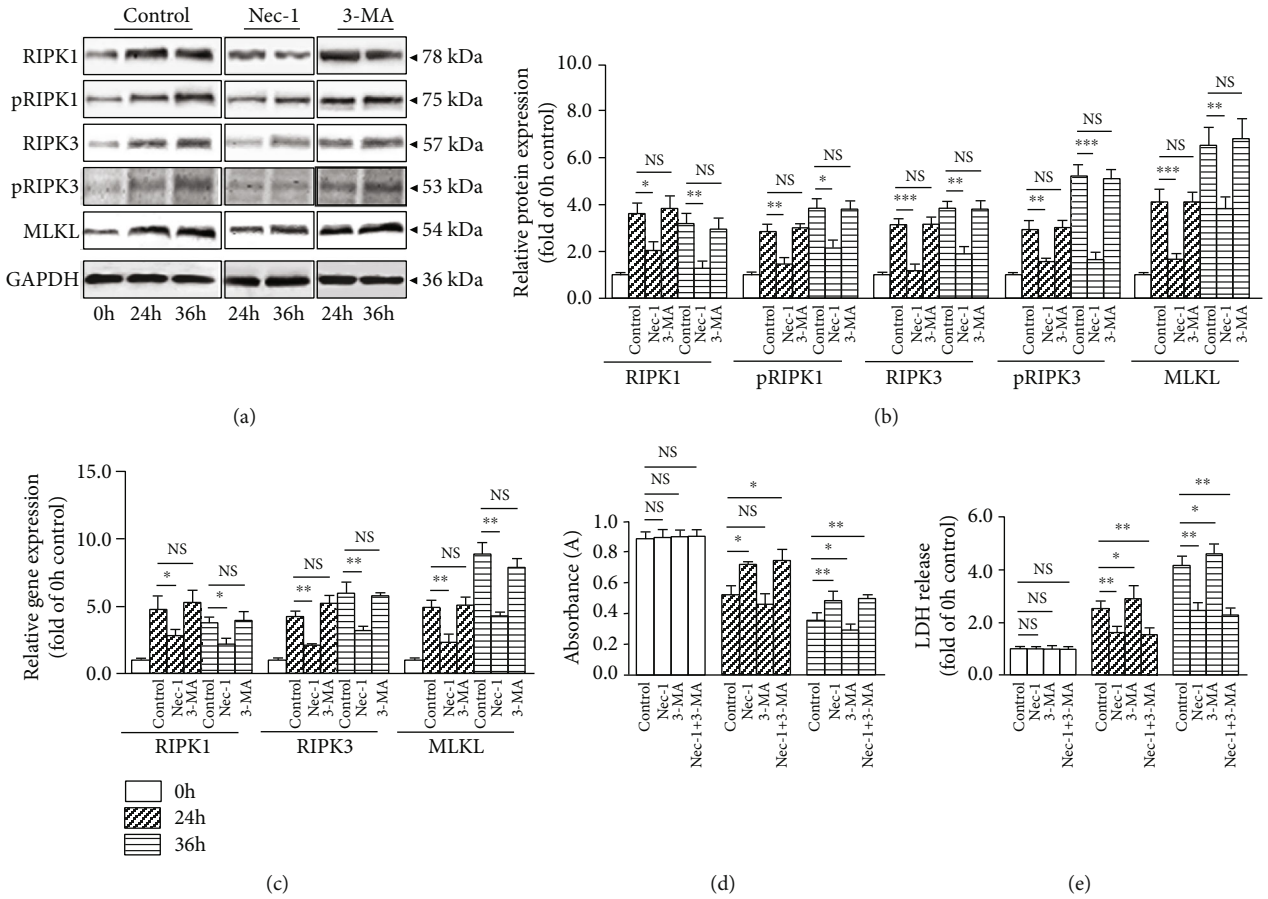

Figure 2: 3-MA (5 mM) had little effect on NP cells necroptosis, and Nec-1+3-MA achieved almost the same effect as Nec-1 treatment in preventing compression-induced NP cells death. (a, b) Western blot and quantitative analysis of necroptosis-related molecules RIPK1, pRIPK1, RIPK3, pRIPK3, MLKL, and GAPDH in NP cells. (c) RT-PCR measured the mRNA expression of necroptosis-related genes RIPK1, RIPK3, MLKL, and GAPDH in NP cells. (d) CCK-8 assay showed the viability change of NP cells. (e) LDH release exhibited the cytotoxicity of NP cells. NS means no significant statistical significance ($^{*}P < 0.05$, $^{**}P < 0.01$, and $^{***}P < 0.001$ vs. control).

3(b)). The Annexin V positive (apoptosis) ratio was increased after 24 and 36 h compression compared with 0 h (Figures 3(c) and 3(d)). The Nec-1 or Z-VAD treatment reduced Annexin V positive ratio at 24 and 36 h (Figures 3(c) and 3(d)). These results suggested that compression resulted in NP cells apoptosis time dependently, which was blocked by Nec-1 or Z-VAD.

3.5. Z-VAD Enhances Compression-Induced NP Cells Necroptosis. To explore whether Z-VAD could affect compression-induced NP cells necroptosis, the expression of RIPK1, pRIPK1, RIPK3, pRIPK3 and MLKL were measured. Different from 3-MA, a time course-related upregulation of RIPK1, pRIPK1, RIPK3, pRIPK3 and MLKL in the protein level and enhanced expression of RIPK1, RIPK3, and MLKL in the gene level were observed following Z-VAD treatment at 24 and 36 h (Figures 4(a)–4(c)). These results suggested that, under compression condition, blockage of apoptosis might result in partial conversion to necroptosis of NP cells.

3.6. Nec-1+Z-VAD Efficiently Protected against Compression-Mediated NP Cells Death. There were no obvious differences in morphology of NP cells between 24 and 36 h time periods [16]. Thus, 36 h compression was chosen for morphology evaluation. Compared with 0 h, 36 h compression caused a majority of cells detaching from the culture plates and displaying morphological changes of necrosis (Figure 5(a)). The morphological observations indicated that Z-VAD offered mild protective effect. Simultaneously, Nec-1 or Nec-1+Z-VAD, especially the Nec-1+Z-VAD treatment, provided a remarkable protective role against compression-induced NP cells death (Figure 5(a)).

The cell viability and LDH release were examined to evaluate NP cells survival. After 24 and 36 h compression, Nec-1, Z-VAD, or Nec-1+Z-VAD treatment increased NP cells viability compared to the control group. This beneficial effect was more prominent following Nec-1+Z-VAD treatment (Figure 5(b)). Likewise, Nec-1+Z-VAD treatment exerted a more effective role than the Nec-1, Z-VAD, or control group in reducing LDH release at both 24 and 36 h time periods (Figure 5(c)). These results indicated that combined inhibition of necroptosis and apoptosis was more effective in protecting against compression-induced NP cells death than inhibition of necroptosis or apoptosis alone.

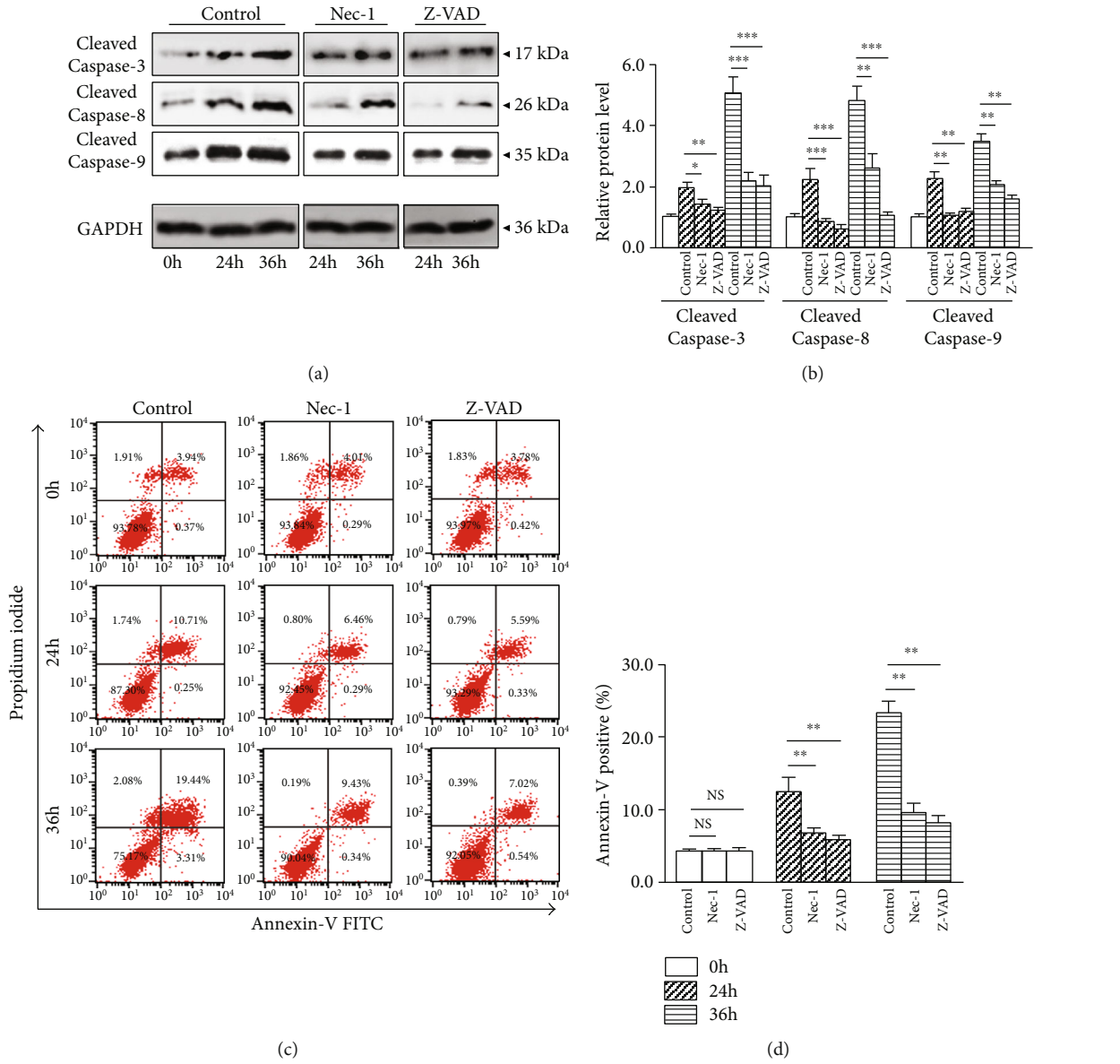

Figure 3: Nec-1 (20 μM) or Z-VAD (20 mM) attenuated 24 and 36 h compression-induced NP cells apoptosis. (a, b) Western blot and quantitative analysis of apoptosis-related molecules Cleaved Caspase-3, Cleaved Caspase-8, and Cleaved Caspase-9 and GAPDH in NP cells. (c, d) Representative dot plot images of apoptosis NP cells by flow cytometry after Annexin V staining and quantitative analysis. Data from treated groups have been normalized to GAPDH. NS means no significant statistical significance ($^{*}P < 0.05$, $^{**}P < 0.01$, and $^{***}P < 0.001$ vs. control).

3.7. Nec-1+Z-VAD Rescues Compression-Mediated MMP Loss and MPTP Opening in NP Cells. The JC-1 aggregates (red fluorescence) are dispersed to monomeric form (green fluorescence) during the process of MMP loss, which could well reflect mitochondrial dysfunction. After 24 and 36 h compression, a time-dependent MMP loss occurred, as demonstrated by the decrease in red fluorescence and increase in green fluorescence compared with the 0 h group (Figures 6(a) and 6(b)). When treated with Nec-1, Z-VAD, or Nec-1+Z-VAD, especially the Nec-1+Z-VAD group, 24 and 36 h compression-stimulated MMP loss was efficiently rescued (Figures 6(a) and 6(b)). A significant feature of mitochondrial dysfunction is enhanced opening of MPTP. After 24 and 36 h compression, as shown in (Figure 6(c)), the relative fluorescence intensity (RFI) value of NP cells was gradually decreased, implying that enhanced MPTP opening occurred when compared with 0 h. In the presence of Nec-1, Z-VAD, or Nec-1+Z-VAD, especially in the Nec-1+Z-VAD group, 24 and 36 h compression-induced decrease of RFI was notably restored (Figure 6(c)). Taken together, these results implied that Nec-1+Z-VAD ameliorated NP cells injury via restraining excessive MPTP opening and MMP loss.

3.8. Nec-1+Z-VAD Alleviates Compression-Induced Oxidative Stress of NP Cells. Mitochondria have been generally considered as a crucial source of oxidative stress, and excessive activation of oxidative stress indirectly reflects mitochondrial dysfunction. Compared with the 0 h group,

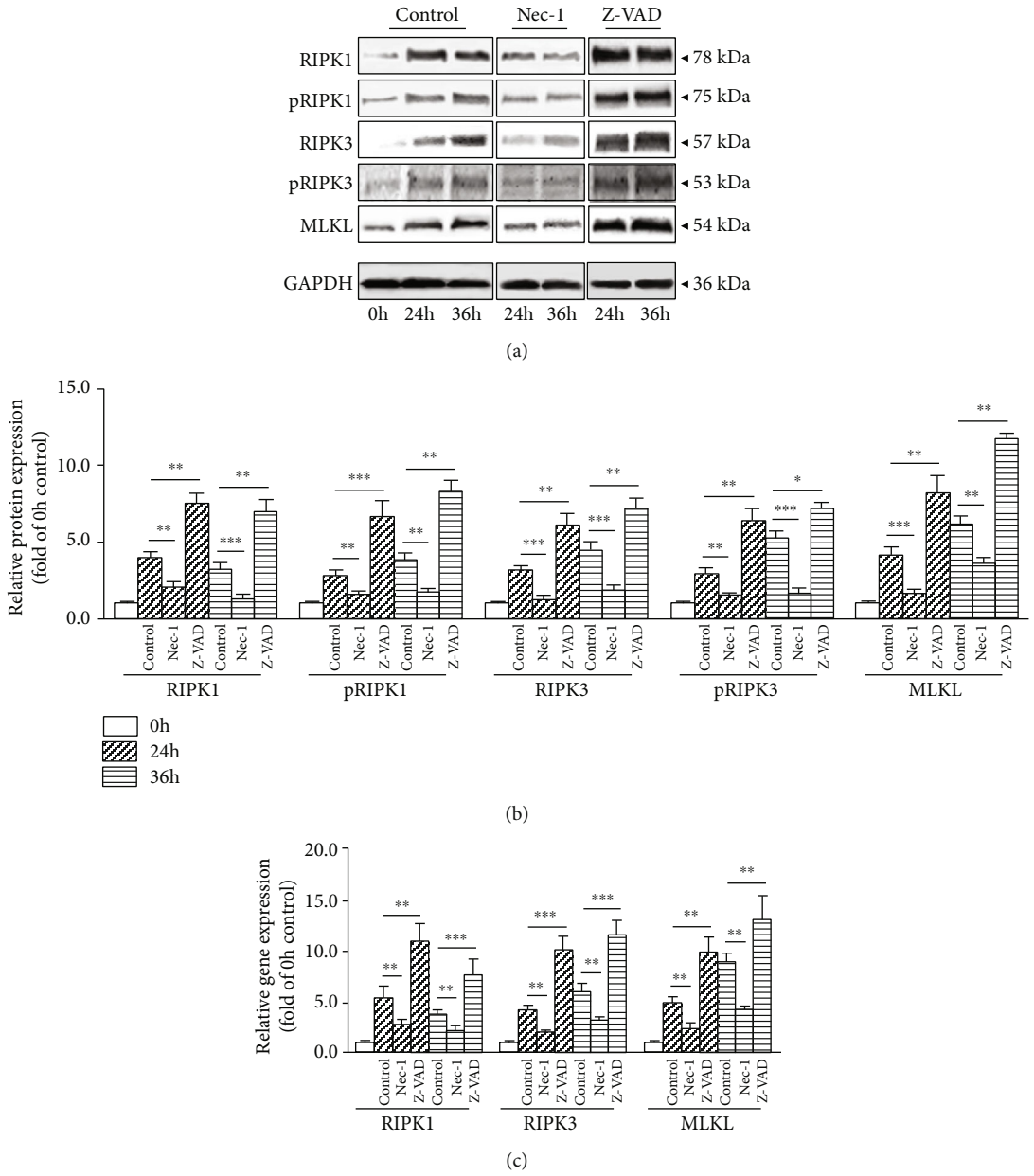

Figure 4: Z-VAD (20 mM) enhanced 24 and 36 h compression-induced NP cells necroptosis. (a, b) Western blot and quantitative analysis of necroptosis-related molecules RIPK1, pRIPK1, RIPK3, pRIPK3, MLKL, and GAPDH in NP cells. (c) RT-PCR measured the mRNA expression of necroptosis-related genes RIPK1, RIPK3, MLKL, and GAPDH in NP cells. Data from treated groups have been normalized to GAPDH ($^{*}P < 0.05$, $^{**}P < 0.01$, and $^{***}P < 0.001$ vs. control).

the ROS production (as indicated by DCFH-DA) was elevated after 24 and 36 h compression (Figures 7(a) and 7(b)). Similarly, an enhanced mtROS generation (MitoSOX fluorescence) was observed at both 24 and 36 h (Figure 7(c)). Treatment with Nec-1, Z-VAD, or Nec-1+Z-VAD, especially the Nec-1+Z-VAD treatment, reduced both the total ROS and mtROS fluorescence intensity (Figures 7(a)–7(c)).

MDA is positively correlated with oxidative stress damage, and SOD is an antioxidative enzyme. The MDA content was gradually increased while SOD activity was decreased in NP cells following 24 and 36 h compression (Figures 7(d) and 7(e)). Similar to ROS, treatment with Nec-1, Z-VAD, or Nec-1+Z-VAD, especially the Nec-1+Z-VAD group, notably blocked the upregulation of MDA content and downregulation of SOD activity at 24 and 36 h (Figures 7(d) and 7(e)). These results implied that Nec-1+Z-VAD attenuated compression-induced NP cells death might through alleviating oxidative stress.

4. Discussion

It has been well documented that a main contributor of IVD degeneration is NP cells death, which can be notably enhanced by compression [22, 23]. In the current study, we reported that autophagy was a downstream effect of

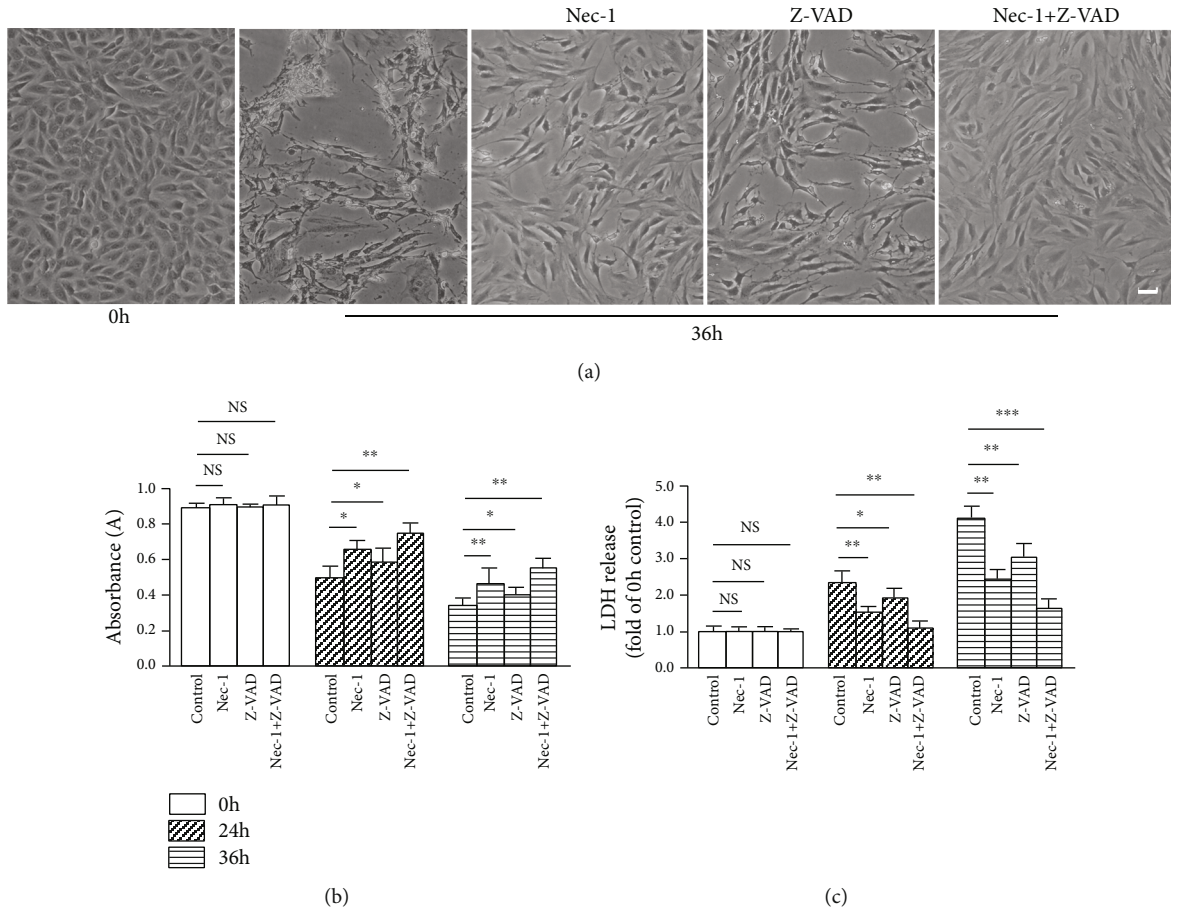

Figure 5: Nec-1+Z-VAD notably inhibited compression-induced NP cells death. (a) The morphological change of NP cells was observed by an optical microscope. (b) CCK-8 assay showed the viability change of NP cells. (c) LDH release exhibited the cytotoxicity of NP cells. Scale bars = 20 μm. ($^{*}P < 0.05$, $^{**}P < 0.01$, and $^{***}P < 0.001$ vs. control).

necroptosis. Meanwhile, the mutual conversion between necroptosis and apoptosis might exist, and synergetic inhibition of necroptosis and apoptosis enables more efficient survival of NP cells compared with inhibition of necroptosis alone, which might be closely related with mitochondrial dysfunction-oxidative stress pathway.

Necroptosis is a brand-new type of PCD. Blockage of necroptosis inhibits compression-induced NP cells death [16]. As for the interactive effect between necroptosis and autophagy, there mainly exist three different views including upregulation of necroptosis following activation of autophagy [24], autophagy attenuating necroptosis [25], or autophagy as a downstream consequence of necroptosis [26]. Hence, the interaction between necroptosis and autophagy needs further study to clarify. In our preliminary experiments, we discovered that Nec-1 blocked compression-induced NP cells autophagy.

We focus on the interaction between necroptosis and autophagy of NP cells. The Nec-1 treatment prevented 24 and 36 h compression-mediated increase of LC3II and Beclin1. Nec-1 also attenuated compression-induced MDC positive ratio at 24 and 36 h. Meanwhile, 3-MA had little influence on RIPK1, RIPK3 and MLKL expression as well as RIPK1 and RIPK3 phosphorylation. Therefore, we concluded that necroptosis might be an upstream mediator of autophagy. Then, we explored whether combined inhibition of necroptosis and autophagy could efficiently protect against compression-induced NP cells death. The data indicated that Nec-1+3-MA exerted roughly the same effect as Nec-1 alone in preventing NP cells viability loss and cell death. These results are consistent with those of Lin et al., who confirm that autophagy is a downstream effect of necroptosis [26]. This might be partly attributed to the fact that RIPK1, the key promoter of necroptosis, could mediate the occurrence of autophagy too [27].

Hence, the following study mainly investigates the mutual regulative effect between necroptosis and apoptosis in NP cells. Literatures indicate that blockage of apoptosis enhances or decreases necroptosis, implying that inhibition of apoptosis could potentiate or attenuate the progression toward necroptosis [28, 29]. Furthermore, inhibition of necroptosis is reported to promote or decrease apoptosis too [30, 31]. Therefore, systematical elucidation of the "cross-talk effect" between necroptosis and apoptosis is expected to provide effective intervention targets for inhibiting NP cells death. We observed that Nec-1 obviously blocked Cleaved Caspase-3, Cleaved Caspase-8, and Cleaved Caspase-9 expression and Annexin V positive ratio in NP cells.

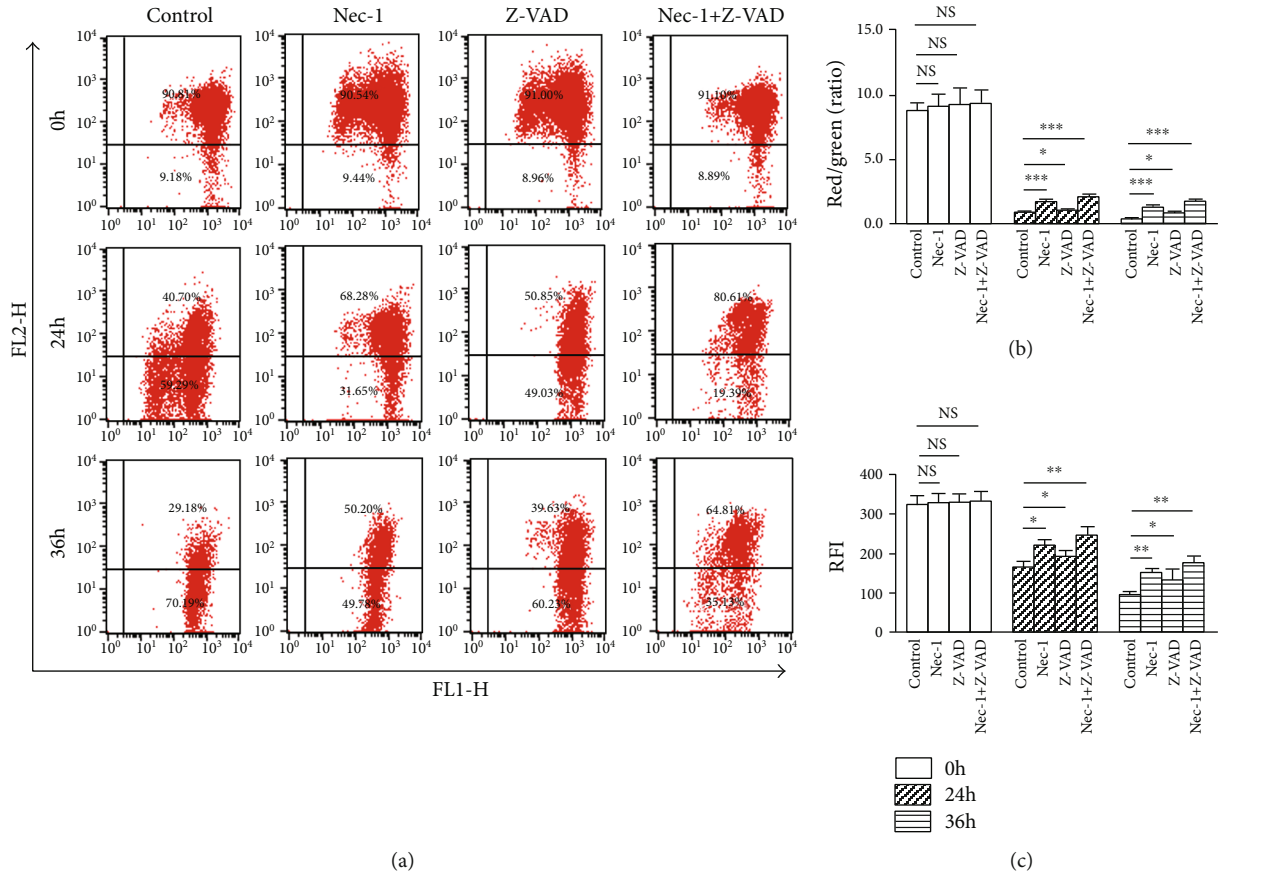

FIGURE 6: Nec-1+Z-VAD efficiently rescued 24 and 36 h compression-mediated MMP loss and MPTP opening in NP cells. (a) Representative dot plot images after JC-1 staining by flow cytometry in NP cells. (b) The quantitative analysis of JC-1 fluorescence intensity was expressed as the red/green ratio in NP cells. (c) The quantitative analysis of RFI of MPTP in NP cells by flow cytometry. NS means no significant statistical significance ($^{*}P < 0.05$, $^{**}P < 0.01$, and $^{***}P < 0.001$ vs. control).

Oppositely, when treated with Z-VAD, an enhanced expression of RIPK1, pRIPK1, RIPK3, pRIPK3 and MLKL were detected. That is to say, Nec-1 protected against compression-induced NP cells apoptosis and blockage of apoptosis resulted in partial conversion to necroptosis.

After 24 and 36 h compression, Nec-1+Z-VAD treatment achieved a more prominent effect in reducing NP cells death compared with Nec-1 or Z-VAD. Generally, Caspase-8 plays a switching role in the process of necroptosis and apoptosis. When Caspase-8 is activated, it could cleave RIPK3 and initiate apoptosis via formation of Complex IIa which contains RIPK1, RIPK3, Caspase-8, etc. However, when the Caspase-8 pathway is blocked or deleted, it could phosphorylate RIPK1 and RIPK3. The phosphorylated RIPK1 and RIPK3 then form Complex IIb (also termed necrosome) including RIPK1, RIPK3, and TNFR-associated death domain (TRADD), ultimately initiating necroptosis [32]. Therefore, we speculate that the protective role of Nec-1+Z-VAD is largely attributed to the blockage of the shunt between necroptosis and apoptosis.

Synergetic inhibition of necroptosis and apoptosis is indeed effective in inhibiting NP cells death. However, what is the underlying mechanism? Mitochondria have been recognized to have a critical role in cellular bioenergetics and redox [33, 34]; thus far, the precise mechanism of mitochondrial dysfunction in necroptosis or apoptosis remains elusive [18–21]. Generally, mitochondria are not only the major source of oxidative stress but also the vulnerable aim of oxidative stress [35]. The moderate activation of oxidative stress could promote cell survival; however, the overactivation of oxidative stress results in necroptosis, apoptosis, or cell death [36, 37]. Mitochondrial dysfunction and oxidative stress often interact with each other and synergistically determine the ultimate fate of cells [35, 38].

The contribution of combined inhibition of necroptosis and apoptosis to mitochondrial dysfunction and oxidative stress remains unclear in NP cells. It was displayed that 24 and 36 h compression provoked a time-dependent mitochondrial dysfunction. The Nec-1+Z-VAD treatment efficiently blocked MPTP opening and MMP loss in NP cells. Considering that enhanced MPTP opening directly results in mitochondrial injury, the protective role might be largely attributed to restrained opening of MPTP. Additionally, the ROS and mtROS production were remarkedly inhibited by Nec-1 or Nec-1+Z-VAD, especially in the Nec-1+Z-VAD group. The above results suggested that Nec-1+Z-VAD capably alleviates mitochondrial dysfunction and oxidative stress. The underlying mechanism might be similar to the protective effect of synergetic inhibition of necroptosis and apoptosis on NP cells survival, which was discussed above.

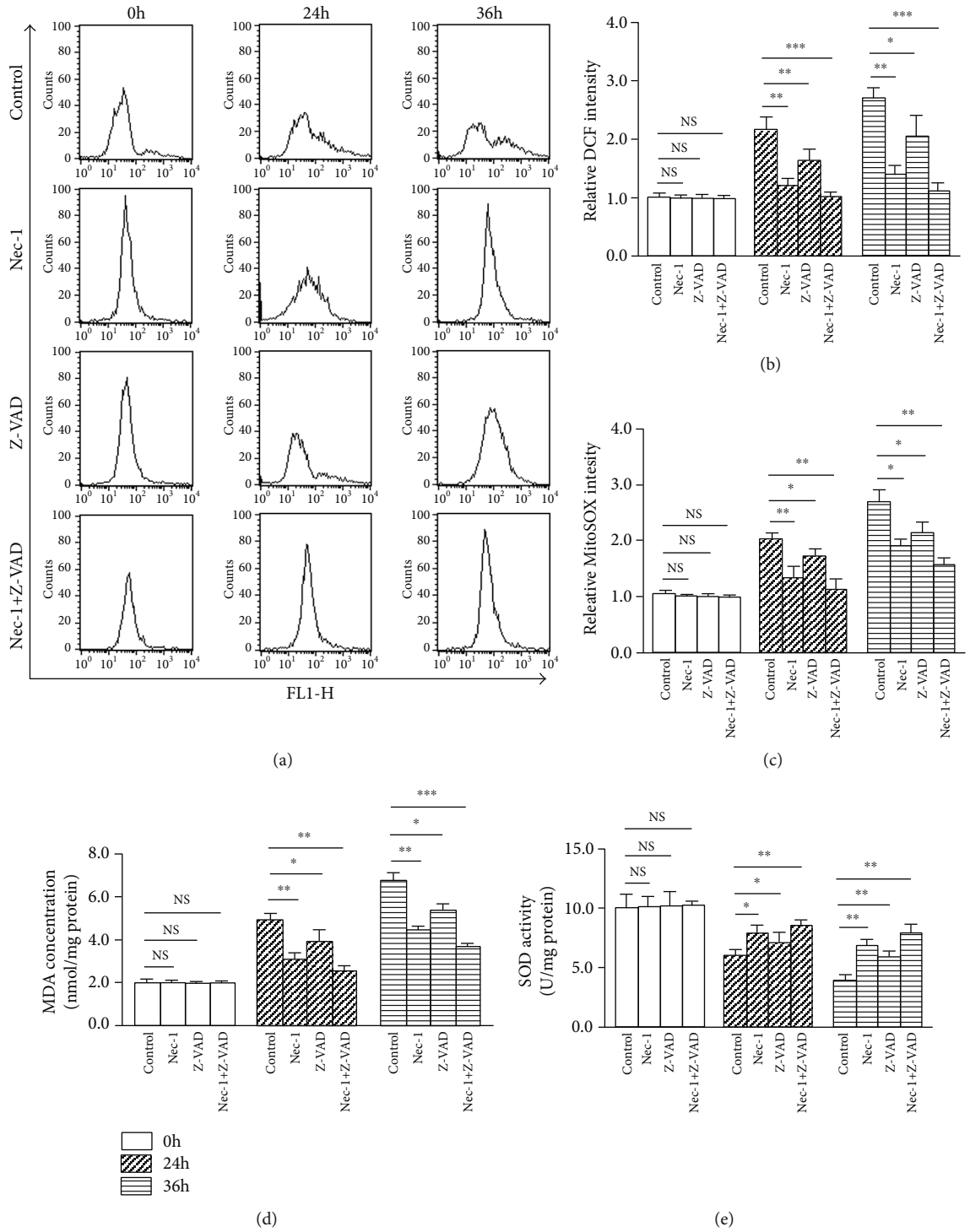

Figure 7: Nec-1+Z-VAD alleviated 24 and 36 h compression-provoked oxidative stress of NP cells. (a) Representative dot plot images after the labeling of fluorescent probe DCFH-DA in NP cells by flow cytometry. (b) The quantitative analysis of ROS in NP cells by flow cytometry. (c) The quantitative analysis of mtROS in NP cells by flow cytometry. (d) TBA method measured the content of MDA in NP cells. (e) The activity of SOD in NP cells was evaluated by spectrophotometry. NS means no significant statistical significance ($^{*}P < 0.05$, $^{**}P < 0.01$, and $^{***}P < 0.001$ vs. control).

In conclusion, autophagy might be a downstream effect of necroptosis and the interaction between necroptosis and apoptosis existed in NP cells. Combined inhibition of necroptosis and apoptosis enables predominant effect on NP cells survival, which might be largely attributed to restored mitochondrial function. The synergistic utilization of Nec-1 and Z-VAD is a worthwhile strategy in reducing compression-induced NP cells death or even delaying IVD degeneration.

Data Availability

The data in the manuscript have been repeated at least three times and are all available. The data can be accessed from Songfeng Chen (email: csfzdyfygk@163.com) and Hongjian Liu (email: fccliuhj@zzu.edu.cn).

Conflicts of Interest

The authors declare that they have no conflict of interest.

Authors' Contributions

Songfeng Chen, Qing Tian, Shitao Lu, and Hongjian Liu designed the research. Songfeng Chen, Qing Tian, and Chunfeng Shang performed the experiments. Lin Yang, Na Wei, Guowei Shang, and Yanhui Ji acquired and analyzed the data. Songfeng Chen, Shitao Lu, and Hongwei Kou conceived the study and wrote the manuscript. The integrity of this work is guaranteed by Songfeng Chen and Hongjian Liu. Songfeng Chen, Qing Tian and Chunfeng Shang contributed equally to this work.

Acknowledgments

This study was supported by the National Natural Science Foundation of China (Grant No. 81902253), the Key R&D and Promotion Program of the Science and Technology Department of Henan Province (Grant No. 192102310111, 192102310118, and 182102310512), and the Youth Innovation Fund of the First Affiliated Hospital of Zhengzhou University (Grant No. YNQN 2017037).

References

[1] C. D. Daly, P. Ghosh, A. C. W. Zannettino et al., "Mesenchymal progenitor cells primed with pentosan polysulfate promote lumbar intervertebral disc regeneration in an ovine model of microdiscectomy," *Spine*, vol. 18, no. 3, pp. 491–506, 2018.

[2] D. Hoy, L. March, P. Brooks et al., "The global burden of low back pain: estimates from the Global Burden of Disease 2010 study," *Annals of the Rheumatic Diseases*, vol. 73, no. 6, pp. 968–974, 2014.

[3] K. Luoma, H. Riihimaki, R. Luukkonen, R. Raininko, E. Viikari-Juntura, and A. Lamminen, "Low back pain in relation to lumbar disc degeneration," *Spine*, vol. 25, no. 4, pp. 487–492, 2000.

[4] M. C. Cornejo, S. K. Cho, C. Giannarelli, J. C. Iatridis, and D. Purmessur, "Soluble factors from the notochordal-rich intervertebral disc inhibit endothelial cell invasion and vessel formation in the presence and absence of pro-inflammatory cytokines," *Osteoarthritis and Cartilage*, vol. 23, no. 3, pp. 487–496, 2015.

[5] L. Zhao, H. Lin, S. Chen et al., "Hydrogen peroxide induces programmed necrosis in rat nucleus pulposus cells through the RIP1/RIP3-PARP-AIF pathway," *Journal of Orthopaedic Research*, vol. 36, no. 4, pp. 1269–1282, 2017.

[6] S. E. Gullbrand, J. Peterson, J. Ahlborn et al., "ISSLS Prize Winner: Dynamic loading-induced convective transport enhances intervertebral disc nutrition," *Spine*, vol. 40, no. 15, pp. 1158–1164, 2015.

[7] H. Hirata, T. Yurube, K. Kakutani et al., "A rat tail temporary static compression model reproduces different stages of intervertebral disc degeneration with decreased notochordal cell phenotype," *Journal of Orthopaedic Research*, vol. 32, no. 3, pp. 455–463, 2014.

[8] G. Li, Y. Song, Z. Liao et al., "Bone-derived mesenchymal stem cells alleviate compression-induced apoptosis of nucleus pulposus cells by N6 methyladenosine of autophagy," *Cell Death & Disease*, vol. 11, no. 2, p. 103, 2020.

[9] N. Boos, S. Weissbach, H. Rohrbach, C. Weiler, K. F. Spratt, and A. G. Nerlich, "Classification of age-related changes in lumbar intervertebral discs: 2002 Volvo Award in basic science," *Spine*, vol. 27, no. 23, pp. 2631–2644, 2002.

[10] Y. Fuchs and H. Steller, "Live to die another way: modes of programmed cell death and the signals emanating from dying cells," *Nature Reviews Molecular Cell Biology*, vol. 16, no. 6, pp. 329–344, 2015.

[11] N. Jaiswal, C. K. Maurya, D. Arha et al., "Fructose induces mitochondrial dysfunction and triggers apoptosis in skeletal muscle cells by provoking oxidative stress," *Apoptosis*, vol. 20, no. 7, pp. 930–947, 2015.

[12] N. Lalaoui, L. M. Lindqvist, J. J. Sandow, and P. G. Ekert, "The molecular relationships between apoptosis, autophagy and necroptosis," *Seminars in Cell & Developmental Biology*, vol. 39, pp. 63–69, 2015.

[13] J. Lin, S. Kumari, C. Kim et al., "RIPK1 counteracts ZBP1-mediated necroptosis to inhibit inflammation," *Nature*, vol. 540, no. 7631, pp. 124–128, 2016.

[14] D. Wallach and T. B. Kang, "Programmed cell death in immune defense: knowledge and presumptions," *Immunity*, vol. 49, no. 1, pp. 19–32, 2018.

[15] S. Chen, X. Lv, B. Hu et al., "Critical contribution of RIPK1 mediated mitochondrial dysfunction and oxidative stress to compression-induced rat nucleus pulposus cells necroptosis and apoptosis," *Apoptosis*, vol. 23, no. 5-6, pp. 299–313, 2018.

[16] S. Chen, X. Lv, B. Hu et al., "RIPK1/RIPK3/MLKL-mediated necroptosis contributes to compression-induced rat nucleus pulposus cells death," *Apoptosis*, vol. 22, no. 5, pp. 626–638, 2017.

[17] L. Ou, S. Lin, B. Song, J. Liu, R. Lai, and L. Shao, "The mechanisms of graphene-based materials-induced programmed cell death: a review of apoptosis, autophagy, and programmed necrosis," *International Journal of Nanomedicine*, vol. 12, pp. 6633–6646, 2017.

[18] Y. S. Ko, H. Jin, S. W. Park, and H. J. Kim, "Salvianolic acid B protects against oxLDL-induced endothelial dysfunction under high-glucose conditions by downregulating ROCK1-mediated mitophagy and apoptosis," *Biochemical Pharmacology*, vol. 174, p. 113815, 2020.

[19] H. Zhou, P. Zhu, J. Guo et al., "Ripk3 induces mitochondrial apoptosis via inhibition of FUNDC1 mitophagy in cardiac IR injury," *Redox Biology*, vol. 13, pp. 498–507, 2017.

[20] S. W. G. Tait, A. Oberst, G. Quarato et al., "Widespread mitochondrial depletion via mitophagy does not compromise necroptosis," *Cell Reports*, vol. 5, no. 4, pp. 878–885, 2013.

[21] V. S. Marsden, T. Kaufmann, L. A. O'Reilly, J. M. Adams, and A. Strasser, "Apaf-1 and caspase-9 are required for cytokine withdrawal-induced apoptosis of mast cells but dispensable for their functional and clonogenic death," *Blood*, vol. 107, no. 5, pp. 1872–1877, 2006.

[22] S. Li, W. Hua, K. Wang et al., "Autophagy attenuates compression-induced apoptosis of human nucleus pulposus cells via MEK/ERK/NRF1/Atg7 signaling pathways during intervertebral disc degeneration," *Experimental Cell Research*, vol. 370, no. 1, pp. 87–97, 2018.

[23] P. Li, Y. Gan, H. Wang et al., "Dynamic compression effects on immature nucleus pulposus: a study using a novel intelligent and mechanically active bioreactor," *International Journal of Medical Sciences*, vol. 13, no. 3, pp. 225–234, 2016.

[24] A. Dey, S. B. Mustafi, S. Saha, S. K. D. Dwivedi, P. Mukherjee, and R. Bhattacharya, "Inhibition of BMI1 induces autophagy-mediated necroptosis," *Autophagy*, vol. 12, no. 4, pp. 659–670, 2016.

[25] Y. Matsuzawa-Ishimoto, Y. Shono, L. E. Gomez et al., "Autophagy protein ATG16L1 prevents necroptosis in the intestinal epithelium," *The Journal of Experimental Medicine*, vol. 214, no. 12, pp. 3687–3705, 2017.

[26] S.-Y. Lin, S.-Y. Hsieh, Y.-T. Fan et al., "Necroptosis promotes autophagy-dependent upregulation of DAMP and results in immunosurveillance," *Autophagy*, vol. 14, no. 5, pp. 778–795, 2018.

[27] N. Zhang, Y. Chen, R. Jiang et al., "PARP and RIP1 are required for autophagy induced by 11'-deoxyverticillin A, which precedes caspase-dependent apoptosis," *Autophagy*, vol. 7, no. 6, pp. 598–612, 2011.

[28] B. Shan, H. Pan, A. Najafov, and J. Yuan, "Necroptosis in development and diseases," *Genes & Development*, vol. 32, no. 5-6, pp. 327–340, 2018.

[29] L. P. Daley-Bauer, L. Roback, L. N. Crosby et al., "Mouse cytomegalovirus M36 and M45 death suppressors cooperate to prevent inflammation resulting from antiviral programmed cell death pathways," *Proceedings of the National Academy of Sciences of the United States of America*, vol. 114, no. 13, pp. E2786–E2795, 2017.

[30] H. Anderton, E. Bandala-Sanchez, D. S. Simpson et al., "RIPK1 prevents TRADD-driven, but TNFR1 independent, apoptosis during development," *Cell Death and Differentiation*, vol. 26, no. 5, pp. 877–889, 2019.

[31] D. Martin-Sanchez, M. Fontecha-Barriuso, S. Carrasco et al., "TWEAK and RIPK1 mediate a second wave of cell death during AKI," *Proceedings of the National Academy of Sciences of the United States of America*, vol. 115, no. 16, pp. 4182–4187, 2018.

[32] W. J. Kaiser, H. Sridharan, C. Huang et al., "Toll-like receptor 3-mediated necrosis via TRIF, RIP3, and MLKL," *The Journal of Biological Chemistry*, vol. 288, no. 43, pp. 31268–31279, 2013.

[33] M. Y. Ansari, N. M. Khan, I. Ahmad, and T. M. Haqqi, "Parkin clearance of dysfunctional mitochondria regulates ROS levels and increases survival of human chondrocytes," *Osteoarthritis and Cartilage*, vol. 26, no. 8, pp. 1087–1097, 2018.

[34] H. A. Deveci, Y. Akyuva, G. Nur, and M. Nazıroğlu, "Alpha lipoic acid attenuates hypoxia-induced apoptosis, inflammation and mitochondrial oxidative stress via inhibition of TRPA1 channel in human glioblastoma cell line," *Biomedicine & Pharmacotherapy*, vol. 111, pp. 292–304, 2019.

[35] I. Terruzzi, A. Montesano, P. Senesi et al., "L-carnitine reduces oxidative stress and promotes cells differentiation and bone matrix proteins expression in human osteoblast-like cells," *BioMed Research International*, vol. 2019, Article ID 5678548, 13 pages, 2019.

[36] D. Carlisi, G. Buttitta, R. Di Fiore et al., "Parthenolide and DMAPT exert cytotoxic effects on breast cancer stem-like cells by inducing oxidative stress, mitochondrial dysfunction and necrosis," *Cell Death & Disease*, vol. 7, no. 4, article e2194, 2016.

[37] W. Zheng, C.-Y. Zhou, X.-Q. Zhu et al., "Oridonin enhances the cytotoxicity of 5-FU in renal carcinoma cells by inducting necroptotic death," *Biomedicine & Pharmacotherapy*, vol. 106, pp. 175–182, 2018.

[38] Z. Li, S. Chen, K. Ma et al., "CsA attenuates compression-induced nucleus pulposus mesenchymal stem cells apoptosis via alleviating mitochondrial dysfunction and oxidative stress," *Life Sciences*, vol. 205, pp. 26–37, 2018.

Hindawi
BioMed Research International
Volume 2020, Article ID 3101358, 16 pages
https://doi.org/10.1155/2020/3101358

Research Article

Different Dose Regimens of Intravenous Tranexamic Acid in Adolescent Spinal Deformity Surgery: A Systematic Review and Meta-Analysis

Zhencheng Xiong,[1,2] **Kexin Wu**,[3] **Jiayu Zhang**,[4] **Delong Leng**,[5] **Ziyi Yu**,[6] **Chi Zhang**,[1,7,8] **and Ping Yi**[9]

[1]*Institute of Medical Technology, Peking University Health Science Center, Beijing, China*
[2]*Peking University Third Hospital, Beijing, China*
[3]*Postgraduate School, Dalian Medical University, Dalian, China*
[4]*Graduate School of Peking Union Medical College, Chinese Academy of Medical Sciences, Beijing, China*
[5]*Department of Clinical Medicine, School of Clinical Medicine, Bengbu Medical College, Bengbu, China*
[6]*Department of Urology, Peking University Cancer Hospital & Institute, Beijing, China*
[7]*Department of Orthopedics, Peking University International Hospital, Beijing, China*
[8]*School of Chinese Materia Medica, Beijing University of Chinese Medicine, Beijing, China*
[9]*Department of Spine Surgery, China-Japan Friendship Hospital, Beijing, China*

Correspondence should be addressed to Chi Zhang; chi.zhang@case.edu and Ping Yi; 13811758985@139.com

Received 18 July 2020; Revised 6 November 2020; Accepted 12 November 2020; Published 28 November 2020

Academic Editor: Xiao Wang

Objective. To evaluate the efficacy and safety of different dose regimens of intravenous (IV) tranexamic acid (TXA) in adolescent spinal deformity surgery. *Methods*. Two researchers independently searched multiple databases, including PubMed, Embase, Cochrane Library, and Web of Science to find studies that met the inclusion criteria. A meta-analysis was performed based on the guidelines of the *Cochrane Reviewer's Handbook*. *Results*. Six randomized controlled trials (RCTs) and eleven non-RCTs were identified, including 1148 patients. According to different dose regimens of IV TXA, the included studies were divided into the high-dose group and the low-dose group. Compared with placebo, both groups had less total blood loss (TBL) (high dose: WMD = −1737.55, 95% CI: (-2247.16, -1227.94), $P < 0.001$, $I^2 = 0\%$; low dose: WMD = −528.67, 95% CI: (-666.06, -391.28), $P < 0.001$, $I^2 = 0\%$), intraoperative blood loss (IBL) (high dose: WMD = −301.48, 95% CI: (-524.3, -78.66), $P = 0.008$, $I^2 = 60.3\%$; low dose: WMD = −751.14, 95% CI: (-967.21, -535.08), $P < 0.001$, $I^2 = 0\%$), and blood transfusion rates (high dose: RR = 0.19, 95% CI: (0.1, 0.37), $P < 0.001$, $I^2 = 0\%$; low dose: RR = 0.4, 95% CI: (0.18, 0.91), $P = 0.029$, $I^2 = 57\%$). High-dose IV TXA use was associated with more vertebral fusion segments (WMD = 0.53, 95% CI: (0.23, 0.82), $P < 0.001$, $I^2 = 31.2\%$). Low-dose IV TXA use was associated with shorter operative time (WMD = −18.43, 95% CI: (-26.68, -10.17), $P < 0.001$, $I^2 = 0\%$). *Conclusion*. High-dose and low-dose IV TXA were effective in reducing TBL, IBL, and blood transfusion rates without increasing complications in adolescent patients undergoing spinal deformity surgery. Low-dose IV TXA was effective in reducing the operative time. Both the high-dose and low-dose groups had similar preoperative and postoperative Hb levels compared to the control group.

1. Introduction

Perioperative blood loss is a major problem in surgery, especially in complex high-risk surgical procedures, such as spinal deformity surgery [1]. As we all know, the posterior column and three column osteotomies may be the more commonly used procedures in spinal deformity surgery, although it may bring significant risks [2]. Some spinal diseases require spinal deformity surgery for further deterioration, including degenerative scoliosis, adolescent idiopathic

scoliosis (AIS), degenerative lumbar kyphosis, posttraumatic kyphosis, and Duchenne muscular dystrophy (DMD) [3]. AIS, a complex three-dimensional deformity of the spine, is defined as a lateral curvature of the spine > 10° in the coronal plane [4]. AIS correction surgery and other spinal deformity surgeries are associated with significant blood loss. Increased blood loss brings many clinical risks, including hemodynamic instability, progressive multiple organ dysfunction, transfusion reaction, hypersensitivity, and increased risk for infection [5]. Therefore, how to reduce perioperative blood loss during spinal deformity surgery has become a hot topic for spinal surgeons. At present, many hemostatic drugs, including tranexamic acid (TXA), are used to prevent significant blood loss in spinal deformity surgery [2].

TXA, a synthetic lysine analogue, exerts an antifibrinolytic effect through binding to the lysine-binding sites on plasminogen molecules and inhibiting fibrinolysis [6]. Some clinical studies and meta-analyses show that intravenous (IV) TXA can reduce blood loss and allogeneic blood transfusion without the high risk of complications such as pulmonary embolism (PE), deep vein thrombosis (DVT), or other [1–5, 7–23]. For IV TXA in spinal deformity surgery, high-dose and low-dose stratification can be performed. In one study, Raman et al. [24] demonstrated that high-dose TXA was more effective than low-dose TXA in reducing blood loss and blood transfusion requirements in spinal deformity surgery. The high-dose group in this study used three dosage regimens [24]. However, the number of studies that directly compare high-dose TXA and low-dose TXA is limited. The optimal dosage scheme of TXA in spinal deformity surgery is still controversial. Therefore, we conducted this meta-analysis to evaluate the efficacy and safety of different dose regimens of IV TXA in adolescent spinal deformity surgery. This meta-analysis sets the definition of high-dose IV TXA to include any dose ≥ 20 mg/kg or >1 g. On the contrary, it is a low-dose regimen. We divided the studies that met the criteria into a high-dose group and a low-dose group and conducted a subgroup analysis of the dose for the same outcome measurements.

2. Materials and Methods

2.1. Search Strategy. To obtain all relevant studies, two researchers independently searched multiple databases according to Cochrane Collaboration guidelines, such as PubMed (1966 to April 1, 2020), Embase (1980 to April 1, 2020), Cochrane Library (1980 to April 1, 2020), and Web of Science (1965 to April 1, 2020). Literature was searched with the MeSH terms and corresponding keywords (connecting via Boolean operators "AND or OR"), including "tranexamic acid or TXA", "intravenous", "spine deformity", "spine surgery", "scoliosis", "spinal deformity surgery", and "adolescent". We set the search language limit to English. Two researchers reviewed potential articles based on the titles and abstracts and identified the full text of eligible articles according to the inclusion and exclusion criteria. Then, by reading the full text, we further filter the selected literature. Besides, the reference lists of all retrieved studies were screened to identify potentially relevant studies. If there was disagreeable literature between the two researchers, our research team would discuss to reach a consensus. This meta-analysis was conducted based on the Preferred Reporting Items for Systematic Reviews and Meta-Analyses (PRISMA) statement [25].

2.2. Study Selection. Inclusion criteria for this meta-analysis are the following: (1) all studies involved the comparison of the effect of IV TXA versus a placebo or control group in patients undergoing adolescent spinal deformity surgery; (2) randomized controlled trials (RCTs) or non-RCTs meet the criteria; (3) the study population has a diagnosis of spinal deformities, such as AIS, posttraumatic kyphosis, and degenerative lumbar scoliosis; (4) the study population all had spinal instrumentation and fusion surgery in professional medical institutions due to spinal deformities; (5) the study population had no history of spinal surgery and no history of a bleeding disorder or antifibrinolytic therapy; and (6) data on relevant outcome measurements can be extracted.

The following were excluded from this meta-analysis: (1) studies were not suitable with the inclusion criteria; (2) the types of studies were case reports, case series, conference abstracts, reviews, letters, and editorials; (3) the patient's age is classified as a child, adult, middle adult, or elderly; and (4) data of studies cannot be extracted.

2.3. Data Extraction. Data was extracted independently by two researchers, and then, another researcher collected the data using a spreadsheet. Disagreements in the data extraction process were resolved after discussion. The following general characteristics were extracted: first author, publication year, country, study type, number of participants (IV TXA: control), surgical procedure, age, body mass index (BMI), gender, intervention (IV TXA: control), outcome measurements, and transfusion criteria.

2.4. Quality Assessment. According to the Cochrane Handbook for Systematic Reviews, two researchers independently assessed the quality of each included RCT [26]. A "risk of bias" table was created with the following elements: (i) random sequence generation; (ii) allocation concealment; (iii) blinding of participant and personnel; (iv) blinding of outcome assessment; (v) incomplete outcome data; (vi) selective reporting; and (vii) other bias. Each of the above sections has a higher risk of bias, a lower risk of bias, and an unclear risk of bias, depending on the actual content of each RCT [26].

The Newcastle-Ottawa scale (NOS) was used to assess the quality of included non-RCTs [27]. In this scale, there are three major items (selection, comparability, and outcome), which can be subdivided into eight detailed quality items. In "selection" and "outcome," each quality item can be awarded a maximum of one star. In "comparability," up to two stars can be given. One star represents one point, and the higher the score, the higher the quality assessment [27]. We set low-quality, moderate-quality, and high-quality studies at a score of 0-3, 4-6, and 7-9, respectively.

2.5. Statistical Analysis. Data for the same outcome measurements in all studies were summarized in the same table. Outcome measurements were divided into subgroups according

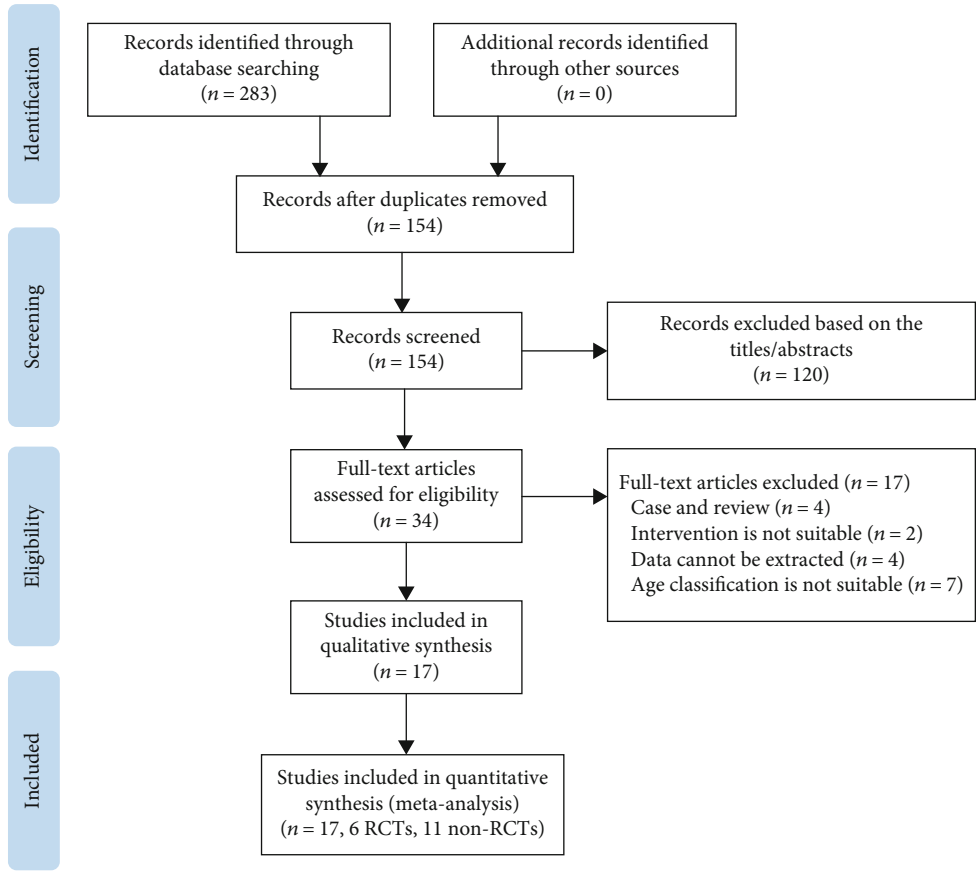

Figure 1: Flow diagram of the study selection process for the meta-analysis.

to the dosage regimen or recording time. The continuous data was analyzed by using weighted mean difference (WMD) and 95% confidence interval (CI), such as total blood loss (TBL), intraoperative blood loss (IBL), preoperative and postoperative hemoglobin (Hb) levels, operative time, number of vertebral segments fused, and estimated blood loss per fusion segment. Dichotomous data, such as blood transfusion rates, was analyzed using the risk ratio (RR) and 95% CI. The heterogeneity of the included studies was evaluated using the χ^2 test and I^2 test. When the value of I^2 is 25%, 50%, and 75%, it is regarded as low, medium, and high heterogeneity [28]. When $I^2 > 50\%$, $P < 0.1$, we performed a random-effects model; otherwise, a fixed-effects model was performed [28]. All statistical analyses were undertaken using STATA software version 16.0 (Stata Corporation, College Station, Texas, USA) and RevMan 5.3 for Windows (Cochrane Collaboration, Oxford, UK). If $P < 0.05$, the results of this meta-analysis were considered statistically significant.

3. Results

3.1. Search Results. A total of 283 potentially relevant articles were generated, including PubMed ($n = 48$), Cochrane Library ($n = 38$), Web of Science ($n = 43$), and Embase ($n = 154$) based on search strategy and inclusion criteria. After screening the titles and abstracts, 120 articles were excluded due to duplicate articles, conference abstracts, case reports, letters, reviews, and irrelevant studies. Based on the inclusion and exclusion criteria, the full text of the remaining 34 articles was evaluated for eligibility. Finally, 6 RCTs and 11 non-RCTs were included in this meta-analysis [4, 5, 7–21]. Figure 1 is a flow diagram of the study selection.

3.2. Study Characteristics. Six RCTs and 11 non-RCTs involving 1148 patients were analyzed in this meta-analysis [4, 5, 7–21]. All included studies were published between 2001 and 2019 [4, 5, 7–21]. The characteristics of all included studies are shown in Table 1. The efficacy and safety of different dose regimens of IV TXA in adolescent spinal deformity surgery had been compared in all studies. A total of 9 studies were high-dose regimens [4, 5, 8–10, 15–17, 19], and the remaining 8 studies were low-dose regimens [7, 11–14, 18, 20, 21]. Of these 9 studies, 3 studies were RCTs [5, 8, 10], and the rest were non-RCTs [4, 9, 15–17, 19]. Among these studies with the high-dose regimen, there are 6 studies with the same dose regimen, all with a loading dose of 100 mg/kg infused before skin incision and a maintenance dose of 10 mg/kg/h [8, 9, 15–17, 19]. Of these 8 studies, 3 studies were RCTs [7, 13, 21], and the rest were non-RCTs [11, 12, 14, 18, 20]. Among them, there are 4 studies with the same dose regimen, all with a loading dose of 10 mg/kg infused before skin incision and a maintenance dose of 1 mg/kg/h

Table 1: Characteristics of all the trials included in the meta-analysis.

Study	Country	Study type	Mean age (years) T:C	No. of patients T:C	Male T:C	Mean BMI (kg/m^2) T:C	Disease diagnosis	Surgical methods	TXA dosing (loading + maintenance)	Transfusion criteria	Outcome measures
Neilipovitz et al., [7]	Canada	RCT	14.1/13.7	22/18	12/5	NP	AIS	PSF	10 mg/kg + 1 mg/kg/h	Hb < 7 g/dL	(2), (3), (4), (5), and (6)
Sethna et al., [8]	USA	RCT	13.6/14.0	23/21	17/13	NP	AIS	Spinal fusion	100 mg/kg + 10 mg/kg/h	NP	(2), (3), and (6)
Xu et al., [10]	China	RCT	19.1/20.4	20/20	12/7	NP	AIS	Spinal fusion	20 mg/kg + 10 mg/kg/h	NP	(3)
Verma et al., [13]	USA	RCT	15.3/15.01	36/47	4/16	21.19/21.92	AIS	PSF	10 mg/kg + 1 mg/kg/h	NP	(1), (6), and (7)
Goobie et al., [5]	USA	RCT	14.9/14.7	56/55	10/13	21.1/22.2	AIS	PSF	50 mg/kg + 10 mg/kg/h	NP	(2), (3), (4), (6), and (7)
Saleh et al., [21]	Egypt	RCT	14.6/14.6	25/25	11/11	NP	AIS	PSF	10 mg/kg + 1 mg/kg/h	NP	(3)
Shapiro et al., [7]	USA	RCS	13.9/14.0	20/36	NP	NP	DMD	PSF	100 mg/kg + 10 mg/kg/h	NP	(1), (3), and (6)
Yagi et al., [11]	Japan	RCS	15.2/15.5	43/63	3/4	NP	AIS	PSF	1 g + 100 mg/h	Hb < 7 g/dL	(1), (3), (5), and (6)
Lykissas et al., [12]	USA	RCS	14.7/13.5	25/24	4/2	NP	AIS	PSF	100 mg + 10 mg/h	Hb < 7 g/dL	(2), (4)
Xie et al., [16]	China	RCS	18.9/18.6	26/33	11/15	NP	Spinal deformity	PSF	100 mg/kg + 10 mg/kg/h	NP	(1), (3)
Berney et al., [14]	Ireland	RCS	15.3/16.4	31/25	9/10	20.3/21.2	AIS	PSF with pedicle screws	15 mg/kg + 10 mg/kg/h	Hb < 7 g/dL	(4)
Ng et al., [17]	China	RCS	15.16/15.31	55/35	NP	19.03/17.76	AIS	PSF with pedicle screws	100 mg/kg + 10 mg/kg/h	Hb < 8 g/dL	(1), (6)
da Rocha et al., [15]	Brazil	RCS	18.0/21.6	21/19	NP	NP	Spinal deformity	PSF with pedicle screws	100 mg/kg + 30 mg/kg/h	NP	(2), (3), and (6)
Sui et al., [18]	China	RCS	15.5/16.2	71/66	22/21	17.1/16.9	AIS	PSF with pedicle screws	100 mg/kg + 10 mg/kg/h	NP	(4)
Jones et al., [19]	USA	RCS	16.1/15.2	18/18	2/3	22.2/20.2	AIS	PSF	10 mg/kg + 1 mg/kg/h	NP	(3), (6), and (7)
Ohashi et al., [20]	Japan	RCS	15.1/14.8	30/33	1/5	NP	AIS	PSF	1 g + 100 mg/h	NP	(2), (5), and (6)
Bosch et al., [4]	USA	RCS	13.7/13.5	30/58	4/11	NP	AIS	PSF	30 mg/kg + 10 mg/kg/h	Hb < 7 g/dL	(3), (6), and (7)

T: TXA group; C: control group. TXA: tranexamic acid; RCT: randomized controlled trial; RCS: retrospective controlled study; BMI: body mass index; AIS: adolescent idiopathic scoliosis; DMD: Duchenne muscular dystrophy; PSF: posterior spinal fusion; Hb: hemoglobin; NP: not provided. Outcome measures: (1) total blood loss; (2) intraoperative blood loss; (3) operative time; (4) blood transfusion rate; (5) Hb level; (6) number of vertebral segments fused; (7) estimated blood loss per fusion segment.

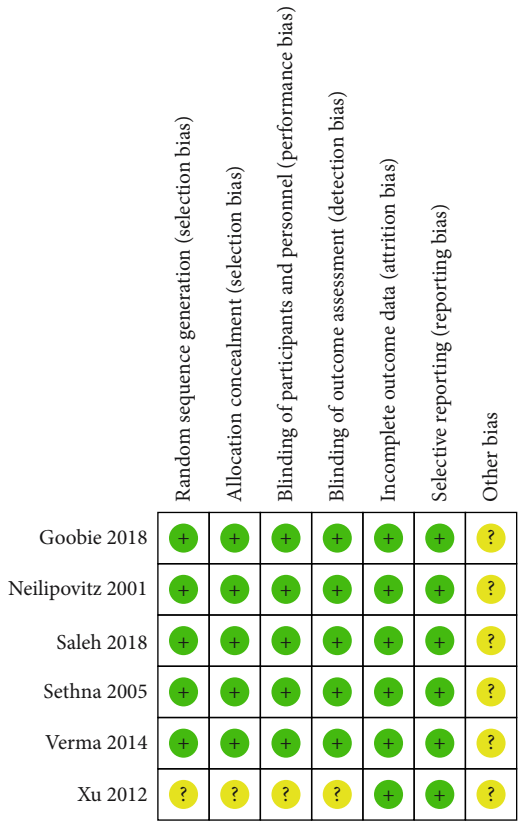

FIGURE 2: Risk of bias summary: +: low risk of bias; −: high risk of bias; ?: bias unclear.

[7, 13, 18, 21]. Among the 1148 adolescent patients, the mean ages ranged from 13.5 to 21.6, and the sample sizes of the IV TXA group ranged from 18 to 71 [4, 5, 7–21]. Of the 17 studies, the main diagnosis of 14 studies was AIS [4, 5, 7, 8, 10–14, 17–21], one study was DMD [9], and the remaining were other spinal deformities [15, 16]. The surgical method used in 15 studies [4, 5, 7, 9, 11–21] was posterior spinal fusion. These studies mainly include three surgical methods, all of which were spinal deformity surgery [4, 5, 7–21].

3.3. Risk of Bias. Figure 2 shows the risk of bias assessment for the 6 RCTs [5, 7, 8, 10, 13, 21]. A total of 5 RCTs were considered to have a low risk of bias [5, 7, 8, 13, 21]. Random sequence generation, allocation concealment, blinding of participants and personnel, and blinding of outcome assessment were found in five studies [5, 7, 8, 13, 21]. None of the six RCTs found selective reports [5, 7, 8, 10, 13, 21].

Table 2 shows the risk of bias assessment for the 11 non-RCTs [4, 9, 11, 12, 14–20]. According to the NOS, 5 studies received 8 points [11, 14, 16, 17, 20], and 6 studies received 7 points [4, 9, 12, 15, 18, 19], indicating that the quality of included studies was acceptable.

3.4. Results of the Meta-analysis

3.4.1. TBL. As shown in Figure 3, the forest plot shows the effect of the high-dose IV TXA regimen compared with the low-dose IV TXA regimen on TBL during adolescent spinal deformity surgery. Five studies provided TBL as the primary outcome measurement [9, 11, 13, 16, 17]. TBL was divided into 2 subgroups according to different dosage regimens. A total of 3 studies (205 patients) [9, 16, 17] provided data on TBL for the high-dose regimen, and 2 studies (189 patients) [11, 13] provided data on TBL for the low-dose regimen. Because there was no significant heterogeneity ($I^2 < 50\%$), a fixed-effects model was used. There was a statistically significant difference in TBL between the high-dose TXA group and the control group based on the results of the pooled analysis (WMD = −1737.55, 95% CI: (-2247.16, -1227.94), $P < 0.001$, $I^2 = 0\%$). And there was a statistically significant difference in TBL between the low-dose TXA group and the control group (WMD = −528.67, 95% CI: (-666.06, -391.28), $P < 0.001$, $I^2 = 0\%$).

3.4.2. IBL. As shown in Figure 4, the forest plot shows the effect of the high-dose IV TXA regimen compared with the low-dose IV TXA regimen on IBL during adolescent spinal deformity surgery. Six studies provided IBL as the primary outcome measurement [5, 7, 8, 12, 15, 20]. IBL was divided into 2 subgroups according to different dosage regimens. A total of 3 studies (195 patients) [5, 8, 15] provided data on IBL for the high-dose regimen, and 3 studies (152 patients) [7, 12, 20] provided data on IBL for the low-dose regimen. Because of the significant heterogeneity ($I^2 > 50\%$, $P < 0.1$), a random-effects model was used. There was a statistically significant difference in IBL between the high-dose TXA group and the control group based on the results of the pooled analysis (WMD = −301.48, 95% CI: (-524.3, -78.66), $P = 0.008$, $I^2 = 60.3\%$). And there was a statistically significant difference in IBL between the low-dose TXA group and the control group (WMD = −751.14, 95% CI: (-967.21, -535.08), $P < 0.001$, $I^2 = 0\%$).

3.4.3. Operative Time. As shown in Figure 5, the forest plot shows the effect of the high-dose IV TXA regimen compared with the low-dose IV TXA regimen on operative time during adolescent spinal deformity surgery. Eleven studies provided operative time as the secondary outcome measurement [4, 5, 7–11, 15, 16, 18, 21]. Operative time was divided into 2 subgroups according to different dosage regimens. A total of 7 studies (438 patients) [4, 5, 8–10, 15, 16] provided data on operative time for the high-dose regimen, and 4 studies (232 patients) [7, 11, 18, 21] provided data on operative time for the low-dose regimen. Because there was no significant heterogeneity ($I^2 < 50\%$), a fixed-effects model was used. There were no statistically significant differences in operative time between the high-dose TXA group and the control group based on the results of the pooled analysis (WMD = 10.86, 95% CI: (-2.51, 24.24), $P = 0.111$, $I^2 = 0\%$). However, there was a statistically significant difference in operative time between the low-dose TXA group and the control group (WMD = −18.43, 95% CI: (-26.68, -10.17), $P < 0.001$, $I^2 = 0\%$).

3.4.4. Blood Transfusion Rate. As shown in Figure 6, the forest plot shows the effect of the high-dose IV TXA regimen compared with the low-dose IV TXA regimen on the blood

Table 2: The Newcastle-Ottawa Scale (NOS) for assessing the quality of non-RCTs.

Study	Selection	Comparability	Outcomes	Total scores (maximum 9)
Shapiro et al., [9]	2	2	3	7
Yagi et al., [11]	4	2	2	8
Lykissas et al., [12]	3	2	2	7
Xie et al., [16]	3	2	3	8
Berney et al., [14]	4	2	2	8
Ng et al., [17]	4	2	2	8
da Rocha et al., [15]	2	2	3	7
Sui et al., [18]	3	2	2	7
Jones et al., [19]	3	2	2	7
Ohashi et al., [20]	4	2	2	8
Bosch et al., [4]	3	2	2	7

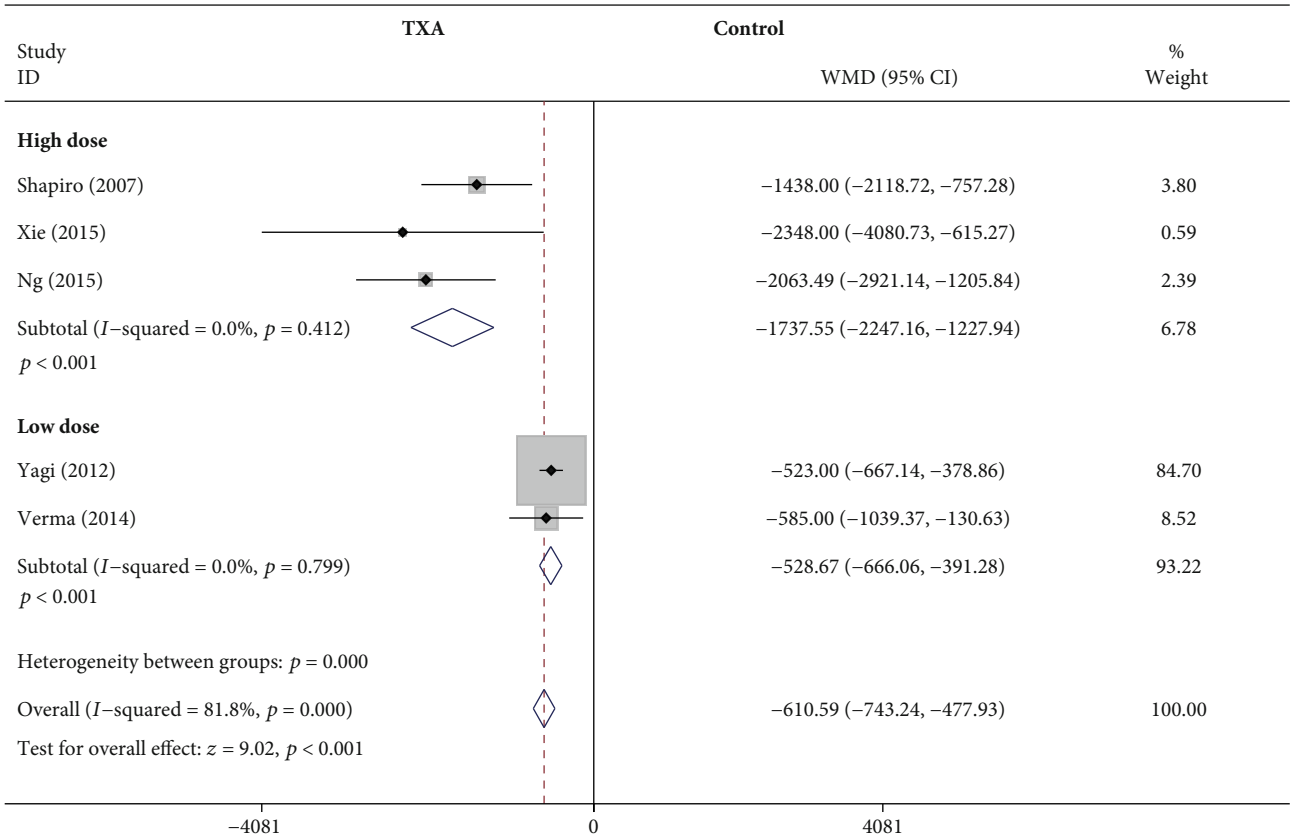

Figure 3: Forest plot showing the effect of high-dose IV TXA regimen compared with low-dose IV TXA regimen on TBL during adolescent spinal deformity surgery. IV: intravenous; TXA: tranexamic acid; TBL: total blood loss; WMD: weighted mean difference.

transfusion rate during adolescent spinal deformity surgery. Five studies provided the blood transfusion rate as the secondary outcome measurement [5, 7, 12, 14, 19]. The blood transfusion rate was divided into 2 subgroups according to different dosage regimens. A total of 2 studies (248 patients) [5, 19] provided data on the blood transfusion rate for the high-dose regimen, and 3 studies (145 patients) [7, 12, 14] provided data on the blood transfusion rate for the low-dose regimen. Because of the significant heterogeneity ($I^2 > 50\%$, $P < 0.1$), a random-effects model was used. There was a statistically significant difference in the blood transfusion rate between the high-dose TXA group and the control group (RR = 0.19, 95% CI: (0.1, 0.37), $P < 0.001$, $I^2 = 0\%$). And there was a statistically significant difference in the blood transfusion rate between the low-dose TXA group and the control group

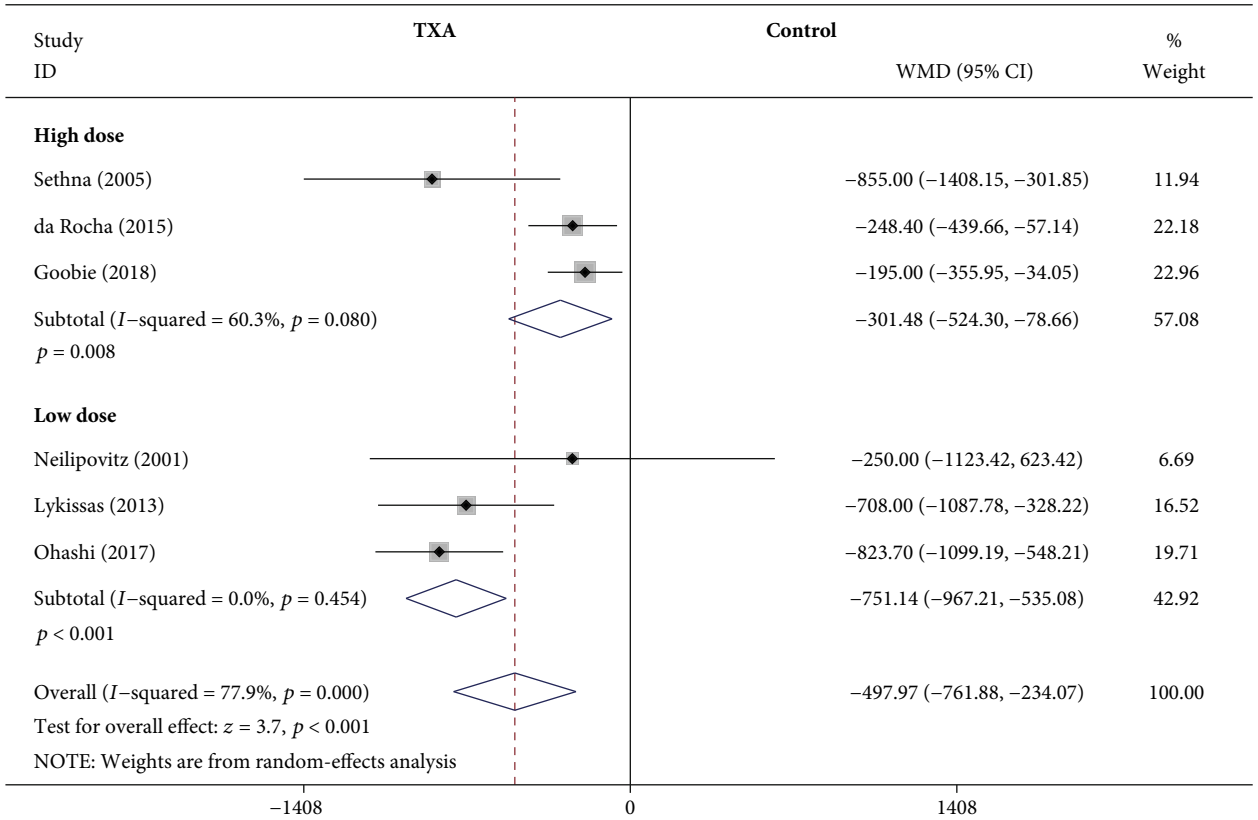

Figure 4: Forest plot showing the effect of high-dose IV TXA regimen compared with low-dose IV TXA regimen on IBL during adolescent spinal deformity surgery. IBL: intraoperative blood loss.

based on the results of the pooled analysis (RR = 0.4, 95% CI: (0.18, 0.91), $P = 0.029$, $I^2 = 57\%$).

3.4.5. Preoperative and Postoperative Hb Levels. As shown in Figure 7, the forest plot shows the effect of low-dose IV TXA on Hb level compared with the control group during adolescent spinal deformity surgery. Three studies provided preoperative and postoperative Hb levels as the secondary outcome measurement [7, 11, 20]. Hb was divided into 2 subgroups according to different time points. A total of 3 studies (209 patients) [7, 11, 20] provided data on the preoperative Hb level and postoperative 24 h Hb level. Because of the significant heterogeneity ($I^2 > 50\%$, $P < 0.1$), a random-effects model was used. There were no statistically significant differences in preoperative and postoperative Hb levels between the low-dose TXA group and the control group based on the results of the pooled analysis (preoperative: WMD = 2.88, 95% CI: (-0.41, 6.18), $P = 0.086$, $I^2 = 0\%$; postoperative 24 h: WMD = 4.03, 95% CI: (-2.05, 10.11), $P = 0.194$, $I^2 = 62.2\%$).

3.4.6. Number of Vertebral Segments Fused. As shown in Figure 8, the forest plot shows the effect of the high-dose IV TXA regimen compared with the low-dose IV TXA regimen on the number of vertebral segments fused during adolescent spinal deformity surgery. Eleven studies provided the number of vertebral segments fused as the secondary outcome measurement [4, 5, 7–9, 11, 13, 15, 17, 18, 20]. The number of vertebral segments fused was divided into 2 subgroups according to different dosage regimens. A total of 6 studies (429 patients) [4, 5, 8, 9, 15, 17] provided data on the number of vertebral segments fused for the high-dose regimen, and 5 studies (328 patients) [7, 11, 13, 18, 20] provided data on the number of vertebral segments fused for the low-dose regimen. Because there was no significant heterogeneity ($I^2 < 50\%$), a fixed-effects model was used. There were no statistically significant differences in the number of vertebral segments fused between the low-dose TXA group and the control group based on the results of the pooled analysis (WMD = −0.05, 95% CI: (-0.42, 0.32), $P = 0.783$, $I^2 = 8\%$). However, there was a statistically significant difference in the number of vertebral segments fused between the high-dose TXA group and the control group (WMD = 0.53, 95% CI: (0.23, 0.82), $P < 0.001$, $I^2 = 31.2\%$).

3.4.7. Estimated Blood Loss per Fusion Segment. As shown in Figure 9, the forest plot shows the effect of the high-dose IV TXA regimen compared with the low-dose IV TXA regimen on estimated blood loss per fusion segment during adolescent spinal deformity surgery. Four studies provided estimated blood loss per fusion segment as the secondary outcome measurement [4, 5, 13, 18]. Estimated blood loss per fusion segment was divided into 2 subgroups according to different dosage regimens. A total of 2 studies (199 patients) [4, 5] provided data on estimated blood loss per fusion segment for the high-dose regimen, and 2 studies (108 patients) [13, 18]

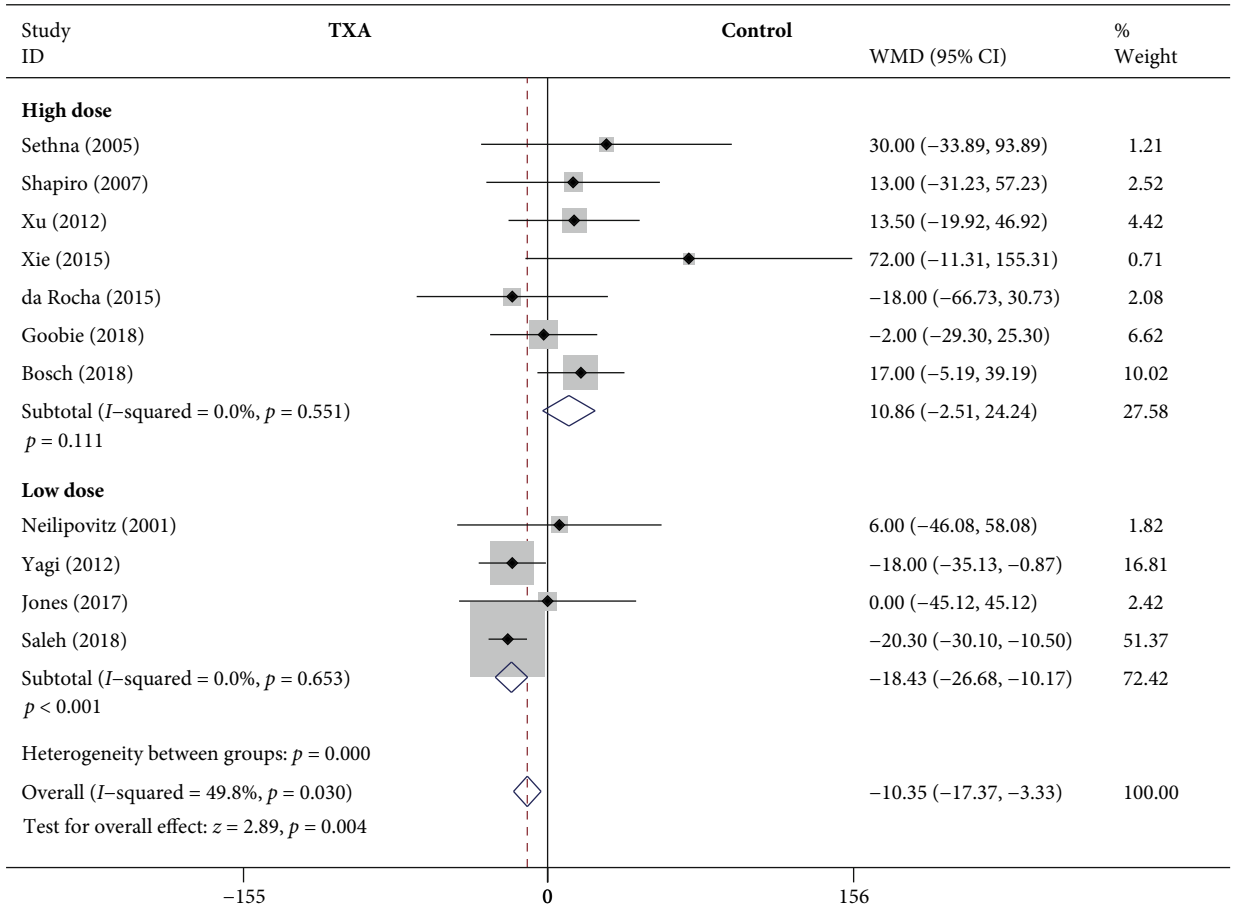

Figure 5: Forest plot showing the effect of high-dose IV TXA regimen compared with low-dose IV TXA regimen on operative time during adolescent spinal deformity surgery.

provided data on estimated blood loss per fusion segment for the low-dose regimen. Because of the significant heterogeneity ($I^2 > 50\%$, $P < 0.1$), a random-effects model was used. There were no statistically significant differences in estimated blood loss per fusion segment between the high-dose TXA group and the control group based on the results of the pooled analysis (WMD = −11.94, 95% CI: (-44.74, 20.86), $P = 0.476$, $I^2 = 87.4\%$). And there were no statistically significant differences in estimated blood loss per fusion segment between the low-dose TXA group and the control group (WMD = −32.33, 95% CI: (-70.91, 6.25), $P = 0.1$, $I^2 = 61.7\%$).

3.4.8. Adverse Event. None of the included 17 studies reported adverse events, such as DVT/PE, allergic reaction, angina, myocardial infarction, new-onset arrhythmia, pneumonia, wound problem, and urinary tract infection. Comparing the differences in adverse events of different dosage regimens, more high-quality research is still needed.

3.5. Publication Bias. The funnel plot, Begg's funnel plot, and Egger's test were used to assess publication bias and were usually performed in at least 10 studies. No publication bias was detected by Begg's test due to all P values > 0.05 for TBL, IBL, operative time, blood transfusion rate, or number of vertebral segments fused (Begg's test, $P = 0.221$, $P = 0.707$, $P = 0.213$, $P = 0.806$, and $P = 0.876$, respectively). The remaining outcome measurements were not suitable for Begg's test and Egger's test due to too few studies. Figure 10 shows Begg's test for publication bias.

3.6. Sensitivity Analysis. Sensitivity analysis was conducted to assess the stability of the pooled result. Based on the results of the pooled analysis, high heterogeneity ($I^2 > 50\%$, $P < 0.1$) was found in IBL, blood transfusion rate, preoperative and postoperative Hb levels, and estimated blood loss per fusion segment. Because only two studies have been included in different subgroups of estimated blood loss per fusion segment, its high heterogeneity may be due to the limited number of studies. For other outcome measures, we found that when excluding any study, the results did not find significant changes, thus confirming the robustness and reliability of the results of this meta-analysis (Figure 11). The sources of high heterogeneity in this meta-analysis may be as follows: (1) the number of the studies included in each subgroup is limited; (2) the differences between the included studies are inherent; (3) the doses, methods of use, and operators are not exactly the same among the included studies; (4) the sample size and the collection time of outcome measures are not exactly the same among the included studies; and (5) the diagnosis and operation of the patients are not the same.

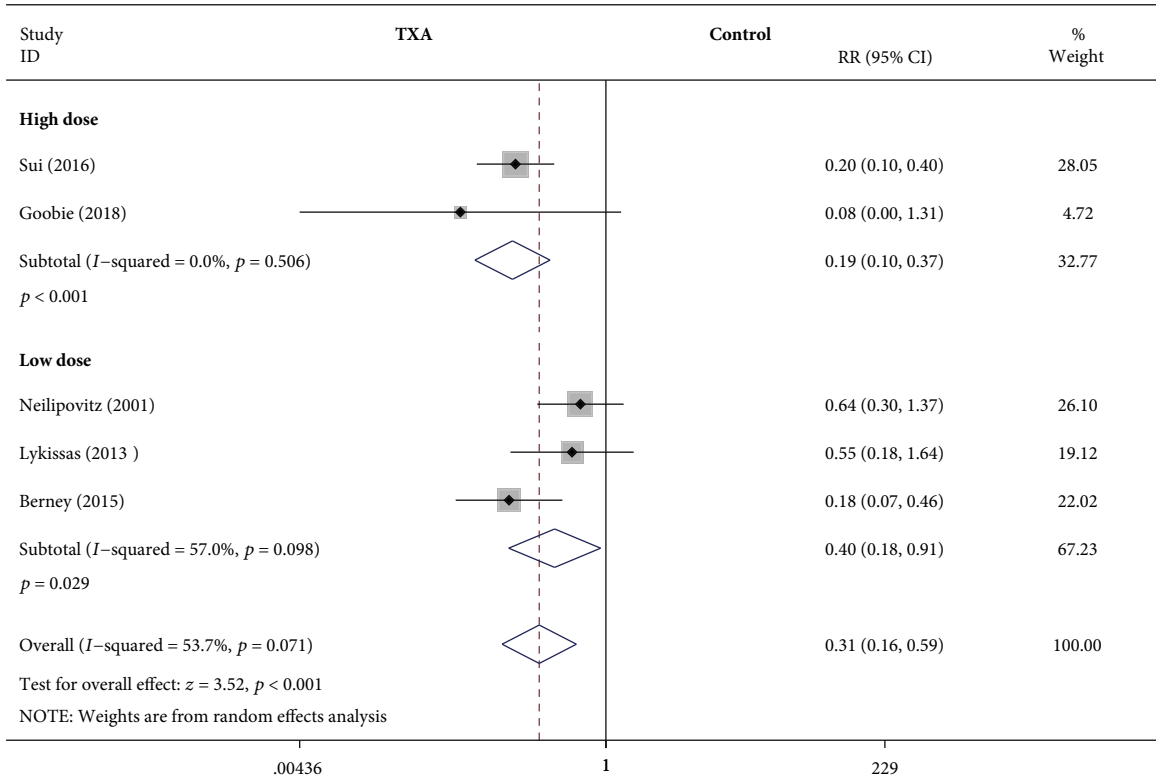

Figure 6: Forest plot showing the effect of high-dose IV TXA regimen compared with low-dose IV TXA regimen on blood transfusion rate during adolescent spinal deformity surgery. RR: risk ratio.

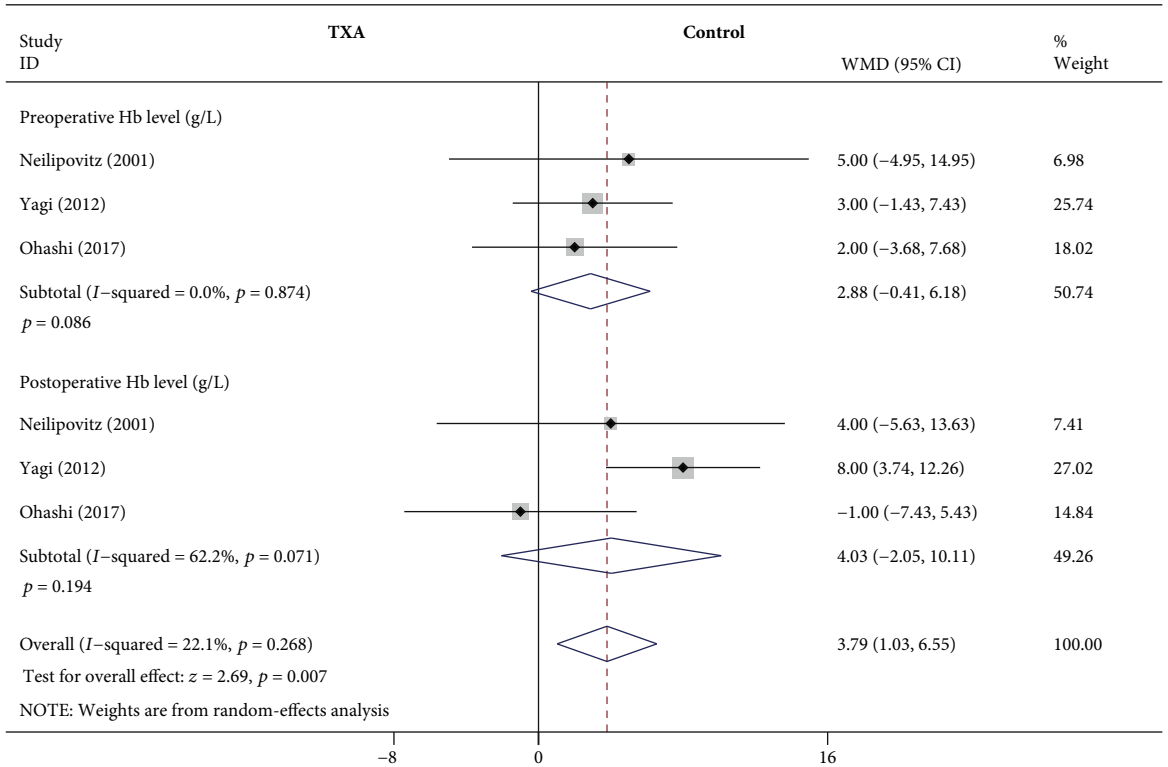

Figure 7: Forest plot showing the effect of low-dose IV TXA on Hb level compared with the control group during adolescent spinal deformity surgery. Hb: hemoglobin.

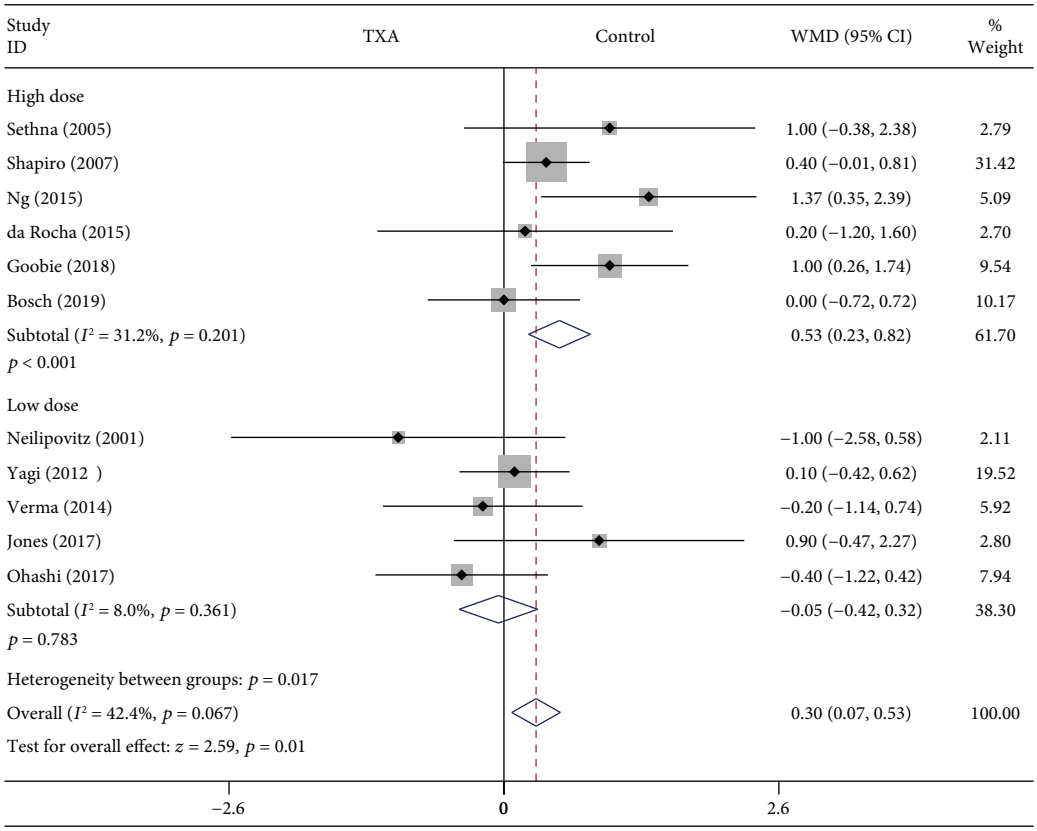

Figure 8: Forest plot showing the effect of high-dose IV TXA regimen compared with low-dose IV TXA regimen on the number of vertebral segments fused during adolescent spinal deformity surgery.

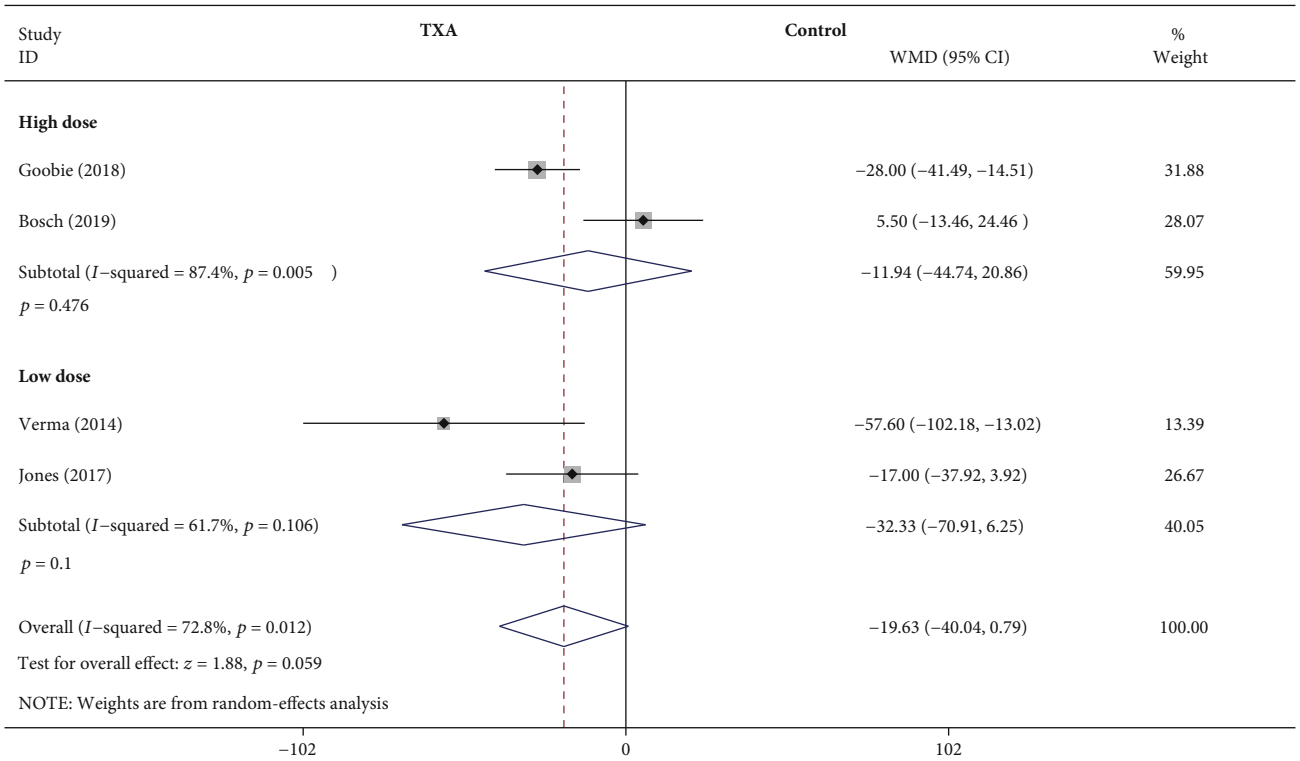

Figure 9: Forest plot showing the effect of high-dose IV TXA regimen compared with low-dose IV TXA regimen on estimated blood loss per fusion level during adolescent spinal deformity surgery.

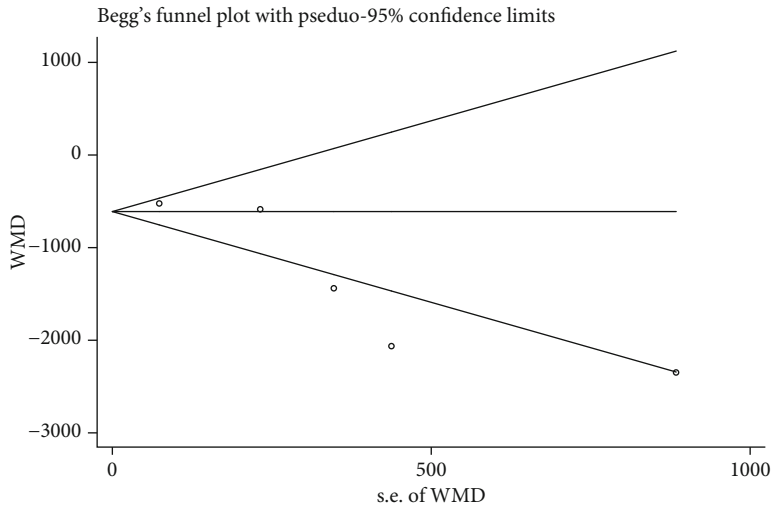

(a)

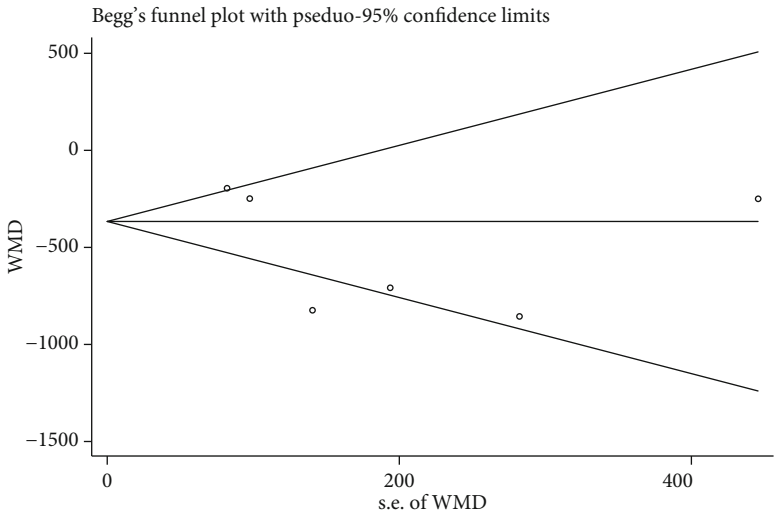

(b)

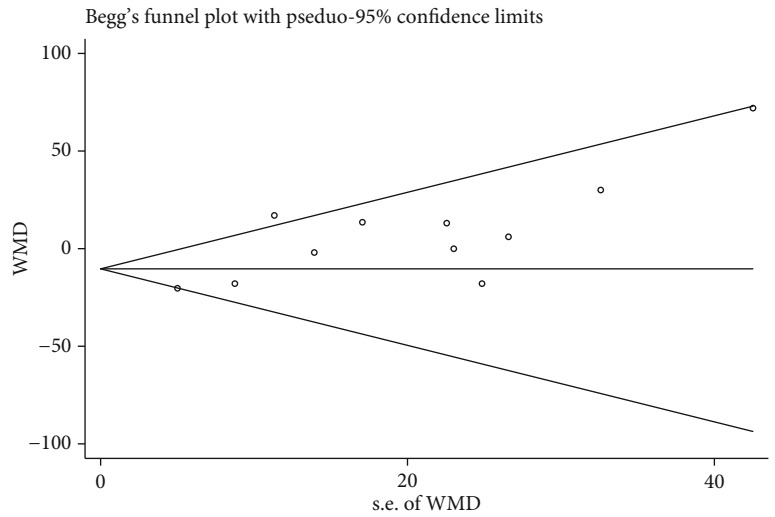

(c)

Figure 10: Continued.

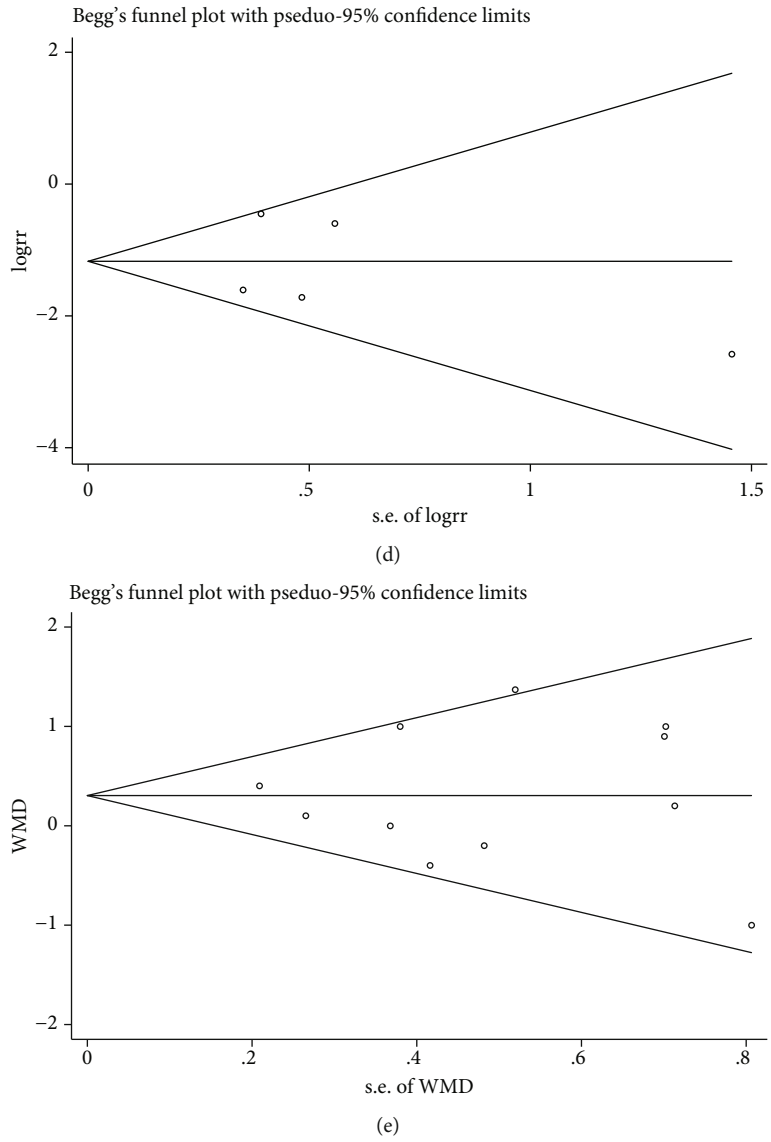

Figure 10: Begg's test for publication bias: (a) TBL, (b) IBL, (c) operative time, (d) blood transfusion rate, and (e) number of vertebral segments fused.

4. Discussion

This meta-analysis is ultimately a step to popularize the general application of TXA in spinal deformity surgery to reduce adolescent scoliosis. The results of the pooled analysis showed that the significant effect of reducing perioperative blood loss and blood transfusion rate might make TXA the drug of choice. TXA, as an antifibrinolytic drug, is currently mainly used in orthopedic, cardiac, and spine surgery to treat or prevent excessive perioperative blood loss [6]. TXA was administered through a variety of routes, including IV, topical, and oral. IV TXA is usually given intravenously at a certain loading dose before incision and a certain maintenance dose until the skin closure [1–5, 7–23]. Due to the difference in the loading dose and maintenance dose, the clinical effect of TXA may be significantly different. Raman et al. [24] demonstrated that high-dose TXA (loading dose: 30-50 mg/kg, maintenance dose: 1-5 mg/kg/h) was more effective than low-dose TXA (loading dose: 10-20 mg/kg, maintenance dose: 1-2 mg/kg/h) in reducing blood loss and blood transfusion requirement in adult spinal deformity surgery. Grant et al. [29] demonstrated that the use of high-dose TXA (loading dose: 20 mg/kg, maintenance dose: 10 mg/kg/h) resulted in a 50% reduction in transfusion requirements for AIS. Johnson et al. [30] demonstrated that high-dose TXA (loading dose: 50 mg/kg, maintenance dose: 5 mg/kg/h) was more effective than low-dose TXA (loading dose: 10 mg/kg, maintenance dose: 1 mg/kg/h) in reducing blood loss and transfusion requirements in spinal deformity surgery. Based on the above research results, we can see that different dosage regimens of IV TXA may produce significantly different clinical results. Therefore, the optimal dosage regimens of TXA are still a clinical problem to be solved by more high-quality RCTs in the future.

The dosage regimen of TXA should be considered when weighing risks and benefits. At present, the commonly used

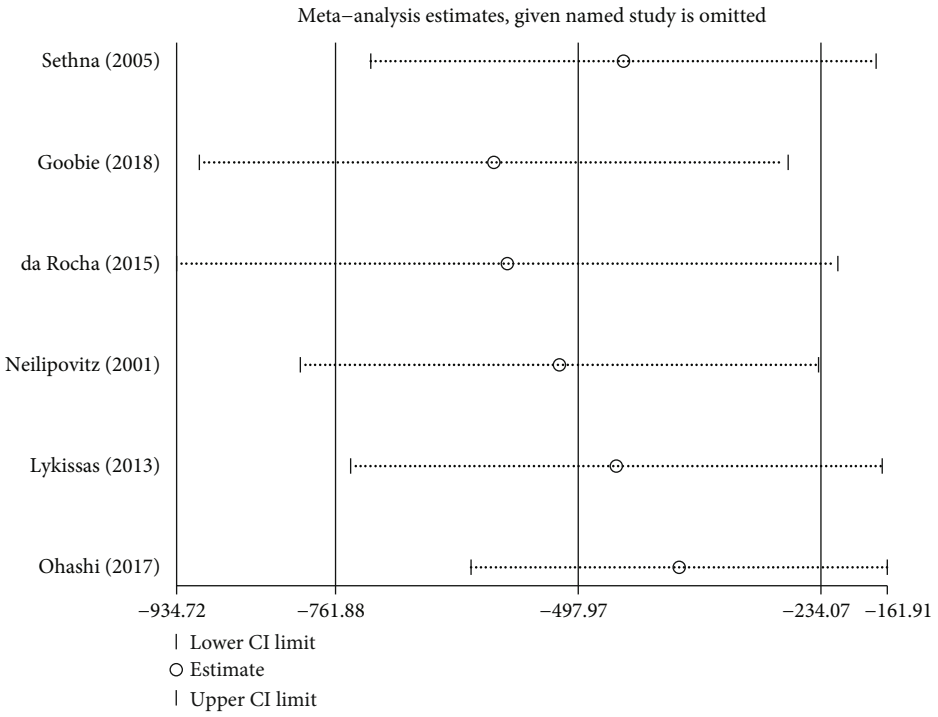

(a)

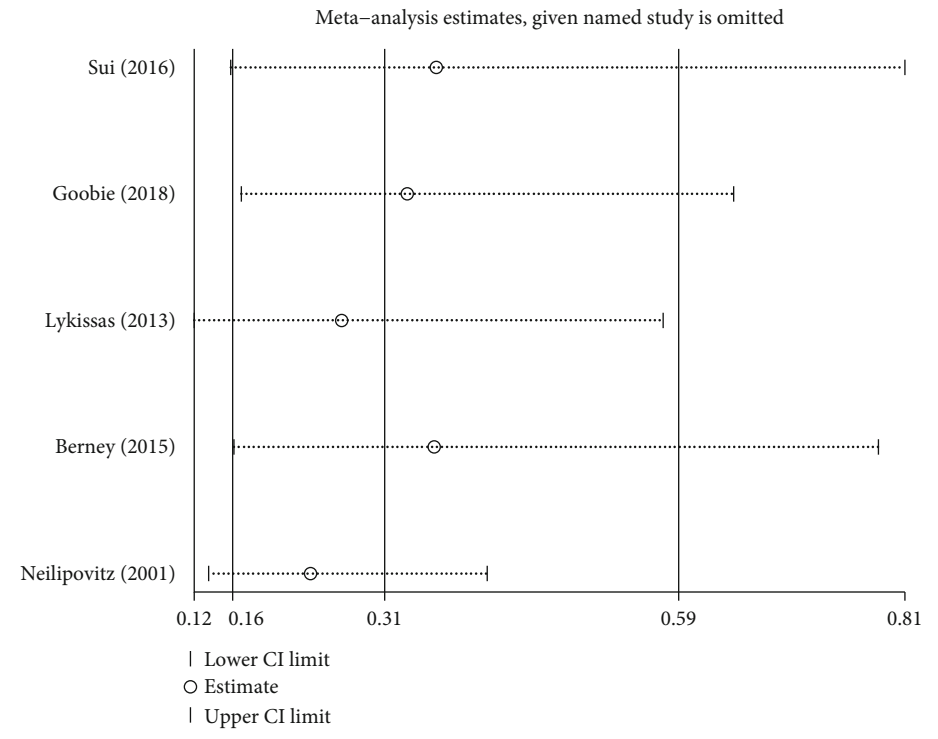

(b)

Figure 11: Continued.

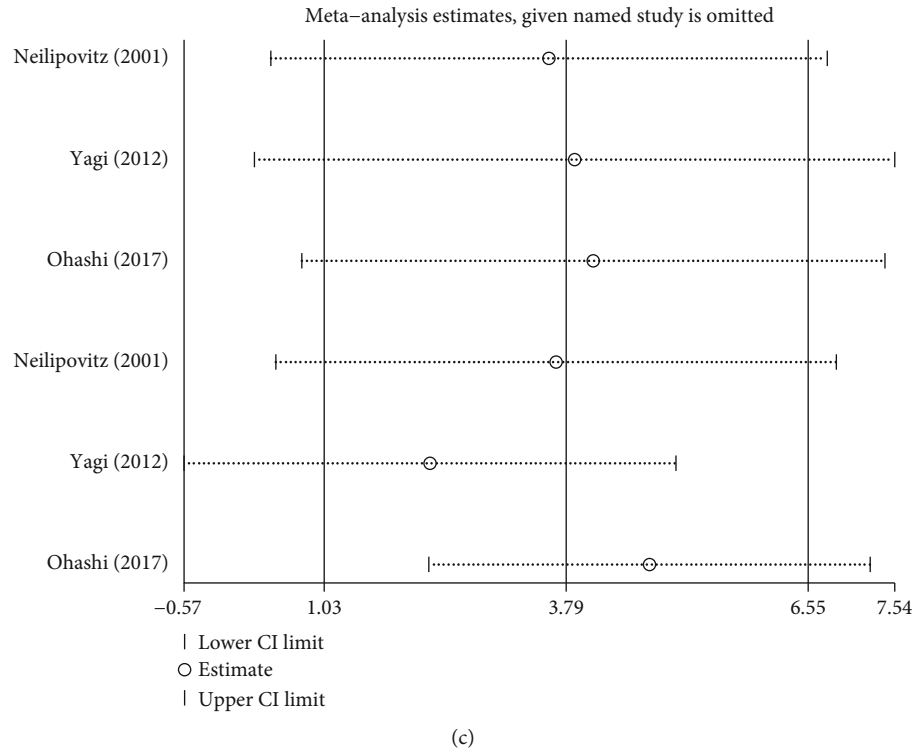

(c)

Figure 11: Sensitivity analysis for confirmation of the stability of the pooled result: (a) IBL, (b) blood transfusion rate, and (c) preoperative and postoperative Hb levels.

low-dose regimen is the loading dose of 10 mg/kg and the maintenance dose of 1 mg/kg/h [7, 13, 18, 21]. For example, Neilipovitz et al. [7] demonstrated that the administration of low-dose TXA in patients with AIS undergoing posterior spinal fusion surgery had the potential to reduce perioperative blood transfusion requirements. In a study published in 2018 with the same dosage regimen, the same conclusion was found [31]. These studies reported not only the benefits of low-dose TXA but also the risks. Choi et al. [2] found that there were 2 cases of DVT/PE and 2 cases of allergic reaction in the TXA group, but not in the control group. Peters et al. [1] found that there was one case of PE in the TXA group, but not in the control group. On the contrary, the commonly used high-dose regimen is the loading dose of 100 mg/kg and the maintenance dose of 10 mg/kg/h [8, 9, 15–17, 19]. For example, Sethna et al. [8] demonstrated that intraoperative administration of high-dose TXA significantly reduced blood loss during spinal deformity surgery in AIS. The same result has been confirmed in the research in recent years [16–18]. These studies reported not only the benefits of high-dose TXA but also the risks. Kaabachi et al. [32] found that there were 11 cases of vomiting in the TXA group, but not in the control group. Based on the few studies above, it is speculated that low-dose TXA may have more complications than high-dose TXA. However, such speculative results are not rigorous, so more research is still needed in the future to compare the complications of TXA with different dosage regimens.

The application of TXA has rich experience in orthopedic surgery in our hospital. For example, Yue et al. [33] found that TXA effectively reduced the blood loss of unicompartmental knee arthroplasty in patients with anemia, reducing the rate of blood transfusion, without increasing the risk of DVT. Zhu et al. [34] found that the use of TXA in total hip arthroplasty can reduce the blood transfusion rate and reduce TBL and IBL, without increasing the risk of thrombosis. Our surgery team also adopted a low-dose regimen (loading dose: 10 mg/kg; maintenance dose: 1 mg/kg/h) in spinal deformity surgery. Preliminary trials found that TXA effectively reduced the blood transfusion rate and TBL without increasing the risk of thrombosis. However, the optimal dosage regimens of IV TXA in spinal deformity surgery are still controversial. The relationship between the TXA dose and blood loss control is unclear. Therefore, more high-quality RCTs are still needed in the future to explore the optimal dosage regimens of TXA, not only in adolescent spinal deformity surgery but also for different surgical methods.

4.1. Limitations. Because of the quantity and quality of the included studies, this meta-analysis has some limitations. Firstly, the number of included RCTs is quite limited, and many studies have incomplete data and relatively low quality. Secondly, the start and end times of the loading and maintenance doses of TXA in different studies are not the same. Thirdly, the loading dose and maintenance dose of TXA in the same dosage regimen are not completely consistent. Fourthly, surgical methods, disease diagnosis, and transfusion criteria of the same dosage regimen are not completely consistent. Finally, the number of non-RCTs is relatively large, and the heterogeneity of some results is relatively high.

5. Conclusion

This meta-analysis compares the effects of TXA with different dosage regimens in adolescent spinal deformity surgery. The results of the above analysis indicated that high-dose and low-dose IV TXA were effective in reducing TBL, IBL, and blood transfusion rates without increasing complications in adolescent patients undergoing spinal deformity surgery. Low-dose IV TXA was effective in reducing the operative time. Both the high-dose and low-dose groups had similar preoperative and postoperative Hb levels compared to the control group. Due to the limited number and quality of studies related to some outcome measurements, more high-quality RCTs are still needed in the future to supplement existing conclusions.

Data Availability

The data supporting this meta-analysis is from previously reported studies and datasets, which have been cited.

Conflicts of Interest

The authors declare that there are no conflicts of interest regarding the publication of this article.

Authors' Contributions

Zhencheng Xiong and Kexin Wu are joint first authors.

Acknowledgments

This work was supported by the Beijing Municipal Science & Technology Commission (Grant number: Z181100001818006).

References

[1] A. Peters, K. Verma, K. Slobodyanyuk et al., "Antifibrinolytics reduce blood loss in adult spinal deformity surgery: a prospective, randomized controlled trial," *Spine*, vol. 40, no. 8, pp. E443–E449, 2015.

[2] H. Y. Choi, S.-J. Hyun, K.-J. Kim, T.-A. Jahng, and H.-J. Kim, "Effectiveness and safety of tranexamic acid in spinal deformity surgery," *Journal of Korean Neurosurgical Society*, vol. 60, no. 1, pp. 75–81, 2017.

[3] M. J. Colomina, M. Koo, M. Basora, J. Pizones, L. Mora, and J. Bagó, "Intraoperative tranexamic acid use in major spine surgery in adults: a multicentre, randomized, placebo-controlled trial†," *British Journal of Anaesthesia*, vol. 118, no. 3, pp. 380–390, 2017.

[4] P. Bosch, T. S. Kenkre, D. Soliman, J. A. Londino, and N. E. Novak, "Comparison of the coagulation profile of adolescent idiopathic scoliosis patients undergoing posterior spinal fusion with and without tranexamic acid," *Spine Deformity*, vol. 7, no. 6, pp. 910–916, 2019.

[5] S. M. Goobie, D. Zurakowski, M. P. Glotzbecker et al., "Tranexamic acid is efficacious at decreasing the rate of blood loss in adolescent scoliosis surgery: a randomized placebo-controlled trial," *The Journal of Bone and Joint Surgery American*, vol. 100, no. 23, pp. 2024–2032, 2018.

[6] Z. C. Xiong, J. Liu, P. Yi, H. Wang, and M. Tan, "Comparison of intravenous versus topical tranexamic acid in nondeformity spine surgery: a meta-analysis," *BioMed Research International*, vol. 2020, Article ID 7403034, 12 pages, 2020.

[7] D. T. Neilipovitz, K. Murto, L. Hall, N. J. Barrowman, and W. M. Splinter, "A randomized trial of tranexamic acid to reduce blood transfusion for scoliosis surgery," *Anesthesia and Analgesia*, vol. 93, no. 1, pp. 82–87, 2001.

[8] N. F. Sethna, D. Zurakowski, R. M. Brustowicz, J. Bacsik, L. J. Sullivan, and F. Shapiro, "Tranexamic acid reduces intraoperative blood loss in pediatric patients undergoing scoliosis surgery," *Anesthesiology*, vol. 102, no. 4, pp. 727–732, 2005.

[9] F. Shapiro, D. Zurakowski, and N. F. Sethna, "Tranexamic acid diminishes intraoperative blood loss and transfusion in spinal fusions for duchenne muscular dystrophy scoliosis," *Spine*, vol. 32, no. 20, pp. 2278–2283, 2007.

[10] C. Xu, A. Wu, and Y. Yue, "Which is more effective in adolescent idiopathic scoliosis surgery: batroxobin, tranexamic acid or a combination?," *Archives of Orthopaedic and Trauma Surgery*, vol. 132, no. 1, pp. 25–31, 2012.

[11] M. Yagi, J. Hasegawa, N. Nagoshi et al., "Does the intraoperative tranexamic acid decrease operative blood loss during posterior spinal fusion for treatment of adolescent idiopathic scoliosis?," *Spine*, vol. 37, no. 21, pp. E1336–E1342, 2012.

[12] M. G. Lykissas, A. H. Crawford, G. Chan, L. A. Aronson, and M. J. Al-Sayyad, "The effect of tranexamic acid in blood loss and transfusion volume in adolescent idiopathic scoliosis surgery: a single-surgeon experience," *Journal of Children's Orthopaedics*, vol. 7, no. 3, pp. 245–249, 2013.

[13] K. Verma, T. Errico, C. Diefenbach et al., "The relative efficacy of antifibrinolytics in adolescent idiopathic scoliosis," *The Journal of Bone and Joint Surgery American Volume*, vol. 96, no. 10, article e80, 2014.

[14] M. J. Berney, P. H. Dawson, M. Phillips, D. F. Lui, and P. Connolly, "Eliminating the use of allogeneic blood products in adolescent idiopathic scoliosis surgery," *European Journal of Orthopaedic Surgery & Traumatology: Orthopedie Traumatologie*, vol. 25, Suppl 1, pp. 219–223, 2015.

[15] V. M. da Rocha, A. G. C. de Barros, C. D. Naves et al., "Use of tranexamic acid for controlling bleeding in thoracolumbar scoliosis surgery with posterior instrumentation," *Revista Brasileira de Ortopedia*, vol. 50, no. 2, pp. 226–231, 2015.

[16] J. Xie, L. G. Lenke, T. Li et al., "Preliminary investigation of high-dose tranexamic acid for controlling intraoperative blood loss in patients undergoing spine correction surgery," *The Spine Journal*, vol. 15, no. 4, pp. 647–654, 2015.

[17] B. K. W. Ng, W. W. Chau, A. L. H. Hung, A. C. N. Hui, T. P. Lam, and J. C. Y. Cheng, "Use of tranexamic acid (TXA) on reducing blood loss during scoliosis surgery in Chinese adolescents," *Scoliosis*, vol. 10, no. 1, 2015.

[18] W. Y. Sui, F. Ye, and J. L. Yang, "Efficacy of tranexamic acid in reducing allogeneic blood products in adolescent idiopathic scoliosis surgery," *BMC Musculoskeletal Disorders*, vol. 17, no. 1, 2016.

[19] K. E. Jones, E. K. Butler, T. Barrack et al., "Tranexamic acid reduced the percent of total blood volume lost during adolescent idiopathic scoliosis surgery," *International Journal of Spine Surgery*, vol. 11, no. 4, p. 27, 2017.

[20] N. Ohashi, M. Ohashi, N. Endo, and T. Kohno, "Administration of tranexamic acid to patients undergoing surgery for adolescent idiopathic scoliosis evokes pain and increases the

infusion rate of remifentanil during the surgery," *PLoS One*, vol. 12, no. 3, article e0173622, 2017.

[21] A. N. Saleh and R. H. Mostafa, "Increased nociception following administration of different doses of tranexamic acid in adolescent idiopathic scoliosis surgery," *The Open Anesthesia Journal*, vol. 12, no. 1, pp. 61–68, 2018.

[22] T. Alajmi, H. Saeed, K. Alfaryan, A. Alakeel, and T. Alfaryan, "Efficacy of tranexamic acid in reducing blood loss and blood transfusion in idiopathic scoliosis: a systematic review and meta-analysis," *Journal of Spine Surgery*, vol. 3, no. 4, pp. 531–540, 2017.

[23] Y. Zhang, H. Liu, F. He, A. Chen, H. Yang, and B. Pi, "Does tranexamic acid improve bleeding, transfusion, and hemoglobin level in patients undergoing multilevel spine surgery? A systematic review and meta-analysis," *World Neurosurgery*, vol. 127, pp. 289–301, 2019.

[24] T. Raman, C. Varlotta, D. Vasquez-Montes, A. J. Buckland, and T. J. Errico, "The use of tranexamic acid in adult spinal deformity: is there an optimal dosing strategy?," *The Spine Journaly*, vol. 19, no. 10, pp. 1690–1697, 2019.

[25] D. Moher, A. Liberati, J. Tetzlaff, D. G. Altman, and for the PRISMA Group, "Preferred reporting items for systematic reviews and meta-analyses: the PRISMA statement," *BMJ*, vol. 339, no. jul21 1, article b2535, 2009.

[26] J. P. T. Higgins, D. G. Altman, P. C. Gotzsche et al., "The Cochrane Collaboration's tool for assessing risk of bias in randomised trials," *BMJ*, vol. 343, no. oct18 2, article d5928, 2011.

[27] J. Zhong, K. Cao, B. Wang, X. Zhou, N. Lin, and L. Huading, "The perioperative efficacy and safety of tranexamic acid in adolescent idiopathic scoliosis," *World Neurosurgery*, vol. 129, pp. e726–e732, 2019.

[28] J. P. T. Higgins, S. G. Thompson, and J. J. Deeks, "Measuring inconsistency in meta-analyses," *BMJ*, vol. 327, no. 7414, pp. 557–560, 2003.

[29] J. A. Grant, J. Howard, J. Luntley, J. Harder, S. Aleissa, and D. Parsons, "Perioperative blood transfusion requirements in pediatric scoliosis surgery: the efficacy of tranexamic acid," *Journal of Pediatric Orthopedics*, vol. 29, no. 3, pp. 300–304, 2009.

[30] D. J. Johnson, C. C. Johnson, S. M. Goobie et al., "High-dose versus low-dose tranexamic acid to reduce transfusion requirements in pediatric scoliosis surgery," *Journal of Pediatric Orthopedics*, vol. 37, no. 8, pp. e552–e557, 2017.

[31] L. M. Carabini, N. C. Moreland, R. J. Vealey et al., "A randomized controlled trial of low-dose tranexamic acid versus placebo to reduce red blood cell transfusion during complex multilevel spine fusion surgery," *World Neurosurgery*, vol. 110, pp. e572–e579, 2018.

[32] O. Kaabachi, W. Koubaa, D. Chafii, and R. Ouezzini, "Tranexamic acid reduces blood transfusion requirements in scoliosis surgery," *European Journal of Anaesthesiology*, vol. 24, Supplement 39, p. 67, 2007.

[33] J. A. Yue, Q. D. Zhang, and X. Z. Guo, "Tranexamic acid used in unicompartmental knee arthroplasty for patients with anemia," *Orthopedic Journal of China*, vol. 28, pp. 1345–1349, 2020.

[34] Q. Z. Zhu, C. X. Yu, X. Z. Chen, and P. Lin, "Tranexamic acid reduces blood loss in hip arthroplasty for senile femoral neck fracture," *Chinese Journal of Orthopaedic Trauma*, vol. 20, pp. 623–626, 2018.

Hindawi
BioMed Research International
Volume 2020, Article ID 8861347, 11 pages
https://doi.org/10.1155/2020/8861347

Research Article

Characterization of the Subchondral Bone and Pain Behavior Changes in a Novel Bipedal Standing Mouse Model of Facet Joint Osteoarthritis

Miao Li,[1,2] Wen-qing Xie,[3] Miao He,[3] Deng-jie Yu,[3] Da-qi Xu,[2,4] Wen-feng Xiao,[3,5] and Yong Cao[1,2,5]

[1]*Department of Spine Surgery and Orthopaedics, Xiangya Hospital, Central South University, 410008 Changsha, China*
[2]*Key Laboratory of Organ Injury, Aging and Regenerative Medicine of Hunan Province, 410008 Changsha, China*
[3]*Department of Orthopaedics, Xiangya Hospital, Central South University, 410008 Changsha, China*
[4]*Department of Sports Medicine, Xiangya Hospital, Central South University, 410008 Changsha, China*
[5]*National Clinical Research Center for Geriatric Disorders, Xiangya Hospital, Central South University, 410008 Changsha, China*

Correspondence should be addressed to Wen-feng Xiao; wenfeng_xiao@163.com and Yong Cao; caoyong1912@163.com

Received 8 September 2020; Revised 22 September 2020; Accepted 12 October 2020; Published 9 November 2020

Academic Editor: Shen Liu

Background. The subchondral bone parallels with the progression of osteoarthritis (OA). However, the biomechanical properties and histopathological changes of subchondral bone changes in the lumbar facet joint (LFJ) after long-term axial loading on the spine have not been explored. In this study, we aimed to investigate the subchondral bone histopathological changes that occur in the LFJ and pain behaviors in a novel bipedal standing mouse model. *Methods*. Sixteen 8-week-old male C57BL/6 mice were randomly assigned into bipedal standing and control groups. A finite element stimulate model based on the micro-CT data was generated to simulate the von Mises stress distribution on the LFJ during different positions. The spine pain behaviors tests were analysis. In addition, the change in the subchondral bone of the LFJ was assessed by histological and immunohistochemistry staining. *Results*. The computerized simulation of the von Mises stress distribution in the superior articular process of LFJ at the spine level 5 in the lying position increased and reached a maximum value at the bipedal standing posture. The spine pain behavior test revealed that the threshold of pressure tolerance decreased significantly in bipedal groups relative to control groups, whereas the mechanical hyperalgesia of the hind paw increased significantly in bipedal groups relative to control groups. The axial load accelerates LFJ degeneration with increased histological scores in bipedal groups. The expression of type II collagen and aggrecan (ACAN) was significantly decreased in the bipedal groups compared with the control groups, whereas the expression of MMP13 was increased. Compared with the control groups, the osteoclast activity was activated with higher TRAP-positive staining and associated with increased CD-31-positive vessels and GCRP-positive nerve ending expression in the subchondral bone of LFJ. *Conclusion*. Collectively, long-term axial loading induces the development of spine hyperalgesia in mice associate with increased osteoclast activity and aberrant angiogenesis and nerve invasion into the subchondral bone of LFJ that stimulates the natural pathological change in human LFJ OA. These results indicate that aberrant bone remodeling associate with aberrant nerve innervation in the subchondral bone has a potential as a therapeutic target in LFJ OA pain.

1. Background

Lumbar facet joint (LFJ) osteoarthritis (OA) is implicated as an important cause of low back pain, which in turn places an enormous burden on the social health-care system [1, 2]. The facet joint has a similar characteristic as those of other synovial joints, such as the knee, and plays an important role in load transmission of the spine. However, the facet joint OA has to date received far less critical investigation than knee OA [1]. The fact that pain originating from the LFJ is a common cause

of low back pain, and that the prevalence of LFJ OA pain has been estimated to range from 7 to 75% among the elderly population reporting low back pain [1, 3–5].

The LFJ is a true synovial joint composed of the articular cartilage covering the surfaces of each of facts, a thickened layer of subchondral bone, a synovium, and an articular capsule [1, 6]. The LFJ OA is viewed as an organ disease that affects the entire facet joints and is characterized pathologically by focal loss of the articular cartilage associated with subchondral bone change, varying degrees of osteophyte formation and synovitis [1, 7, 8].

Pain from the LFJ probably derives from multiple tissues of the facet joint [9]. A recent study revealed that their capsule tissue is well innervated by the free nerve during degeneration [1, 10]. The mechanoreceptors and upregulated inflammatory cytokines have also been identified in the facet joint capsular tissue in degenerative disc disease that could be the source of pain [9]. Recently, increasing evidence suggests that the contribution of the subchondral bone to the physiopathology of OA is of great interest.

The subchondral bone is a shock absorber in weight-bearing joints and plays a crucial role in the initiation and progression of OA [11]. It is now recognized that the subchondral bone is responsible for peripheral neuronal sensitization and can result in normal activities, causing pain. In OA conditions, inflammation and sensory nerve growth have been noted to coexist in the subchondral bone, indicating that it could be an important source of pain in OA [9]. As subchondral bone abnormalities appear in OA, this may be the target that leads to novel approaches for the development of OA pain treatment.

Biomechanical testing of isolated spinal segments has demonstrated that up to 33% of the total axial load of the spine segment can be borne by facet joints [12, 13]. Excessive mechanical loading can contribute to the initiation of spine degeneration [12, 14]. A previous investigation also found great variation in intradiscal pressure (IDP) when the sheep were standing from the lying position and 5- to 6-fold greater than the IDP recorded in the lying position [15, 16]. It is highly needed for the development of an animal model of noninvasive cumulative axial loading on the spine by making the animal maintain an upright posture to mimic the processes of degeneration in humans. Ao and Wang constructed a novel bipedal standing mouse model by placing them in limited water to induce the bipedal posture for a long period of time that can simulate the pathogenesis of spinal degeneration caused by increased axial load stress [17].

This model successfully reproduced LFJ degeneration; however, the 3D microstructure and histopathology of the subchondral bone change in osteoarthritic facet joints have not been extensively explored. In this study, we aimed to investigate the subchondral bone microstructure and histopathological features that occur in facet joints, and the pain behaviors change obtained from a bipedal standing mouse model.

2. Methods

2.1. Experimental Animals. All animal procedures in this study were conducted with the approval of the Animal Ethics Committee of the Xiangya hospital of Central South University (protocol number: 2019N0106). Sixteen C57BL/6 mice (8 weeks old) were purchased from the Animal Center of Central South University (Changsha, China) and randomly divided into two groups of eight mice each, the normal control and experimental groups. In the experimental groups, the mice were placed in a beaker containing limited water to induce the bipedal standing posture according to a previously described protocol. The mice in the control group were placed in the same chamber without the added water. These mice in the two groups underwent two different interventions for a total of 6 hours each day and were free to access food and water. Six months after the intervention, all mice were anesthetized with an intraperitoneal injection of 5% ketamine hydrochloride plus 0.5% diazepam following the standard protocol. All lumbar spines were harvested and fixed in 10% buffered formalin for micro-CT scanning, finite element analysis, and histopathological analysis. At the schedule timepoint, the mice was placed in a chamber with a prolonged exposure (more than ten minutes) in the CO_2 monitoring continuously until the mice are no longer moving.

2.2. Micro-CT Analysis of the LFJ Subchondral Bone. The fixed lumbar spines from L1 to L5 were captured by a micro-CT scanner (Skyscan 1076, Skyscan, Antwerp, Belgium) with an isotropic voxel size of 6 μm. The X-ray tube voltage was 80 kV, and the current was 100 μA with a 0.5 mm aluminum filter. NRecon and CTVol software was used for transverse 2D cross-sectional reconstructions and 3D image visualization. For the quantitative analysis of the subchondral bone, the parameters including bone volume fraction, which describes the ratio of bone volume over tissue volume (BV/TV, %), three-dimensional trabecular bone thickness (TbTh), the ratio of the bone surface area to bone volume (BS/BV), the trabecular bone number (TB. N, mm), and the trabecular bone space (Tb. Sp, mm) were calculated.

2.3. Computerized Stimulation of the LFJ Stress Distribution. A finite element model of the mouse lumbar spine was developed as previously described with some modifications [18]. Micro-CT tomography images were acquired from the scanning mice. Simpleware (Simpleware, Ltd., Exeter, UK) was used for preprocessing and model reconstruction, and ABAQUS (6.10; Simulia Inc, Providence, Rhode Island, USA) was used for simulation. We developed a 3-dimensional, nonlinear FE model of the lumbar spine that consisted of an L4-5 LFJ using the finite element software Ansys version 1. In this study, facet joints were modeled using a frictionless surface-to-surface contact between zygopophysis with an average gap of 0.2 mm. The facet joint is subjected to the lying and standing position. Loading act on the facet joint must consider that the spine must support the whole-body weight at standing positions. Static analysis is conducted to measure the von Mises stress on the facet joint.

2.4. Histological and Pathological Assessment. The L4-5 LFJ was harvested and decalcified in 10% EDTA (pH 7.4) and embedded in paraffin. A 4-μm-thick crossoriented section

of the superior articular process of L5 was stained with safranin O and fast green (Sigma) to observe the morphology. A histological scoring system was used to characterize the features of the facet joints as previously described. Osteoclast activity was detected by tartrate-resistant acid phosphatase (TRAP) staining according to the standard protocol (Sigma-Aldrich). For immunohistology, slides were first incubated with antigen retrieval buffer (Abcam) and blocking buffer. Then, sections were incubated with anti-MMP13 (1 : 200, Abcam, Cambridge, MA), anti-type II collagen (1 : 200, Abcam, Cambridge, MA), anti-ACAN(1 : 200, Abcam, Cambridge, MA), anti-CD31 (1 : 200, Abcam, Cambridge, MA), and anti-CGRP (1 : 200, Abcam, Cambridge, MA) primary antibodies. For immunofluorescence, the sections were counterstained with 4′,6-diamidino-2-phenylindole (DAPI; Sigma). For immunohistochemistry, a horseradish peroxidase–streptavidin detection system (Dako, Agilent Technologies) was used to detect immunoactivity, followed by counterstaining with ethyl green (Sigma-Aldrich). Or the sections were then counterstained with hematoxylin (Dako). All the sections were observed under the microscope (Zeiss) and scored in a blinded fashion. Five fields of the whole subchondral bone area per specimen per mouse in each group were randomly selected for quantitative histomorphometry analysis.

2.5. Spine Pain Behavioral Assessment. Behavioral testing was performed between two groups before the mice were anesthetized for spine harvested. Vocalization thresholds in response to the force of an applied force gauge (SMALGO algometer; Bioseb) were measured to reflect the spine pain behaviors. Briefly, a sensor tip was directly pressed on the dorsal skin of the mice at the L4–L5 position. The pressure force was increased gradually at a constant speed (50 g/s) until an audible vocalization was heard. The curve of the pressure force was recorded by using BIO-CIS software (Bioseb). Two tests were performed by an observer who was blind to the study design, and the mean value was calculated as the nociceptive threshold. The hind paw withdrawal frequency of mice responding to a mechanical stimulus was determined using von Frey filaments (Stoelting, Wood Dale, IL). Mice were placed individually in acrylic cages with a mesh floor. Von Frey filaments were applied to the mid-plantar surface of the hind paw with enough pressure to buckle the filaments. If the mice withdraw, or shake the paw, it is considered to have had a positive response. Von Frey filament was used to apply physical stimulation at 1 s interval for ten times when the mouse hind paw contacts with the mesh. The force is increased manually until paw withdrawal occurs. At the meantime, the force was record. Mechanical withdrawal frequency was calculated as the percentage of withdrawal times in response to ten stimulations.

2.6. Statistical Analysis. All grouped data are presented as the means ± standard deviations (SD) and analyzed by using SPSS, version 15.0, software (IBM Corp.). Two-tailed unpaired Student's t test was used to compare between two groups. The rest of the data were analyzed using either one-way or two-way ANOVA, with post hoc Tukey's multiple comparisons. A p value of ≤ 0.05 was considered significant.

3. Results

3.1. Von Mises Stress Property of Superior Articular Processes (SAPs) in the LFJ during Different Positions. The mice were placed in a beaker containing limited water to induce the bipedal standing posture (Figure 1(a)). The L5 SAPs have been selected for our region of research interest (ROI) (Figure 1(b)). An established finite element model of the human LFJ was used to stimulate the stress distribution in the superior articular processes (SAPs) in different positions (Figures 1(b) and 1(c)). The simulation began from a lying position, and no contact between the two articular facets was scanned via micro-CT. Since the facet joint supports the physiologic motion of the spine, the articular surfaces remain in contact during the bipedal standing position. It was observed that the computerized simulation of the von Mises stress distribution increased steadily from approximately 0.01 ± 0.0014 MPa in the SAPs of the LFJ at level 5 in the lying position and reached a maximum value of 0.24 ± 0.0376 MPa at the bipedal standing posture (Figures 1(d) and 1(e)).

3.2. Development of Spinal Hypersensitivity in the Bipedal Standing Mice Model. After six months of bipedal standing, the vocalization threshold in response to force applied on the mice spine L4/L5 level was measured. The results demonstrated that pressure tolerance decreased significantly at six months in bipedal standing groups relative to mice than in control groups (Figure 2(a)). In parallel, the von Frey test showed that the paw withdraw frequency increases significantly at 6 months in bipedal standing groups (Figure 2(b)). These results of spinal pain behavior tests indicating that that long-term standing will lead mice to develop spine hyperalgesia.

3.3. Pathologic Change in the Cartilage in the LFJ after Long Bipedal Standing Induction. Cartilage is one of the key anatomical structures of LFJ, and joint degeneration always induces pathological changes in cartilage. As shown in Figure 3(a), the pathologic changes of the degenerated LFJ are clearly presented in the long period of time-bipedal standing mice. Staining with Saf-o revealed reduced cartilage layer thickness, with proteoglycan matrix depletion and chondrocyte loss in the SAPs after 6 months of exercise in bipedal standing groups (Figure 3(a)). To quantify the severity of cartilage degeneration, we evaluated the Osteoarthritis Research Society International (OARSI) scores of the SAPs between the control and the bipedal standing groups. OARSI scores revealed a dramatic increase in OARSI scores in the bipedal group compared to the control group (Figure 3(b)). Moreover, the percentages of MMP13-positive chondrocytes were significantly increased, indicating that a long period of bipedal standing induces LFJ cartilage degradation. In contrast, Col II and ACAN expression indicating a protective marker was significantly reduced in the bipedal groups (Figures 3(a) and 3(b)). Our findings reveal that the novel

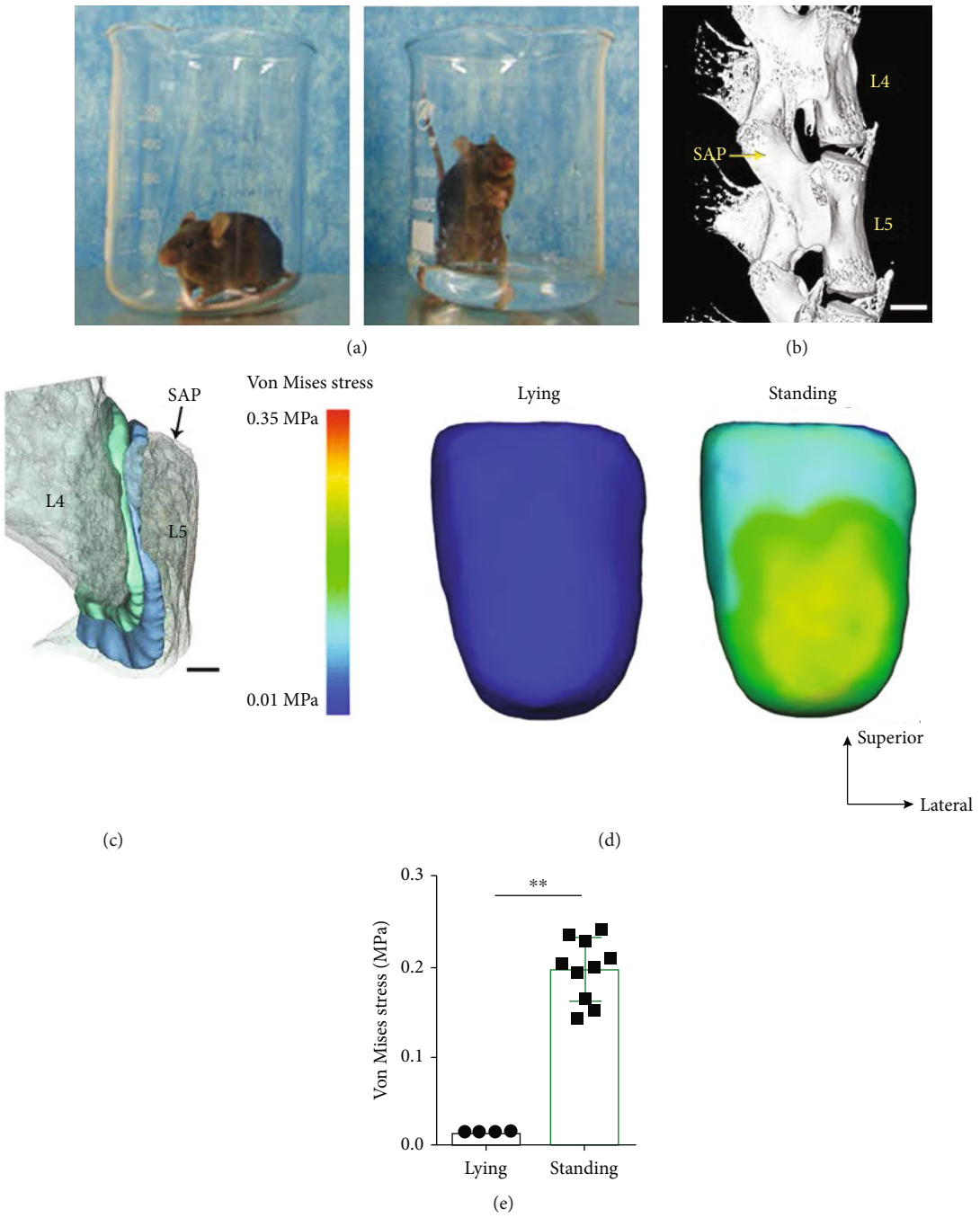

Figure 1: The bipedal standing mouse model and von Mises stress distribution on the surface of SAPs in LFJ.(a)The mice were placed in a beaker with or without limited water to induce the bipedal standing posture. (b) The 3D image of micro-CT scanning of the spine. (c)The finite element stimulation model of SAPs. (d) The von Mises stress distribution on the surface of SAPs during different positions and (e) quantitative analysis data. The data are presented as the mean ± SD. $^{**}p < 0.01$ for differences between the control group and the bipedal standing group. Scale bar = 200 μm.

bipedal standing mouse model caused the normal architecture of the cartilage to be lost, leading to the successful development of LFJ osteoarthritis and consistent with previous reports.

3.4. 3D Morphological Change in the Subchondral Bone in Bipedal Standing-Induced LFJ OA. Since less is known about the 3D morphological change in the subchondral bone in long-term bipedal standing-induced LFJ OA mice, we used micro-CT to visualize the microstructural changes in the subchondral bone of LFJ. As shown in Figure 4(a), the SAPs of L5 were selected; it demonstrated that the bipedal-induced LFJ OA led to collapse that was not limited to the cartilage, and the subchondral bone was also affected. The appearance of a localized cavity on the surface of the subchondral bone could be observed in the bipedal groups, whereas the surface in the

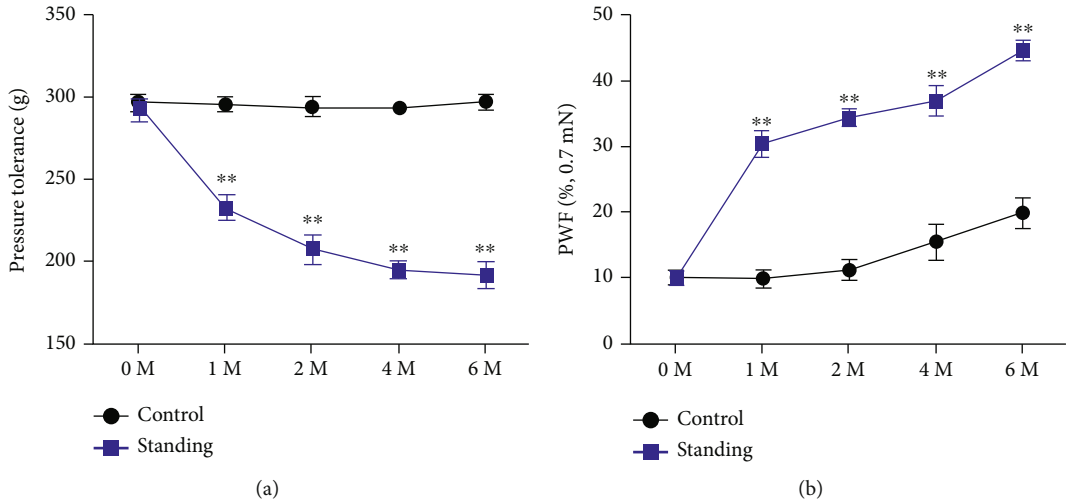

Figure 2: Symptomatic spinal pain behavior in the long-term bipedal standing mouse model. (a). Pressure hyperalgesia of the spine was measured as the force threshold to induce the vocalization by a force gauge. (b). The hind paw withdrawal frequency (PWF) responding to mechanical stimulation (von Frey, 0.7 mN). $^{**}p < 0.01$ for differences between the control group and the bipedal standing group at the corresponding time points.

control group was integrated (Figure 4(b)). Six months of long-term bipedal standing decreased the subchondral bone surface area in SAPs (bipedal standing groups 3.96 ± 0.034 mm^2 vs. control groups $2.02 \pm 0.063\ mm^2$). The subchondral bone BV/TV ratio in LJF OA mice dramatically decreased relative to the control groups (bipedal standing groups 41.46% vs. control groups 21.98%). The Tb. Th and Tb. N of the subchondral bone significantly decreased with abnormal morphology, whereas the ratio of the bone surface area to bone volume and Tb. Sp increased after two months of bipedal standing (Figure 4(c)). The results reveal that altered mechanical loading in LFJ leads to accelerated subchondral bone remodeling and induced subchondral bone resorption.

3.5. Aberrant Nerve Invasion in the Subchondral Bone in Bipedal Standing-Induced LFJ OA. Micro-CT data showed collapsed subchondral bone in the LFJ after long-term bipedal standing. We therefore explored the pathological changes with TRAP staining to visualize the osteoclast activity in the LFJ subchondral bone (Figure 5(a)). Trap staining revealed an increased number of osteoclasts (OC) in the LFJ OA mice (2 ± 1.2) compared to the control mice (8 ± 1.8) (Figure 5(b)). In addition, compared with the sham group, CD-31-positive vessels and GCRP-positive nerve endings increased significantly in LFJ OA mice (Figures 5(a) and 5(b)). However, the exact mechanism underlying the potential contributions of aberrant nerve invasion in the subchondral bone during LFJ osteoarthritis progression is largely unknown. Previous results demonstrate that long-term standing lead mice develop spine hyperalgesia. The spine pain maybe arises from the aberrant nerve invasion in the subchondral bone of LFJ.

4. Discussion

Lumbar spinal facet joint arthritis is considered clinically important sources of low back pain [19]. Animal models of LFJ OA are used extensively in research of its pathogenesis [20, 21]. Human beings are bipedal, and the loading acts on the lumbar spine were often assumed to be different from those in quadrupeds [22]. Thus, the biomechanical microenvironment of the lumbar spinal segments in humans is not the case in mice [17]. Therefore, as an essential step in the effort to explore the pathogenesis associated with facet joint degeneration, it is necessary to establish an animal model for properly representing human natural OA of LFJ.

Recently, research focusing on LFJ OA has been conducted using various animal models [2, 21]. In our current study, we reproduced a natural LFJ OA in a novel bipedal standing mouse model that was consistent with a previously described model [17]. Such an animal model is completely different from the chemically induced LF OA models, which creates a chemical injury to trigger LF OA and cannot stimulate the real pathological processes involved in human LFJ OA. Mechanical loading within a physiological range is necessary to maintain the spine in a healthy state [14, 23, 24]. LFJ is exposed to surprisingly large mechanical loads during standing movement. With lying or standing forces at the LFJ surface may vary from near zero to several times the whole-body weight within a period of 1 second [12, 25].

Although mechanotransduction can maintain tissue homeostasis in the joint, this process can also lead to tissue degeneration [26]. After increased long-term axial load stress on the LFJ in the bipedal standing mice, the aberrant mechanical loading act on the LFJ surface leads to cartilage degeneration, loss of extracellular matrix, and a decrease in proteoglycan, causing LFJ OA [17]. Subchondral bone changes in bone turnover, mineralization, and volume result in altered apparent are the typical hallmarks in the large knee joint OA development [27–30]. For the first time, to our knowledge, we characterized the histopathology feature change in the subchondral bone of LFJ OA after the long-term bipedal standing posture in mice. Micro-CT vividly demonstrated that the aberrant bone

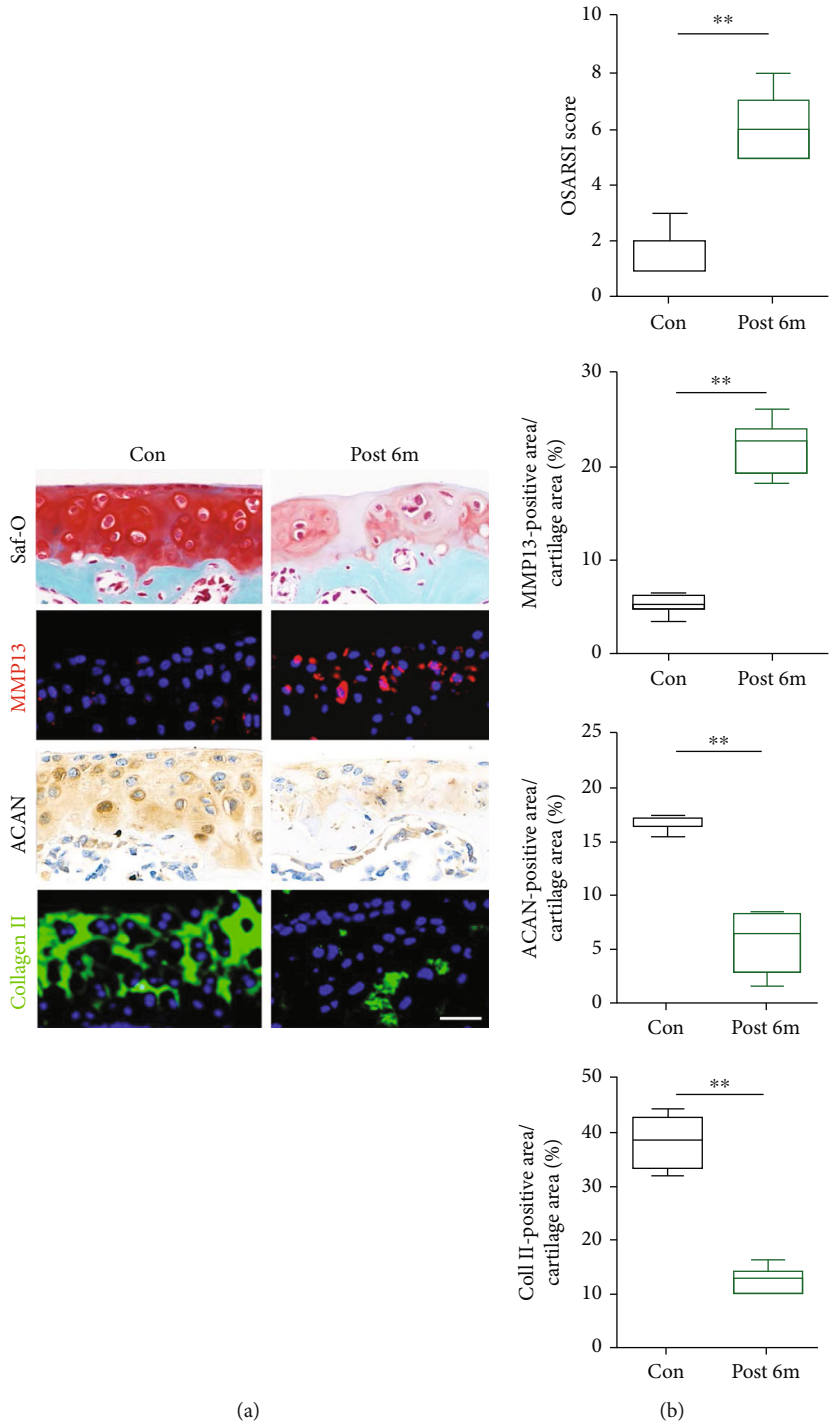

Figure 3: Axial loading acts on the spine to induce LFJ cartilage degradation. (a) Histological change in the LFJ with safranin O staining (upper). Changes in the expression of MMP13, ACAN (middle), and type II collagen (lower) in the LFJ cartilage with immunofluorescent and immunohistochemistry staining. (b) Quantitative analysis of LFJ cartilage degeneration in different groups and evaluation of MMP13-positive area, ACAN positive areas, and type II collagen-positive area in the LFJ cartilage. The data are presented as the mean ± SD. $^{**}p < 0.01$ for differences between the control group and the bipedal standing group. Scale bar = 40 μm.

remodeling occurs in the subchondral bone during LFJ progression. Specifically, elevated osteoclast activity was found in the subchondral bone of LFJ accompanied by increased new blood vessel growth and aberrant nerve invasion. These results indicate that the aberrant nerve and vessel growth in the subchondral bone, after long bipedal standing, could be an important origin of LFJ OA pain and laid the important pathogenetic basis for the development of low back pain caused by LFJ OA. The axis mechanical loading act on the LFJ could activate

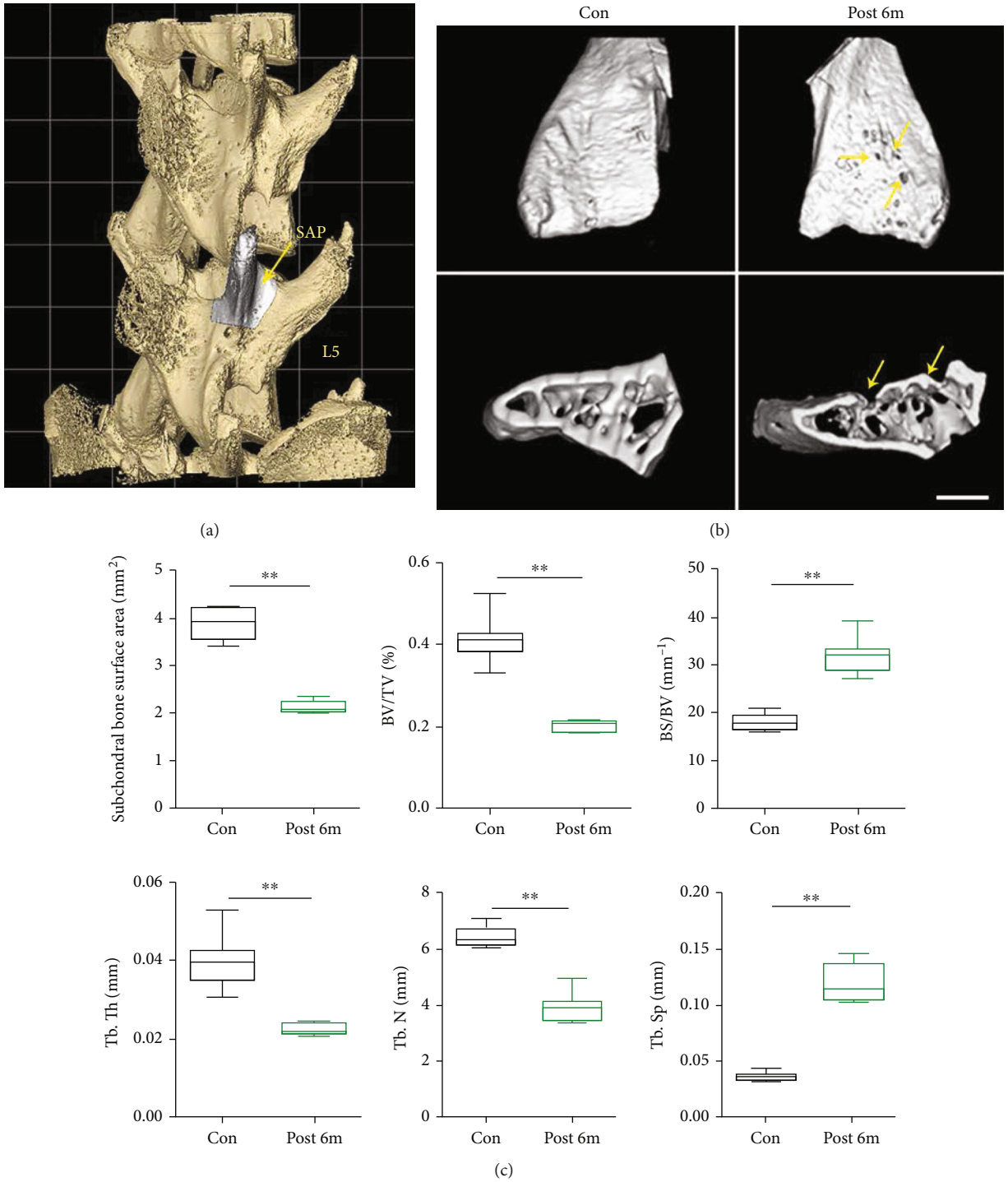

Figure 4: Axial loading led to the subchondral bone collapse. (a) The 3D image of SAP of lumbar 5. (b) 3D micro-CT image of the LFJ subchondral bone between control and bipedal standing mouse models. A series of subchondral bone cavities were visualized in a 6-month long bipedal standing mouse model. (c) Quantitative analysis of the morphological parameters of the subchondral bone change in different groups. The data are presented as the mean ± SD. $^{**}p < 0.01$ for differences between the control group and the bipedal standing group. Scale bar = 200 μm.

nerve endings and modulate the signals in the nervous system to initiate the development of OA pain.

In animal models, the inhibition of the subchondral bone remodeling with pharmacological agents has demonstrated efficacy in the treatment of OA [28, 31, 32]. Our findings also suggest that the subchondral bone could be a therapeutic target for the management of LFJ OA pain. The increased remodeling rate in the subchondral bone of LFJ OA may be initiated by the excessive axial loading on the surface of LFJ, leading to the activation of the osteoclast activity [28,

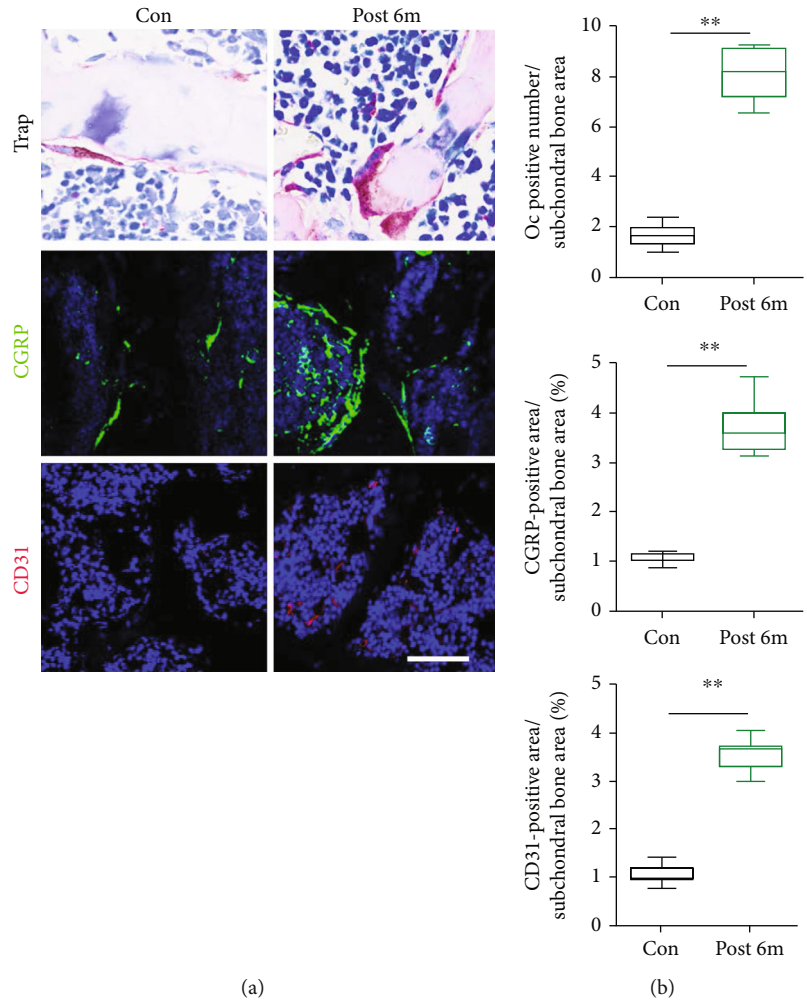

Figure 5: Mechanical loading accelerated subchondral bone resorption and aberrant vessel and nerve invade in the subchondral bone of LFJ. (a) Representative TRAP (upper), CGRP (middle), and CD-31- (lower-) positive blood vessel staining in LFJ were selected from different groups. (b) Quantitative analysis of osteoclast positive number, CGRP-positive areas, and CD31-positive areas in LFJ. The data are presented as the mean ± SD. $^{**}p < 0.01$ for differences between the control group and the bipedal standing group. Scale bar = 40 μm.

33]. However, whether the aberrant nerve invasion and angiogenesis in the subchondral bone of LFJ OA were induced by osteoclasts is still unclear. How the mechanical loading signals acted on LFJ are converted into chemical information and leading activation of downstream signaling cascades in osteoclasts has rarely been explored. Osteoclast lineage cells are essential for bone remodeling and play an important role in maintaining bone homeostasis [34].

Beyond resorption, studies reveal several unanticipated roles for osteoclasts, which could secrete multiple factors, such as cytokines (clastokines) and growth factors, in the regulation of the bone remodeling cycle in health and disease status [35, 36]. A study showed that preosteoclasts secrete platelet-derived growth factor-BB (PDGF-BB) to induce angiogenesis coupled with osteogenesis during the bone remodeling process [37]. OA progression promotes both nerve and vessel growth in the osteoarthritic subchondral bone in the knee joint, leading to OA pain [33].

Other mechanisms may also exist for the osteoclast activation mediating pain. In cancer-associated bone pain (CABP), osteoclasts create an acidic extracellular microenvironment by secreting protons, which activate acid-sensing nociceptors and contribute to bone pain [38]. In ovariectomize (OVX) mice, two main classes, acid-sensing nociceptors, the transient receptor potential channel vanilloid subfamily member 1 (TRPV1), and acid-sensing ion channels (ASICs), are expressed in the sensory neurons innervating the bone and elicit pain signals when activated by acid stimuli related to the osteoclast activation during bone resorption [39]. Thus, the development of a specific osteoclast inhibitor targeting osteoclasts in the aberrant subchondral bone remodeling in LFJ OA may have effective pharmacological treatments that slow or halt disease progression and alleviating pain.

It would also be meaningful in future studies to examine the secrete factors by osteoclasts in the subchondral bone in a bipedal standing-induced LFJ OA model. In addition, mouse models offer the opportunity for genetic modification, and the corresponding genetically modified mice need to determine the main factor release by osteoclast-induced

innervation in the subchondral bone in response to axial loading added on the LFJ [33].

The LFJ is a complicated biomechanical structure in the spine and has a complex mechanical performance [12]. Recently, there has been a growing interest in exploring the biomechanics and physiology of facet joints. Owing to the anatomical property of the spine, the mechanical behavior of the facet joint in each spinal segment is completely different [12, 40]. Thus, the axis mechanical stimulation act on the surface of each LFJ will initiate different intracellular signal cascade activations in various tissue components of the LFJ. This cascade includes the intracellular milieu (protein translation, gene transcription, posttranslational signaling) and intercellular signaling. However, this response has not been well defined in the subchondral bone of LFJ. The LFJ is formed by two adjacent vertebrae with the inferior articular process and superior articular process [12, 25]. The anatomy variations imply that the mechanical properties and cellular response vary within each part of the articular process. In our study, the superior articular process of the lumbar 5 segment was selected for systemic analysis. It will be interesting to further characterize the mechanical properties and physiology of LFJs among each segment.

5. Conclusion

Collectively, long-term axial loading induces the development of spine hyperalgesia in mice associate with increased osteoclast activity and aberrant angiogenesis and nerve invasion into the subchondral bone of LFJ that stimulate the natural pathological change in human LFJ OA. These results indicate that the aberrant bone remodeling associate with aberrant neve innervation in the subchondral bone has a potential as a therapeutic target in multiple LFJ OA pain.

Abbreviations

OA: Osteoarthritis
LFJ: Lumbar facet joint
IDP: Intradiscal pressure
SAPs: Superior articular processes
OC: Osteoclast
OARSI: Osteoarthritis Research Society International
TRPV1: Transient receptor potential channel vanilloid subfamily member 1
ASICs: Acid-sensing ion channels
OVX: Ovariectomize.

Data Availability

The datasets used and analyzed during the current study are available from the corresponding author on reasonable request.

Ethical Approval

This study was in accordance with the ethical standards of the Institutional and National Research Council and with the 1964 Helsinki Declaration and its later amendments or comparable ethical standards. All animal procedures in this study were conducted with the approval of the Animal Ethics Committee of the Xiangya Hospital of Central South University (protocol number: 2019N0106).

Conflicts of Interest

The authors have no conflicts of interest to declare.

Authors' Contributions

Material preparation, data collection and analysis were performed by ML, WQX, MH, and DJY. The first draft of the manuscript was written by ML, and YC made meaningful corrections to the structure and research design of the article and guided statistical methods and data processing. WFX, DQX, and YC contributed to the concept and design of the study and participated in the revision of the manuscript. All authors have read and approved the final manuscript.

Acknowledgments

This work was supported by the National Natural Science Foundation of China (81874030, 81902224), Natural Science Foundation of Hunan Province (2020JJ3060, 2019JJ50959), Innovation-Driven Project of Central South University (2020CX045), Wu Jieping Medical Foundation (320.6750.2020-03-14), and CMA Young and Middle-aged Doctors Outstanding Development Program-Osteoporosis Specialized Scientific Research Fund Project (G-X-2019-1107-12).

References

[1] A. C. Gellhorn, J. N. Katz, and P. Suri, "Osteoarthritis of the spine: the facet joints," *Nature Reviews Rheumatology*, vol. 9, no. 4, pp. 216–224, 2013.

[2] T. Wu, S. Ni, Y. Cao, S. Liao, J. Hu, and C. Duan, "Three-dimensional visualization and pathologic characteristics of cartilage and subchondral bone changes in the lumbar facet joint of an ovariectomized mouse model," *The Spine Journal*, vol. 18, no. 4, pp. 663–673, 2018.

[3] R. C. Lawrence, C. G. Helmick, F. C. Arnett et al., "Estimates of the prevalence of arthritis and selected musculoskeletal disorders in the United States," *Arthritis and Rheumatism*, vol. 41, no. 5, pp. 778–799, 1998.

[4] L. Kalichman, L. Li, D. H. Kim et al., "Facet joint osteoarthritis and low back pain in the community-based population," *Spine*, vol. 33, no. 23, pp. 2560–2565, 2008.

[5] P. Suri, D. J. Hunter, J. Rainville, A. Guermazi, and J. N. Katz, "Presence and extent of severe facet joint osteoarthritis are associated with back pain in older adults," *Osteoarthritis and Cartilage*, vol. 21, no. 9, pp. 1199–1206, 2013.

[6] C. H. Lee, C. K. Chung, and C. H. Kim, "The efficacy of conventional radiofrequency denervation in patients with chronic low back pain originating from the facet joints: a meta-analysis of randomized controlled trials," *The Spine Journal*, vol. 17, no. 11, pp. 1770–1780, 2017.

[7] A. P. Goode, A. E. Nelson, V. B. Kraus, J. B. Renner, and J. M. Jordan, "Biomarkers reflect differences in osteoarthritis phenotypes of the lumbar spine: the johnston county

osteoarthritis project," *Osteoarthritis and Cartilage*, vol. 25, no. 10, pp. 1672–1679, 2017.

[8] A. Nakamura, Y. R. Rampersaud, S. Nakamura et al., "MicroRNA-181a-5p antisense oligonucleotides attenuate osteoarthritis in facet and knee joints," *Annals of the Rheumatic Diseases*, vol. 78, no. 1, pp. 111–121, 2018.

[9] J. S. Kim, M. H. Ali, F. Wydra et al., "Characterization of degenerative human facet joints and facet joint capsular tissues," *Osteoarthritis and Cartilage*, vol. 23, no. 12, pp. 2242–2251, 2015.

[10] S. P. Cohen and S. N. Raja, "Pathogenesis, diagnosis, and treatment of lumbar zygapophysial (facet) joint pain," *Anesthesiology*, vol. 106, no. 3, pp. 591–614, 2007.

[11] J. Bleil, R. Maier, A. Hempfing et al., "Histomorphologic and histomorphometric characteristics of zygapophyseal joint remodeling in ankylosing spondylitis," *Arthritis & Rhematology*, vol. 66, no. 7, pp. 1745–1754, 2014.

[12] N. V. Jaumard, W. C. Welch, and B. A. Winkelstein, "Spinal facet joint biomechanics and mechanotransduction in normal, injury and degenerative conditions," *Journal of Biomechanical Engineering*, vol. 133, no. 7, p. 071010, 2011.

[13] Y. Liu, C. G. Shi, X. W. Wang et al., "Timing of surgical decompression for traumatic cervical spinal cord injury," *International Orthopaedics*, vol. 39, no. 12, pp. 2457–2463, 2015.

[14] H. J. Wilke, S. Krischak, and L. Claes, "Biomechanical comparison of calf and human spines," *Journal of Orthopaedic Research*, vol. 14, no. 3, pp. 500–503, 1996.

[15] A. Kettler, L. Liakos, B. Haegele, and H. J. Wilke, "Are the spines of calf, pig and sheep suitable models for pre-clinical implant tests?," *European Spine Journal*, vol. 16, no. 12, pp. 2186–2192, 2007.

[16] K. R. Wade, P. A. Robertson, A. Thambyah, and N. D. Broom, "How healthy discs herniate: A biomechanical and microstructural study investigating the combined effects of compression rate and flexion," *Spine*, vol. 39, no. 13, pp. 1018–1028, 2014.

[17] X. Ao, L. Wang, Y. Shao et al., "Development and characterization of a novel bipedal standing mouse model of intervertebral disc and facet joint degeneration," *Clinical Orthopaedics and Related Research*, vol. 477, no. 6, pp. 1492–1504, 2019.

[18] A. A. Claeson and V. H. Barocas, "Computer simulation of lumbar flexion shows shear of the facet capsular ligament," *The Spine Journal*, vol. 17, no. 1, pp. 109–119, 2017.

[19] Z. M. Beresford, R. W. Kendall, and S. E. Willick, "Lumbar facet syndromes," *Current Sports Medicine Reports*, vol. 9, no. 1, pp. 50–56, 2010.

[20] T. Wang, M. H. Pelletier, C. Christou, R. Oliver, R. J. Mobbs, and W. R. Walsh, "A novel in vivo large animal model of lumbar spinal joint degeneration," *The Spine Journal*, vol. 18, no. 10, pp. 1896–1909, 2018.

[21] S. Ni, Y. Cao, S. Liao et al., "Unilateral osteotomy of lumbar facet joint induces a mouse model of lumbar facet joint osteoarthritis," *Spine*, vol. 44, no. 16, pp. E930–E938, 2019.

[22] H. Preuschoft, "Mechanisms for the acquisition of habitual bipedality: are there biomechanical reasons for the acquisition of upright bipedal posture?," *Journal of Anatomy*, vol. 204, no. 5, pp. 363–384, 2004.

[23] N. H. Hart, S. Nimphius, T. Rantalainen, A. Ireland, A. Siafarikas, and R. U. Newton, "Mechanical basis of bone strength: influence of bone material, bone structure and muscle action," *Journal of Musculoskeletal & Neuronal Interactions*, vol. 17, 2017.

[24] J. A. Actis, J. D. Honegger, D. H. Gates, A. J. Petrella, L. A. Nolasco, and A. K. Silverman, "Validation of lumbar spine loading from a musculoskeletal model including the lower limbs and lumbar spine," *Journal of Biomechanics*, vol. 68, pp. 107–114, 2018.

[25] H. J. Kim, H. J. Chun, H. M. Lee et al., "The biomechanical influence of the facet joint orientation and the facet tropism in the lumbar spine," *The Spine Journal*, vol. 13, no. 10, pp. 1301–1308, 2013.

[26] Q. Bian, L. Ma, A. Jain et al., "Mechanosignaling activation of TGFβ maintains intervertebral disc homeostasis," *Bone Research*, vol. 5, no. 1, 2017.

[27] G. Li, J. Yin, J. Gao et al., "Subchondral bone in osteoarthritis: insight into risk factors and microstructural changes," *Arthritis Research & Therapy*, vol. 15, no. 6, p. 223, 2013.

[28] G. Zhen, C. Wen, X. Jia et al., "Inhibition of TGF-β signaling in mesenchymal stem cells of subchondral bone attenuates osteoarthritis," *Nature Medicine*, vol. 19, no. 6, pp. 704–712, 2013.

[29] A. J. Barr, T. M. Campbell, D. Hopkinson, S. R. Kingsbury, M. A. Bowes, and P. G. Conaghan, "A systematic review of the relationship between subchondral bone features, pain and structural pathology in peripheral joint osteoarthritis," *Arthritis Research & Therapy*, vol. 17, no. 1, 2015.

[30] M. A. J. Finnilä, J. Thevenot, O. M. Aho et al., "Association between subchondral bone structure and osteoarthritis histopathological grade," *Journal of Orthopaedic Research*, vol. 35, no. 4, pp. 785–792, 2017.

[31] S. Kwan Tat, D. Lajeunesse, J. P. Pelletier, and J. Martel-Pelletier, "Targeting subchondral bone for treating osteoarthritis: what is the evidence?," *Best Practice & Research. Clinical Rheumatology*, vol. 24, no. 1, pp. 51–70, 2010.

[32] Z. Cui, J. Crane, H. Xie et al., "Halofuginone attenuates osteoarthritis by inhibition of TGF-β activity and H-type vessel formation in subchondral bone," *Annals of the Rheumatic Diseases*, vol. 75, no. 9, pp. 1714–1721, 2016.

[33] S. Zhu, J. Zhu, G. Zhen et al., "Subchondral bone osteoclasts induce sensory innervation and osteoarthritis pain," *The Journal of Clinical Investigation*, vol. 129, no. 3, pp. 1076–1093, 2019.

[34] L. J. Raggatt and N. C. Partridge, "Cellular and molecular mechanisms of bone remodeling," *The Journal of Biological Chemistry*, vol. 285, no. 33, pp. 25103–25108, 2010.

[35] J. F. Charles and A. O. Aliprantis, "Osteoclasts: more than "bone eaters"," *Trends in Molecular Medicine*, vol. 20, no. 8, pp. 449–459, 2014.

[36] R. Florencio-Silva, G. R. S. Sasso, E. Sasso-Cerri, M. J. Simões, and P. S. Cerri, "Biology of bone tissue: structure, function, and factors that influence bone cells," *BioMed Research International*, vol. 2015, Article ID 421746, 17 pages, 2015.

[37] H. Xie, Z. Cui, L. Wang et al., "PDGF-BB secreted by preosteoclasts induces angiogenesis during coupling with osteogenesis," *Nature Medicine*, vol. 20, no. 11, pp. 1270–1278, 2014.

[38] T. Yoneda, M. Hiasa, Y. Nagata, T. Okui, and F. White, "Contribution of acidic extracellular microenvironment of cancer-colonized bone to bone pain," *Biochimica et Biophysica Acta (BBA) - Biomembranes*, vol. 1848, no. 10, pp. 2677–2684, 2015.

[39] K. Kanaya, K. Iba, T. Dohke, S. Okazaki, and T. Yamashita, "TRPV1, ASICS and P2X2/3 expressed in bone cells simultaneously regulate bone metabolic markers in ovariectomized mice," *Journal of Musculoskeletal & Neuronal Interactions*, vol. 16, no. S, pp. 145–151, 2016.

[40] T. Gao, Q. Lai, S. Zhou et al., "Correlation between facet tropism and lumbar degenerative disease: a retrospective analysis," *BMC Musculoskeletal Disorders*, vol. 18, no. 1, p. 483, 2017.

Hindawi
BioMed Research International
Volume 2020, Article ID 8538463, 9 pages
https://doi.org/10.1155/2020/8538463

Research Article

Mechanism of Abnormal Chondrocyte Proliferation Induced by Piezo1-siRNA Exposed to Mechanical Stretch

Yi Sun,[1] **Ping Leng**,[2] **Dawei Li**,[1] **Huanshen Gao**,[1] **Zhenghui Li**,[1] **Chenkai Li**,[1] **and Haining Zhang**[1]

[1]*Department of Joint Surgery, The Affiliated Hospital of Qingdao University, Qingdao 266000, China*
[2]*Department of Pharmacy, The Affiliated Hospital of Qingdao University, Qingdao 266000, China*

Correspondence should be addressed to Haining Zhang; 2018025794@qdu.edu.cn

Received 15 August 2020; Revised 7 October 2020; Accepted 23 October 2020; Published 5 November 2020

Academic Editor: Shen Liu

Objective. To investigate the effect of small interfering RNA targeting mechanosensitive ion channel protein Piezo1 (Piezo1-siRNA) on abnormal chondrocyte proliferation exposed to mechanical stretch. *Methods*. Construct and screen effective Piezo1-siRNA sequences and explore an appropriate method to transfect lentiviral vector into chondrocytes exposed to mechanical stretch. Western blot and RT-PCR were used to detect the mRNA and protein expression of Piezo1, Kif18A, and β-tubulin, respectively. Flow cytometry was used to measure the changes in the chondrocyte cycle. The proliferation of chondrocyte was evaluated by cell counting kit-8. *Results*. According to the mRNA and protein expression of Piezo1, the effective siRNA sequence was successfully screened. Compared with the 0 h group, mechanical stretch upregulated the expression of Piezo1, Kif18A, and β-tubulin, resulting in chondrocyte cycle arrest and eventually inhibiting chondrocyte proliferation. Moreover, Piezo1-siRNA transfection effectively blocks this process and promotes the proliferation of chondrocyte. *Conclusion*. Piezo1-siRNA can reduce the inhibition of chondrocyte proliferation induced by mechanical stretch via downregulating the expression of Kif18A and inhibiting the depolymerization of microtubules. Piezo1-siRNA plays a protective role in chondrocytes, which provides a potential method for the treatment of OA under abnormal mechanical stimulation.

1. Introduction

Osteoarthritis (OA) is a degenerative disease of bone and articular cartilage, which is caused by mechanical and biological factors [1–3]. Degenerative changes of articular cartilage are closely related to abnormal proliferation of chondrocyte [4, 5], in which mechanical stretch stress plays a crucial role [6]. It has been reported that the proliferation of chondrocytes under different mechanical stretch was varied, and the proliferation of chondrocytes decreased with the extension of mechanical stretch time. However, the potential molecular mechanisms of abnormal proliferation of chondrocyte exposed to mechanical stretch have not been elucidated [7].

Piezo1 is a novel type of nonselective mechanically sensitive ion channel which is different from other ion channels in structure and gating mechanism [8, 9]. It converts mechanical signals into chemical signals and engages in cell proliferation, apoptosis, and metabolism [10]. Previous studies have reported that the expression of Piezo1 in chondrocyte exposed to different mechanical stretch is various, and chondrocyte proliferation is closely associated with the time of mechanical stretch [11]. However, whether Piezo1 is involved in mechanical stretch-induced abnormal proliferation of chondrocytes is still unclear.

Microtubule kinesin, a kind of motor protein with ATPase activity, plays a significant role in the dynamic changes of microtubules and intracellular material transport [12]. Recently, it has been found that Kif18A, a member of the kinesin-8 family, participates in many biological functions of cells, such as spindle formation, chromosome separation, cell division, microtubule polymerization, and depolymerization [13]. The morphology and microtubule of chondrocytes were changed under mechanical stretch [14]. Combined with previous studies, we propose a hypothesis

Table 1: Interfering sequences and negative control sequences.

Oligo name	Oligo sequence
Piezo1-siRNA1	5′-GATCCGCGTCATCATCGTGTGTAAGATTCAAGAGATCTTACACACGATGATGACGCTTTTTTG-3′ 3′-AATTCAAAAAAGCGTCATCATCGTGTGTAAGATCTCTTGAATCTTACACACGATGATGACGCG-5′
Piezo1-siRNA2	5′-GATCCGCGTCTTCCTTAGCCATTACTTTCAAGAGAAGTAATGGCTAAGGAAGACGCTTTTTTG-3′ 3′-AATTCAAAAAAGCGTCTTCCTTAGCCATTACTTCTCTTGAAAGTAATGGCTAAGGAAGACGCG-5′
Piezo1-siRNA3	5′-GATCCGCCTCAAGTACTTCATCAACTTTCAAGAGAAGTTGATGAAGTACTTGAGGCTTTTTTG-3′ 3′-AATTCAAAAAAGCCTCAAGTACTTCATCAACTTCTCTTGAAAGTTGATGAAGTACTTGAGGCG-5′
Negative control	5′-GATAGCGTCCATCATCGTGTGTAAGATTCAAGAGATCTTACACACGATGATGACGCTTTTTTG-3′ 3′-AATAGCGTCAAGCGTCATCATCGTGTGTAAGATCTCTTGAATCTTACACACGATGATGACGCG-5′

that mechanical stretch can upregulate the expression of Piezo1 in chondrocytes and then activate the microtubule kinesin Kif18A, resulting in increased microtubule depolymerization and cell proliferation inhibition. To confirm the hypothesis, we conducted an experiment to investigate the expression of Piezo1, Kif18A, and β-tubulin in chondrocytes exposed to mechanical stretch. The cell cycle and proliferation of chondrocyte were also measured by flow cytometry and cell counting kit-8. In addition, siRNA was used to silence the expression of Piezo1 in order to provide a potential drug target for chondrocyte protection under mechanical stretch.

2. Materials and Methods

2.1. Chondrocyte Culture. This project was approved by the Ethics Committee of the Affiliated Hospital of Qingdao University. All patients were informed and signed consent. Chondrocytes were harvested from articular cartilage derived from the OA patients undergoing total knee arthroplasty. Cartilage tissue was briefly washed with phosphate-buffered saline (PBS) containing 400 U/ml penicillin and 0.4 mg/ml streptomycin (Hyclone, USA) for 3 times. The samples were cut into 1 mm^3 granules under aseptic conditions. After trypsin and collagenase (Solaibio, China) sequential digestion for 4 h, the cells were collected after 1000 r/min centrifugation. The cells were added to DMEM (Gibco, USA) containing 15% fetal bovine serum (Gibco, USA). After counting, the cells were inoculated in a 25 cm^2 culture bottle and cultured in a 5% CO_2 incubator (Sanyo, Japan) at 37°C in a humid atmosphere.

2.2. Chondrocyte Identification. The primary chondrocytes were inoculated into the 12-well plate containing glass cover slips. When the cell fusion rate reached 70, the chondrocytes were fixed with 4% paraformaldehyde (Solaibio, China) for 15 min, followed by permeabilization with 0.2% Triton X-100 (MP Biomedicals, USA) for 5 min. After washing, the cells were preincubated for 30 min in 5% BSA to prevent nonspecific antibody binding. The human type II collagen (Novus Biologicals, USA) antibody was incubated overnight at 4°C. AlexaFluor 488 Goat Anti-Rabbit lgG (diluted 1 : 2000; Invitrogen, USA) was added to incubate for 30 min. The dye solution of diaminobenzidine (DAB) was dyed and observed under an inverted optical microscope (Olympus GX51, Olympus, Japan).

The cells were fixed with 4% polyformaldehyde for 1 h, then washed by water for 15 min and by distilled water once, and then stained with 1% toluidine blue for 3 h. 95% alcohol was added, the excess dye was washed out, and the cells were observed under an inverted optical microscope.

2.3. Construction of Piezo1-siRNA. The construction of the virus vector was completed by Gemma gene (Shanghai). All sequences were specific oligonucleotide chains with 63 bD (Table 1). The vector pHBLV-U6-ZsGreen-PGK-Puro cut the negative control sequence away to obtain the skeleton by BamHI, EcoRI enzyme, and then, the target sequence was inserted into the U6 promoter to regulate its expression. The lentivirus vector contained ZsGreen (GFP) regulated by CMVIE promoter and puro resistant gene initiated by PKG promoter. Virus titer was determined by a hole-by-hole dilution titer assay (1.0×10^8 TU/ml) after virus collection.

2.4. Screening of Lentivirus Vectors. The chondrocytes were divided into 5 groups: a (blank control), b (Piezo1-siRNA1), c (Piezo1-siRNA2), d (Piezo1-siRNA3), and e (negative control). Totally, 50 μl lentivirus vector, containing each interference sequence and negative control sequence, was added to the culture medium, respectively. The titer is 1×10^8 TU/ml. The same amount of culture medium solution was added in group a. After 48 h, the cells were observed and counted under a fluorescence microscope. After 96 h, the cells were collected. Western blot and RT-PCR were used to detect the mRNA and protein expression of Piezo1, respectively.

2.5. Construction of Mechanical Stretch Model of Chondrocytes. The chondrocytes were inoculated into the Flexcell aseptic membranous 6-well plate (Flexcell, USA), cultured in 2.5 ml low-glucose DMEM containing 10% fetal bovine serum each well. The chondrocytes were divided into three groups: blank control group, lentivirus empty vector group, and lentivirus interference sequence group. When cell fusion reaches 40%, the selected effective lentivirus was added and the empty vector virus 50 μl per well. The virus titer is 1×10^8 TU/ml. The culture plates were placed in the multichannel cell stretch stress loading system FX-4000T (Flexcell, USA) in a 5% CO_2 incubator at 37°C in a humid

Table 2: Oligo sequences of the target genes.

Oligo name		Oligo sequence
Piezo1	Forward primer	5′-CATCTTGGTGGTCTCCTCTGTCT-3′
	Reverse primer	5′-CTGGCATCCACATCCCTCTCATC-3′
Kif18A	Forward primer	5′-GCAGCTCAATGATTCTCTTAGC-3′
	Reverse primer	5′-TTACACTTCGAGCTCTTGATGT-3′
β-Tubulin	Forward primer	5′-ATTCCAACCTTCCAGCCTGC-3′
	Reverse primer	5′-CCAGAACTTGGCACCGATCT-3′
GAPDH	Forward primer	5′-GCACCGTCAAGGCTGAGAAC-3′
	Reverse primer	5′-TGGTGAAGACGCCAGTGGA-3′

atmosphere. Because of the different stretch times applied to cells, each group was divided into five subgroups, and the cyclic stretch of 0 h/2 h/12 h/24 h/48 h was loaded, respectively, with the amplitude of 20% and the period of 10 times/min.

2.6. Detection of Cell Proliferation by Cell Counting Kit-8 (CCK-8). The cells of each group were obtained by trypsin digestion and centrifugation. After counting, 5 μl cell suspensions were inoculated into a 96-well plate and supplemented with culture medium. After 6 h of culture, 10 μl CCK-8 solution was added to each well and the number of cells was measured. The operation was carried out according to the manufacturer's instructions.

2.7. Detection of Cell Cycle by Propidine Iodide (PI) Single Staining Flow Cytometry. Each group of cells was washed twice with 1 ml PBS. The cells were immobilized by absolute ethyl alcohol at 4°C for 2 h. Each sample was resuspended with 200 μl precooled PBS, then added with 10 μl RNA enzyme (Beyotime, China) and 25 μl PI staining solution (Beyotime, China). The cells were fully suspended at 37°C for 30 min. Red fluorescence and light scattering were detected by flow cytometry at 488 nm wavelength. The cell DNA content and light scattering analysis were analyzed by FlowJo v10 software, and the percentage of cells in each cycle was analyzed by a self-cell cycle model.

2.8. RT-PCR. Each group was added RNAiso (TaKaRa, Japan) to extract the total RNA. The PrimeScript RT reagent kit (TaKaRa, Japan) was used to reverse RNA to cDNA. Then, the SYBR Premix Ex Taq II kit (TaKaRa, Japan) was used for RT-PCR. The CT values of Piezo1, Kif18A, β-tubulin, and GAPDH genes were obtained by the FTC-2000 system (Applied Biosystems, China), and the parameters were as follows: predenaturation: 95°C for 30 seconds, 1 cycle; PCR: 95°C for 5 seconds, 60°C for 30 seconds, and 72°C for 30 seconds for 40 cycles. The relative expression of the target gene was calculated by $2^{-\Delta\Delta Ct}$. GAPDH, Piezo1, Kif18A, and β-tubulin primers were produced by Shanghai Bioengineering Company (Table 2).

2.9. Western Blot. Cells were lysed with the precooled RIPA lysate (Solarbio, China). The supernatant was obtained after centrifugation at 4°C for 12000 r/min. After adding an appropriate amount of sample buffer to the protein sample, the protein samples and standard protein marker were added to polyacrylamide gel and then electrophorized. After electrophoresis, the protein was transferred to the polyvinylidene fluoride membrane. The membranes immersed in the target protein antibody (dilution concentration 1 : 5000; Abcam, China) were incubated overnight at 4°C. The second antibody (dilution concentration 1 : 10000; Abcam, China) was added for 1 h. The enhanced chemiluminescence reagent was used to detect the target proteins. GAPDH was used as the internal control.

2.10. Statistical Analysis. The data were processed by SPSS19.0 statistical software, the measurement data were expressed as the mean ± standard deviation (SD), a t -test was used when the two independent groups of measurement data were compared, and the percentage of the cell cycle was tested by the Poisson distribution data z -test. One-way ANOVA was used to compare the mean values of multiple samples. $P < 0.05$ was defined as statistically significant.

3. Results

3.1. Cell Identification. The chondrocytes were fusiform or polygonal, mononuclear, or polynucleolar and adherent to the wall (Figure 1(a)). Immunohistochemical staining showed that the cytoplasm of chondrocytes was brown and the nucleus was blue, indicating that type II collagen exists in the cytoplasm of chondrocytes (Figure 1(b)). Toluidine blue staining showed that the cytoplasm of chondrocytes was purple blue and the background was light blue (Figure 1(c)) indicating that glycosaminoglycan exists in the matrix surrounding the chondrocytes.

3.2. Lentivirus Transfection into Chondrocytes and Screening of Effective Sequences. After 72 h of transfection, the complex number of infection was calculated and the transfection efficiency was measured. It was calculated that the average number of infection was 30 ± 4 TU/cell in each group with 50 μl viral fluid, and the transfection efficiency was 0%, 91.88%, 92.33%, and 94.23%, respectively (Figure 2(a)). The mRNA expression of Piezo1 in the Piezo1-siRNA3

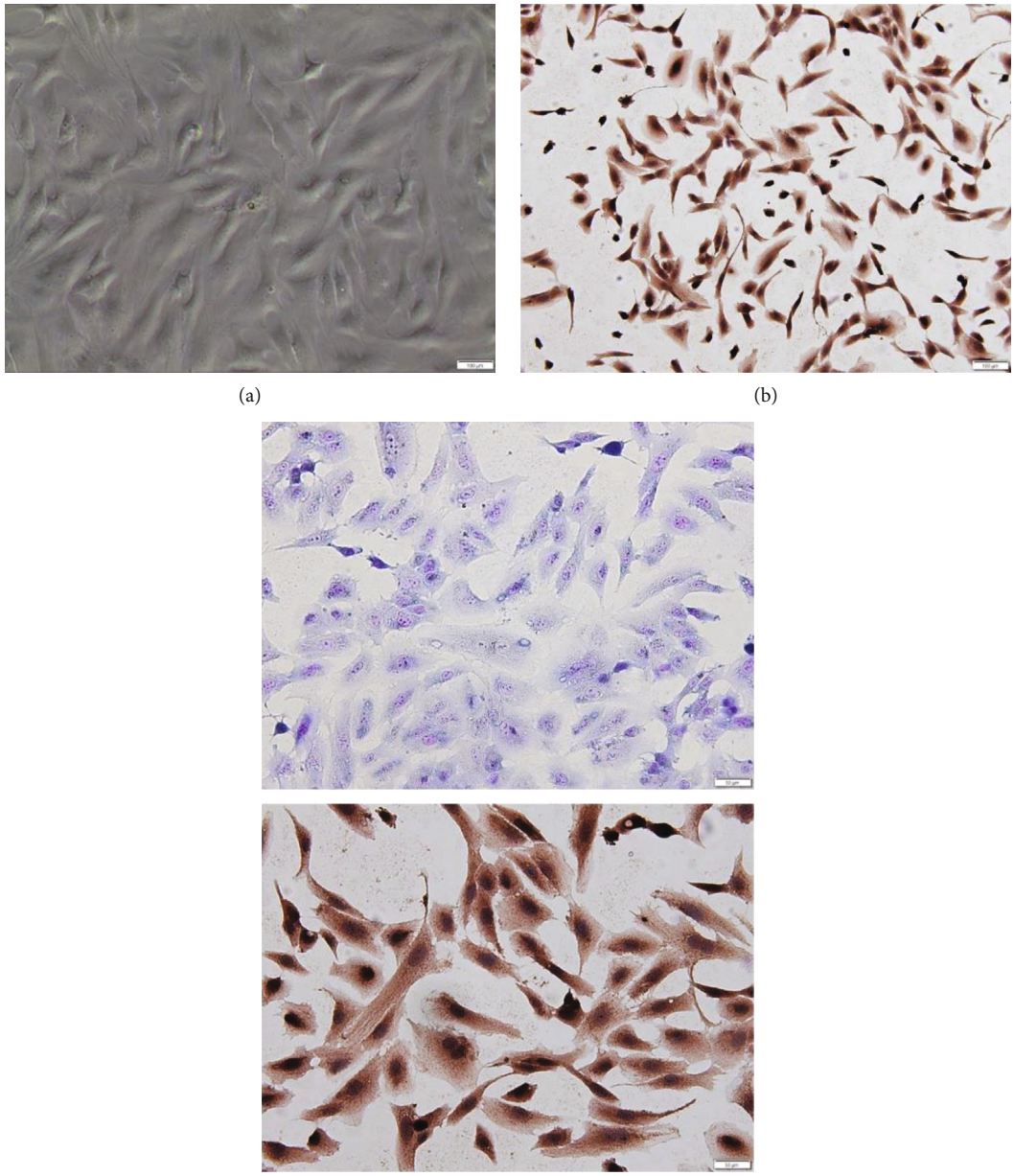

(a) (b) (c)

Figure 1: Cell culture and identification: (a) second-generation chondrocytes, mononuclear, and polynucleolus; (b) type II collagen immunohistochemical staining; (c) toluidine blue staining of chondrocytes.

group was significantly decreased than that in the negative group ($P < 0.01$) (Figure 2(b)). Similar results were also observed in the protein expression of Piezo1 (Figure 2(c)), so the Piezo1-siRNA3 could be used as the effective sequence of the Piezo1 silencing vector.

3.3. Detection of Cell Proliferation by CCK-8. The OD values of the blank control group and the lentivirus empty vector group were measured at different time points to make the broken line diagram (Figure 3(a)). According to the graph, there was no difference between the OD values of the two groups at each time point ($P > 0.05$). After the lentiviral interference vector Piezo1-siRNA3 was added, the cell proliferation showed different changes in different mechanical stress groups. With the extension of stretching time, cell proliferation first increased and then decreased. The cell proliferation was the highest at 2 h and the lowest at 48 h. However, after mechanical stretch for 2 h, the proliferation rate of the Piezo1-siRNA group was lower than that in the blank control group after 2 h, and there was a significant difference between the Piezo1-siRNA group and the blank control group ($P < 0.05$) (Figure 3(b)).

3.4. Detection of Cell Cycle by Flow Cytometry. Cell cycle results of the blank control group and Piezo1-siRNA group are shown in Figure 4 and Table 3. In the control group, there

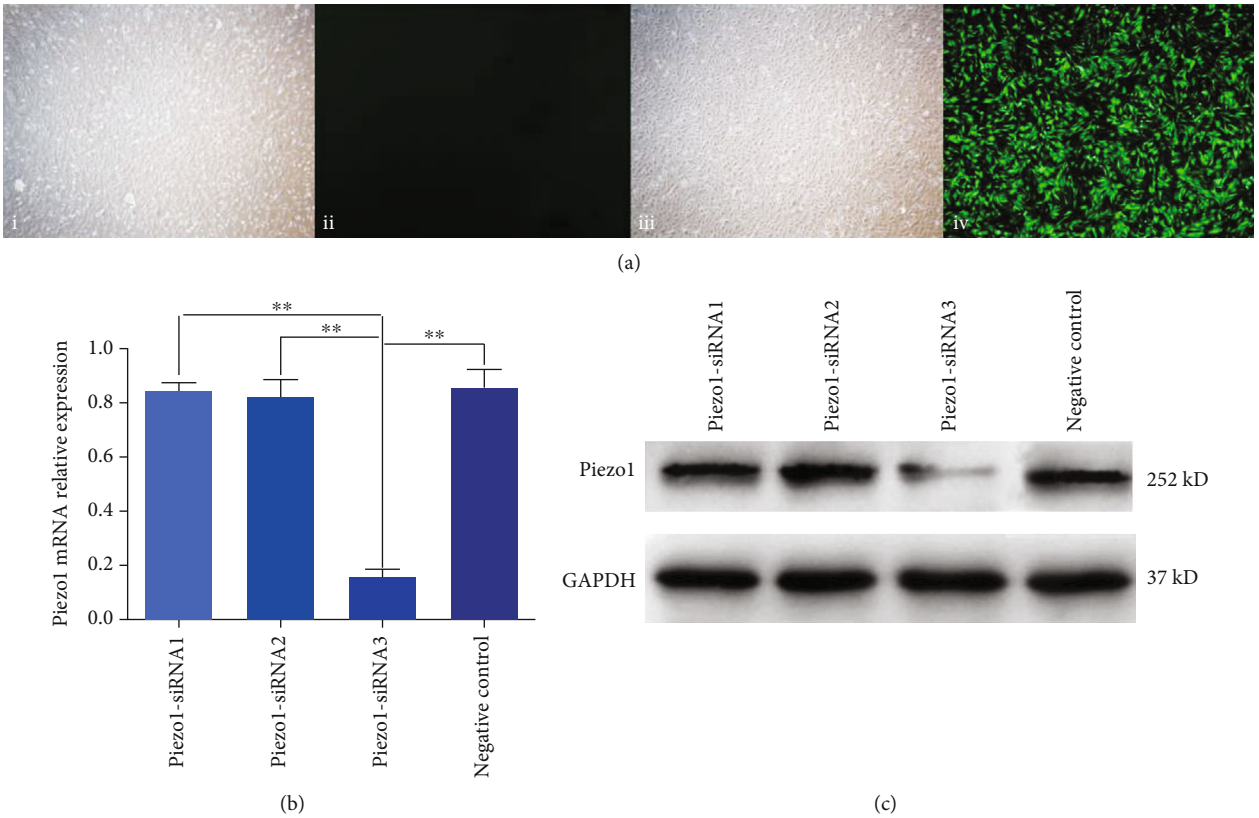

FIGURE 2: Screening of effective lentivirus sequences. (a) The efficiency of lentivirus transfection in each group, green fluorescence as lentivirus vector; i and ii show a group of lentivirus-free vectors observing cells in the same field of vision under normal and fluorescent light sources; iii and iv indicated that the lentivirus vector group was added to observe the same visual field cells under normal and fluorescent light sources, and the lentivirus was transferred into the cells. (b) The relative mRNA expression of Piezo1. (c) The results of protein expression of Piezo1 protein.

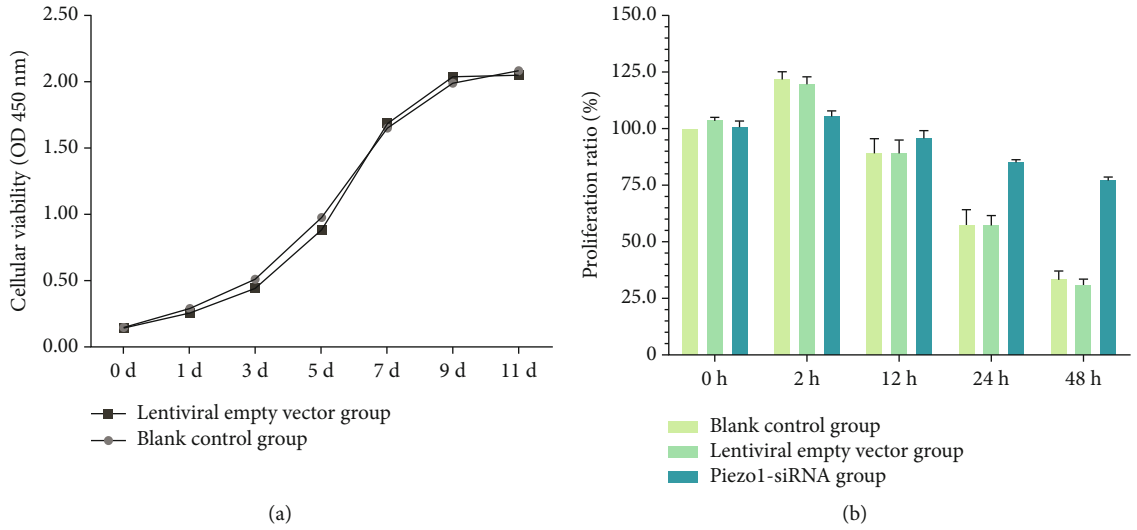

FIGURE 3: Detection of cell proliferation by cell counting kit-8. (a) Detecting the effect of lentivirus on cell proliferation under different days, there was no significant difference in the number of living cells between the two groups. (b) The results of cell proliferation in each group under different stretch.

was no difference in the percentage of cells in the G2/M phase ($P > 0.05$). Compared with the 0 h blank control group, the percentage of G2/M phase cells in the 12 h/24 h/48 h blank control group was significantly different ($P < 0.05$), and the percentage of the G2/M phase cell in the 24 h blank control group was the highest, which was significantly higher than

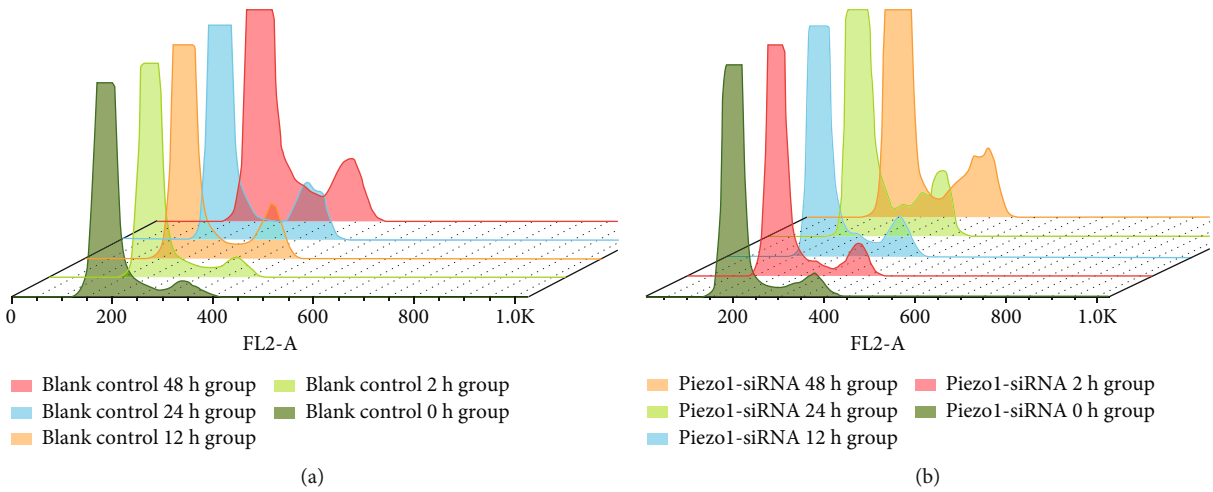

Figure 4: The cell cycle composite columnar map analyzed by FlowJo v10; the high peak represented the G0/G1 phase, and the low peak represented the G2/M phase. The values obtained are shown in Table 3. (a) The periodic distribution of different stretch times in the blank control group. (b) The periodic distribution of different stretch times in the Piezo1-siRNA group.

Table 3: Percentage of cells in the blank control group and the lentiviral interference group at different stress times.

Group name		< diploid (%)	Cell cycle (%)			> tetraploid (%)
			G0/G1	S	G2/M	
Blank control	48 h group	7.89	61.90	20.80	**6.37	0.48
Blank control	24 h group	4.17	71.70	13.30	**8.16	1.05
Blank control	12 h group	10.80	62.60	17.10	**5.65	0.54
Blank control	2 h group	10.90	68.70	11.50	5.31	0.19
Blank control	0 h group	16.60	64.60	27.50	4.06	2.01
Piezo1-siRNA	48 h group	24.70	51.90	14.90	*4.86	0.33
Piezo1-siRNA	24 h group	2.34	70.20	20.10	*4.85	0.18
Piezo1-siRNA	12 h group	6.65	78.20	8.96	*4.00	0.38
Piezo1-siRNA	2 h group	4.19	72.10	15.80	*5.68	0.32
Piezo1-siRNA	0 h group	8.22	58.10	25.00	4.61	0.83

**vs. blank control 0 h group, z -test, $P < 0.05$; *vs. Piezo1-siRNA 0 h group, z-test, $P > 0.05$.

that in the 0 h blank control group. There was no difference in the percentage of G2/M phase cells in the Piezo1-siRNA group under different stretch times (compared with the 0 h group, $P > 0.05$).

3.5. RT-PCR Results of Piezo1, Kif18A, and β-Tubulin. The mRNA expression characteristics of Piezo1 and Kif18A in the blank control group and empty vector group were basically the same, showing the first increase and then decrease, and reached the maximum expression after 24 h mechanical stretch (Figures 5(a) and 5(b)). Upon transfection with Piezo1-siRNA, there was no significant difference in mRNA expression of Piezo1 among the groups ($P > 0.05$), and the expression of Kif18A and β-tubulin decreased ($P > 0.05$, Figure 5(c)).

3.6. Western Blotting Results of Piezo1, Kif18A, and β-Tubulin. The expression of Piezo1 in chondrocytes changed with the extension of mechanical stretch time, and the expression of Piezo1 protein was significantly inhibited by transfection of siRNA. The protein expression of Kif18A and β-tubulin in chondrocytes exposed to mechanical stretch was consistent with that of mRNA expression. After transfection with Piezo1-siRNA, the expression of Kif18A and β-tubulin decreased significantly ($P < 0.05$). (Figure 5(d)).

4. Discussion

Previous studies have reported that Piezo1 can mediate chondrocyte apoptosis by regulating the polymerization and depolymerization of cytoskeleton. However, it is not clear whether Piezo1 plays a role in the proliferation of chondrocytes exposed to mechanical stretch [15]. Therefore, the purpose of this study is to investigate the biomechanical effects of chondrocytes cultured in vitro, focusing on whether Piezo1 regulates the proliferation of chondrocytes, and the potential role of cytoskeleton and kinesin in this process. In vitro exposure to mechanical stretch of chondrocyte proliferation results showed that moderate stretch (2 h) promoted the proliferation of chondrocytes, but excessive stretch led

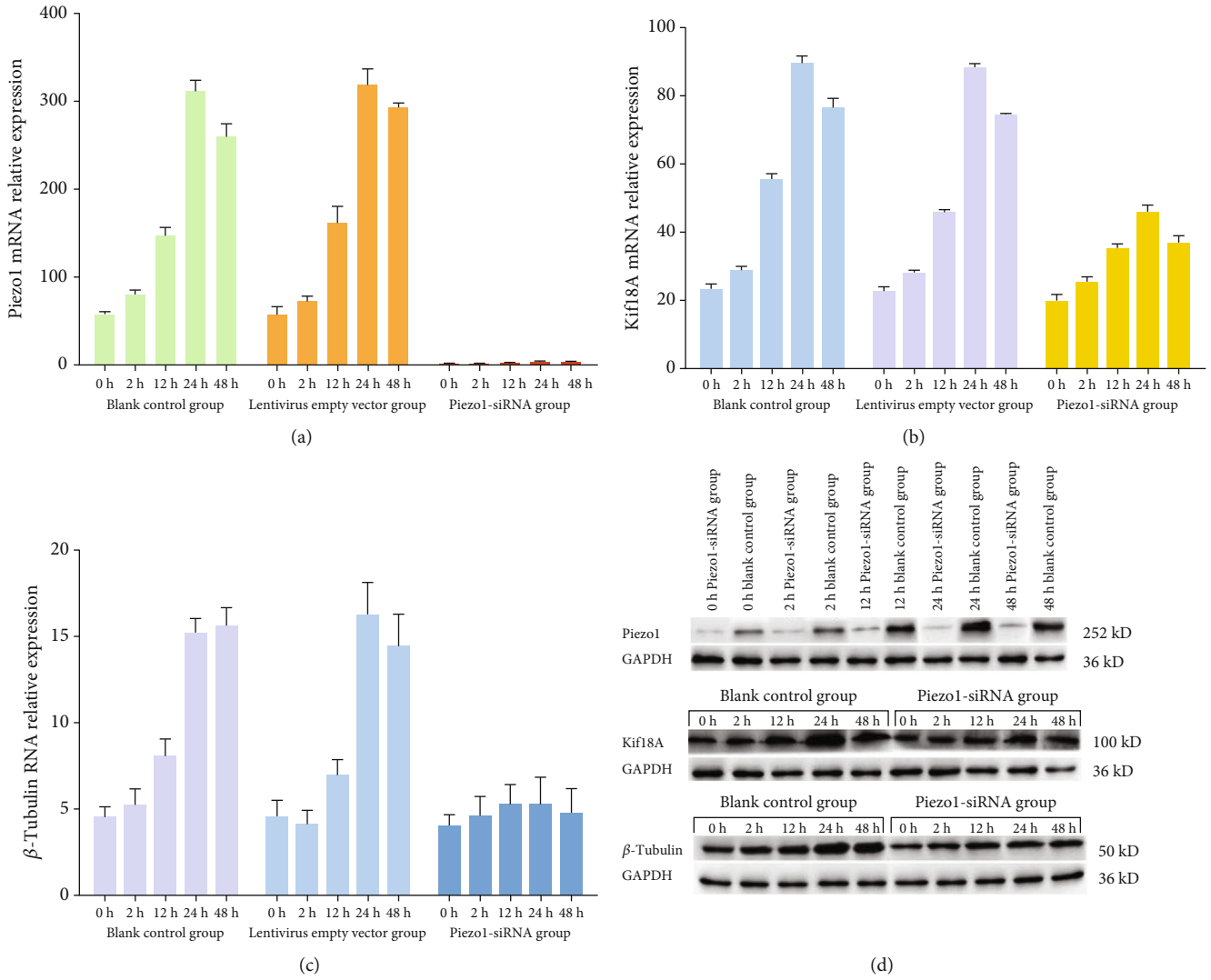

FIGURE 5: The expression of Piezo1, Kif18A, and β-tubulin: (a) the mRNA expression of Piezo1; (b) the mRNA expression of Kif18A; (c) the mRNA expression of β-tubulin; (d) the protein expression of Piezo1, Kif18A, and β-tubulin.

to abnormal proliferation of chondrocytes. Transfection of Piezo1-siRNA effectively reduced the abnormal proliferation of chondrocytes caused by excessive mechanical stretch. In addition, we found that mechanical stretch promoted the expression of Piezo1 to a certain extent, which made the inhibitory effect of mechanical stretch on cell proliferation more significant. These results confirm that Piezo1 plays an important role in regulating the proliferation of chondrocytes under mechanical stimulation. Inhibition of Piezo1 effectively reduced the injury of chondrocytes induced by mechanical stretch.

Kif18A regulates the stability of microtubules through the activity of microtubule depolymerization enzyme, resulting in cytoskeleton changes [16]. Kif18A expression was significantly increased in the mitotic phase of eukaryotic cells, indicating that it may participate in the process of mitosis, but the specific mechanism is unclear [17, 18]. In recent years, some researchers have found that Piezo1 is closely associated with cytoskeleton. Gottlieb et al. [19] found that the current intensity of the cell membrane decreased by stimulating the channel on the cell surface pretreated with cytochalasin D, indicating that actin is responsible for the transmission of mechanical stimulation. Previous studies have reported that cytoskeleton plays a mechanical protective role on Piezo1, which means that intact cytoskeleton increases the difficulty of activating Piezo1 [20, 21]. The destruction of cytoskeleton integrity makes the same mechanical stretch that mediates larger cell morphological changes, which enhances the activation of Piezo1 [22]. Combined with the research reports [13], we speculate that the abnormal proliferation of chondrocytes under mechanical stretch may be closely related to cytoskeleton and kinesin. Our results showed that the protein and mRNA expression of Kif18A increased with the extension of mechanical stretch time. Compared with the empty vector group, the expression of Kif18A in the Piezo1-siRNA group was markedly decreased, which implied that the activation of Piezo1 could promote the overexpression of Kif18A. The activation mechanism may be related to the

changes in the intracellular calcium level after the opening of channels, which still needs to be explored. We also confirmed that the expression of β-tubulin upregulated with the extension of mechanical stretch time, and the expression of β-tubulin in the empty vector group was higher than that in the Piezo1-siRNA group. We speculate that activated Kif18A destroys the integrity of cytoskeleton by playing the role of microtubule depolymerizing enzyme, thus promoting the expression of Piezo1 and forming a positive feedback loop [23]. The expression of Piezo1 in the 24 h group was significantly higher than that in the 12 h group, which supported our hypothesis. Interestingly, compared with the mechanical stretch group for 24 h, the Piezo1 expression and cell viability of the 48 h mechanical stretch group were lower. Combined with the experimental results of Grishchuk [16], we believe that excessive mechanical stretch may exceed the tolerance of cells, causing cell proliferation arrest and inducing apoptosis. Cell cycle analysis showed that the percentage of G2/M phase cells in the 24 h mechanical stretch group was significantly higher than that in the 0 h group, suggesting that Kif18A expression increases and cytoskeleton depolymerization promotes cell cycle arrest, which is consistent with the results of Huang et al. [24] in the study of Kif18s-induced microtubule depolymerization leading to chromosome arrangement defects and mitotic stagnation after excessive aggregation of microtubules at the positive tip of microtubules. It is concluded that Piezo1 can induce cytoskeleton destruction and inhibit the proliferation of chondrocytes by activating Kif18A to depolymerize microtubules.

5. Conclusions

In this study, we found that Piezo1-siRNA effectively interferes with Piezo1 expression and alleviates mechanical stretch-mediated inhibition of chondrocyte proliferation. Our conclusion is that mechanical stretch activates Piezo1, resulting in the overexpression of Kif8a, which leads to microtubule depolymerization, destroys the integrity of cytoskeleton, and inhibits the mitosis of cells. Transfection of Piezo1-siRNA effectively blocked the pathway and corrected the abnormal proliferation of cells. Therefore, Piezo1-siRNA may protect the cartilage of patients with osteoarthritis, which provides a potential method for the treatment of persistent progression of OA under abnormal mechanical stimulation. However, the changes in intracellular chemical signals, the response of cytoskeleton to Piezo1, and whether there are other ways to inhibit cell proliferation after Piezo1 activation need further study and discussion.

Data Availability

The data used to support the findings of this study are available from the corresponding author upon request.

Conflicts of Interest

There is no conflict of interest regarding the publication of this paper.

Acknowledgments

This work was supported by the National Natural Science Foundation of China (NO. 81672197).

References

[1] F. Guilak, "Biomechanical factors in osteoarthritis," *Best Practice & Research. Clinical Rheumatology*, vol. 25, no. 6, pp. 815–823, 2011.

[2] G. Sakalauskiene and D. Jauniskiene, "Osteoarthritis: etiology, epidemiology, impact on the individual and society and the main principles of management," *Medicina (Kaunas, Lithuania)*, vol. 46, no. 11, pp. 790–797, 2010.

[3] K. D. Brandt and R. S. Fife, "Ageing in relation to the pathogenesis of osteoarthritis," *Clinics in Rheumatic Diseases*, vol. 12, no. 1, pp. 117–130, 1986.

[4] M. Varela-Eirin, J. Loureiro, E. Fonseca et al., "Cartilage regeneration and ageing: targeting cellular plasticity in osteoarthritis," *Ageing Research Reviews*, vol. 42, pp. 56–71, 2018.

[5] M. B. Goldring and S. R. Goldring, "Osteoarthritis," *Journal of Cellular Physiology*, vol. 213, no. 3, pp. 626–634, 2007.

[6] T. B. Birmingham, R. Moyer, K. Leitch et al., "Changes in biomechanical risk factors for knee osteoarthritis and their association with 5-year clinically important improvement after limb realignment surgery," *Osteoarthritis and Cartilage*, vol. 25, no. 12, pp. 1999–2006, 2017.

[7] J. P. Pelletier, J. Martel-Pelletier, and S. B. Abramson, "Osteoarthritis, an inflammatory disease: potential implication for the selection of new therapeutic targets," *Arthritis and Rheumatism*, vol. 44, no. 6, pp. 1237–1247, 2001.

[8] M. Zhong, Y. Komarova, J. Rehman, and A. B. Malik, "Mechanosensing Piezo channels in tissue homeostasis including their role in lungs," *Pulmonary Circulation*, vol. 8, no. 2, p. 2045894018767393, 2018.

[9] B. Coste, J. Mathur, M. Schmidt et al., "Piezo1 and Piezo2 are essential components of distinct mechanically activated cation channels," *Science*, vol. 330, no. 6000, pp. 55–60, 2010.

[10] B. J. McHugh, R. Buttery, Y. Lad, S. Banks, C. Haslett, and T. Sethi, "Integrin activation by Fam38A uses a novel mechanism of R-Ras targeting to the endoplasmic reticulum," *Journal of Cell Science*, vol. 123, Part 1, pp. 51–61, 2009.

[11] J. Zhang, Y. Zhou, T. Huang et al., "PIEZO1 functions as a potential oncogene by promoting cell proliferation and migration in gastric carcinogenesis," *Molecular Carcinogenesis*, vol. 57, no. 9, pp. 1144–1155, 2018.

[12] Q. CHEN, B. CAO, N. NAN et al., "Elevated expression of KIF18A enhances cell proliferation and predicts poor survival in human clear cell renal carcinoma," *Experimental and Therapeutic Medicine*, vol. 12, no. 1, pp. 377–383, 2016.

[13] J. T. Kevenaar, S. Bianchi, M. van Spronsen et al., "Kinesin-binding protein controls microtubule dynamics and cargo trafficking by regulating kinesin motor activity," *Current Biology*, vol. 26, no. 7, pp. 849–861, 2016.

[14] E. S. Oswald, P. H. Chao, J. C. Bulinski, G. A. Ateshian, and C. T. Hung, "Chondrocyte nuclear response to osmotic loading," *Conference Proceedings: Annual International Conference of the IEEE Engineering in Medicine and Biology Society*, vol. 2006, pp. 3659–3661, 2006.

[15] K. Saotome, S. E. Murthy, J. M. Kefauver, T. Whitwam, A. Patapoutian, and A. B. Ward, "Structure of the

mechanically activated ion channel Piezo1," *Nature*, vol. 554, no. 7693, pp. 481–486, 2018.

[16] E. L. Grishchuk, "A slippery walk to the microtubule-end," *Biophysical Journal*, vol. 104, no. 11, pp. 2324-2325, 2013.

[17] A. Czechanski, H. Kim, C. Byers, I. Greenstein, J. Stumpff, and L. G. Reinholdt, "Kif18A is specifically required for mitotic progression during germ line development," *Developmental Biology*, vol. 402, no. 2, pp. 253–262, 2015.

[18] M. O. Jortikka, J. J. Parkkinen, R. I. Inkinen et al., "The role of microtubules in the regulation of proteoglycan synthesis in chondrocytes under hydrostatic pressure," *Archives of Biochemistry and Biophysics*, vol. 374, no. 2, pp. 172–180, 2000.

[19] P. A. Gottlieb, C. Bae, and F. Sachs, "Gating the mechanical channel Piezo1: a comparison between whole-cell and patch recording," *Channels (Austin, Tex.)*, vol. 6, no. 4, pp. 282–289, 2014.

[20] A. H. Lewis and J. Grandl, "Mechanical sensitivity of Piezo1 ion channels can be tuned by cellular membrane tension," *eLife*, vol. 4, 2015.

[21] R. Syeda, M. N. Florendo, C. D. Cox et al., "Piezo1 channels are inherently mechanosensitive," *Cell Reports*, vol. 17, no. 7, pp. 1739–1746, 2016.

[22] C. D. Cox, C. Bae, L. Ziegler et al., "Removal of the mechanoprotective influence of the cytoskeleton reveals PIEZO1 is gated by bilayer tension," *Nature Communications*, vol. 7, no. 1, p. 10366, 2016.

[23] Y. Hou, C. Chen, S. Zhou, Y. Li, D. Wang, and L. Zhang, "Fabrication of an integrated cartilage/bone joint prosthesis and its potential application in joint replacement," *Journal of the Mechanical Behavior of Biomedical Materials*, vol. 59, pp. 265–271, 2016.

[24] Y. Huang, Y. Yao, H. Z. Xu, Z. G. Wang, L. Lu, and W. Dai, "Defects in chromosome congression and mitotic progression in KIF18A-deficient cells are partly mediated through impaired functions of CENP-E," *Cell Cycle*, vol. 8, no. 16, pp. 2643–2649, 2014.

Hindawi
BioMed Research International
Volume 2020, Article ID 4035306, 12 pages
https://doi.org/10.1155/2020/4035306

Research Article

Rapamycin-Induced Autophagy Promotes the Chondrogenic Differentiation of Synovium-Derived Mesenchymal Stem Cells in the Temporomandibular Joint in Response to IL-1β

Wenjing Liu,[1,2] Haiyun Luo,[2] Ruolan Wang,[3] Yiyuan Kang,[3] Wenting Liao,[4] Yangpeng Sun,[4] Guodong Chen,[1] and Longquan Shao[2]

[1]*Shunde Hospital, Southern Medical University (The First People's Hospital of Shunde), Foshan 528308, China*
[2]*Stomatological Hospital, Southern Medical University, Guangzhou 510280, China*
[3]*Nanfang Hospital, Southern Medical University, Guangzhou 510515, China*
[4]*Department of Oral and Maxillofacial Surgery, Guanghua School of Stomatology, Hospital of Stomatology, Sun Yat-sen University, Guangzhou 510055, China*

Correspondence should be addressed to Guodong Chen; chenzejia99@163.com and Longquan Shao; shaolongquan@smu.edu.cn

Received 25 May 2020; Accepted 28 September 2020; Published 22 October 2020

Academic Editor: Yu Sheng Li

Cartilage defects in temporomandibular disorders (TMD) lead to chronic pain and seldom heal. Synovium-derived mesenchymal stem cells (SMSCs) exhibit superior chondrogenesis and have become promising seed cells for cartilage tissue engineering. However, local inflammatory conditions that affect the repair of articular cartilage by SMSCs present a challenge, and the specific mechanism through which the function remains unclear. Thus, it is important to explore the chondrogenesis of SMSCs under inflammatory conditions of TMD such that they can be used more effectively in clinical treatment. In this study, we obtained SMSCs from TMD patients with severe cartilage injuries. In response to stimulation with IL-1β, which is well known as one of the most prevalent cytokines in TMD, MMP13 expression increased, while that of SOX9, aggrecan, and collagen II decreased during chondrogenic differentiation. At the same time, IL-1β upregulated the expression of mTOR and decreased the ratio of LC3-II/LC3-I and the formation of autophagosomes. Further study revealed that rapamycin pretreatment promoted the migration of SMSCs and the expression of chondrogenesis-related markers in the presence of IL-1β by inducing autophagy. 3-Benzyl-5-((2-nitrophenoxy)methyl)-dihydrofuran-2(3H)-one (3BDO), a new activator of mTOR, inhibited autophagy and increased the expression of p-GSK3βser9 and β-catenin, simulating the effect of IL-1β stimulation. Furthermore, rapamycin reduced the expression of mTOR, whereas the promotion of LC3-II/LC3-I was blocked by the GSK3β inhibitor TWS119. Taken together, these results indicate that rapamycin enhances the chondrogenesis of SMSCs by inducing autophagy, and GSK3β may be an important regulator in the process of rapamycin-induced autophagy. Thus, inducing autophagy may be a useful approach in the chondrogenic differentiation of SMSCs in the inflammatory microenvironment and may represent a novel TMD treatment.

1. Introduction

Temporomandibular disorder (TMD) is a common disease in the maxillofacial region. Irreversibly damaged cartilage in TMD leads to severe pain and mandibular movement disorders. Currently, the primary TMD treatments, including occlusal plates, drugs, physical or psychological treatments, joint irrigation, or surgical intervention, can alleviate symptoms but cannot repair damaged cartilage.

With the development of regenerative medicine, stem cell-based tissue engineering technology provides a new opportunity for cartilage reconstruction. However, mesenchymal stem cells (MSCs) from different sources exhibit different characteristics. For instance, in vitro assays have shown that synovium-derived MSCs (SMSCs) exhibit stronger proliferation abilities, slower cell senescence, and better chondrogenic abilities than MSCs from other sources in vitro, such as bone marrow MSCs and adipose MSCs [1].

Thus, SMSCs may be the best candidate for articular cartilage repair. With the progress and development of research, the survival, proliferation, and differentiation properties of MSCs have been shown to differ with respect to the local disease [2]. The results of our previous study also showed that inflammatory factors associated with TMD stimulate the inflammatory secretion from SMSCs, which may not be conducive to chondrocyte regeneration [3]. Therefore, investigating the differential capacity and mechanisms of SMSCs in the inflammatory microenvironment is necessary to provide new insights into the TMD treatment.

Autophagy is an important mechanism for maintaining the balance of the intracellular environment by degrading cell metabolites and restoring functional cellular proteins. At the same time, autophagy plays a regulatory role in stem cell proliferation and multidirectional differentiation. Studies have focused on the effects of autophagy with respect to chronic inflammation of the synovium[4, 5]. However, whether autophagy plays a role in the chondrogenesis of SMSCs under inflammatory conditions has not yet been investigated. Glycogen synthase kinase 3β (GSK3β) regulates the degradation of β-catenin and affects the activity of the Wnt/β-catenin pathway, which plays an important role in cartilage regeneration and differentiation [6, 7]. However, the relationship between GSK3β and autophagy remains uncertain. A previous study demonstrated that GSK3β stimulates the unc-51 like kinase 1 (ULK1) to elicit autophagy [8], and subsequent studies showed that GSK3 positively regulates the mammalian target of rapamycin complex 1 (mTORC1) to inhibit autophagic activity[9]. Therefore, the effect of GSK3β on autophagy during the chondrogenic differentiation of SMSCs in the presence of inflammatory cytokines remains elusive.

As an important inflammatory cytokine in the initiation and development of TMD, IL-1β was widely used to simulate the inflammatory microenvironment of TMD in vitro[10, 11]. In this study, we showed that IL-1β inhibited the autophagy and chondrogenic differentiation of SMSCs. Rapamycin, a target for mTOR and an autophagy activator, promoted the chondrogenesis of SMSCs in response to IL-1β stimulation. Moreover, GSK3β inhibition disrupted the rapamycin-mediated activation of autophagy during chondrogenic induction. These findings may provide a theoretical foundation for the use of rapamycin in cell-based therapies in cartilage regeneration and TMD.

2. Materials and Methods

2.1. SMSCs Were Cultured In Vitro. The synovium intima specimens were obtained in open temporomandibular joint surgery from 10 TMD patients with severe cartilage tissue injuries. The study was approved by the Institutional Ethics Board of the Stomatology Hospital, Sun Yat-sen University (ERC-2017-8). The specimens were isolated from 25 to 64 years old patients without systemic diseases and local application of medicines, with 8 females and 2 males. The sample providers signed informed consent before surgery.

The obtained synovial membranes were cut into pieces and digested with 4 mg/mL type I collagenase (Sigma-Aldrich, USA) for 2.5 hours at 37°C. After centrifugation, the precipitates were cultured in low glucose Dulbecco's modified Eagle medium (DMEM; Gibco, USA) with 10% fetal bovine serum (FBS; Gibco, USA) at 37°C. The cells from each sample were mixed and passaged at a ratio of 1 : 3, and cells from passages 4–8 were used for all subsequent experiments.

2.2. Surface Phenotype Identification of SMSCs by Flow Cytometry. The cells were harvested and incubated with different surface marker antibodies, including CD73 (1 : 11; Miltenyi Biotec, Germany), CD44, CD90, CD105, CD11b, HLA-DR, CD45, CD34 (1 : 20; BD Biosciences, USA), and isotype control (1 : 20; BD Biosciences, USA), then washed with PBS. The cell fluorescence was detected through FC500 Flow Cytometer (Beckman Coulter, USA) and analyzed with the CXP Software (Beckman Coulter, USA).

2.3. Multilineage Differentiation of SMSCs

2.3.1. Osteogenic Differentiation. SMSCs were cultured in six-well plates with osteogenic induction medium, which composed of high glucose DMEM (Gibco, USA), 10 mM sodium β-glycerophosphate (Santa Cruz Biotechnology, USA), 10% FBS, 50 μg/L ascorbic acid-2-phosphate (Wako, Japan), and 100 nM dexamethasone (MP Biomedicals, USA). The control group was cultured with complete culture medium. After induction for 2 weeks, the cells in the plates were fixed and stained with alizarin red solution (Cyagen, USA). The gene expression levels of alkaline phosphatase (ALP) and runt-related transcription factor 2 (RUNX2) were quantitated by reverse-transcription quantitative polymerase chain reaction (qRT-PCR).

2.3.2. Adipogenic Differentiation. The SMSCs of the induction group were replaced with adipogenic induction medium consisted of high-glucose DMEM, 0.5 μM isobutyl methylxanthine (Sigma-Aldrich, USA), 10% FBS, 1 μM dexamethasone (MP Biomedicals, USA), 10 μg/mL insulin (Telenbiotech, China), and 200 μM indomethacin (Sigma-Aldrich, USA). After 2 weeks of incubation, the cells were fixed and stained with oil red O (Cyagen, USA). The gene expression of peroxisome proliferator-activated receptor gamma (PPARG) 2 and lipoprotein lipase (LPL) were determined by qRT-PCR.

2.3.3. Chondrogenic Differentiation. SMSCs (3×10^5) were harvested and placed in a 15 mL centrifuge tube with chondrogenic induction medium (Stem Chondro Diff Kit; Invitrogen, USA). After incubation for 2 weeks, the cartilage pellets were fixed and paraffin-embedded. The sample sections were stained with alcian blue staining reagent for 30 min to detect the glycosaminoglycan and collagen II (1 : 100; Cell Signaling Technology, USA); immunohistochemical staining was performed following the manufacturers' instructions. The gene expression of aggrecan (ACAN), matrix metallopeptidase 13 (MMP13) and sex-determining region Y-type high mobility group box gene 9 (SOX9) in the chondrogenic pellets were detected by qRT-

Table 1: Oligonucleotide primers used in PCR.

Gene	Primer sequence
RUNX2	Fw 5′-TCAACGATCTGAGATTTGTGGG-3′
	Rv 5′-GGGGAGGATTTGTGAAGACGG-3′
ALP	Fw 5′-CAGTTGAGGAGGAGAACCCG-3′
	Rv 5′-CACATATGGGAAGCGGTCCA-3′
PPARG2	Fw 5′-GCAAACCCCTATTCCATGCTG-3′
	Rv 5′-CACGGAGCTGATCCCAAAGT-3′
LPL	Fw 5′-CAAGAGTGAGTGAACAAC-3′
	Rv 5′-AATTATGCTGAAGGACAAC-3′
SOX9	Fw 5′-ACACACAGCTCACTCGACCTTG-3′
	Rv 5′-AGGGAATTCTGGTTGGTCCTCT-3′
MMP13	Fw 5′-GACTGGTAATGGCATCAAGGGA-3′
	Rv 5′-CACCGGCAAAAGCCACTTTA-3′
ACAN	Fw 5′-CTTCCGCTGGTCAGATGGAC-3′
	Rv 5′-CGTTTGTAGGTGGTGGCTGTG-3′
GAPDH	Fw 5′-GACAGTCAGCCGCATCTTCT-3′
	Rv 5′-TTAAAAGCAGCCCTGGTGAC-3′

PCR. The control group was cultured with a complete culture medium instead of chondrogenic induction medium.

2.4. Reagent Preparation. IL-1β (PeproTech, USA) was dissolved in double-distilled water. Rapamycin (Selleck, USA) and 3-benzyl-5-((2-nitrophenoxy) methyl)-dihydrofuran-2(3H)-one (3BDO) (Selleck, USA) were dissolved in dimethyl sulfoxide (DMSO; MP Biomedicals, USA). The cells cultured in the medium without rapamycin and 3BDO were also contained 0.1% DMSO.

2.5. Immunohistochemical Staining. The sections for cartilage pellets were dewaxed and rehydrated and then incubated with 3% H_2O_2. After antigen retrieval, blocked with 5% bovine serum albumin (BSA, Leagene, China). The sections were incubated with primary antibody (Collagen II, 1 : 100, Cell Signaling Technology, USA; SOX9, 1 : 50, Santa Cruz Biotechnology, USA) overnight at 4°C. After washed with phosphate-buffered saline (PBS; Gibco, USA), the slides were incubated in secondary antibody (Boster, China), streptavidin-biotin complex, and 3,3′-diaminobenzidine (DAB; Boster, China) follow one another. The stained sections onto microscope slides were evaluated by light microscopy (Leica, Germany).

2.6. Immunofluorescence Assay. SMSCs were seeded on glass coverslips in 24-well plates and treated as the experiment group processing. After another 24 hours, the chondrogenic induction cells were fixed and subsequently treated with 0.3% Triton X-100 (MP Biomedicals, USA). After washed with PBS, the cells were then incubated in 5% BSA. Then, the cells were incubated with microtubule-associated protein light chain 3 (LC3) rabbit monoclonal antibody (1 : 100; Abcam, USA) overnight at 4°C. The negative control group was treated with 1% BSA instead of the primary antibody. The FITC-conjugated goat antirabbit IgG (1 : 100; Proteintech, USA) was added for 1 hour and then incubated with DAPI staining solution (Leagene, China) for 15 min. The coverslip was dried and sealed with antifluorescence quenching agent (Beyotime, China). The cells were observed under laser confocal microscopy (FV10i, Olympus, Japan).

2.7. Transmission Electron Microscopy. The cells were fixed in 2.5% glutaraldehyde and embedded with epoxy resin (Sigma-Aldrich, USA). The sample sections were stained with lead citrate (Sigma-Aldrich, USA) and assessed under the electron microscope (JEM-2100F, Hitachi, Japan).

2.8. Cell Migration Assay. SMSCs were seeded on a 24-well plate. After 80% confluence of cells, the complete culture media was replaced by low glucose DMEM with 1% FBS for 24 hours. A scratch was taken by a sterile pipette tip (1 mL) in each well. The exfoliated cells were removed with PBS and then added reagents according to the experiment grouping. The initial images were taken under an inverted microscope (Leica, Germany). After 24 hours, the cells were fixed and stained with crystal violet solution. The images were taken by using a stereomicroscope (Leica, Germany).

2.9. QRT-PCR Assay. The total RNA of each sample was extracted according to the manufacturer's instructions. Reverse transcription obtained cDNA using the prime script RT Kit (Takara, Japan). Finally, the relative mRNA expression levels for the RUNX2, ALP, LPL, PPARG2, SOX9, ACAN, and MMP13 were determined by PCR with SYBR Premix Ex TM Taq II (Takara, Japan). The glyceraldehyde 3-phosphate dehydrogenase (GAPDH) expression was used as the reference for relative quantitative statistics. The primers for these genes are listed in Table 1.

2.10. Western Blot Analysis. The proteins were extracted and measured using the BCA Protein Assay Kit (Thermo Fisher, USA). The denatured proteins were electrophoretically separated and transferred onto polyvinylidene difluoride (PVDF) membranes (Millipore, USA). After blocked with 5% BSA for 1 hour at room temperature, the membranes were immersed with the primary antibodies (Collagen II, 1 : 1000, Cell Signaling Technology, USA; LC3, 1 : 1000, Abcam, USA; p-mTOR, 1 : 1000, Cell Signaling Technology, USA; mTOR, 1 : 1000, Cell Signaling Technology, USA; GSK3β, 1 : 1000, Huabio, China; p-GSK3βser9, 1 : 1000, Huabio, China; β-catenin, 1 : 1000, Cell Signaling Technology, USA; GAPDH, 1 : 2000, Abcam, USA) overnight at 4°C, respectively. After washed with TBST (Beyotime Biotechnology, China), the membranes were incubated with IgG conjugated to horseradish peroxidase (1 : 2000; Santa Cruz Biotechnology, USA). The protein bands were visualized by using an ECL kit (Merck Millipore, USA). The relative expression level of specific protein was quantified by the optical density of the target

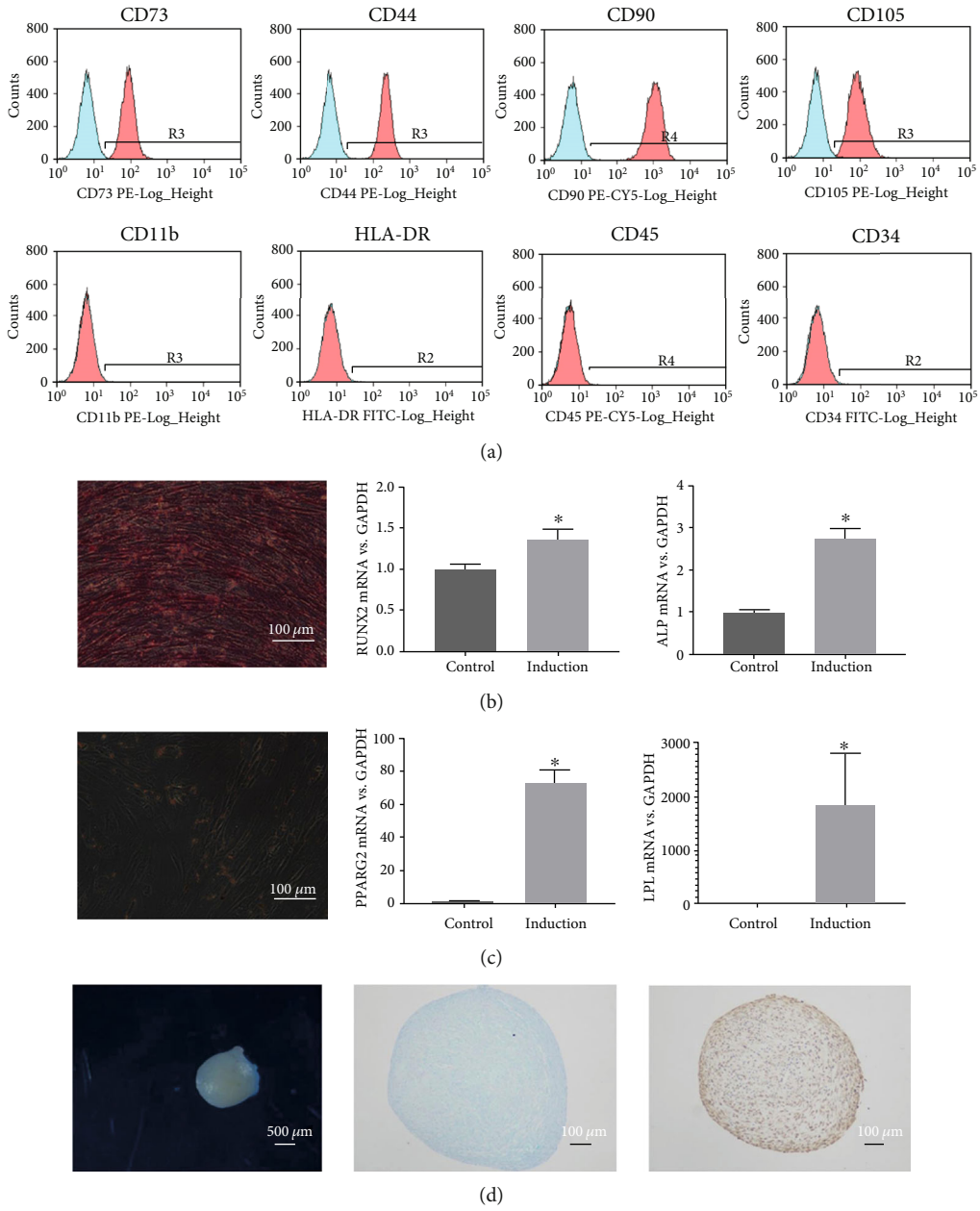

FIGURE 1: Characterization of SMSCs in the temporomandibular joint. (a) SMSCs tested positive for CD90, CD73, CD105, CD44, and negative for CD34, CD11b, CD45, HLA-DR. (b) Alizarin red staining of SMSCs cultured in osteogenic medium for 2 weeks, and the relative levels of RUNX2 and ALP mRNA in the control and osteogenic induction groups (scale bars = 100 μm; * indicates $p < 0.05$). (c) Oil red O staining of SMSCs after adipogenic induction for 2 weeks, and the relative levels of PPARG2 and LPL mRNA in the control and adipogenic induction groups (scale bars = 100 μm; * indicates $p < 0.05$). (d) Cartilage pellet formed in the chondrogenic medium over 2 weeks (scale bars = 500 μm); alcian blue staining and collagen II immunohistochemical staining of cells in the pellet (scale bars = 100 μm).

band against that of GAPDH using a Bio-Rad image analyzer (Bio-Rad, USA).

2.11. Statistical Analysis. The results were analyzed through the GraphPad software, and the data are expressed as mean ± standard deviation (SD) of three biological replicates. Student's t test was used for comparisons between the two groups, while one-way ANOVA was used for analyzing more than two groups. p values <0.05 were considered statistically significant.

3. Results

3.1. Characterization of SMSCs. SMSCs grew with adherence and expressed CD73, CD105, CD44, and CD90 but not CD11b, HLA-DR, CD34, and CD45 (Figure 1(a)).

Additionally, SMSCs exhibited multipotent differentiation potential under specific induction. After osteogenic medium induction, the differentiation of SMSCs was evidenced by significant calcium mineralization with alizarin red staining. The gene expression of osteogenic markers,

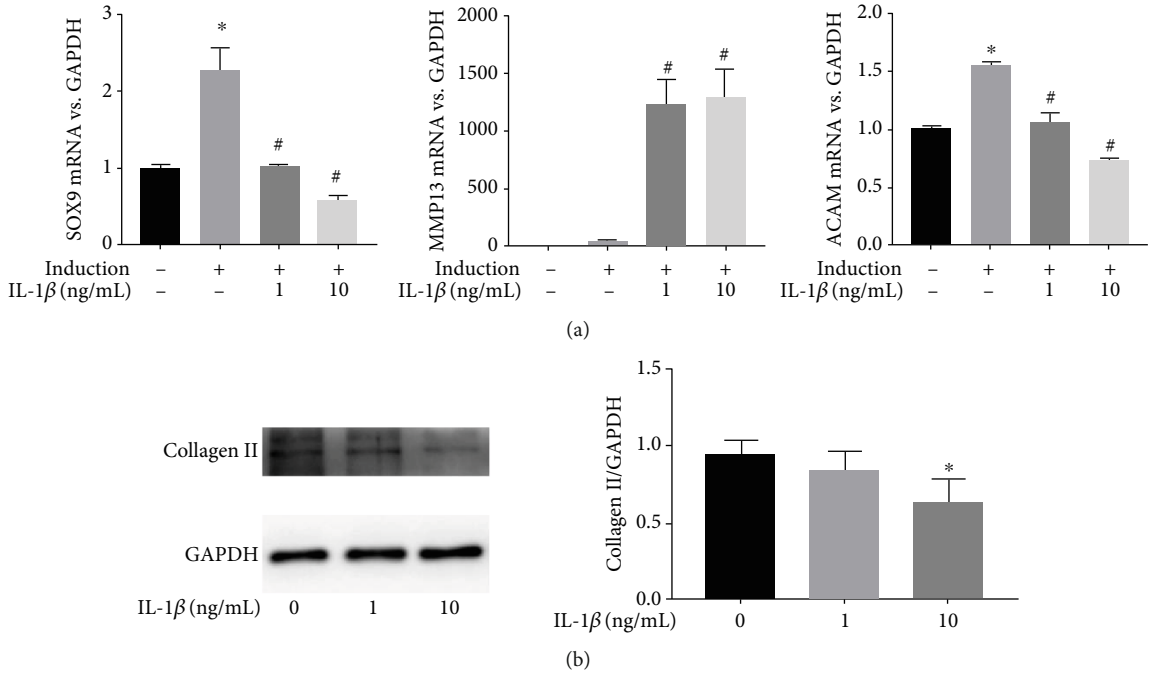

Figure 2: IL-1β impedes the chondrogenesis of SMSCs. (a) Relative levels of SOX9, MMP13, and ACAN mRNA during the chondrogenic differentiation of SMSCs treated with or without IL-1β for 2 weeks (* indicates $p < 0.05$ compared with the control group; $^\#$ indicates $p < 0.05$ compared with the chondrogenic induction group without IL-1β stimulation). (b) Collagen II protein expression was detected by a western blot assay (* indicates $p < 0.05$ compared with the chondrogenic induction group without IL-1β stimulation).

RUNX2 and ALP, in the induced group was higher than that observed in the control group ($p = 0.013$, $p < 0.001$) (Figure 1(b)). In addition, we observed lipid droplets and positive staining for oil red O after 2 weeks of adipogenic differentiation. The gene expression of adipogenic markers, PPARG2 and LPL, in the induced group was higher than that observed in the control group ($p = 0.028$, $p < 0.001$) (Figure 1(c)). In addition, in the chondrogenic differentiation group, the cartilage pellets were observed. The cartilage pellet sections showed positive alcian blue staining, and collagen II was highly expressed in the immunohistochemical analysis (Figure 1(d)).

3.2. IL-1β Inhibits the Chondrogenesis of SMSCs. IL-1β initiates a cascade of inflammatory responses in TMD and ultimately leads to tissue destruction. We observed that the chondrogenic differentiation ability of SMSCs decreased when cultured in chondrogenic induction medium supplemented with 1 or 10 ng/mL IL-1β for 2 weeks. Furthermore, the gene expression of MMP13 increased ($p < 0.001$), while that of SOX9 and ACAN decreased with increasing concentrations of IL-1β ($p < 0.001$, $p < 0.001$) (Figure 2(a)). In addition, the western blotting results showed that collagen II expression decreased accordingly in the IL-1β-mediated chondrogenic induction group ($p = 0.049$) (Figure 2(b)).

3.3. IL-1β Inhibits the Autophagy of SMSCs during Chondrogenic Induction. To investigate the role of autophagy in the chondrogenesis of inflammatory SMSCs, we assessed the number of autophagosomes and the expression of the autophagy-related indicators mTOR and LC3 in the different groups. Transmission electron microscopy images showed that the number of autophagosomes was decreased in the high IL-1β stimulation group compared with that observed in the control group 24 h after chondrogenic induction (Figure 3(a)). Furthermore, the protein expression of p-mTOR was upregulated ($p = 0.018$), while the ratio of LC3II/LC3I was decreased ($p = 0.038$) in SMSCs after a 24 h treatment with IL-1β based on western blot results (Figure 3(b)). Moreover, immunofluorescence assay results showed that the number of LC3-positive punctures in SMSCs significantly decreased 24 hours after treatment with IL-1β to mediate chondrogenic induction (Figure 3(c)). When the cells were treated with rapamycin, autophagy was activated, and the number of LC3-positive punctures in SMSCs was increased accordingly (Figure 3(c)).

3.4. Rapamycin Promotes the Migration and Chondrogenesis of SMSCs. MSC migration to damaged tissue and colonization are prerequisites for tissue repair. The crystal violet staining results showed that the scratch width was larger at 24 hours in the IL-1β treatment group than that observed in the control group ($p = 0.002$). In the rapamycin group, scratch closure was significantly increased compared to that observed in SMSCs without rapamycin ($p < 0.001$) (Figure 4), suggesting that rapamycin-induced autophagy enhanced the migration of SMSCs.

With respect to chondrogenesis, rapamycin significantly increased the gene expression of SOX9 and ACAN in cartilage pellets in the presence of IL-1β ($p < 0.001$, $p = 0.004$) but decreased the MMP13 expression ($p < 0.001$) (Figure 5(a)). Similar results were observed by histological

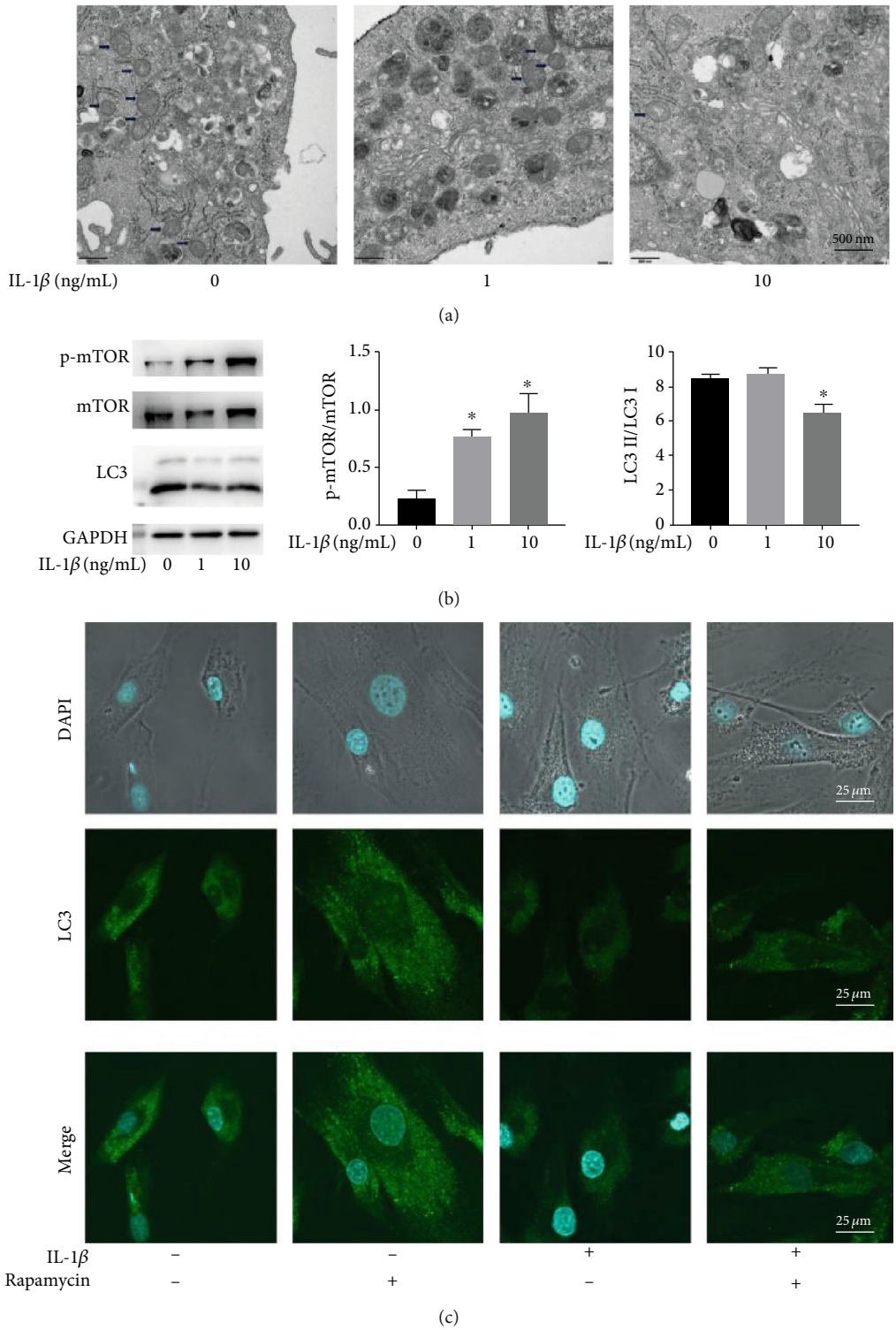

Figure 3: IL-1β inhibits autophagy in SMSCs by activating mTOR. (a) Transmission electron microscopy images showing autophagosomes in SMSCs after chondrogenic induction for 24 h (arrows, scale bars = 500 nm). (b) Expression of the autophagy-related proteins mTOR and LC3 in SMSCs treated with IL-1β (* indicates $p < 0.05$ compared with the control group). (c) SMSCs were seeded on glass coverslips for 24 h in the chondrogenic induction culture medium, chondrogenic induction culture medium supplemented with 100 nM rapamycin, chondrogenic induction culture medium supplemented with 10 ng/mL IL-1β, or with a 1-h preincubation with 100 nM rapamycin prior to the addition of 10 ng/mL IL-1β in the chondrogenic induction culture medium, and LC3-positive punctures were observed in an immunofluorescence assay (scale bars = 25 μm).

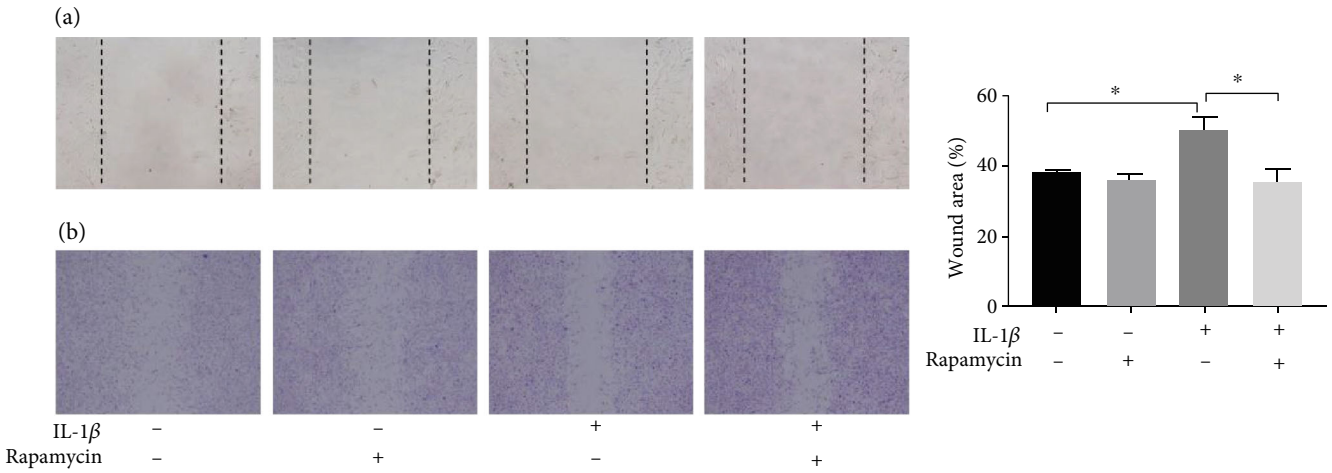

FIGURE 4: Rapamycin promotes the migration of SMSCs. (a) Scratch was made in SMSCs, which were seeded in a 24-well plate. (b) The scratch width was stained with crystal violet solution in each group after 24 h (* indicates $p < 0.05$).

staining with respect to the formation of alcian blue deposits, and the number of SOX9- and collagen II-positive cells was increased in cartilage pellets pretreated with rapamycin compared to that observed in the group treated with IL-1β alone ($p = 0.040$, $p = 0.004$, $p = 0.010$) (Figure 5(b)).

3.5. Rapamycin Upregulates the Autophagy of SMSCs through GSK3β. The inhibition of the GSK3β activity and the expression of β-catenin can activate the Wnt/β-catenin signalling pathway, which was reported to affect the cartilage function and metabolism. To study the effect of GSK3β inhibition in autophagy in chondrogenesis, we examined the changes of GSK3β, β-catenin, and LC3 expression in inflammatory SMSCs by western blot assays. We observed that cells treated with IL-1β had increased levels of p-GSK3βser9 and β-catenin ($p = 0.047$, $p = 0.035$). Consistent with the effect of IL-1β, cells treated with 3BDO (50 μg/mL), an activator of mTOR signalling, led to autophagy inhibition and higher levels of p-GSK3βser9 and β-catenin than was observed in the control treatment ($p = 0.059$, $p = 0.048$). In contrast, rapamycin pretreatment decreased the p-GSK3βser9 and β-catenin in the SMSCs produced by IL-1β treatment ($p = 0.002$, $p = 0.0497$). The activity of GSK3β is inhibited when phosphorylated at serine 9. Furthermore, the addition of the GSK3β inhibitor TWS119 in the IL-1β+rapamycin treatment group disrupted the autophagic activity and reduced the expression of LC3-II/LC3-I ($p = 0.026$) (Figure 6). These results show that GSK3β may be a key downstream target of mTOR and play a role in regulating autophagy.

4. Discussion

The prevalence of TMD is increasing and has become the second most important musculoskeletal disorder affecting the quality of life [12]. Along with inflammatory progression, the injured articular cartilage in TMD has limited capacity to heal. The application of MSCs and tissue engineering technology to repair cartilage destruction has become a hotspot in the field of TMD treatment[13]. MSCs can be derived from specific tissues including the bone marrow, blood, teeth, muscle, and skin, showing different advantages in the proliferation efficiency or pluripotency capacity. SMSCs have been shown to be the best choice for cartilage repair [1, 14]. A study showed the number of synovial fluid-derived MSCs, which is similar to SMSCs, increased along with the radiological grading of osteoarthritis [15]. However, the cartilage repair ability of the existing MSCs still needs to be further elucidated.

Recent studies have revealed that the local microenvironment can affect the biological potential of stem cells by initiating signal transduction. For example, inflammatory factors or bacterial components in periodontitis can affect the osteogenic differentiation of periodontal ligament MSCs [16, 17]. In response to IL-1β, TNF-α, or coculture with leukocytes, the osteogenic differentiation ability of adipose MSCs is enhanced, while the chondrogenic and adipogenic differentiation ability is impaired[18, 19]. Our previous study also showed that in the inflammatory microenvironment, the synovial fluid-derived MSCs exhibit an increased secretion of IL-6 and IL-8, which are the primary catabolic cytokines of the cartilage matrix [20]. Furthermore, SMSCs from the hip joints of individuals with osteoarthritis showed greater osteogenic and adipogenic potentials, whereas the cells from patients with femoroacetabular impingement syndrome showed greater chondrogenic potential [2]. Thus, the properties of MSCs are closely associated with specific pathologies, and inflammatory cytokines are one of the main obstacles affecting the multilineage differentiation. During the process of chondrogenesis, ACAN and collagen II are the main cartilage matrix components. SOX9 is one of the primary regulators of chondrogenic differentiation and promotes the expression of chondrocyte matrix components (including ACAN and collagen II). By contrast, MMP13 is a major matrix proteinase that targets collagen II, which plays an important role in cartilage degradation. Therefore, we detected the relative expression of the

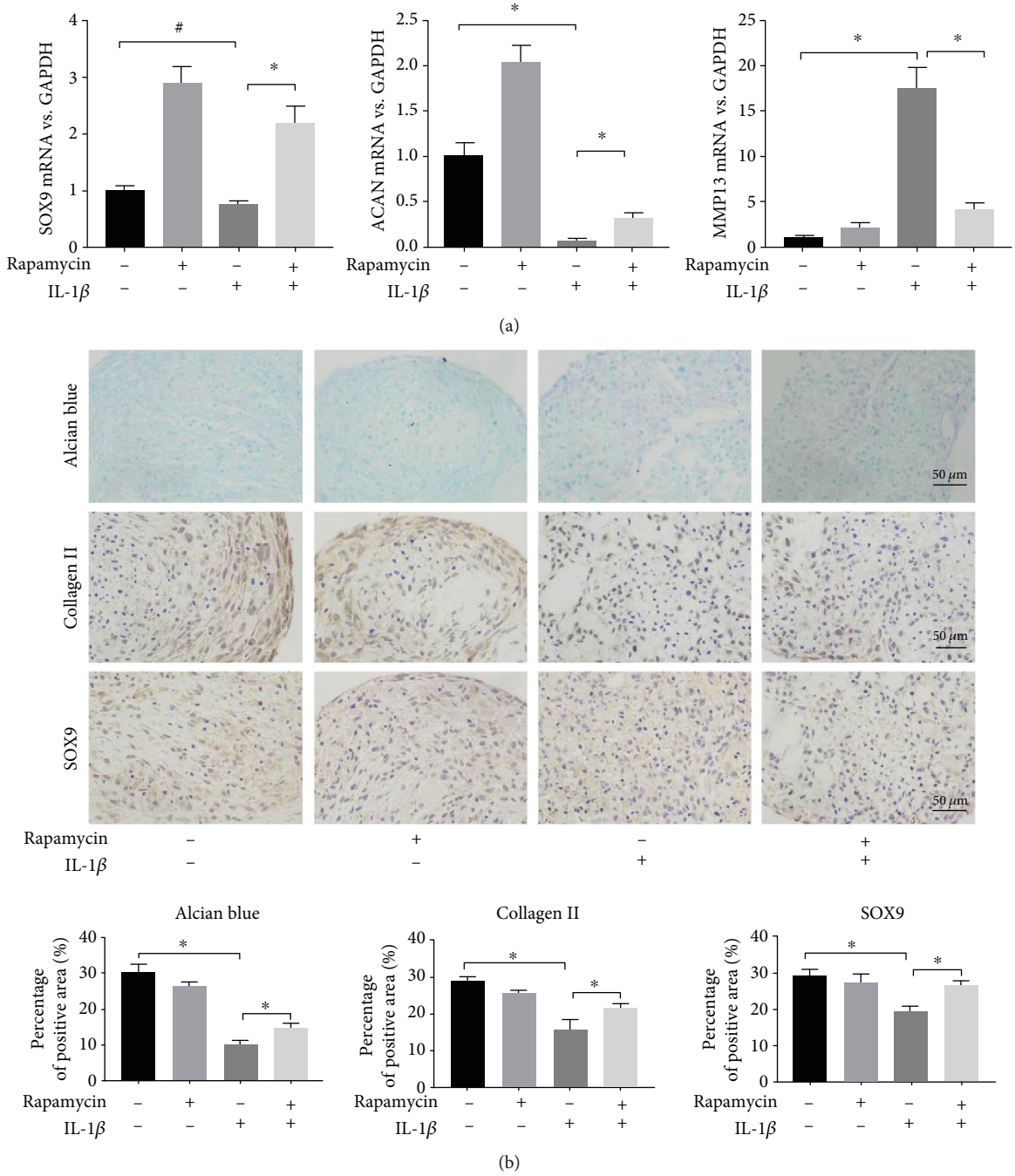

Figure 5: Rapamycin enhances the chondrogenesis of SMSCs. (a) Relative levels of SOX9, ACAN, and MMP13 mRNA in each group in response to chondrogenic induction for 2 weeks as detected by qRT-PCR (* indicates $p < 0.05$, # indicates $p < 0.10$). (b) Alcian blue staining and collagen II- and SOX9-positive immunostained cells in the cartilage pellet of each group (scale bars = 50 μm) (* indicates $p < 0.05$).

above related biomarkers in the presence of IL-1β, which is the main inflammatory cytokine in TMD [20], and found that the chondrogenesis of SMSCs decreased.

Autophagy dynamically maintains cell self-renewal and metabolism. Autophagy activation has been shown to occur during the multidifferentiation of MSCs, including the osteogenic differentiation of the dental pulp MSCs [21], the adipogenic [22] and neuron-induced differentiation [23] of bone marrow MSCs, and the skeletal muscle differentiation of human tonsil-derived MSCs [24]. However, the role of autophagy in chondrogenesis is seldom reported in the literature. Moreover, decreased autophagy results in the accumulation of reactive oxygen species, which leads to mitochondrial dysfunction and promotes the apoptosis of synovial cells [4]. In contrast, the decreased levels of autophagy have been observed in the synovium of adjuvant arthritis

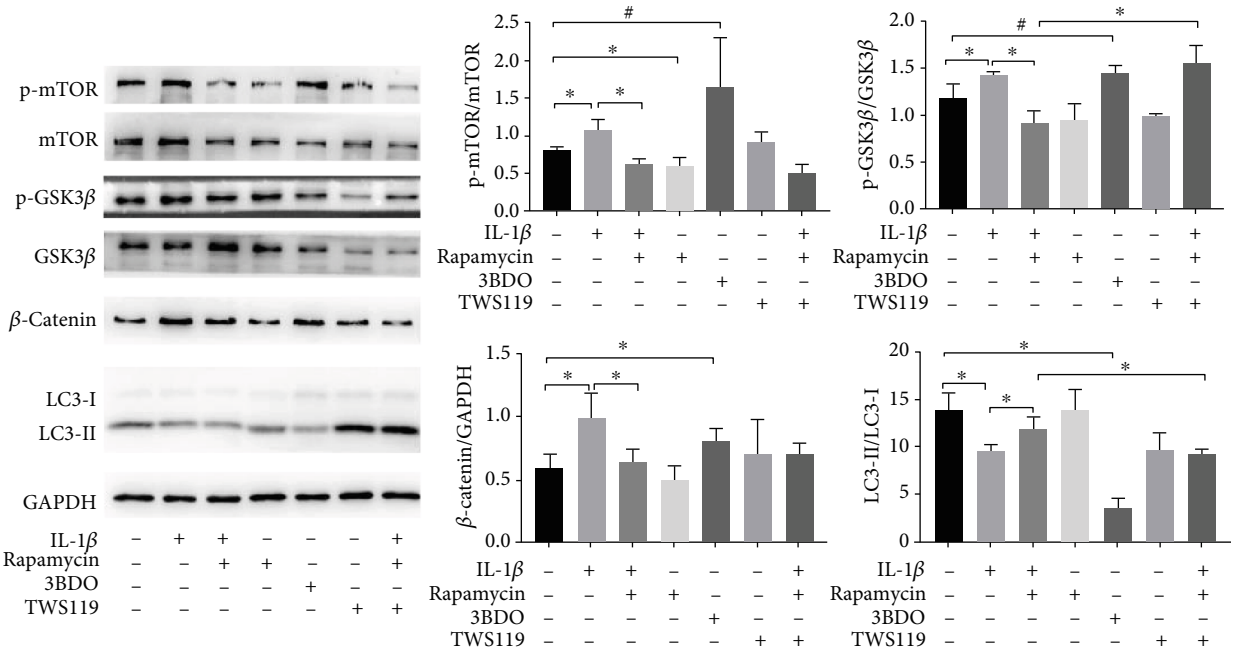

Figure 6: Rapamycin upregulates autophagy in SMSCs through GSK3β. Protein expression levels of mTOR, GSK3β, β-catenin, and LC3 in SMSCs in each group were detected by western blot assays (* indicates $p < 0.05$, $^\#$ indicates $p < 0.10$).

rats, leading to the excessive proliferation of synovial cells [5]. The dual roles of autophagy in the regulation of synovial cells are not conducive to the homeostasis of the intra-articular environment. Therefore, we speculated that autophagy may be involved in the disabling of chondrogenic differentiation by SMSCs, and the results of this study demonstrated that the autophagy levels decreased in chondrogenic induction experiments with IL-1β. However, the relationship between autophagy and the chondrogenic differentiation of SMSCs needs to be explored in further experiments. Decreased autophagy-related gene expression has been observed in damaged chondrocytes, and enhanced autophagy can slow the pathological progression of osteoarthritis [25, 26]. In addition, autophagy deficiency may affect the growth plate chondrocytes, leading to cartilage development delays [27, 28]. Autophagy has been suggested to be involved in the development and metabolism of cartilage. However, the effect of autophagy on cellular processes may vary depending on the cell sources with specific activating signals. For example, Wang et al. reported that low-intensity pulsed ultrasound promotes rat bone marrow MSC chondrogenesis by inhibiting beclin1-mediated autophagy[29]. In addition, Zhang et al. observed that low-intensity pulsed ultrasound increased the autophagy level of macrophages through SQSTM1-dependent autophagic degradation in osteoarthritis [30]. Whether autophagy plays a role in the chondrogenic differentiation of SMSCs and the associated mechanism has not yet been reported. mTOR is a conserved protein kinase and the key regulator of autophagy. mTOR inhibition-mediated autophagy is an important signalling pathway in the differentiation of MSCs [21]. We found that the expression of mTOR was increased during the IL-1β-induced chondrogenesis. Further studies showed that rapamycin increased the autophagy level and promoted the migration and chondrogenic differentiation of SMSCs in response to IL-1β. These results suggest that rapamycin-activated autophagy can promote the chondrogenic differentiation of SMSCs in the inflammatory microenvironment. This finding may explain the protective role of rapamycin in articular cartilage from osteoarthritis [31, 32]. Intriguingly, it was demonstrated that the activity of mTOR is different in the early and late stages of osteogenic differentiation [21]. Therefore, the role of autophagy throughout the process of chondrogenic differentiation should be elucidated in greater detail in future studies.

As a serine protein kinase, GSK3β is widely involved in cell growth, differentiation, and signal transduction. Furthermore, GSK3β was shown to promote the chondrogenic differentiation of MSCs and maintain the phenotype of chondrocytes in vitro by stimulating the expression of collagen II and aggrecan [33]. Additionally, the activation of GSK3β participates in the ubiquitination of β-catenin and the degradation of the proteasome. β-catenin, a key protein of Wnt signaling, also affects the differentiation and maturation of chondrocytes and promotes the degradation of the cartilage matrix [34]. Consistent with these findings, our results demonstrated that the activity of GSK3β was inhibited and the β-catenin expression was increased in SMSCs in response to IL-1β, having an unfavourable effect on chondrogenesis. The regulation of GSK3β can have a dual role in many physiological processes. Some studies have demonstrated that GSK3β inhibition promotes autophagy by targeting the mTOR pathway or lysosomal biogenesis [35, 36]. However, p-GSK3βser9 can function as a downstream

regulator of mTOR [37]. GSK3β inhibition via the high expression of p-GSK3βser9 has been shown to cause resistance to rapamycin in cancer cell lines [38, 39]. Furthermore, GSK3β inhibition is known to lead to the accumulation of β-catenin, which has been shown to inhibit autophagy [40]. Different outcomes suggest that the role of GSK3β in autophagy depends on cell lines, culture conditions, and duration of exposure. Our results showed that the expression of p-GSK3βser9 and β-catenin is increased and that autophagy is inhibited in SMSCs following mTOR activator. Furthermore, a GSK3β inhibitor reversed the effect of rapamycin-induced autophagy in inflammatory SMSCs. Thus, GSK3β may be a key downstream target of mTOR that affects the level of autophagy. However, the effect of this specific relationship on chondrogenesis still requires additional verification. In our study, we investigated the role of autophagy in the chondrogenesis of SMSCs in response to IL-1β and found that rapamycin-induced autophagy promotes the chondrogenic differentiation of SMSCs through GSK3β and β-catenin.

There are several limitations to this study. The SMSCs used in this study were obtained from patients without distinguishing the differences in age and sex, knowing these variables are important since they can lead to differences in autophagy and chondrogenic differentiation observed in vitro. Furthermore, the long-term and stable effects of rapamycin in inducing autophagy should be conducted through in vivo experiments in future studies.

5. Conclusions

The inhibition of autophagy in SMSCs in response to IL-1β may be an important factor and mechanism for insufficient cartilage repair. This study showed that rapamycin can induce autophagy through GSK3β and promote the chondrogenic differentiation of SMSCs. These findings may shed light on the development of new therapeutic strategies for TMD.

Data Availability

The data used to support the findings of this study are included in the article.

Conflicts of Interest

The authors declare no conflicts of interest in relation to this paper.

Authors' Contributions

SLQ and CGD conceived the study. LWJ, LHY, LWT, SYP, and WRL did the experimental work. LWJ wrote and reviewed the manuscript. KYY provided technical support for the experimental operation.

Acknowledgments

We would like to thank the National Natural Science Foundation of China, the Medical Scientific Research Foundation of Guangdong Province, and the Science Foundation of Southern Medical University for providing financial assistance (81870786, 81900989, B2018119, PY2018N093), and the Postdoctoral sustentation fund of Shunde district, Foshan city.

References

[1] H. Koga, T. Muneta, T. Nagase et al., "Comparison of mesenchymal tissues-derived stem cells for in vivo chondrogenesis: suitable conditions for cell therapy of cartilage defects in rabbit," *Cell and Tissue Research*, vol. 333, no. 2, pp. 207–215, 2008.

[2] Y. Murata, S. Uchida, H. Utsunomiya et al., "Differentiation potential of synovial mesenchymal stem cells isolated from hip joints affected by femoroacetabular impingement syndrome versus osteoarthritis," *Arthroscopy*, vol. 36, no. 8, pp. 2122–2133, 2020.

[3] W. Liao, J. Sun, W. Liu et al., "HDAC10 upregulation contributes to interleukin 1β-mediated inflammatory activation of synovium-derived mesenchymal stem cells in temporomandibular joint," *Journal of Cellular Physiology*, vol. 234, no. 8, pp. 12646–12662, 2019.

[4] W. Cao, J. Zhang, G. Wang, J. Lu, T. Wang, and X. Chen, "Reducing-autophagy derived mitochondrial dysfunction during resveratrol promotes fibroblast-like synovial cell apoptosis," *The Anatomical Record*, vol. 301, no. 7, pp. 1179–1188, 2018.

[5] Y. L. Wang, J. Liu, L. Wan, L. P. Ruan, and W. F. Ye, "Effect of Xinfeng capsule on Beclin 1/PI3K-AKT-mTOR of adjuvant arthritis rats," *Chinese Journal of Integrated Traditional and Western Medicine*, vol. 37, no. 4, pp. 464–469, 2017.

[6] P. Meo Burt, L. Xiao, and M. M. Hurley, "FGF23 regulates Wnt/β-Catenin signaling-mediated osteoarthritis in mice overexpressing high-molecular-weight FGF2," *Endocrinology*, vol. 159, no. 6, pp. 2386–2396, 2018.

[7] Z. Shu, X. Miao, T. Tang, P. Zhan, L. Zeng, and Y. Jiang, "The GSK-3β/β-catenin signaling pathway is involved in HMGB1-induced chondrocyte apoptosis and cartilage matrix degradation," *International Journal of Molecular Medicine*, vol. 45, no. 3, pp. 769–778, 2020.

[8] S. Y. Lin, T. Y. Li, Q. Liu et al., "Protein phosphorylation-acetylation cascade connects growth factor deprivation to autophagy," *Autophagy*, vol. 8, no. 9, pp. 1385-1386, 2012.

[9] L. Avrahami, R. Paz, K. Dominko, S. Hecimovic, C. Bucci, and H. Eldar-Finkelman, "GSK-3-TSC axis governs lysosomal acidification through autophagy and endocytic pathways," *Cellular Signalling*, vol. 71, article 109597, 2020.

[10] A. Sorenson, K. Hresko, S. Butcher et al., "Expression of Interleukin-1 and temporomandibular disorder: contemporary review of the literature," *Cranio*, vol. 36, no. 4, pp. 268–272, 2018.

[11] H. Tabeian, B. F. Betti, C. C. Dos Santos et al., "IL-1β damages fibrocartilage and upregulates MMP-13 expression in fibrochondrocytes in the condyle of the temporomandibular joint," *International Journal of Molecular Sciences*, vol. 20, no. 9, p. 2260, 2019.

[12] P. Balthazard, V. Hasler, D. Goldman, and F. Grondin, "Association of cervical spine signs and symptoms with temporomandibular disorders in adults: a systematic review

protocol," *JBI Evidence Synthesis*, vol. 18, no. 6, pp. 1334–1340, 2020.

[13] S. Y. Song, J. Hong, S. Go et al., "Interleukin-4 gene transfection and spheroid formation potentiate therapeutic efficacy of mesenchymal stem cells for osteoarthritis," *Advanced Healthcare Materials*, vol. 9, no. 5, article 1901612, 2020.

[14] E. J. Kubosch, G. Lang, D. Furst et al., "The potential for synovium-derived stem cells in cartilage repair," *Current Stem Cell Research & Therapy*, vol. 13, no. 3, pp. 174–184, 2018.

[15] I. Sekiya, M. Ojima, S. Suzuki et al., "Human mesenchymal stem cells in synovial fluid increase in the knee with degenerated cartilage and osteoarthritis," *Journal of orthopaedic research: official publication of the Orthopaedic Research Society*, vol. 30, no. 6, pp. 943–949, 2012.

[16] Y. Tang, L. Liu, P. Wang, D. Chen, Z. Wu, and C. Tang, "Periostin promotes migration and osteogenic differentiation of human periodontal ligament mesenchymal stem cells via the Jun amino-terminal kinases (JNK) pathway under inflammatory conditions," *Cell Proliferation*, vol. 50, no. 6, p. e12369, 2017.

[17] C. Li, B. Li, Z. Dong et al., "Lipopolysaccharide differentially affects the osteogenic differentiation of periodontal ligament stem cells and bone marrow mesenchymal stem cells through Toll-like receptor 4 mediated nuclear factor κB pathway," *Stem Cell Research & Therapy*, vol. 5, no. 3, p. 67, 2014.

[18] L. Brandt, S. Schubert, P. Scheibe et al., "Tenogenic properties of mesenchymal progenitor cells are compromised in an inflammatory environment," *International Journal of Molecular Sciences*, vol. 19, no. 9, p. 2549, 2018.

[19] K. Bahrampour Juybari, T. Kamarul, M. Najafi, D. Jafari, and A. M. Sharifi, "Restoring the IL-1β/NF-κB-induced impaired chondrogenesis by diallyl disulfide in human adipose-derived mesenchymal stem cells via attenuation of reactive oxygen species and elevation of antioxidant enzymes," *Cell and Tissue Research*, vol. 373, no. 2, pp. 407–419, 2018.

[20] W. Liu, Y. Sun, Y. He et al., "IL-1β impedes the chondrogenic differentiation of synovial fluid mesenchymal stem cells in the human temporomandibular joint," *International Journal of Molecular Medicine*, vol. 39, no. 2, pp. 317–326, 2017.

[21] A. Pantovic, A. Krstic, K. Janjetovic et al., "Coordinated time-dependent modulation of AMPK/Akt/mTOR signaling and autophagy controls osteogenic differentiation of human mesenchymal stem cells," *Bone*, vol. 52, no. 1, pp. 524–531, 2013.

[22] B. Q. Song, Y. Chi, X. Li et al., "Inhibition of notch signaling promotes the adipogenic differentiation of mesenchymal stem cells through autophagy activation and PTEN-PI3K/AKT/mTOR pathway," *Cellular Physiology and Biochemistry: International Journal of Experimental Cellular Physiology, Biochemistry, and Pharmacology*, vol. 36, no. 5, pp. 1991–2002, 2015.

[23] B. Li, P. Duan, C. Li et al., "Role of autophagy on bone marrow mesenchymal stem-cell proliferation and differentiation into neurons," *Molecular Medicine Reports*, vol. 13, no. 2, pp. 1413–1419, 2016.

[24] S. Park, Y. Choi, N. Jung et al., "Autophagy induction in the skeletal myogenic differentiation of human tonsil-derived mesenchymal stem cells," *International Journal of Molecular Medicine*, vol. 39, no. 4, pp. 831–840, 2017.

[25] L. W. Huang, T. C. Huang, Y. C. Hu et al., "Zinc protects chondrocytes from monosodium iodoacetate-induced damage by enhancing ATP and mitophagy," *Biochemical and Biophysical Research Communications*, vol. 521, no. 1, pp. 50–56, 2020.

[26] Y. Ge, S. Zhou, Y. Li et al., "Estrogen prevents articular cartilage destruction in a mouse model of AMPK deficiency via ERK-mTOR pathway," *Annals of Translational Medicine*, vol. 7, no. 14, p. 336, 2019.

[27] X. Jin, X. Kang, L. Zhao et al., "Cartilage ablation of Sirt 1 causes inhibition of growth plate chondrogenesis by hyperactivation of mTORC1 signaling," *Endocrinology*, vol. 160, no. 12, pp. 3001–3017, 2019.

[28] X. Wang, H. Qi, Q. Wang et al., "FGFR3/fibroblast growth factor receptor 3 inhibits autophagy through decreasing the ATG12-ATG5 conjugate, leading to the delay of cartilage development in achondroplasia," *Autophagy*, vol. 11, no. 11, pp. 1998–2013, 2015.

[29] X. Wang, Q. Lin, T. Zhang et al., "Low-intensity pulsed ultrasound promotes chondrogenesis of mesenchymal stem cells via regulation of autophagy," *Stem Cell Research & Therapy*, vol. 10, no. 1, p. 41, 2019.

[30] B. Zhang, H. Chen, J. Ouyang et al., "SQSTM1-dependent autophagic degradation of PKM2 inhibits the production of mature IL1B/IL-1β and contributes to LIPUS-mediated anti-inflammatory effect," *Autophagy*, vol. 16, no. 7, pp. 1262–1278, 2020.

[31] B. Carames, A. Hasegawa, N. Taniguchi, S. Miyaki, F. J. Blanco, and M. Lotz, "Autophagy activation by rapamycin reduces severity of experimental osteoarthritis," *Annals of the Rheumatic Diseases*, vol. 71, no. 4, pp. 575–581, 2012.

[32] X. Wu, Y. Cai, S. Lu et al., "Intra-articular injection of chloramphenicol reduces articular cartilage degeneration in a rabbit model of osteoarthritis," *Clinical Orthopaedics and Related Research*, vol. 477, no. 12, pp. 2785–2797, 2019.

[33] J. S. Rockel, M. Grol, S. M. Bernier, and A. Leask, "Cyclic AMP regulates extracellular matrix gene expression and metabolism in cultured primary rat chondrocytes," *Matrix biology: journal of the International Society for Matrix Biology*, vol. 28, no. 6, pp. 354–364, 2009.

[34] X. Wang, F. M. F. Cornelis, R. J. Lories, and S. Monteagudo, "Exostosin-1 enhances canonical Wnt signaling activity during chondrogenic differentiation," *Osteoarthritis and Cartilage*, vol. 27, no. 11, pp. 1702–1710, 2019.

[35] T. Liu, S. Zong, P. Luo et al., "Enhancing autophagy by down-regulating GSK-3β alleviates cisplatin-induced ototoxicity in vivo and in vitro," *Toxicology Letters*, vol. 313, pp. 11–18, 2019.

[36] C. Parr, R. Carzaniga, S. M. Gentleman, F. Van Leuven, J. Walter, and M. Sastre, "Glycogen synthase kinase 3 inhibition promotes lysosomal biogenesis and autophagic degradation of the amyloid-β precursor protein," *Molecular and Cellular Biology*, vol. 32, no. 21, pp. 4410–4418, 2012.

[37] H. H. Zhang, A. I. Lipovsky, C. C. Dibble, M. Sahin, and B. D. Manning, "S6K1 regulates GSK3 under conditions of mTOR-dependent feedback inhibition of Akt," *Molecular Cell*, vol. 24, no. 2, pp. 185–197, 2006.

[38] D. R. Laks, J. A. Oses-Prieto, A. G. Alvarado et al., "A molecular cascade modulates MAP1B and confers resistance to mTOR inhibition in human glioblastoma," *Neuro-Oncology*, vol. 20, no. 6, pp. 764–775, 2018.

[39] L. He, D. L. Fei, M. J. Nagiec et al., "Regulation of GSK3 cellular location by FRAT modulates mTORC1-dependent cell growth and sensitivity to rapamycin," *Proceedings of the National Academy of Sciences of the United States of America*, vol. 116, no. 39, pp. 19523–19529, 2019.

[40] J. Chen, H. Wang, C. Luo et al., "Chd 8 rescued TBI-induced neurological deficits by suppressing apoptosis and autophagy via Wnt signaling pathway," *Cellular and molecular neurobiology.*, vol. 40, no. 7, pp. 1165–1184, 2020.